Characterisation of the Pulsed-laser Induced Phase Transformation and Osteogenic Properties of Photo-active Iron-Calcium Phosphate Biominerals

Emaan Hamad Alsubhe

Submitted in accordance with the requirements for the degree of Doctor of Philosophy

The University of Leeds

The School of Chemical and Process Engineering

Faculty of Engineering and Physical Sciences

November, 2019

The candidate confirms that the work submitted is her own and that appropriate credit has been given where reference has been made to the work of others.

This copy has been supplied on the understanding that it is copyright material and that no quotation from the thesis may be published without proper acknowledgement.

” وقل ربي زدني علما”

“Say, o my lord increase me in knowledge” [1].

Acknowledgements

Firstly, I would like to express my sincere gratitude to my supervisor professor Animesh Jha for his continuous support and assistance of my PhD research and study. His advice and feedback were essential to improve my knowledge and write my thesis. I am grateful to Dr Antonios Anastasiou for his continuous patience and encouragement without his guidance and constant feedback over the past 4 years this PhD would not have been achievable. A special thankyou to Dr El Mostafa Raif for his invaluable advice and support during all the biological experiments.

Also, I would like to acknowledge Mr M Javed, Dr S Myers, Mr S Micklethwaite, Dr Z Aslam, Mrs D Cochrane, Mr S Lloyd, Dr F Esat and Dr C Maddi for their laboratory assistance. I also would like to thank my colleagues; Neelam Iqbal, Dina Abdulaziz, Evangelos Daskalakis, Sandeep Kumar and Aseel Aljaboori for sharing knowledge and experience also for the great time in Leeds.

I would like to thank Taibah University for their financial support during my PhD study and for giving me the opportunity to complete this study.

A special thankyou to my friends Kheir, Amirah, Aishah, Shoug and Fatimah for their love and support which made Leeds a home. I am extremely thankful to my parents, my sisters and my brothers for their prayers and encouragements. Without my parents love and support I would not have managed to begin and complete this research degree.

Finally, to my wonderful son Azzam and beautiful daughter Fajr, thank you for being patient, understanding and supportive especially over the past 4 years. Words cannot express the love, support and patience of my beloved husband Fahad. Thank you for the continuous motivation and support throughout all the struggles that I faced to complete my thesis.

Abstract

Personalised medicine and near patient manufacturing are two emerging concepts in tissue engineering. They are based on the design and manufacture of individual bone grafts which are dependent on the needs of individual patients. To date, the most efficient method to achieve this is through selective laser sintering (SLS), which has been one of the most developed and successfully applied techniques [2]. Various forms of calcium phosphates (CaP) have been used so far for scaffold manufacturing through SLS because of their compositional and structural similarity with the mineral within human bone and teeth. The main drawback of bone and tissue-like materials has been the lack of vascularisation which limits blood supply to essential healing areas. Recently there has been an increasing interest in Fe^{2+}\Fe^{3+} doped calcium phosphates due to the essential function of iron in regulating oxygen through hemoglobin in human body [3]. In addition, it was reported that doping brushite ($CaHPO_4.2H_2O$) with Fe^{2+}/Fe^{3+} ions, improved energy absorption and controlled the volume of energy absorbed region [4]. The Incorporation of Fe within CaP's lattice resulted in the characteristic thermal phase transformation temperatures to shift to lower values, thereby promoting densification and sintering.

The aim of the present work is to identify an optimum doping concentration of sintered β-CPP ($Ca_2P_2O_7$) doped with Fe ions. The mechanical properties, biological response and the scaffold fabrication potential in relation to laser-matter interaction will be fully investigated.

Various concentrations of iron (0 mol%, 5 mol%, 10 mol%, 20 mol% and 30 mol% by substituting ca^{2+}) doped brushite powder were synthesised and sintered at temperature of 1000ºC for 5hrs. A femtosecond pulse laser emitting at a wavelength of 800 nm with 1 KHz repetition rate was used to create micro-channels in the surface of the samples to investigate the effect of surface properties in cell behaviour.

Table of contents

List of Figures

List of Tables

List of Publications

A. Paper published

The conference paper that have been published are:

- E. Alsubhe, A. Anastasiou, C. Maddi, El. M. Raif, P. V. Giannoudis, and A. Jha, "Interaction of Femtosecond Pulsed Lasers with Fe^{2+} and Fe^{3+} Doped Calcium Phosphates for Bone Tissue Engineering". Optical Society of America. https://doi.org/10.1364/BODA.2019.JT4A.36. This is a conference paper presented at the Biophotonics Congress: Optics in the Life Sciences Congress 2019, Tucson, Arizona United States 15–17 April 2019. The paper discussed the effect of Fe^{2+}/Fe^{3+} doping CaP inducing of laser-matter interaction and how this interaction affected the biological response.

B. Papers for future submission

The papers that are going to be submitted between December and March 2020 are:

- E. Alsubhe, A. Anastasiou, El. M. Raif, M. Mehrabi, A. Hassanpour, P. V. Giannoudis, A. Jha, "Analysis of the Osteogenic and Mechanical Characteristics of Iron (Fe^{2+}/Fe^{3+})-doped β-calcium Pyrophosphate ". This paper investigates the effect of Fe^{2+}/Fe^{3+} ions on the brushite structure as an initial phase. The characterisation of initial FeCaP samples and sintered samples using thermal annealing are also discussed. In addition, the effect of sintered FeCaP samples relating to mechanical and biological properties are presented.
- E. Alsubhe, A. Anastasiou, C. Maddi, El. M. Raif, P. V. Giannoudis, and A. Jha, "Femtosecond pulsed laser micromachining of Fe^{2+}/Fe^{3+}-ion doping β-calcium pyrophosphate for Bone Tissue Engineering". In this paper, we investigated how different concentrations of Fe^{2+}/Fe^{3+} ions-doped Cap minerals and how this affected the laser-matter interaction. Phase transformation of samples after laser interaction are characterised using different techniques. The effect of micromachining on cell attachments is also investigated.

Abbreviations

CaP	Calcium phosphate biomaterials
HAP	Hydroxyapatite
TCP	Tricalcium phosphate
β-CPP	β-calcium pyrophosphate
FeCaP	Fe doped calcium phosphate
XRD	X-ray powder diffraction
GIXRD	Grazing incidence x-ray diffraction
FTIR	Fourier infrared spectroscopy
ATR	Attenuated total reflectance
SEM	Scanning electron microscopy
EDX	Energy dispersive X-ray
STA	Simultaneous thermal analysis
TGA	Thermogravimetric analysis
DTA	Differential thermal analysis
TEM	Transmission electron microscopy
ALP	Alkaline phosphatase
ATP	Adenosine triphosphate
ZP	Zeta potential
XPS	X-ray photoelectron spectroscopy
AAS	Atomic absorption spectroscopy
SLS	Selective laser sintering
UV-Vis	Ultraviolet visible spectroscopy
BFM	Bright field optical microscope

Chapter 1 Introduction and objectives

Chapter introduction

This chapter started with a brief introduction of bone structure and the need for bone material tissues that have an ideal properties as bone scaffold and can overcome the shortage of other bone material scaffolds. The main aim and the outline of this project were discussed.

1.1 Overview

Bones are considered to be one of the most important structures in the body since they support the body weight and provide essential regenerative cells for healing the damaged tissue.70% of bones consist of calcium phosphate (CaP) in its hydroxyapatite form (HAp) whilst the 20% are composed of soft tissues [5]. In the case of an injury, the bone is able to regenerate itself. Also a bone can be regenerated as a part in the development of the skeletal system [6, 7]. Nevertheless, delays in healing of union-fractures that can take more than six months to heal, non-union fractures where broken bone cannot be healed without surgical intervention and/or defects of long bone as well the number of patients with bone disorders have increased dramatically during the last decade [8, 9]. This observation is driving the need to establish an effective strategy for bone fracture healing.

During the process of bone defect surgery, various fundamental factors are considered in what is known as the diamond concept. This includes: osteoconductivity of scaffold, osteoinductivity, osteogenic cells, osteointegration with host tissue, sufficient vascularization and mechanical stability [10]. Autografts are generally considered as the gold standard for bone regeneration. However, the need of second surgery accompanied with pain and site morbidity have limited their applications. Allografts also have been utilised for bone repair. The high cost and disease transmission restricted their applications as well [11, 12].

A significant work has been done regarding new biomaterials that could be used in scaffold fabrication for bone regeneration [11]. The aim of the biomaterials that have been investigated so far, was either to present an optimised biological performance (i.e. biocompatibility and enhanced cell proliferation) or to have mechanical properties similar to that of natural bone. In recent years, there has been an increasing interest in calcium phosphate biomaterials (CaP) because of their chemical compositions and structure that are similar to hard human tissue. In addition, CaP is known to have excellent biocompatibility and osteoconductivity.

A key issue of using CaP is their poor mechanical properties. However, this issue can be addressed through anionic and/or cationic substitution ions such as zinc Zn^{2+}, Na^{+} and iron Fe^{2+}\Fe^{3+} into CaP crystal lattice. In addition, the main challenge faced by many researchers is the creation of an adequate vasculature network, since it is important for supplying oxygen and nutrients to the cells [13]. $Fe^{2+/}Fe^{3+}$ ion is a major area of interest because of its biological properties since it plays a crucial role in regulation and transportation of oxygen from lunges to the rest human tissues thereby transporting the nutrients which enable cells to survive [14]. Therefore, it might stimulate angiogenesis in the scaffold.

The processing potential of the biomaterial is critical to determining the appropriate manufacturing route that will lead to the fabrication of the scaffold. Current trends in tissue engineering as for example personalised medicine and near patient manufacturing, favour the use of additive manufacturing techniques with selective laser sintering (SLS) being one of the most well established and widely used methodologies. However, biomaterials that have good interaction with lasers are needed. The improvement of the mechanical properties of CaP biomaterials as well sintering process enhancement were achieved through the addition of $Fe^{2+/}Fe^{3+}$ as a dopant during sintering process done using femtosecond pulsed laser at 1045 nm and 1GHz [4, 15]. Using this technique, sintering can be localised without affecting the surrounding area, therefore, it can be safe to use in tissue engineering applications with proper scaffold materials. Micromachining using femtosecond laser in the scaffold can induce the cell adhesion that is the basic factor to induce cell growth.

1.2 General objectives

The overall aim of my project is to design mineral phase which can be readily processed using a femtosecond pulsed laser for meeting at least three of the four essential conditions for damage bone restoration. These three conditions are load bearing biomechanical, osteoconductivity and

osteogenesis. Since CaP mineral is widely used the part of my overall aim will examine:

- The laser-matter interaction for the fabrication of personalised scaffolds.
- The mechanical properties.
- The biological responses (cell adhesion and proliferation).

1.3 Document structure

- Chapter 1: This thesis begins by brief introduction of this project, followed by the purpose and objectives of the PhD research work.
- Chapter 2: This chapter provides a brief overview of the structure of bones and their significant role in human body. Bone defects have been also considered in this part. Different forms of calcium phosphate materials were reviewed. The use of femtosecond pulsed laser for bone tissue materials to develop mechanical properties and biological behaviour was also discussed.
- Chapter 3: This chapter begins by laying out the materials that were used for the research and looked at the methodology that was used to accomplish the aims of the research work. .
- Chapter 4: this chapter presents and discusses the findings of experimental work, and characterisation of the synthesised and sintered materials using different techniques such as XRD, FTIR and SEM. Measurements of hardness and Young modulus were also included in this chapter. The influence of different concentration of Fe ion on cytotoxicity assay and cell proliferations for all sintered samples was discussed.
- Chapter 5: In this chapter, results from micromachining using femtosecond pulsed laser ablation was presented including characterization of the materials before and after laser irradiations.

The effect of Fe ion concentrations on the ablation mechanisms and thus in cell adhesion was discussed.

- Chapter 6: The influence of the Fe ion concentration on transform crystalline structure into amorphous phase was investigated looking at pH, zeta potential and classical nucleation theory. In addition, the effect of dopant concentrations in the activation energy as well the sintering process were also illustrated.
- Chapter 7: The main findings of this research were summarised in this chapters, along with suggestions for future work.

Chapter 2 Literature review

Chapter introduction

Bones are very significant part on the body since they not only support the weight, but also provide essential regenerative functions. A damaged bone has the potential for healing, provided the following essential functions are enabled. These are: supporting angiogenesis for carrying nutrients for tissue restoration, provide environment osteogenesis leading formation of hard minerals by using the growth factors and bone morphogenic proteins, available in situ and support mechanical function by load transmission. The absence of any one of the above factors becomes apparent when a damaged bone does not heal. In our body, there is a limited supply of bone for tissue transplant. During surgery autologous tissue is harvested for transplant for promoting healing. Allografts are foreign body tissues, which are often mixed with bone cement [16] and harvested autograft. In cases of bone restoration surgery, when there is shortage of autologous and allograft tissues, xenograft (animal) extracellular matrix may also be used. However, the rejection rates for allografts and xenografts are much higher than that when autologous tissues are used [17]. Bone tissue materials such as polymers, bio-glass ceramic and calcium phosphate minerals (CaP) have been investigated to overcome the shortage of autograft, allograft and xenograft. Since bones consist of some elements such as Mg, Zn and Fe ions, they were incorporated with bone materials to enhance efficiency of the scaffold. Additionally, using femtosecond pulsed lasers could create structures that support both mechanical and biological properties of materials.

Chapter summary

In this chapter, the structure and function of bones was discussed. The advantages and disadvantages of autograft allograft and xenograft were briefly mentioned. The needs for bone tissue materials with good biological response and can be found in relatively huge quantity such as polymers, bioglass ceramic, titanium and its alloys was also investigated. Since CaP minerals have chemical compositions structure similar to human hard tissue, they were studied extensively. However, their poor mechanical properties limit their applications. Various ions doped CaP minerals was mentioned and the interest focus of using Fe^{2+}/Fe^{3+} ions as a dopant materials was also investigated. Finally, the positive effect of ablation and sintering using femtosecond pulsed laser on both biological performance and mechanical properties was discussed.

2.1 Background of bone regeneration

2.1.1 Bone structure and function

Bones are the most important structures in the body as they carry the body weight and provide essential regenerative cells for healing the damaged tissue. They consist of tissues such as cells and blood vessels and also minerals and water. In addition, bones play an essential role in the formation of blood inside bone marrow. 70% of bones is composed of calcium phosphate in the form of hydroxyapatite (HAp) [5]. By examining the anatomy bones it is evident that the mineralized structure has cortical and cancellous bone structures as shown in Figure 2.1. Cortical bones possess a lower level of porosity than cancellous bones, therefore higher mechanical properties to support body and less blood vessels. In contrast, since the porosity in cancellous bones is higher than in cortical bones, it lowers their mechanical properties. The concentration of blood vessels in this type of bones is higher than that in the cortical bones.

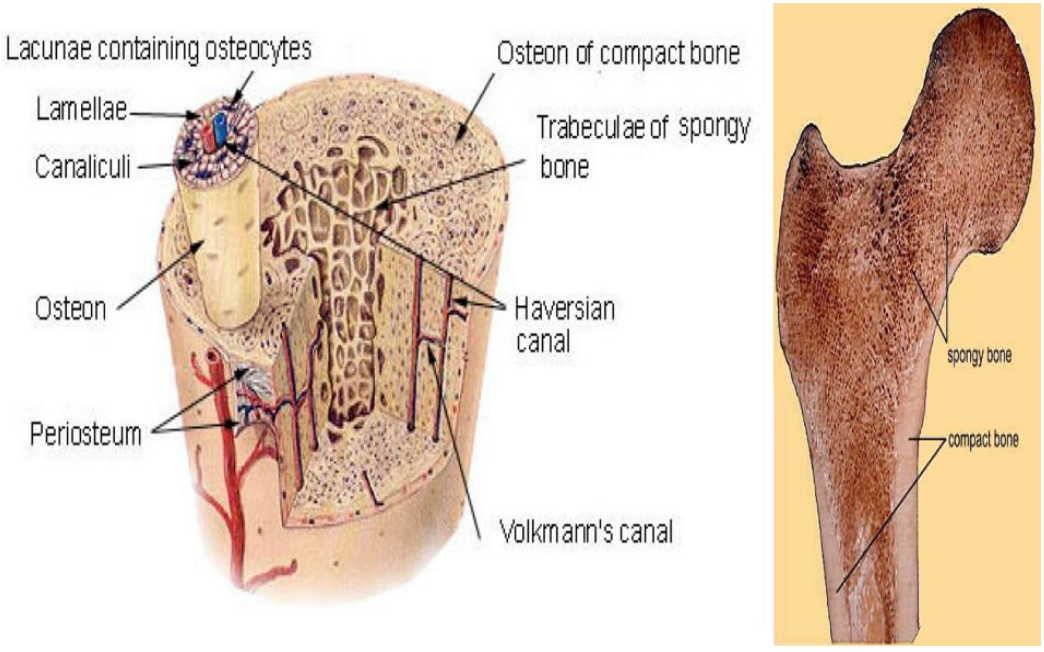

Figure 2.1: Structure of bone includes the two types cancellous (spongy) and cortical (compact) bone [5].

Cancellous bone consists of a network of trabeculae with rod or plate-like structure and a diameter of rod ranged between 50-300µm. Whereas, a

cortical type is composed of osteon system, in this system the collagen fibres arrange in sheet structure called lamella with channel of blood vessels in the centre. As shown in Figure 2.1, osteon forms an onion-like structure, it is built first through the osteoclast that forms the cavity, then it is filled by osteoblast forming the cement layer and lamella.

2.1.2 Bone biology and regeneration potential

Bone is a regenerative tissue which heals without scar, it has the ability for regeneration after an injury or as a part of skeletal development [6, 7]. A series of biological operation are involved during the process of bone regeneration for fracture healing in order to restore the bone and its function. In this operation bone cells are involved. Bone cells are osteoclasts that are responsible for bone resorption, osteoblasts which form bones and osteocytes that work to regulate osteoclast and osteoblast activities during bone remodelling [18]. Factors such as growth factors and calcitonin are also contributed in this process. Bone matrix is also involved in bone regeneration process by releasing molecules that are important for activating bone cells as well it supplies the mechanical reinforcement.

The new generated bone has mostly the same properties of the previous bone to the extent that it cannot be distinguished from the undamaged bone [6]. However, any disparity between osteoblasts and osteoclasts can lead to different bone diseases such as osteoporosis. Also, in some cases, the healing process may take either long time or cannot proceed. For instance, 13% of tibia fracture healing are accompanied either with non-union fracture healing or delay union fracture healing. Further, large quantity of bone generation is in high demand in some orthopedic surgery [6].

2.1.3 Osteoporosis and bone fractures

Osteoporosis refers to a reduction of bone mass therefore, the risk of bone fracture increases [19, 20]. As shown in Figure 2.2 below, the risk of osteoporosis varies between genders; women have a greater percentage of hip fracture at the age of 50 in comparison to men (between 11 and 18%) in USA and northern Europe [19, 21]. In Denmark, a high percentage

occupancy of hospital beds is associated with the hip fracture [21]. Therefore, orthopaedic surgeons have attempted to use different techniques in order to find a better method for bone regeneration.

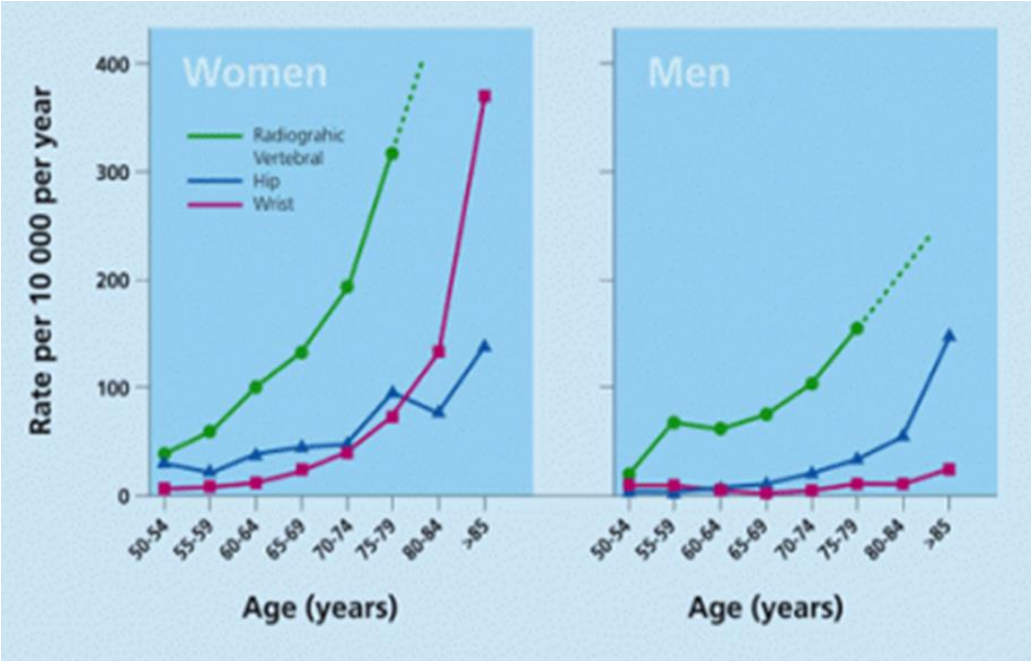

Figure 2.2: Illustration of the vertebral, hip and distal forearm fractures according to gender and age [22].

2.2 Bone tissue engineering

2.2.1 Autograft, allograft and xenograft

As previously mentioned that bone has the ability to repair injury, however, long bone defects, non-union fracture healing or the delay of union fracture healing induce surgeons to find out a solution for helping bone fracture healing [8]. During bone defect surgery, various essential factors of the bone tissue materials must be taken into account. Firstly, the graft that is applied should have the ability to support bone and works as a framework, this process is known as osteoconduction. The second factor is osteoinduction of the graft materials which is the process that induces osteogenesis. Osteogenesis is the produce of bone cells (osteoclast, osteoblast and osteocytes) to form new bones. Finally, osteointegration, where the graft tissues connect with the host tissues, should be achieved [23-25].

Autograft is the tissue which is harvested from the patient and it is considered as a gold standard for bone regeneration. Due to the accessibility to great quality and quantity of cancellous bone in iliac crest, it is the most commonly selected graft site [26] . However, the need of second surgery which increases the overall surgical time, the pain, infection and the delay of cure time shorten their utilisations [27]. Further, in some cases like in orthopaedic and maxillofacial surgery that are caused by tumour resection or infection a high quantity of bone tissue materials are required, which limits the quantity of harvested autologous tissue. For this reason, the surgeon may carefully select and autograft mixed with disinfected allograft.

An allograft is derived from cadaver or living healthy donor and is more abundant than autograft for surgical use. The advantages of allograft over autograft is a high quantity of allograft that can be customised in various shapes such as dowels and strips [8]. The disadvantages of allografts are morbidity and disease transmission [11, 12], which is why there is a downside of using cadaveric and healthy donor allograft, triggering autoimmune response of the body after transplant for rejecting the implant which tends to compromise the healing process. Due to the immune response in particular when using living tissues, allografts are hardly applied. The second allografts suppliers can be in a frozen or freeze-dried form.

The transportation of disease through allografts could be reduced during the preparation procedure. For instance, in bone repair with fresh-frozen allograft it was associated with transmission of HIV virus. Whereas, using freeze-dried form, the transmission of the virus did not occur. However, the mechanical properties and biological performance of the bone will be lowered and there is the probability that osteogenesis process may not commence [27, 28].

In cases of bone restoration surgery, when there is shortage of autologous and allograft tissues, xenograft (animal) extracellular matrix may also be used. This kind of grafts are usually used with allograft or growth factors.

To avoid the transportation of diseases and the immune response, the organic materials were removed from the xenograft. However, this result in poor osteogenic performance when use for bone repair [29].

These drawbacks make it necessity for finding a new path for bone regeneration having the essential factors for a prober bone healing as well to overcome the deficiency of bone graft materials [30]. Thus, synthetic bone tissue materials have been investigated.

2.2.2 Bone synthetic materials

For an ideal synthetic bone material, it must have the essential factors to form and heal bone as mentioned earlier. Beside these factors, biocompatibility and the mechanical properties of these materials should be similar to that of human hard tissue. Various materials have been synthesised for bone regeneration such as the metals and alloys of titanium, polymers (polylactic-co-glycolic acid (PLGA) and polycaprolactone (PCL), ceramic and glassy materials (calcium phosphate and bioactive glasses), and polymer-ceramic composites, Table 2.1 [31, 32].

2.2.2.1 Titanium and its alloys

The key factor of the scaffold for bone is to support bone by working as osteoconductive as well to allow cells for attachment and proliferation therefore, formation of healthy bone [33]. Titanium and its alloys have been used in bone regeneration/replacement due to their biocompatibility and excellent mechanical properties [33]. They have been used in bone regeneration particularly in total joint implants. Titanium is considered as a high biocompatible materials in comparison to other metals biomaterials such as stainless steels [34]. One of its advantages, it forms a TiO_2 passive layer that serves as a corrosion protection layer [34].

The obstacles of using titanium alone are its poor bioactivity and lower osteointegration also are not bioresorbable. To overcome these limitations autograft was employed with titanium mesh cage to improve its efficiency in spin fusion [35]. However, the higher stiffness of titanium implant than the natural bone may damage the adjacent bones [36]. Therefore, bone

synthetic materials that have mechanical properties similar to bone as well biodegradable and osteointegration properties is required.

Table 2.1: Examples of bone materials with their advantages and drawbacks to use as a bone repair [30].

Bone materials	**Examples**	**Advantages**	**Drawbacks**
Natural polymers	Protein: collagen, fibrin. Polysaccharides: alginate, chitosan.	Biocompatibility, bioactivity and biodegradability.	High degradation ratio Poor mechanical strength
Synthetic polymers	polylactic-co-glycolic acid (PLGA), polylactic acid (PLA)		
Bioglasses ceramic	Silicate bioactive glasses (45S5)	Biocompatibility, biodegradability osteocondictive and osteoinductive.	Poor mechanical properties Brittleness
Composites	Hydroxyapatite HAp coatings on titanium HAp/chitosan	Combination of ceramics, polymers and metals advantages	Combination of ceramics, polymers and metals disadvantages
Calcium phosphate ceramics	Hydroxyapatite HAp β-Tricalcium phosphate (β-TCP) Brushite	Biocompatibility, biodegradability osteoconductive and osteoinductive.	Poor mechanical properties Brittleness
Metals	Titanium and its alloys Stainless Steel	Excellent mechanical properties	Poor osteointegration Corrosion

2.2.2.2 Polymers

Polymers are used as bone graft materials due to their bioresorbable properties, two types of polymers have been investigated:

2.2.2.2.1 Natural polymers

Natural polymers include proteins such as collagen and fibrin gels or polysaccharides such as chitosan and alginate. Since bones consist of natural polymers such as collagen, these polymers have been used for substitute collagenous structure of natural bone. Beside biocompatibility, natural polymers support adhesion of cells and cell proliferation [32].

2.2.2.2.2 Synthetic polymers

Synthetic polymer is a type of bone cement which is the material that consist of two elements: powder (polymers or amorphous powder) and liquid. The most common polymer bone cements that have been used in bone scaffolds are polycaprolactone (PCL), polylactic-co-glycolic acid (PLGA), polylactic acid (PLA) and polyglycolic acid (PGA) [37]. When using a PLGA copolymer scaffold, the degradation rate can be controlled by modifying the ratio of its monomers [38]. The advantages of using polymers as scaffold are; it is bioresorbable and has biocompatible properties [39].

Perhaps the most serious disadvantage of both types of polymers is poor mechanical properties that restrict their applications to non-load bearing only. Other drawbacks are the lack quantity of natural polymers and the reduction of bioactivity for synthetic polymers (cell adhesion).Therefore, researchers have incorporated some of these polymers with other bone graft materials such as ceramics [40].

2.2.2.3 Bioactive glasses

It was found that some glass compositions are biocompatible and had a good bonding with host bone. The reason of good bonding was put down to the surface layer of calcium deficient, carbonated phosphate that bioactive glass forms during implantation [41]. Thus, bioactive glass ceramic

scaffolds have been investigated to apply as a bone graft materials due to their high osteointegration and osteoinduction.

There is a lot of literature on bioglass, which was invented by Late Professor Larry Hench at the University of Florida [42]. After the first report, there was another report on the bio-activity of a different type of bio-glass in Turku, Finland, which were reported such as silicate glass S53P4 that consists of Na_2O 23; CaO 20; B_2O_5 4; SiO_2 53 (wt%) [43, 44]. Bioglass is used for bone regeneration due to its biological function. When ions release from bioglass such as calcium and phosphorus they could lead to increase in the pH which can induce cell proliferation and differentiation (pH 7.5-9). In addition, both calcium and phosphours ions are also induce biomenralisation of bioglass materials.

Xynos et al. [45], reported the use of bioactive glasses 45S5 contains 45% SiO_2, 24.4% CaO, 24.5% Na_2O and 6% P_2O_5 for enhancing bone formation. In a comparative study of bioactive glass with the control cells in culture media without 45S5 after six days, the density of osteoblast alkaline phosphate ALP activity in 45S5 was higher than the control substrates. Nevertheless, bioactive glasses enclose in non-load-bearing applications when used alone due to poor mechanical properties and inadequate fracture toughness [46]. Therefore, they can be better utilised as a coatings of polymer structures [41].

2.2.2.4 Composites

Polymer- bioactive glasses/ceramic composites were developed to combine the benefits of the biological and mechanical properties of two bone materials types. For example, using bioactive glass for coating polymer to induce the bioactive conduct to the polymer structure [41]. For ceramic composites, the strength of ceramics is better than in the polymers, while polymers are flexible and have a higher degradation rate than ceramics [32]. Since bioglass has bioactivity properties and polymers are known for their toughness, Bonfield et al. [47], synthesised bioglass® polyethylene composite that might be used in load bearing applications.

Based on the fact that bone is composed of 70% inorganic mineral and 20% of bone is collagen and other organic materials, polymers (e.g: collagen, polyethylene) have been combined with calcium phosphate ceramics such as HAp by Bonfield and co-workers [47-49]. In certain cases, autograft from patient may be needed therefore second surgery is required [32].

Additionally, owing to the bioactivity and osteointegration of ceramics, surgeons have been incorporating ceramics with titanium and its alloys. Due to the chemical compositions that are similar to human hard tissue calcium phosphate minerals, can be used as a composite materials or alone. [34, 50].

2.2.2.5 Calcium phosphate ceramics CaPs

The investigation of calcium phosphate (CaP) ceramics for manufacturing materials in orthopaedics is of particular interest because of their chemical and structural similarities with the natural mineral of bone [51, 52]. The CaP cements are utilised in two different types: apatite forms (basic) and acidic, as shown in Table 2.2 [53]. Hydroxyapatite HAp is the generic calcium phosphate with a chemical formula ($Ca_{10}(PO_4)_6(OH)_2$). Examples of acidic form of CaPs are brushite ($CaHPO_4.2H_2O$), monetite ($CaHPO_4$), and tricalcium phosphate (TCP) ($Ca_3(PO_4)_2$).

2.2.2.5.1 Hydroxyapatite (HAp)

As explained above, the hydroxyapatite HAp is used widely in bone replacement since the majority of natural bone consists of 70% HAP. The crystal structure of HAp was discovered in 1964, which is a hexagonal system with a space group $P6_3/m$ and lattice parameters a, b= 9.432 Å, c=6.881 Å. It consists of two calcium ion sites Ca(I) (columnar) and Ca(II) (hexagonal) [54, 55]. Different methods have been adopted to synthesis of HAp also other forms of CaP can be used for the preparation. For example, monetite was used to synthesise HAp in order to improve the morphology control. Ma et al. [56], employed microwaves to ensure the transformation of monetite to HAp form.

Table 2.2: Different forms of calcium phosphate depending on their ratios [57-69].

Calcium phosphate	Formula	Ca/P molar ratio	pH	Lattice parameters	Space group	Density (g/cm^3)	Young's modulus	Hardness
Hydroxyapatite (HAP)	$Ca_{10}(PO_4)_6(OH)_2$	1.67	9-11	a, b= 9.432 Å, c=6.881 Å	$P6_3/m$	3.16	14GPa	0.14GPa
Brushite	$CaHPO_4{\cdot}2H_2O$	1.0	4-6	a = 5.812Å, b= 15.180 Å, c = 6.239Å	I2/a	2.30	7.4 GPa	0.9GPa
β-Tricalcium phosphate (TCP)	$Ca_3(PO_4)_2$	1.5	8	*a* = 10.439Å, *c* = 37.375Å	$R3_C$	3.07	24GPa	0.63GPa
Octacalcium phosphate (OCP)	$Ca_8(HPO_4)_2(PO_4)_4{\cdot}5H_2O$	1.33	5-6	*a* = 19.692Å, *b* = 9.523Å, *c* = 6.835Å	$P1^-$	2.67	-	-
Monetite	$CaHPO_4$	1.0	4-6	a = 6.91 Å, b = 6.627 Å, c = 6.998 Å	$P1^-$	2.93	0.35 GPa	0.12GPa
β-calcium pyrophosphate (β-CPP)	$Ca_2P_2O_7$	1.5		a,b=6.684 Å, c=24.144 Å.	$P4_1$	3.09	-	0.32GPa

2.2.2.5.2 Brushite

Brushite is also identified as dicalcium phosphate dihydrate and is considered as a precursor for apatite phase. First characterisation of brushite was in 1865 by George Brush [70]. It is a monoclinic crystal with space group I2/a [71]. Brushite is comprised of layer structure which consists of sheets of polyhedral CaO_8 and tetrahedral PO_4. Two oxygen atoms from CaO_8 are bound to water while phosphate groups are bound to the remaining six oxygen [72]. It is a crystalline form that can be prepared from an aqueous solution in an acidic pH from 4-6 and temperature of 37 ºC. The morphology of brushite crystal is well known to have a plate-like structure [73].

Brushite has been utilised as a bone replacing materials because of its fast setting reaction, availability of starting materials and good biological properties [74]. As well, its degradation ratio is much higher than HAp, therefore, it has been applied in bone tissue materials [75].

2.2.2.5.3 Monetite

Monetite or dicalcium phosphate anhydrous has a triclinic structure, with that has $P1^-$ space group [76]. It can be prepared by the dehydration of brushite. Also synthesis of brushite at a low pH can lead to the formation of monetite phase.

2.2.2.5.4 β-calcium pyrophosphate (β-CPP)

CPP with formula ($Ca_2P_2O_7$) can be formed through the heating of brushite at temperature higher than 370ºC [4]. It contains three polymorphs including: α, β, and γ [77]. β-CPP is a tetragonal structure with space group $P4_1$ and was first studied by Webb [78].

β-CPP form has been studied as a bone graft material. In its comparison with HAp, it provides a higher resorption rate than HAp, as well It is a non-toxic and bioactive material [79, 80]. β-CPP can be prepared by thermal sintering of brushite between 700-1000℃ [4, 81].

The solubility of CaP materials depends on the pH is presented in Figure 2.3 where the physiological pH is equal to 7.4. As the calcium to phosphor ratio increases Ca/P, the basicity of material increases, Table 2.2 [82]. In Figure 2.3, HAp is the most stable material at pH>5, while the most soluble CaP is brushite and monetite at pH higher than 5 since they form in an acidic solution.

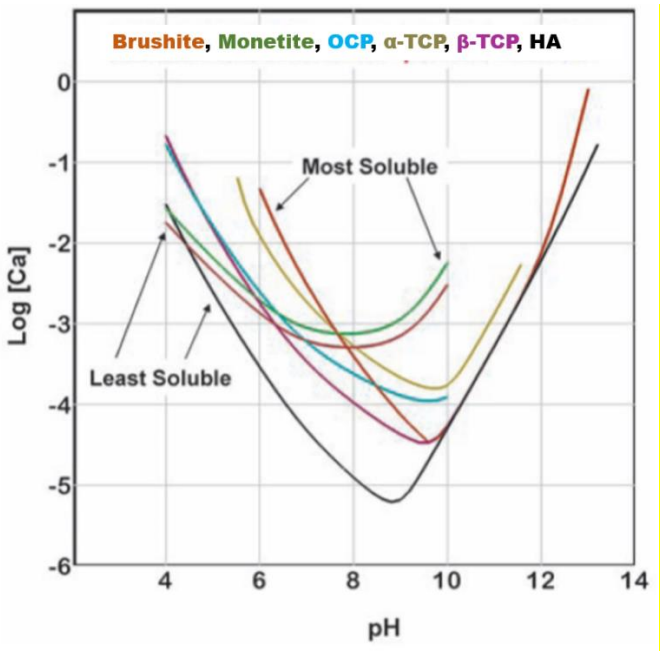

Figure 2.3: the solubility of CaP materials (brushite, monetite, OCP, α-TCP, β-TCP and HAp) as a function of pH [83].

2.2.2.5.5 Applications of calcium phosphate minerals for bone tissue engineering

Uchida et al. [84], employed HAp as an implant for bone repair after amputation of tumours in 60 patents at different bone sites. They found that HAp integrated well with host bone as well as osteoblast cells in HAp implants were observed. However, no evidence of degradation was observed even after a long period (more than 5 years).

Matsmuine et al.[85], reported comparable reports on the use of HAp as a bone filler for defect restoration. According to this report, osteointegration

and new bone formation were observed after tumour resection surgery. Furthermore, no toxic or infection of the implants were revealed. In their short- term study, it was particularly observed that the HAp implant presented a lower resorption rate.

In exploring CaP incorporation with titanium, Wang et al. [86], implanted titanium alloy (Ti-6Al-4V) with and without plasma-sprayed HAp coating in femur of dogs for 4, 6 and 24 weeks. In their work, they tested the osteoconduction and osseointegration for both implants with surrounding bone using scanning electron microscopy (SEM). It was found that the implant of titanium coated with HAp had higher new bone formation in comparison with titanium without HAp, indicating the implants were more osteoconductive with HAP and osseointegration was also observed. However, no induction of osseointegration was seen in titanium implants without HAP coating on the SEM.

Since the calcium phosphate minerals are known to have poor mechanical properties, different ions have been incorporated in their lattice such as iron Fe^{2+}/Fe^{3+}, silicon Si^{4+}, magnesium Mg^{2+} and Zn^{2+} in order to enhance both mechanical properties and biological performance of these minerals.

2.2.2.6 Ionic substituted bone synthetic materials

Natural bones consist of various ions such as silicon Si^{4+}, sodium Na^{+}, magnesium Mg^{2+} and play an essential role in bone formation. Using trace elements with calcium phosphate open a new opportunity to improve the mechanical properties of the scaffold, as well as could control the degradation ratio [87]. Studies have been applied these ions in bone regeneration scaffolds to study their effect on bone formation and growth also in mechanical properties.

2.2.2.6.1 Ionic substituted calcium phosphate (CaP)

As mentioned previously, HAp with the formula $Ca_{10}(PO_4)_6(OH)_2$ has been used extensively as bone synthetic materials. Biological HAp is found to have some impurities that can substitute Ca^{2+} [88]. Cation ions (Ca^{2+}) usually prefer to replace by cation ions with similar sizes such as zinc Zn^{2+}

and strontium Sr^{2+}. Whereas, the anion ions (PO^{3-}_4) and OH^- may also be replaced via a combination of anions such F^-, $(CO_3)^{2-}$, $(HCO_3)^-$, SO_4^{2-} and $(HPO_4)^{2-}$ [60]. However, for the replacement of cation or anion ions with different charge needs charge balance by incorporation of additional ions. For instance, the incorporation of carbonate $(CO_3)^{2-}$ into the HAp lattice would replace (PO^{3-}_4) and/ or OH^- that is known as a type-A and type-B substitution. Furthermore, the replacement of (PO^{3-}_4) with silicate ion $(SiO_4)^{4-}$ also need a charge balance which can be established by increasing the electronegative surface. Nevertheless, substitutions of Ca^{2+} has studied widely in bone regeneration more than the anionic substitutions due to their significant effect on biological properties [88].

Since the substitutions of ions in the CaPs lattice change their structure, they can also change their mechanical and biological properties. A number of studies have investigated the effect of ions incorporations in CaPs structure and their properties.

Wange et al. [89], investigated the effect of different concentrations of zinc Zn^{2+}, fluoride F^-, copper Cu^{2+}, strontium Sr^{2+}, and carbonate CO_3^{2-} ions doped CaPs film on biological behaviour. When doped with Cu^{2+} the cell growth decreased when compared to undoped material. When compared with the doped Zn^{2+} ion substitution no difference in the cell density was observed.

Doping using two different ions with CaP was also investigated by Pina et al. [90]. In their work, a substitution of both Zn^{2+} and Zn^{2+}/Sr^{2+} in brushite/βTCP before implantation in trabecular bone of pig model and compared with the control sample β-TCP. The proliferation of osteoblast cells was observed in both Zn-doped and Zn/Sr doped samples. However, doped with Sr^{2+} ions showed higher cell density and new bone formation than the implants doped with only Zn^{2+} ion.

Sr^{2+} is one of the ions that has been used in tissue engineering. In previous study, high concentration of Sr^{2+}, F^- and CO_3^{2-} ions doped CaP a high cells growth was investigated in comparison with undoped CaP, low

concentration of Sr^{2+} doped HAP was found to increase the growth of osteoblast cells and hinder the production of bone resorbable cells (osteoclast cells) [91-93].

The concentration of dopant materials should be taken into consideration as high concentrations of some elements could cause host tissue toxicity or may decrease the mechanical properties as they change the structure [75]. For example, when Zn^{2+} ion replaces Ca^{2+} ion it cause a decrease in lattice parameters since the ionic radius of Zn^{2+} (0.074 nm) is smaller than the ionic radius of Ca^{2+} (0.099 nm), therefore, reduce the cell volume of the material. However, it was found that concentration of more than 20% of both Zn^{2+} and Mg^{2+} (ionic radius 0.072 nm) cannot substitute Ca^{2+} ion [88]. The reduction of cell volume will change the crystal structure and can prevent the crystal growth, thus, reduce the crystallinity of CaP.

In the contrary, Sr^{2+} replace Ca^{2+} ion lead to increase the lattice parameters and cell volume of the CaP as the ionic radius of Sr^{2+} (0.118 nm) is larger than the ionic radius of Ca^{2+} ion and was found that its effect on the unit cell of CaP (β-TCP form) not significant. Therefore, the concentration of Sr^{2+} to replace the Ca^{2+} was up to 80% [88]. Different concentration of Sr^{2+} (0.1, 0.5, 1.0, 1.5, 2.0, 3.0, and 5.0 atom%), were incorporated into α-TCP [94]. The mechanical properties of doped materials with concentration of 1.5, 2.0, 3.0, and 5.0 atom%), were lower than the undoped α-TCP as the Sr^{2+} provides large crystal and change the structure from plate-like to needle-like structure and large voids were observed [94]. Therefore, an optimised concentration of Sr^{2+} was required.

However, the big challenge of bone regeneration is lack of vascularisation, particularly in the long bone graft materials. It was located that materials with high vascularized area provide a high level of new bone formation better than area without vascularisation [95]. Fe^{2+}/Fe^{3+} ions play an important role in oxygen regulation in blood circulation [96]. Therefore, in this project, the effect of Fe-ions as dopant material on bone regeneration was investigated.

2.2.2.6.2 Effect of Iron Fe^{2+}/Fe^{3+} ions in bone regeneration

Recently, Fe^{-}ion has been found to have a major area of interest within the field of orthopaedics because of both its mechanical and biological properties. Fe ion is believed to be a critical element to human life as it has intrinsic capability to deliver and store oxygen through haemoglobin and myoglobin [3]. Haemoglobin (HG) is a protein that delivers most of the oxygen in the human body through the blood [97]. Therefore, the Fe-ions are essential in regulation and transportation of oxygen from lungs to the rest human tissues, thereby supporting cell survival [14]. It also has an important function in bone metabolism [98-100]. In the matter of mechanical properties, doping with Fe^{2+}/Fe^{3+} has been found to improve hardness of the materials [4].

Using Fe ion as a dopant in bone tissue materials exhibited non-toxic results [101, 102]. Fe-doped β-TCP was examined by Manchon et al [102]. Concentrations of 10 mol% and 30 mol% Fe-βTCP implants were operated in a rabbit model. The formation of new bone with osteoblast cells and blood vessels was observed. According to Panseri et al. [103], Fe^{3+}-doped HAP reinforced the osteoblastic cell viability and showed high density of cells in comparison to undoped implant. The key function of scaffold is to support cells adhesion on its surface, the incorporation of Fe^{3+} into CaP scaffold was discovered to enhance the osteoblast cells adhesion [104, 105]. Doping with Fe ion could enhance the degradation rate by creating defects on the CaP scaffold [102]. In Ereiba et al. [106], different concentrations of Fe^{3+} ion (0, 0.05, 0.1, 0.2 and 0.3 mol%) were doped with HAP and their investigations showed that by increase Fe ion concentration the degradation rate and solubility increased.

The biggest challenge was faced by many researchers in large tissue engineering is the creation of vasculature network amongst cell network since it is the micro- and major vasculatures that deliver oxygen and nutrients to the cells [13]. The lack of vasculature compromises cell viability, proliferation and, therefore, leads to tissue integration and ultimately rejection.

2.2.2.6.2.1 Angiogenesis in bone tissue engineering

Angiogenesis is the formation of new blood vessels from the existing vessels, and is crucial in the principle of wound healing and other physiological needs [107]. Although the osteoconduction and osteoinduction are essential steps for bone tissue regeneration, these two steps must be supported and promoted by angiogenesis, which leads to the development of vascularization. Growth factors such as vascular endothelial growth factor (VEGF) have been used in bone regeneration for supporting angiogenesis. However, they are only used for a short period and high doses may also be required [108]. Therefore, a safe and low-cost inorganic materials that could induce angiogenesis are needed.

The Fe^{3+}-ion doping of octacalcium phosphate minerals OCP was found to enhance angiogenesis by Zhang et al [109]. In their study, it was observed that the Fe^{3+}-ions promoted the angiogenic factor in human umbilical vein endothelial cells HUVECs (vascular endothelial growth factor (VEGF) and endothelial nitric oxide synthase (Enos) gene expression).

2.3 Mechanical properties of bone synthetic materials

As mentioned earlier, bones are known to support our body, therefore, characterisation and analysis of mechanical properties such as the hardness, fracture toughness, strength and Young modulus are important properties of bone synthetic materials.

2.3.1 Hardness

Hardness is defined as the measurement of resistance to plastic deformation of material that is caused by mechanical indentation. In this technique measuring the resistance of deformation in material is proceeded by applying load and using an indenter [110].

Hardness depends on the microstructure of a material, the mechanism of microstructure affecting on hardness is explained. Usually in a crystal structure, atoms are arranged in crystal lattice which is 3D array. For example, in a polycrystalline structure may have three kinds of irregularities

(point defects or vacancies, line defects as dislocations, and grain boundaries) which determine the hardness of material hardness [111].

In the case of point defects, three-point defects are placed at a single site of lattice. When an atom is missing from the site it is known as a vacancy defect. For example, the octahedral sites in the Fe_3O_4 inverse spinel may be partially occupied. Whereas, a substitutional defect is said to have occurred when a different atom occupies site of an atom or ionic site. In the context of HAp, the cations, such Sr^{2+} and Zn^{2+} may substitute Ca^{2+} cations, whereas for each biaphosphate $(HPO_4)^{2-}$ ion, can be substituted by a $(CO_3)^{2-}$ion. The last type of defect is called interstitial defect in which an atom occupies sites. The second type of irregularity is line defects that are usually formed as a line defect of atoms or like ions in a single crystal site. Such defects are called dislocation. leads to plastic or permanent deformation therefore, decreasing hardness by the flipping of atoms planes from one side to another of dislocation [111].

Hardness of materials increase when dislocation of planes of ions or atoms are prevented by either intersection of dislocation with interstitial atoms or with another dislocation which so called pinning points [111]. There is a relationship between dislocations and Hall-Petch effect. In the Hall-Petch effect, the hardness increases when the particles size decreases [112]. This increasing of hardness could be assigned to the rise in the amount of grain boundaries area appearing as barriers to stop the dislocation motion. When the material have a large grain size, more dislocation will pile up within the grain and lower force will need to move these dislocations between grains. In contrary, material with small grain size, large force are needed to move dislocations between grains.

Nevertheless, below a critical size of grain (10-20nm), reduction in grain size causes hardness to reduce since the size of dislocations approach grain sizes, this effect is known as the inverse Hall-Petch effect [112]. The mechanism of dislocations motion in this effect is related to grain boundary diffusion, grain boundary sliding or grain rotation [112].

2.3.2 Young modulus

Young modulus is also known as an elastic modulus and it is the reverse proportion between stress and strain according to Hooke's law in the elastic region of material when a load is applied [110].

$$\sigma = E\varepsilon \qquad (2.1)$$

Where, E is elastic modulus, ε is strain and σ defines stress.
The higher the stiffness of a material, the higher the Young modulus. As in hardness, dislocations and impurities can increase or decrease Young modulus.

2.3.3 Fracture toughness

Fracture toughness is defined as the resistance of material to fracture. It depends on the length of cracks that emerge as a result of the impression of the indenter at a particular load. Both the indenter geometry and crack system type such as cone, radial or half penny cracks, should be considered during measurements [113].

For the pyramidal indenter such as Berkovich indenter in nano-indentation test, it can be measured using Lawn Evans Marshall model (LEM):

$$K = \alpha \sqrt{\frac{E}{H}} \frac{P}{C^{3/2}} \qquad (2.2)$$

Where:

- K is the fracture toughness, (MN/m$^{3/2}$) or (MPa. M$^{2/1}$)
- α is LEM coefficient and it depends on geometry of the indenter.
- E is Young's modulus, (GPa)
- H is the hardness, (GPa)
- P is the maximum load, (N)
- C is the cracks length, (m)

2.3.4 Mechanical properties of bone engineering scaffold

Different bone sites have different mechanical properties. For example, the known load-bearing bones are knee, spine and hips since most of the body are supported by them and are the most injured sites [114]. Therefore, in hip fracture, bone synthetic materials should mimic the same properties of hip, as well for knee and spine fracture.

Young modulus and hardness have been measured using nano-indentation technique at a loading rate of 750 μN/s and depth of 1000nm for both human trabecular bone and cortical bone [115, 116]. Young modulus of trabecular in distal femur was 18.14±1.7GPa while for cortical bone in femoral midshaft was 23.45±0.21GPa and 16.58±0.32GPa in longitudinal and transversal directions, respectively. Hardness test for vertebral trabecular from tibia was 468MPa. Whereas, in cortical bone from tibia were 614MPa and 734MPa for the osteons and for the interstitial lamellae in longitudinal direction, respectively [115, 116]. The fracture toughness also was measured of some sites of human bones. For human femur was found to be 6.4 MPa $m^{1/2}$ in longitudinal direction while for human humerus was 3.35 MPa $m^{1/2}$ in the same direction [117].

Table 2.3: Fracture toughness of cortical bone in comparison with other bone replacement materials.

Materials	Fracture toughness
Cortical bone	2-6 MPa $m^{1/2}$ [118]
Titanium alloys	28-108 MPa $m^{1/2}$
HAp	0.5-1 MPa $m^{1/2}$ [118]
β-TCP	0.92±0.04 MPa $m^{1/2}$ [119]
Brushite	0.1 ± 0.02 MPa $m^{1/2}$ [120]

Therefore, suitable mechanical properties for scaffolds can be achieved. Recently, it was shown that Fe^{2+}/Fe^{3+} ions doped brushite improved the mechanical properties of final material products after laser sintering process in comparison to undoped materials [4, 15].

2.4 Beta- calcium pyrophosphate β-CPP as bone graft scaffold

Although, HAP has been employed extensively in bone regeneration/replacement due to its chemical composition similar to bone, β-CPP provides slight similarity of mechanical properties and biological performance to bone [121].

Recently, β-CPP has been suggested as a promising material for human hard tissue [15]. It can be easily formed by sintering of brushite since brushite is believed to have a fast setting reaction as well its stability at room temperature [53]. For biological performance, a mixture of amorphous CPP and brushite was prepared by Grove et al. [121], when comparing these materials with control brushite more bone formation was noticed (33%) of scaffold area and it almost was comparable to trabecula bone 26 to 36% . While for the control only 14% of the area was replaced with bone formation. Also another source of the interest in pyrophosphate is that it might work as a substrate of mineralisation enzyme subsequently increase bone mineralisation and healing [4, 121, 122].

In another studies by Naga el al. [122], an implant of porous alumina scaffold was coated with brushite and then sintered to 1100ºC and 1200ºC which then to transform into β-CPP. After sintering, the transformed β-CPP, when used as implant promoted new bone formation around the implant.

For mechanical properties, sintered β-CPP was found to increase its compressive strength after addition of different concentration (1, 2.5, 5, 7.5, 10, 12 and 15% wt) of $Na_4P_2O_7.10H_2O$ [123]. The value for β-CPP was 159MPa while addition of $Na_4P_2O_7.10H_2O$ up to 5%wt increased the compressive strength to 598 MPa. However, increased the concentration led to coarsening in microstructure and therefore, decreased the densification.

Various methods are utilised to prepare CaP powder including: sol-gel and wet precipitation methods. However, to synthesise ions doped CaP a particular method is considered.

2.5 Synthesis of calcium phosphate mineral for ionic substitution

Various method have been adopted for the synthesis of CaP minerals dependant on the final product that is desired. Synthesis routes such as sol gel, solid-state reactions and wet precipitation method [124]. In this study, wet precipitation method was used to prepare ion doped calcium phosphate material.

2.5.1 Wet chemical precipitation method

Wet Chemical precipitation is the formation of solid substance (precipitate) from an aqueous solutions. In this method different factors are involved such as: pH of the solution, reactants and ratio of the reactant. The different between this method and others methods that the final product is usually crystalline, shorter time is required for final formation and lower temperature as well. Various features can also affect the crystalline structure in this technique: pH, addition of acid, preparation temperature, impurity and concentration of reactants [125].

The reasons for using this method to prepare CaP minerals for bone tissue engineering are : i) to get a single phase without any co-products materials, ii) the careful control of parameters will ensure the reproducibility iii) large quantities are easily obtained and iv) to produce CaPs containing various ionic substitutions [126, 127].

To achieve desirable mechanical properties and biological performance, processing potential of the biomaterial need to be considered which is critical for determining an appropriate manufacturing route that will lead to the fabrication of the scaffold. The current trends in tissue engineering such as personalised medicine and near patient manufacturing, favour the use of additive manufacturing techniques with selective laser sintering (SLS) to be one of the most established and widely used methodologies [128]. In this

regards, femtosecond pulsed laser was selected for use with bone tissue materials.

2.6 Sintering process

The term sintering refers to joining of particles during heat with or without occurring of densifications [129]. Sintering processes are classified into four types depending on the structure and composition of the target material: solid-phase sintering, liquid-phase sintering, vitrification sintering and viscous sintering [130]. The driving force behind sintering is the minimisation of the surface free energy accompanied with densification and/or coarsening [131]. In coarsening, particles sizes increase and can lead to increase in porosity this usually occurs in the first stage of sintering process [132]. Whereas, we say densification occurs when particles are compacted with each other, thus porosity decreases.

In solid-phase sintering, a liquid phase does not exist and the mechanism of atom diffusion, leads to the coalescence of particles and lowers the porosity. On the other hand, a low percentage of liquid in the solid mixture is present in liquid-phase sintering. However, the volume of this liquid may not fill the pore space. Therefore, another process is needed to reach full densification. Likewise for vitrification sintering, liquid is present and it can fill the pores place since the volume of liquid is larger than the solid volume. The formation of the structure after cooling could be crystallization or vitrification. Finally, in the case of glass particles, viscous sintering will take place [130, 133].

The materials presented in this thesis are either in crystalline or amorphous phase, they may be subject to any of the first three sintering processes that have been discussed. When subjected to solid-phase sintering, surface energy reduces with decreasing surface area since the pores reduce which is the driving force of this sintering. There are three stages of this type of sintering: initial, intermediate and final stage, as seen in Figure 2.4 [134].

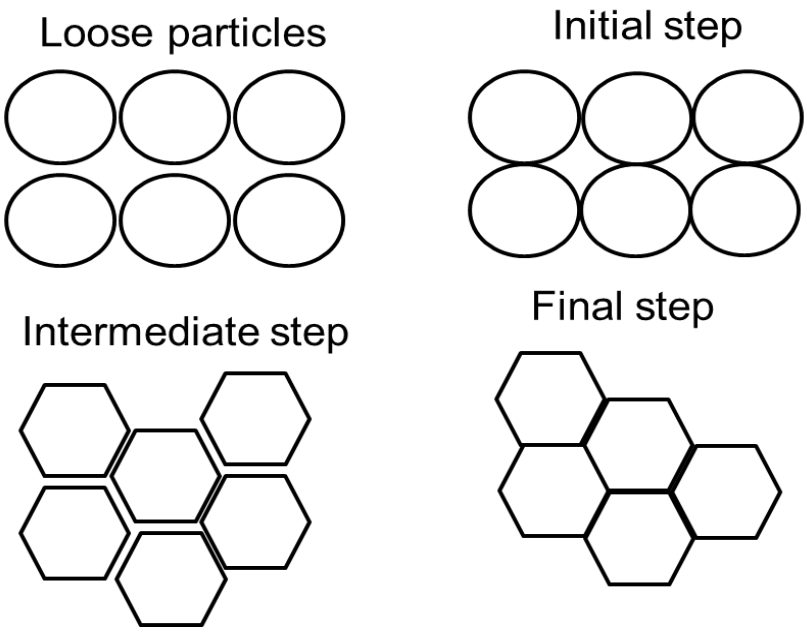

Figure 2.4: Schematic diagram of solid phase sintering stages.

When the sample starts to heat, the distance between adjacent particles decrease which is the initial stage of sintering and only small densification will occur. After that, intermediate stage commences by increasing the contact between particles and each other to form channel-like pores and both grain boundaries and grain growth start to increase. For final stage, the grain growth becomes significant and the microstructure performs by closing pores, therefore, porosity decreases.

Mass transport takes place during solid-phase sintering through various mechanisms: evaporation and condensation, diffusion and plastic flow [130, 133]. The sintering mass transport is divided into two main types of diffusion processes: surface or grain boundary diffusion around the ceramic phase and lattice or bulk diffusion within the grains. A third factor which affects both the surface and lattice diffusion is the metastable strain which may accumulate within material due to processing (pressing, quenching). Both the lattice and surface diffusion rely on the vacancy transport mechanism, however the surface diffusion encounters a lesser kinetic activation barrier than the lattice diffusion. For diffusion transport, the kinetic barrier is dependent on the lattice energy or enthalpy of formation of the intrinsic cation-anion pair which controls the formation of lattice and surface vacant sites [135]. As a result of sintering, the vacancies may rearrange and

introduce porosities, by accumulating them at the energetically favourable sites which might be grain boundaries, dislocations or defects.

A common macroscopic occurrence during sintering is volumetric shrinkage, which may occur when the load is applied during hot pressing, causing plastic deformation which then leads to porous volume reduction and increase in the densification. The mechanisms that accompany with shrinkage during sintering are plastic flow and lattice diffusion within the grains which cause pore reduction or elimination therefore, densification will take place [136]. On the other hand, for evaporation and condensation and surface diffusion, densification will not exist with sintering since the microstructure takes place without shrinkage. In these mechanisms coarsening will occur instead as the driving force of the sintering decreases, as a consequence, high porosity and critical densification reduction can be produced [136].

There are different factors that can affect sintering in a way that changes the sintering rate or develops the mechanical properties of the materials. Generally speaking, elevating temperature will increase the sintering process, however, for different mechanisms the effect of temperature increase may change. Whereas, the effect of dopant on sintering process may vary dependent on the dopant's properties. For example, when the dopant concentration is higher than the solubility limits of solution, a second phase will be present. The replacement of dopant with the material ion that has different charge could increase the concentration of vacancy. Thus, addition of dopant may increase or decrease densification or the rate of sintering process [131].

Since the liquid is present in liquid-phase sintering, the mechanism of mass transport occurs via dissolution and resolidification of the particles. However, densification is lower and another process may be required to attain full densification. While, vitrification sintering mechanisms work by filling the pore space with formation of liquid [131].

Interaction of laser with biomaterials can lead to sintering, therefore, many studies have been published regarding selective laser sintering of various

biomaterials like metal alloys, polymers and bio-glasses. Most recently, considerable interest has been on using FSL laser for bone tissue engineering for various purposes: as cutting and drilling tools for bone regeneration, and for controlling surface morphology of materials as well as a sintering process. However, of particular interest is the investigation of calcium phosphate (CaP) ceramics because of their chemical and structural similarity with the natural mineral of bone [137-139].

2.6.1 Selective laser sintering (SLS) for bone tissue engineering

Nowadays, different material types such as ceramics, polymers and metals in tissue engineering have been fabricated using SLS either directly or indirectly [140]. In this technique, generation of 3D scaffold is thorugh fabrication of layer or through solid freeform material by solidification process in which thermal energy by applying laser beam is needed for sintering [140]. Various type of lasers have been used, as for example CO_2, neodymium-doped yttrium aluminium garnet Nd:YAG and erbium-doped yttrium aluminium garnet laser ER:YAG. The final material produced and its properties including surface morphology and mechanical properties depend on the type of laser.

According to Plank and Einstein equation, the relation between the photonic energy and wavelength are inverse proportional, while a direct relation between photonic energy and frequency, thus, different sources have different photonic energy, eq 2.2 [141]. Therefore, laser parameters (repetition rate, wavelength, diameter of beam and operation mode) are very significant to the process and must be carefully considered [140].

$$E = \frac{hc}{\lambda} \qquad (2.3)$$

Where, h is Plank's constant, c is speed of light and λ is the wavelength.

Sintering using laser induce during the thermal interaction of material with laser when the laser heating fluence is lower than the melting threshold of the solid material that elevate the temperature of the target material [142]. When the temperature rise, the diffusion rate can be induced which lead to

sintering and rearrangement of crystal structure. High temperature can be also achieved which then can cause phase transformations. Self-quenching and thermal stress on the material also may be induced [142]. The advantages of using laser as a sintering process are the precise of sintering of localised area, reduction of cracks and fast processing. Laser thermal interaction with material can be stimulated using continuous wave (CW) lasers and pulse lasers.

2.6.1.1 Continuous wave (CW) lasers

Nd:YAG and CO_2 lasers are common types of CW lasers and have been used in biological applications. Using these lasers techniques during biological application lead to either large area of thermal damage by heat accumulation or intensive tissue damage that take long time to heal [143, 144]. Achieving better results for using lasers in bone tissue regeneration requires a decrease in the effect of the laser on the surrounding tissue by shortening the irradiation time, using a shorter wavelength and considering a pulsed duration. Furthermore, the scaffold materials in bone engineering should have good energy absorption to improve the sintering process.

Femtosecond pulsed laser is an selective laser sintering technique used in sintering processes for biomaterial scaffolds. A comparison between a 120 fs pulsed laser at a wavelength of 1520 nm and a power of 130 mW and a continuous wave CW at 1520 nm and 980 nm and power of 150 mW was conducted by Jha and his colleagues [145]. In their study of Er^{3+} doped monetite and brushite mixed with CaF_2 and $AlPO_4$ for restoring enamel surface, they found that when using a continuous wave laser, long irradiation times were needed to melt the mineral mixture relative to femtosecond pulsed laser. It was also observed that femtosecond pulsed laser produced higher densification of the mineral.

2.6.1.2 Pulsed lasers

Pulsed lasers include long pulsed laser such as nanosecond laser and short pulsed lasers as femtosecond lasers. The physical interaction of laser with material depends on the pulsed duration of the laser, for nanosecond the

pulse duration is > 1 ns, whereas, for femtosecond laser is <1 ps. Thermal diffusion during laser-mater interaction lead to thermal effect that can cause heat-affected zone (HAZ) [146]. It was found that, HAZ using nanosecond pulsed laser result in 10 μm, while using femtosecond pulsed laser was only 0.02 μm [147]. Therefore, femtosecond pulsed laser is used as a sintering process for biological applications.

A femtosecond pulsed laser of a wavelength 1045 nm, with a repetition rate of 1GHz and 130-190 fs was used as a sintering process for $Fe^{2+/}Fe^{3+}$ doped brushite by Anastasiou et al. [4]. The final phase; β-CPP doped with $Fe^{2+/}Fe^{3+}$ had mechanical properties (hardness) that were better than undoped β-CPP. Also, it was found that doping with $Fe^{2+/}Fe^{3+}$ ions improved optical absorption of brushite and sintering was localised without affecting the surrounding area. Therefore, femtosecond pulsed laser can be said to be relatively safe to use in tissue engineering applications with a proper scaffold materials [4].

2.7 Ablation using femtosecond pulsed laser

Scaffolds with micro and/or nano-structures could develop mechanical properties and biological response because these structures could enhance cells adhesion into the scaffold [139]. Additionally, as earlier mentioned titanium scaffold have been found to have been improved by coating with CaP minerals, both mechanisms of coating and micro/nano-structure can be obtained by different techniques. Various techniques have been investigated such as; coating using electrophoretic process and plasma spray [142].

A coating of HAp was achieved on a titanium base alloy through the use of a plasma spray coating process [148]. However, the layer of HAp was brittle that could lead to a collapse of the substrate when placing the scaffold in the body [149, 150]. Additionally, the coating procedure was considered to be relatively complicated and the coating of materials may not be a homogeneous [142]. Another technique used for coating is by sintering the ceramic materials at high temperature in an oven, however, this process was found to decrease the mechanical stability of the titanium. Both

continuous-wave and pulsed Nd:YAG lasers were also employed to coat calcium phosphate on Ti-6Al-4V [150-152]. Nonetheless, as inducted earlier their large heat affected zone HAZ could lead to substrate melting as well.

Excimer lasers have been used widely for fixation process of materials on titanium scaffold as well obtaining micro/nano structure due to their precise channels size in the materials for micromachining applications. However, excimer lasers became an unfavourable technique in some industrial applications due to corrosive gases which are difficult to handle and also because of associated radiation damage of optics

Thus, ultrashort pulse lasers were looked at in direct writing applications since they have some of excimer lasers characterisation in visible and near infrared [153].They have recently been used in micromachining technique that is the process of creation a micrometer-sized structure on the sample surface by the pulse of the laser. ultrashort pulse lasers are suitable for biomaterials applications due to fast process, non-contact with target materials, no need of vacuum equipment and reduction HAZ therefore avoid damaging of surrounded tissue [142, 154]. Nevertheless, in some cases structure changes and thermal stresses could be produced during direct writing process [155].

Femtosecond pulsed laser addresses the issue of HAZ by reducing the heat transport to the area near to the irradiated surface [155-157]. This is achieved by controlling two important parameters of femtosecond pulsed laser: pulse duration and pulse repetition rate. Pulse duration, which is referred as a full width at half maximum of laser peak, should be small to decrease the heat flow to adjacent area of the radiation. High pulse repetition rate (frequency) is also considered to minimise the HAZ. In order to utilise this technique in direct writing applications (micromachining) other parameters also should be taken into account such as: laser wavelength, spot size, speed rate and average power.

There are different types of femtosecond pulsed laser such as ytterbium-doped yttrium aluminum garnet (Yb:YAG), ytterbium-doped potassium

yttrium tungstate (Yb:KYW) and titanium doped sapphire (Ti:Sapphire). Femtosecond pulsed laser has been applied for different materials type including semiconductors, polymers, metals and ceramics and since each material has its thermal and optical properties, the parameters of laser must be changed depending on the properties of the target material [158, 159]. Also, the heat diffusion coefficient and absorptivity of the target samples have an impact on the ablation threshold [154].

The mechanisms that cause ablation or laser-induced breakdown using ultrashort pulse laser are non-linear processes. They are avalanche ionization and multiphoton ionization [153] . For ultrashort pulsed laser, the ablation mechanism takes place via multiphoton ionization. The photons absorbs high energy that cause materials ionization through process called multiphoton absorption. Electrons are excited from valance band to free or conduction band by absorbing photons when $mhv \geq U_I$, where m photons, hv photon energy and U_I is the bandgap [153]. The free electrons absorb the laser light, this process will lead to a production of plasma hence transfer energy to the lattice [154, 160]. Ejection of the materials happens when the energy transferred to the lattice is converted to kinetic energy that causes bonds to break [160, 161]. Because of the small pulse duration and since the responding of materials to heat pulses is in picosecond, heat transfer decreases during laser process so that ablation occurs instead of melting [162].

The advantages of using short pulses femtosecond pulsed laser in micromachining are that ablation of very small and precise structures in the target materials can be done, something that is not really feasible using pico- or nanosecond pulses lasers or even long pulses femtosecond pulsed laser, Figure 2.5 [163]. During ablation, a U-shaped can be formed using long pulsed laser instead of a V-shaped. This result due to the spread of thermal conduction around irradiation area [141].

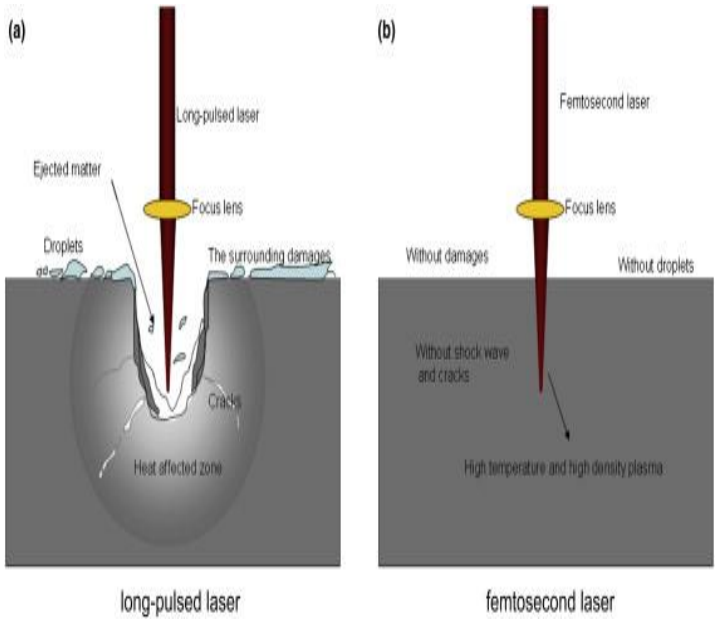

Figure 2.5: Ablation using a) long-pulsed and b) short-pulsed lasers [164].

The ablation mechanism also depends on the optical absorption and thermal properties of the materials. For example, band gap in the semiconductors and insulators is fundamental to laser absorption. In small band gap material, absorption of light takes places when the electrons transfer from valence band to conduction band and then these electrons carry the energy to the lattice. Lower band gap energy requires a lower ablation threshold fluence. On the contrary, for high band gap material, the ablation threshold fluence increases [142, 165, 166]. For instance, in pure silica high laser intensity was required for the ablation due to the high band gap which means low optical absorption properties [167, 168].

2.7.1 Applications of femtosecond laser in bone engineering scaffolds

Femtosecond pulsed laser with a wavelength 790 nm, 30 fs pulse duration, pulse frequency of 1KHz and pulse energy of 400 µJ was used to ablate the calcium alkali phosphate GB14 on Ti-6Al-4V in order to have an ideal ceramic fixation on the titanium implant [149]. In this study no melting of GB14 ceramic was revealed since the conversion of heat into the target material decreased using femtosecond pulsed laser technique.

Additionally, femtosecond pulsed laser has been used for cutting bone tissue. In Girard et al. [144], femtosecond pulsed laser with wavelength of

775 nm was used on cortical bone with ablation threshold of 0.69J/cm^2 was applied. No denotation of significant heat generation for the surrounding area. As well, in their comparison of femtosecond at 775 nm and nanosecond at 532 nm a thermal impact and cell damage in thickness of 14±5 μm and 435±50 μm respectively, was observed. No induction of melting area was present when using femtosecond pulsed laser.

In addition, using femtosecond pulsed laser in direct writing micromachining was found to increase biological adhesion by changing the chemistry of the surface.

2.7.1.1 Micromachining and cell adhesion

Previous research has established the importance of chemical composition and morphology of the surface as well surface energy on increasing the density of cell adhesion and migration therefore cell proliferation [169-171]. Some studies have been proven the increase of osteoblastic cells adhesion on rough surfaces in comparison to smooth surfaces [171].

Titanium is biocompatible and has an excellent mechanical properties. However, it has a low osteointegration. One of the techniques to encourage a rapid integration with host bone is direct writing micromachining. It has been demonstrated the positive influence of micromachining surface on the cell adhesion, therefore may increase cells density which could increase osteointegration of the scaffold [170].

Ulerich et al. [172], used nanosecond pulsed UV laser to controlled the depth of groove in Ti-6Al-4V by manipulating the working distance, the laser intensity and the pulse duration. After they cultured osteoblast cells in their implant, they found that the cells were aligned in the grooves and cell density increased.

The micro-channels or grooves on the scaffold surface serve to organise the cells that is known as a contact guidance [142, 173]. In the contact guidance the cells are arranged along the channel shape. Although, the alignment of cells has advantages in supporting cells growth and adhesion, the understanding of the impact of micro-channels in cell adhesion and

proliferation is still unclear [142, 173]. Chen et al.[174], reported that the reason for cell adhesion therefore cells growth in the micro-channels pattern could be linked to the high concentrations of extracellular matrix proteins interacting with the focal adhesions in these channels. It has been found that focal adhesion were spread over a smooth sample surface in an heterogeneous way whereas on laser treatment samples focal adhesion assembled in the microchannel [175, 176]. It has been found that microchannel surface increased surface area and therefore focal attachment.

Therefore, femtosecond pulsed laser is proposed to be a good technique for both sintering and ablation in terms of improving mechanical properties (hardness, Young modulus) and biological performance (adhesion and proliferation of cells).

2.8 Objectives

Based on the literature review, research specifically investigating the interaction of cells (i.e. osteoblasts) with β-CPP doped with Fe^{2+}/Fe^{3+} (e.g. cell viability, attachment, and proliferation) is still unpublished. Therefore, this research work will make a major contribution to the body of research on β-CPP doping with Fe^{2+}/Fe^{3+} by demonstrating the effect of dopant materials in biological performance and mechanical properties particularly hardness and Young modulus using thermal sintering as a laser simulation and the effect of micro-channels using ablation by femtosecond pulsed laser in cell adhesion as well.

The aim of this work, is to examine a conventional powder sintering route for testing Fe^{2+}/Fe^{3+} doped CaP minerals to obtain β-CPP as potential scaffold for bone tissue regeneration. Since high concentrations of Fe^{2+}/Fe^{3+} ions could lead to tissue damage, various concentrations of Fe^{2+}/Fe^{3+} ions were tested. The objectives of the research include:

- Synthesis of various concentrations of Fe^{2+}/Fe^{3+} doped calcium phosphate minerals in brushite form.

- Sintering of the Fe doped calcium phosphate minerals in order to achieve the transformation into β-CPP form.

- Ascertain the optimum percentage of $Fe^{2+/}Fe^{3+}$ for the desirable mechanical properties (hardness and Young modulus) and compare the results with un-doped materials in β-CPP.

- Investigate the effect of $Fe^{2+/}Fe^{3+}$ concentrations in doped β-CPP materials on cell viability and cells growth.

- Examine the influence of $Fe^{2+/}Fe^{3+}$ concentrations on the interaction with femtosecond pulsed laser using different laser intensities.

- Investigate the influence of micromachining of the top of $Fe^{2+/}Fe^{3+}$ doped β-CPP minerals by ablation mechanism using femtosecond pulsed laser at a wavelength of 800 nm on the wettability properties and therefore cell adhesion.

This section has attempted to provide a summary of literature relating to bone tissue materials, laser sintering of calcium phosphate and Fe doping of CaP. The next chapter describes the materials and methods that have been used to accomplish this study.

Chapter 3 Materials and methods

Chapter introduction

In this chapter, the materials and methods employed in the preparation of Fe^{2+}/Fe^{3+} doped calcium phosphate minerals were discussed. Multiple characterisation techniques that were used to identify the form of calcium phosphate and study the properties of the material as well as the effect of Fe ion on the mineral was also investigated. Techniques covered in this chapter include: scanning and transmission electron microscopy, thermal analysis, X-ray diffraction analysis, Fourier transform infrared spectroscopy (FTIR), Raman spectroscopy, cell attachment and proliferation, etc.

3.1 Materials and methods

3.1.1 Preparation of undoped and Fe^{2+}/Fe^{3+} doped CaP powder

In order to prepare the CaP powders (brushite form ($CaHPO_4 \cdot 2H_2O$)) a precipitation method as described in Anastasiou et al. [4], was followed. 0.1 M of calcium solution was prepared firstly by adding 47.23 g of $Ca(NO_3)_2 \cdot 4H_2O$ (Fisher Chemicals, CAS: 13477-34-4) in 200 ml distilled water. Then 20 ml of this solution was dissolved in 180 ml of distilled water (solution A). While, 0.1 M of phosphate solution was prepared after dissolving 26.41 g of $HPO_4(NH_4)_2$ (Acros Organics, CAS: 7783-28-0) in 200 ml of distilled water then 20 ml of this solution was dissolved in 180 ml of distilled water (solution B). Then solution A was heated to a temperature of 37 ˚C, after which, solution B was introduced dropwise into solution A. The equation for the reaction is described by eq. 3.1 [177].

$$Ca(NO_3)_2 \cdot 4H_2O + HPO_4(NH_4)_2 \rightarrow CaHPO_4 \cdot 2H_2O + 2NH_4NO_3 + 2H_2O \quad (3.1)$$

The resulting mixture was continuously stirred / agitated at 37 °C for 2 h, then left to settle for 1 h for precipitation to occur, images of the experimental setup are shown in Figure 3.1. The precipitate was collected using a filter paper (Whatman grade 44 with 3 μm pores), washed several times with distilled water and dried in air for 24 h at 80 °C (Carbolite furnace).

The synthesis of the Fe^{2+}/Fe^{3+} doped CaP was done following a similar protocol with minor modifications. To introduce Fe^{+2}/Fe^{+3} ions into the system, appropriate quantities of $Fe(NO_3)_3 \cdot 9H_2O$ (VWR Chemicals, CAS: 7782-61-8) was added to solution A in order to achieve doping of (5, 10, 20 and 30 mol%) before the addition of the $HPO_4(NH_4)_2$ solution. During the synthesis process pH was measured using pH meter (HI991001, Hanna). Table 3.1 provides details of sample coding, with percentage Fe content and theoretical empirical formula.

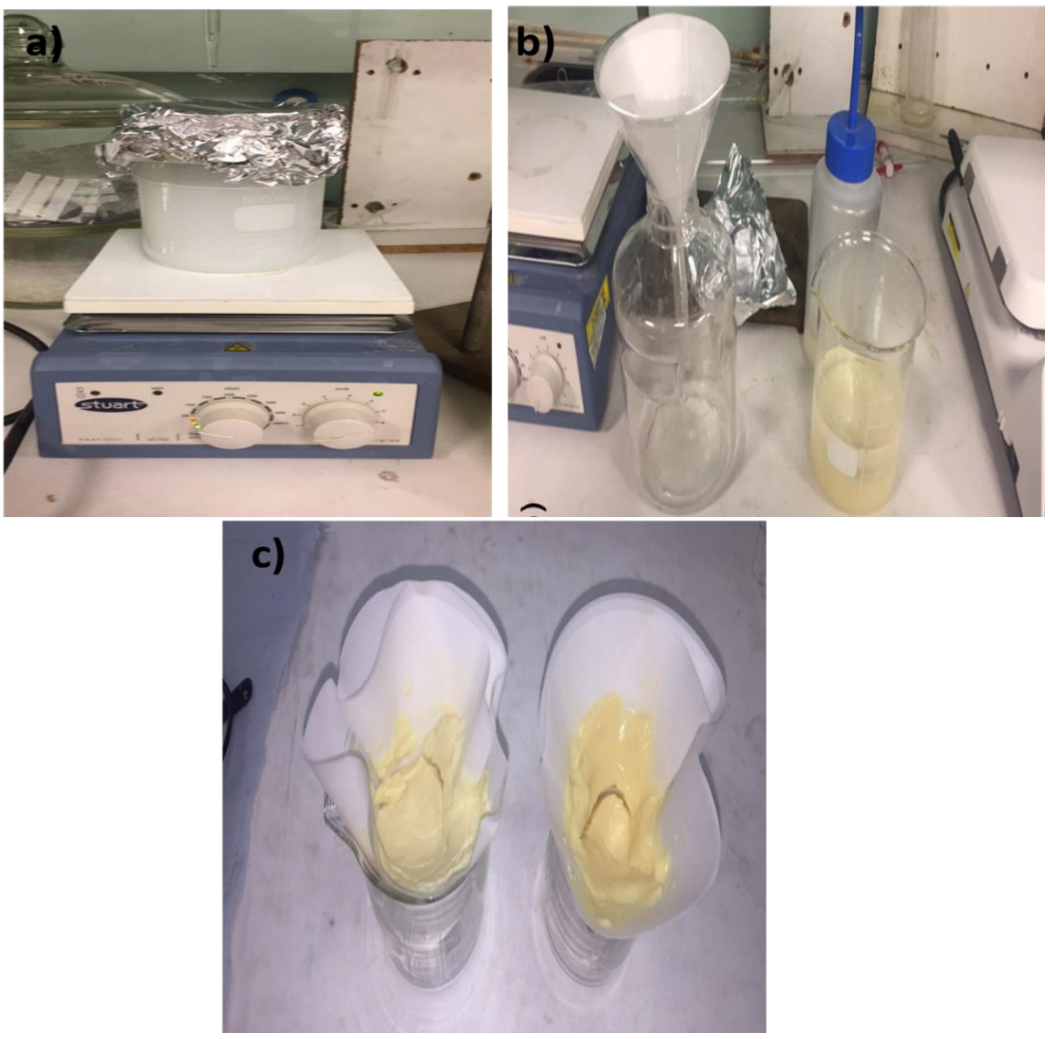

Figure 3.1: Experimental setup for preparing undoped and doped CaP powders a) stirring process, b) and c) filtration process.

Table 3.1: The planned concentrations of Fe^{2+}/Fe^{3+} ions for doping into the CaP minerals and the sample identification number.

Materials code	Fe mol%	Theoretical Formula
0-FeCaP	0 mol%	$CaHPO_4 \cdot 2H_2O$
5-FeCaP	5 mol%	$Ca_{0.95}Fe_{0.05}HPO_4 \cdot 2H_2O$
10-FeCaP	10 mol%	$Ca_{0.9}Fe_{0.1}HPO_4 \cdot 2H_2O$
20-FeCaP	20 mol%	$Ca_{0.8}Fe_{0.2}HPO_4 \cdot 2H_2O$
30-FeCaP	30 mol%	$Ca_{0.7}Fe_{0.3}HPO_4 \cdot 2H_2O$

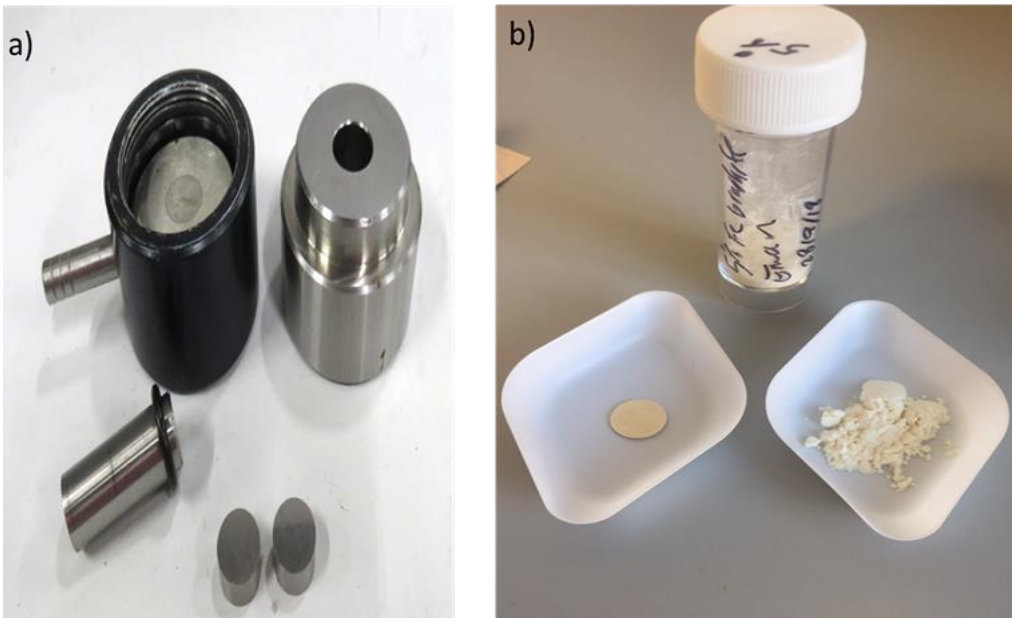

Figure 3.2: a) Die set of 13mm for pressing pellets and b) CaP pellet after pressing the powder.

In order to test the mechanical properties of the synthesized materials, cell growth and laser experiments; the dried materials were grinded using mortar and pestle then the powder were pressed using a 13 mm diameter die of (SPECAC), as shown in Figure 3.2. For each pellet approximately 0.25 g of the corresponding powder was filled inside the die before pressing with a load of 6 ton for 15 min and the thickness was 1mm. As this project was only focused on the hardness and Young modulus using nano-indentation machine. Therefore, changing the size of the sample (thickness and diameter) does not affect the hardness value since it only depends on the sample's surface, indentation geometry and size shape and penetration depth [178, 179]. Further, these dimensions were chosen for cell growth experiments, since better surface area was required for more cells to be attached.

3.1.2 Thermal sintering

To densify the pressed pellets and also to induce phase transformation brushite into β-calcium pyrophosphate, a thermal sintering process was carried out at a temperature of 1000˚C for 5 hrs and heating rate of 10 ˚C/m

under atmospheric conditions using carbolite chamber furnace, as can be seen in Figure 3.3.

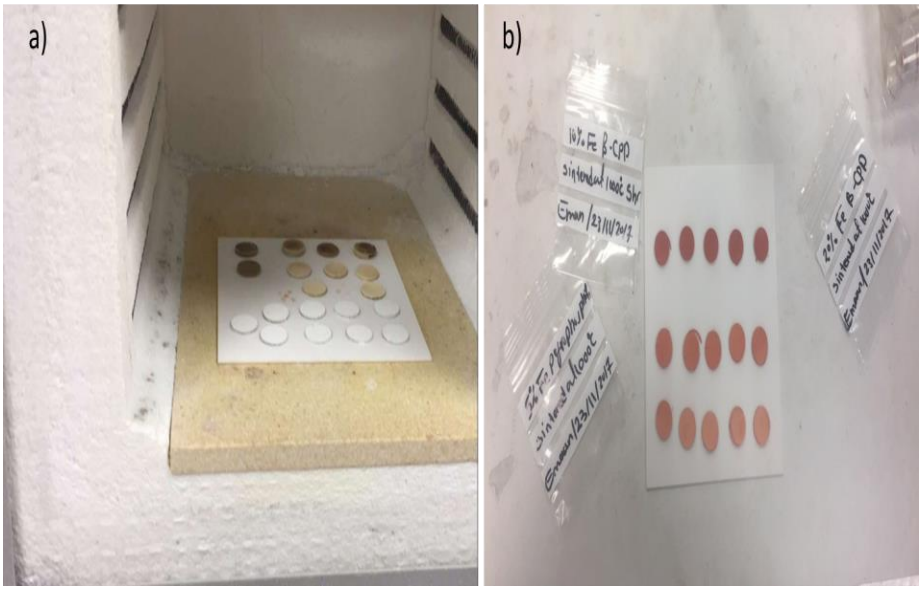

Figure 3.3: a) Sintering procedure using Furnace at 1000ºC for 5 hrs, b) undoped and doped FeCaP pellets after sintering.

3.2 Femtosecond pulsed laser

Femtosecond pulsed laser has been used in different technology applications such as in semiconductors and biological applications [153, 159]. Due to non-contact with target material and reduction of heat-affected zone, it has been applied in cutting, drilling and micromachining for bone engineering. In this work, femtosecond pulsed laser was used for micromachining application in order to examine the effect of microscale structure on cell attachments. A Ti:sapphire laser with mode-locking oscillator using chirped pulse amplification was used.

For ultrafast lasers, the laser gain medium is considered important to produce ultrashort pluses. For example, in laser oscillator, pulses lower than 1 ps can be produced when the emission spectrum in the laser gain medium are continuous and broad. Using Nd:YAG laser, the pulse width in emission spectrum is >30 ps, however, with lasers such as Nd:glass the minimum pulses can be supported is <100 fs. Whereas, the laser emission spectrum in Ti:sapphire laser can afford a pulse of 6 fs. To produce ultrashort pulses, a mode-locked oscillator laser must be used [153]. The

process of mode-locking preserves the phase of the photon quanta within a narrow spectral bandwidth, which then allows tight control over energy delivery at high repetition rate in ultrafast femto-second (10^{-15} s) regime. As a result the interaction time with the matter irradiated with laser undergoes phase transformation which is well beyond the chemical regime. The control of pulse stretching and amplification, first demonstrated by G Mourou and D Strickland in chirped pulse amplification Nobel prize in 2018 [180].

In micromachining applications, microjoule pulse energy is required. Nevertheless, the pulse energy of laser oscillator is usually in nanojoules. Using chirped-pulse amplification (CPA) with oscillator can achieve amplification from nano to micro/millijoule since the direct amplification can lead to optical components damage.

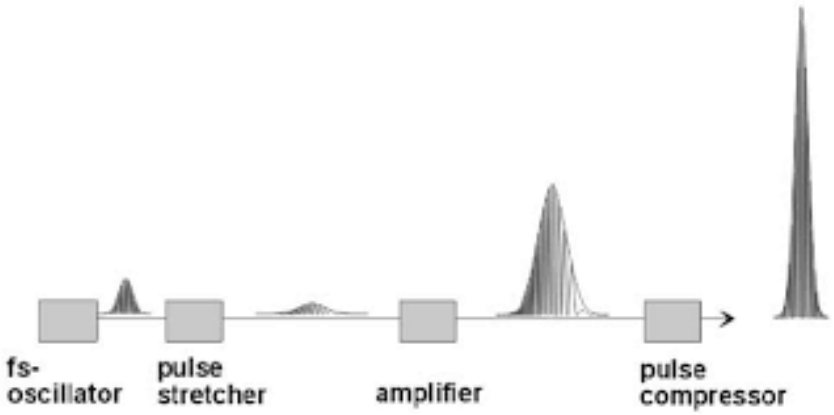

Figure 3.4: Illustration of chirped pulse amplification system [181].

Figure 3.4 shows the principle of laser oscillator using chirped pulse amplification system. In this principle, the pulse width that comes from laser oscillator is stretched in the stretcher in order to minimise the power of the peak. The stretcher is usually fabricated by two optical gratings to alter the ultrashort pulse width. The amplifier consists of a gain medium and a regenerative amplifier that is a Q-switched laser cavity is usually used in this kind of laser for the amplification of the stretched pulse in order to obtain micro or milli joule pulse energy and desired repetition rate. Pockels cell is used with polariser and the coinciding of injection with the Q-switch time for the pulse injection and trapping in the amplifier. Then the pulse will be sent to the compressor, which is made of two optical gratings positioned on opposite side of each other, the long pulse from amplifier is return back to

the short pulse [153]. Frequency-doubled Nd:YAG lasers are usually used as a pump or regenerative lasers for both oscillator and amplifier in the ultrafast lasers.

In the laboratory setup, as can be seen in Figure. 3.5, the laser experiment were performed in ambient atmosphere using a Ti:sapphire amplified femtosecond laser system (Coherant-Libra), which emits radiation at a wavelength of 800 nm with 1 kHz repetition rate and 80-100 fs pulse duration. A working distance of 4.9mm and objective lens of 20x were used. The laser energy was controlled using a polariser and a half-wave plate. Sample was placed in an XYZ transition stage that is controlled by A3200 computer software.

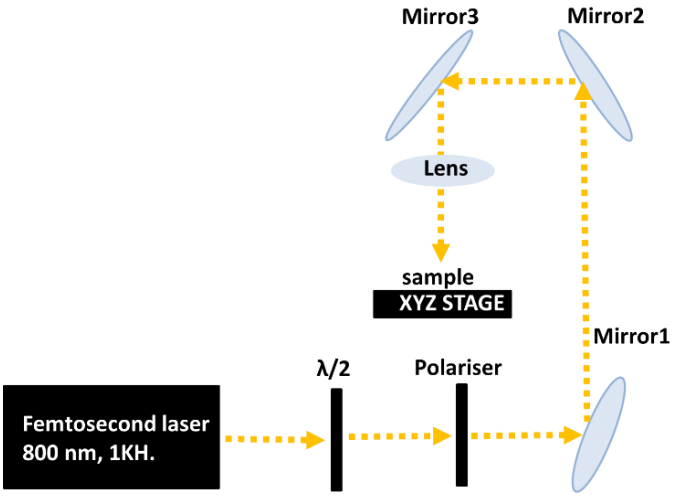

Figure 3.5: Schematic setup of femtosecond pulsed laser.

To investigate the cross section of micro-channels, first samples were mounted in resin moulds using EPOFix kit (Struers). After that, polishing with Grit 320/P400 silicon carbide grinding grit was first applied then P4000 Microcut silicon carbide was used to fine the surface using grinder polisher (BUEHLER-MetaServ 250).

3.3 Characterisation techniques

3.3.1 Structural and phase characterisation

3.3.1.1 X-ray powder diffraction (XRD)

X-ray powder diffraction is an important materials characterisation technique, which helps in the phases and phase volume fraction, crystal structure and lattice parameters, ionic site, and particle size analyses. All of these may be quantified using the powder diffraction technique with the Reitveld analysis.

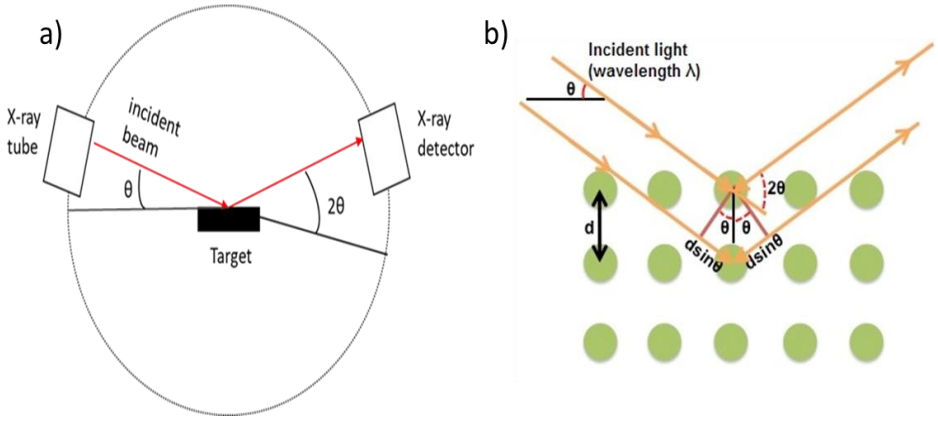

Figure 3.6: Schematic diagram of a) X-ray powder diffraction setup consisting of an X-ray tube, a detector and sample holder and b) schematic description of Bragg's law [182].

A standard XRD set up is composed of three important parts: i) X-ray tube that has a cathode ray tube which produces X-rays by heating the filament inside it, ii) a sample holder for the target material and iii) X-ray detector that is rotated to record the intensity of the reflected X-ray, Figure 3.6a. After the electrons are produced in the x-ray tube, they accelerate and hit the target material and should have energies that are able to eject the electrons inner sell of the target material, then the X-ray diffraction of material will produce according to Bragg's law.

$$n\lambda = 2d \sin\theta \qquad (3.2)$$

Where

- n is an integer (order of reflection)
- λ is the wavelength of the incident X-ray beam (nm).
- d distance between lattice in a crystal.
- θ is the angle of incidence.

Bragg's law states that when the X-rays hit a crystalline ceramic sample, ions generate interference patterns, as shown in Figure 3.6b. These

patterns scatter in different directions and some of them interfere and cancel each other or constructively interfere to produce diffraction patterns when the X-rays are in the right angle and distance to be in-phase with each other. This occurs when the angle of reflection beam is equal to X-ray incident angle [183-185].

The phase constitution of the synthesised and the sintered crystalline material was analysed on using a Bruker D8 advance powder X-Ray diffractometer equipped with a monochromatic Cu Kα radiation source (λ= 1.54Å). A step size of 0.065° and a 2θ scanning range from 10° to 60°, was used at a scan speed of 1° s^{-1} to yield a powder diffraction pattern. For the analysis of the patterns and the identification of the individual peaks the software, HighScore plus (Malvern Analytical) was used. For detecting the volume fraction (ratio) in the mixture samples, Rietveld refinements were applied.

In addition to normal powder XRD, non-ambient X-ray diffraction analysis was carried out using a Philips X'Pert pro MPD XRD equipped with Cu Kα radiation and non-ambient XRD stage (Anton Parr) operated at 40 mA and 40 kv to study phase transformation during the sintering process, at a range of temperature between 30 ˚C and 1000 ˚C for 10hrs and 30 min scan for each temperature and 2θ between 10°- 60°.

3.3.1.1.1 Grazing incidence X-ray diffraction GIXRD

Grazing incidence X-ray diffraction GIXRD was also utilized for the analysis of the crystal structure of the sample surface without the substrate. In contrast with conventional XRD, the incidence angle in GIXRD was fixed between 1º and 3° and only the detector tube was rotated in this angular range interest. The advantage of this technique, is that the incident beam grazes the surface of the material ignoring its underlying substrate because of incidence small angle. Based on this, the angle incidence controls the depth of material analysis instead of 2θ and it is fixed during the scanning [184]. Since the micro-channels created after laser irradiation were only few microns, all the materials after irradiating with a femtosecond pulsed laser were analysed using GIXRD of Philips X'Pert MPD XRD with angle of 2°,

2θ from 10°-60° for 30 mins and a step size of 0.033° and scan speed of 0.028° s^{-1}.

3.3.1.2 Fourier transform infrared spectroscopy (FTIR)

FTIR is a characterization technique that is commonly used to identify the molecular structure of material by detecting the change in dipole moment of molecules when vibration occurs in the IR radiation. The FTIR analysis may be carried out in reflection, and transmission or absorption.

Infrared spectroscopy IR relies on the radiation frequency and dipole moment of the molecules. When molecules absorb energy with frequency radiation that matches the frequency of vibration, vibration trigger when the absorption lead to change in the dipole moment of molecule [186, 187]. The frequency of IR radiation follows eq. 3.3:

$$v = \frac{c}{\lambda} \qquad (3.3)$$

as v is the frequency, c is the light speed and is equal to 3x10^8 m/s and λ is the wavelength.

IR regions divides into three regions: far-IR (400-10 cm^{-1}), mid-IR (4000-400 cm^{-1}) and near-IR (14000-4000 cm^{-1}).

3.3.1.2.1 Attenuated total reflectance (ATR)

Attenuated total reflectance ATR is an accessory of FTIR to measure reflectance and it is adopted to study the surface properties of material [188]. The analysis depth of this instrument is usually from 1-2 microns.

The ATR, is an attenuated total reflection process which follows the total internal reflection principle. The principle behind this technique is as the IR beam is directed into a higher refractive index crystal, an evanescent wave is created due to the internal reflections of the beam from the surface of the crystal. This wave will present orthogonally into the sample and its depth depends on the refractive index of the crystal, the light wavelength and the examined material. Part of the energy of these wave will be absorbed by

the sample while the rest will reflect, the reflected radiation is passed to the detector and then the IR spectrum is generated, Figure 3.7 [189]. The advantages of using ATR are no need for sample preparation and both liquid and solid form can be performed.

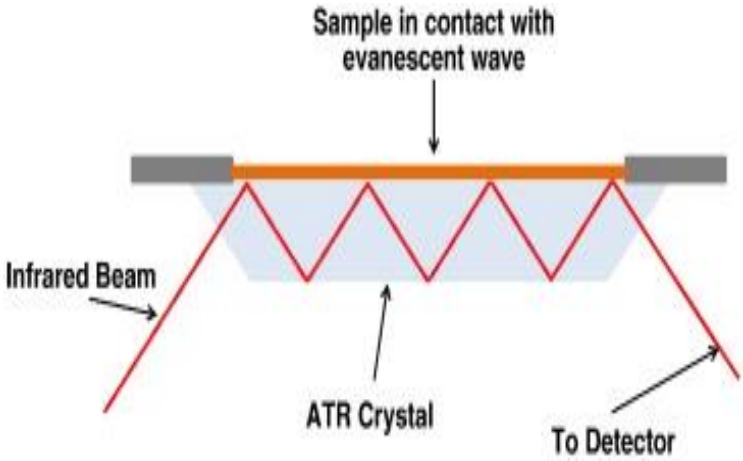

Figure 3.7: Schematic diagram of FTIR-ATR shows the ATR crystal and how the infrared beam passes through the sample [190].

The ATR technique was applied to study the sample structure especially for the samples that presented an amorphous phase. FTIR-ATR (Perkin Elmer) was adopted for FTIR characterization and the range 300 - 3000 cm^{-1} was scanned with a spectral resolution of 4 cm^{-1} for analysing the vibrational spectroscopic features of phases formed before and after the thermal and sintering experiments of FeCaP materials.

3.3.1.3 Scanning electron microscopy (SEM)

SEM is a microscopy technique that can be used to study the morphology of a material. Features such as size and shape of crystal, material compositions and topography of sample surface can be viewed on the SEM [191].The working mechanism of SEM is illustrated in Figure 3.8., An electron gun produces electrons and these electrons are accelerated (energy between 1- 40 KeV) by applying magnetic field through a lens geometry which focusses the electron beam onto a sample, placed in the sample chamber. The electron beam interacts with the sample in different ways including knocking out electrons from the sample. These electrons

release signals in different ways depends on the Coulomb field of electron beam interact with sample electrons (e.g. secondary electrons, backscattered electrons or X-rays). An image of the sample can be recorded when the signal is collected by a detector. Other information can also be gathered depending on the signals.

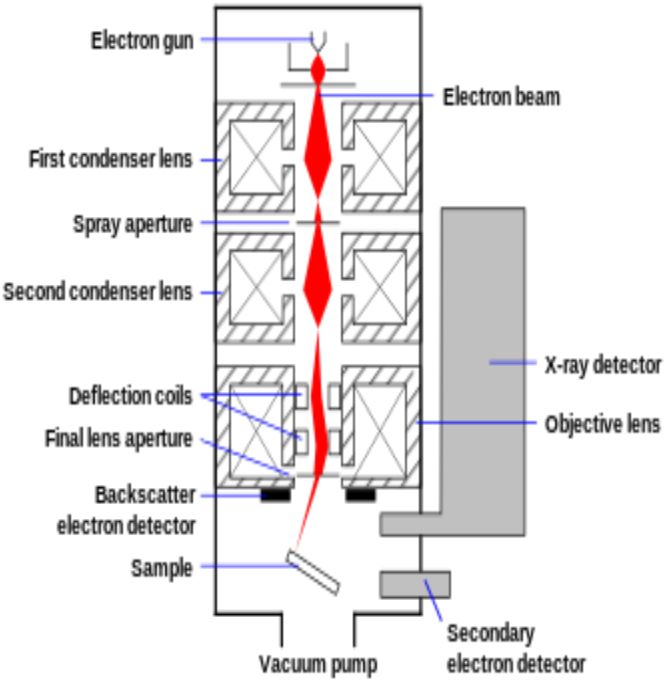

Figure 3.8: Schematic of scanning electron microscopy (SEM) working principle [192].

Secondary electron signals can provide information about a sample's surface topography and morphology. In this operation the electron beam strikes the target and causes an emission of secondary electrons from valence electrons of atoms in the target material. These electrons have a small energy which means only the secondary electrons that are produced near to sample surface emit outside and will be detected whilst the sample will absorb the other electrons that are produced in deep region. Secondary electron signals carry information about sample surface topography and morphology.

To obtain a backscattered image, the electron beam after hitting the target are scattered in the target material and then these electrons are scattered

again backward from the target. The energy of backscattered electrons is higher than secondary electrons, for that reason these electrons be used to obtain information about the compositions of a material. In the backscattered electron image, bright areas are produced from heavy atoms therefore, using backscattered electron is useful for detecting multiphase samples compositions [191].

3.3.1.3.1 Energy dispersive X-ray Spectroscopy (EDX).

Energy dispersive X-ray spectroscopy (EDX) is used for elemental analysis of a material [193]. When the incident electrons hit the target surface, the incident energy is sufficiently large for causing excitation of inner shell electrons in the materials into the vacant orbital, from which when decay produce characteristic X-rays, which are sampled for chemical analysis. Since the energies of emitted X-rays is equal to the difference of energies between ground state and excited state electrons, the characteristic emissions are shown in the energy dispersive spectra as K_{α}, $K_{b,}$ L_{a}. Each individual element has a characteristic X-ray energy [193]. After the emitting of X-rays from the sample, they travel towards the detector where electron-hole pairs are originates with quantities equal to the X-ray energy. Liquid nitrogen is used to cool down the detector to avoid electrical noise.

A Hitachi SU8230 Scanning electron microscopy (SEM), operating at 10 keV and fitted with a cold field emission gun and Oxford Instruments 150 mm^2 SD energy dispersive X-ray (EDX) detector was used for morphological and phase composition analysis of the initial and the sintered minerals. Sample for SEM were prepared by sticking it in the SEM stub using carbon tape then sample surface is coated with carbon or sputter coated to avoid charging effects which cause bright streaks across the scanned image. Prior to SEM analysis, it was necessary to coat the FeCaP surface with a 5 nm thin layer of iridium using Ager high resolution sputter coater followed by vacuum cleaning for 10 minutes using cleaning zone (Quorum Technologies sputter coater and vacuum cleaner) to minimize electrostatic charging during analysis.

3.3.1.4 Raman spectroscopy

Raman is another technique used to determine a material's structure and vibrational mode. In Raman both crystalline structures and amorphous phases can be determined. Using Raman spectroscopy leads to a non-contact with sample, fast and reliable results.

According to quantum theory, when the source emits radiation, the energy of photon is:

$$E_p = hv \qquad (3.4),$$

where v is the photon frequency and h is Plank's constant. When the incident radiation hits a sample a molecule will absorb the energy of photon and will cause the transition of electrons [186]. This leads to a vibration of the molecules of the sample and will causes changes in polarizability of the bond in a particular direction from which a spectrum can be obtained.

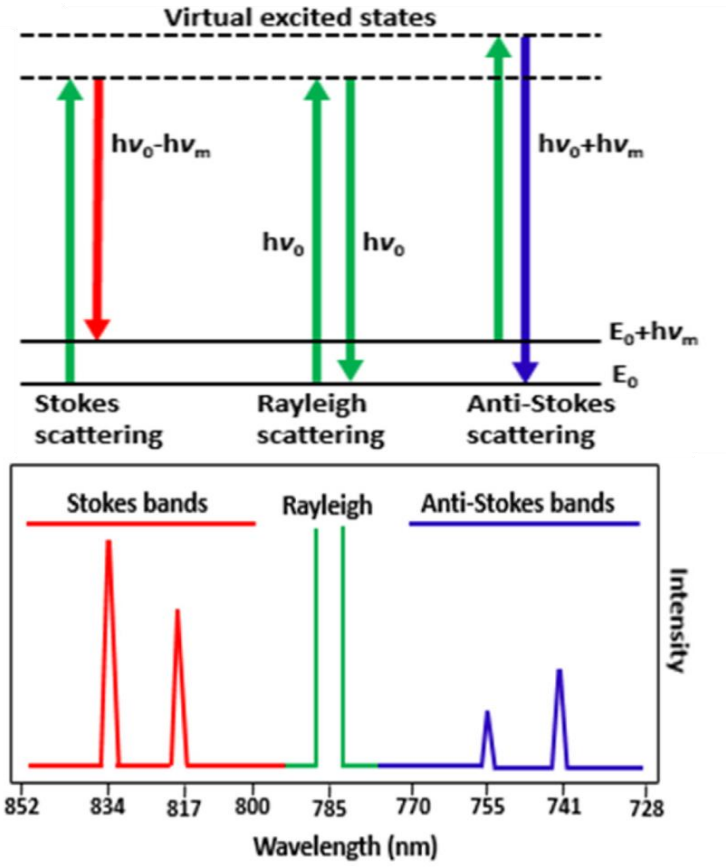

Figure 3.9: Raman spectrum shows Rayleigh and Raman scattering [194].

The mechanism of this technique that a monochromatic laser is directed unto the sample, which then interacts with sample molecules. The

scattering is induced by the deformation of bond in the presence of electro-magnetic field. The radiations scatter in different ways, the scattered radiation with frequency that is equal to the incident beam form the Rayleigh scattering, as shown in Figure 3.9. Whereas the scattered radiation with frequency that is different to the incident beam frequency are called Raman scattering and the fraction of this Raman scattering is small in comparison to Rayleigh scattering. Two lines appear in a Raman spectrum; the stokes and anti-stokes lines. They depend on the value of scattered radiation frequency in comparison to incident beam. When the scattered beam frequency is higher than incident beam, anti-stokes lines form and when the opposite occur, stokes lines manifest in Raman spectrum [195].

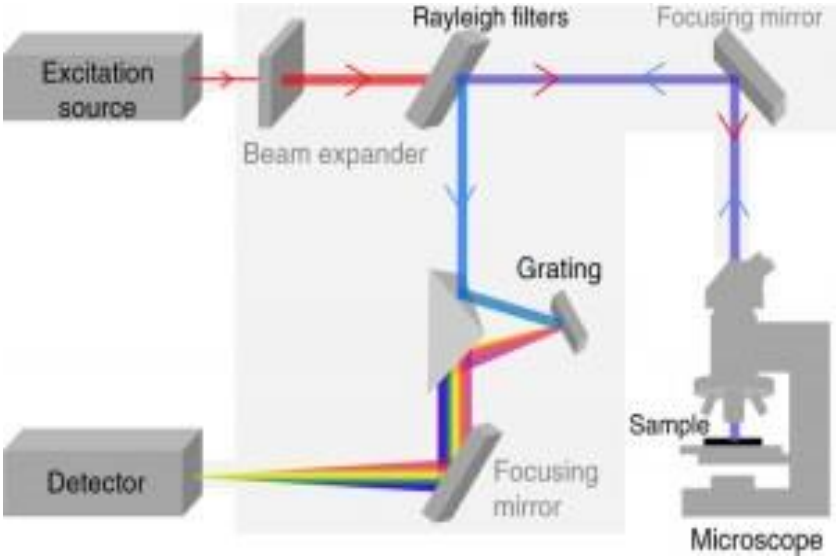

Figure 3.10: Schematic diagram of Raman spectroscopy [196].

Figure 3.10 shows a diagram of Raman spectroscopy. The excitation source is a laser to stimulate Raman scattering. Rayleigh and anti-stokes Raman scattering are eliminated using an edge filter. The passed light of stokes Raman scattering will be dispersed by a grating. Then Raman spectrum generates when the light collected by a detector. In this work, Raman spectroscopy Renishaw inVia with Argon laser at 514 nm and a power of 24.9 mW was carried out in the range of 100-2000 cm^{-1}.

3.3.1.5 Ultraviolet Visible spectroscopy (UV-Vis)

UV-Vis spectroscopy is a technique that is used to measure absorption, reflectance or transmittance of materials. The principle of UV-vis is that when the incident radiation hit the material, molecules will absorb energy when the photon energy of radiation at a specific wavelength matches the required energy for electron excitation [197]. According to Beer-lambert law, the absorbance can be expressed as:

$$A = \varepsilon c l \qquad (3.5),$$

where,

- A is the absorbance
- ε is the molar extinction (dm^3/mol.cm)
- C is the concentration of solution (mol/dm^3).
- L is the path length of cell (cm).

In this study, UV-Vis spectroscopy was carried out to examine the reflectivity of the samples. There are two types of reflection: specular reflection and diffuse reflection. Specular reflection is defined as the reflection of a beam from the surface of a sample in different directions. Diffuse reflection occurs when the light enters the sample and reflect from other sample surface or due to internal reflection. Absorption of diffuse reflected light inside the sample in long light paths occurs if the sample has strong absorption properties while emitting that in the short paths light out of the sample. On the contrary, when the powder has a weak absorption, even long paths light is released out of the sample [198, 199].

Therefore, UV-Vis with an integrating sphere accessory was adopted. Integrating sphere is considered as a diffuse reflectance tool, as seen in Figure 3.11. In this technique a dual light passes through reference port and sample port. Using mirror1 and 2, the light passes through the sample port and hits the sample, then it will scatter. The uniqueness of this tool is that the light keeps scattering again and again until it is either absorbed by any optical material inside the sphere or it escapes through any an open part [200].

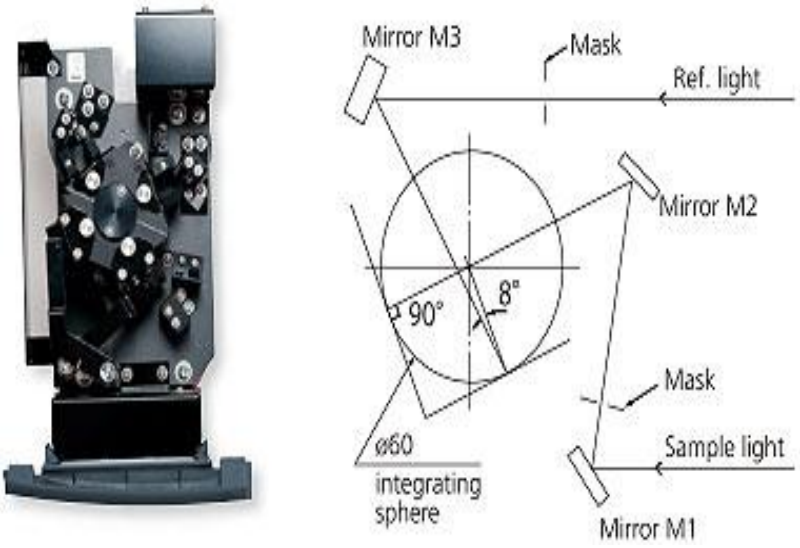

Figure 3.11: UV-Vis reflectance spectroscope showing the work of an integrating sphere tool [201].

In this project, pellet sample was prepared with a diameter of 13mm and thickness of 1.1 mm and the spectralon reflectance material disc was used as a reference. UV-Vis (Perkin Elmer, LAMBDA 950) integrating sphere (60 mm spectralon® sphere accessory) was used to determine the samples reflectivity between wavelengths of 200 and 1500 nm since FSL was used at a wavelength of 800 nm.

3.3.1.6 Transmission electron microscopy (TEM)

TEM is a versatile tool for analysis of structure, composition and properties of materials. An unknown sample structure can also be identified by measuring d-spacing since each material has a unique d-spacing using electron diffraction pattern.

The working principle of TEM is shown in Figure 3.12. In the top of TEM there is an electron gun that releases the electrons by cathode filament and high voltages. The first lens (electromagnetic coil) accelerates these electrons in very high speed [202]. Whereas, the second lens works as a focusing tool to concentrate electrons onto a specific part of the sample. As in SEM, the image formed depends on electron signal of sample different properties can be achieved from TEM. For the normal TEM image, bright field image is produced. Since electrons transmit through the sample, some of these electrons are scattered while other are unscattered electrons. The

area where electrons are scattered appears darker while the area with unscattered electron is a bright area. Therefore, to have a bright field image, an objective aperture is utilised to exclude scattered electrons [203].

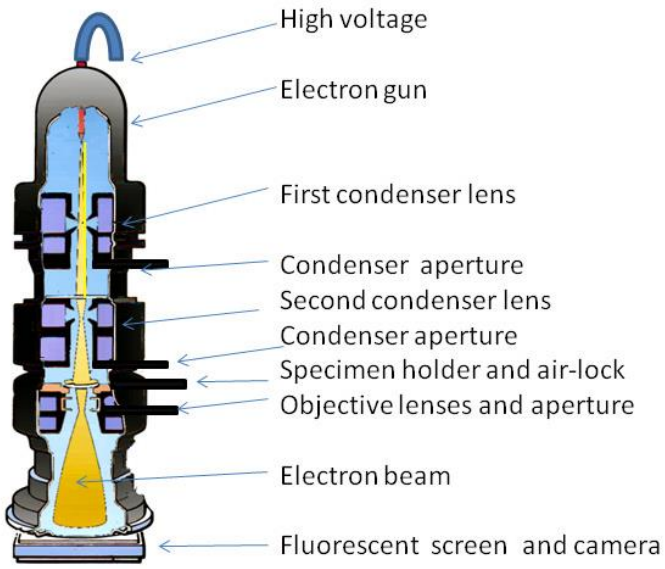

Figure 3.12: Illustration diagram of transmission electron microscope TEM [204].

3.3.1.6.1 Diffraction pattern

Electron diffraction on the TEM can be used to observe crystal structure information (crystal defects and d-spacing between lattices). When electrons transmit through a crystalline material, Bragg scattering is produced. By selecting diffraction aperture to detect this scattering, an image of diffuse rings or array of dots is formed [203].

In this study, TEM was used to verify an amorphous secondary phase that was present in the sample doped with 20 mol% Fe^{2+}/Fe^{3+} ions and to ensure the final crystalline phase after thermal sintering by measuring d-spacing. For TEM imaging, powder samples were dispersed in ethanol by using an ultrasonic bath and a drop of the suspension was placed onto a Lacey Carbon Film (Agar Scientific Ltd). Imaging and analysis of the samples was performed with a FEI Titan-cubed, Themis 300 Transmission Electron Microscope (TEM) equipped with multiple HAADF/ADF/BF STEM detectors and a FEI Super-X, 4-detector EDX system.

3.3.1.7 Zeta potential (ZP)

ZP is a parameter that can be used to determine the stability of a suspension. It is obtained by measuring the value of surface charge between particles in a suspension. When high value charge is measured, the suspension has a good stability because of effective repulsive forces while small value charge is explained instability of suspension due to van der walls force that leads to aggregation. Also, it gives details for the reason of dispersion and aggregation. Therefore, it has been widely used in industries such as medicine, pharmaceuticals and ceramics [205].

Zeta potential measurements were conducted using a Malvern zetasizer with zeta potential cell (cell DTS 1070). A suspension solution was prepared for all FeCaP samples prior to analysis.

3.3.1.8 Optical microscope

Optical microscope is probably the common type of microscope. The main feature of an optical microscope are the lenses and there can be two or more lenses. depending on the type of lenses a microscope has, it can be differentiated to: bright field microscope, dark field microscope and phase contrast microscope [206].

3.3.1.8.1 Bright field optical microscope (BFM)

BFM is referred to a type of optical microscope that has a bright background with dark sample. It consists of an ocular lens, an objective lens, and a stage for the specimen. Most of optical microscopes now, have a camera to take an image of the sample and display on screen instead of using the eyepiece only, Figure 3.13 [207].

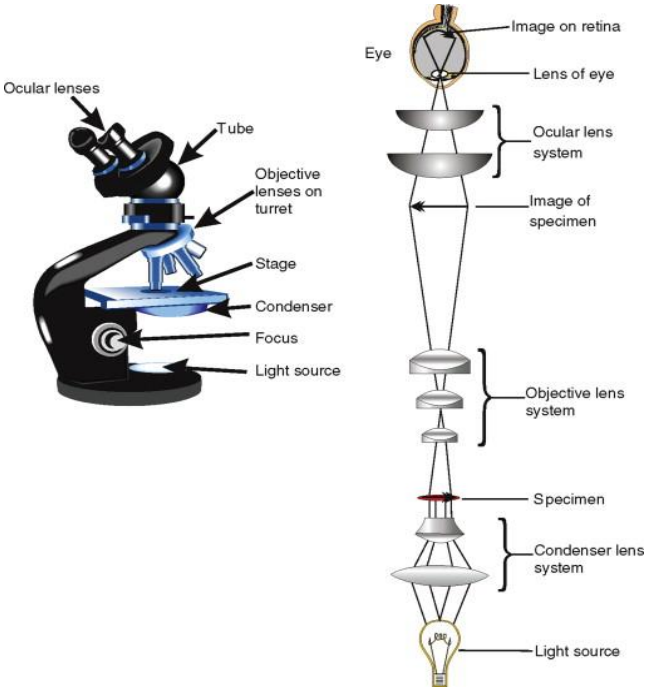

Figure 3.13: Image of optical microscope and its structure [206].

BFM (Olympus with AxioCam MRC5 camera) was used to observe and measure using ZEISS software the threshold of sample after laser ablation. A pellet samples were prepared with diameter of 13 mm and thickness between 1-0.9 mm.

3.3.1.8.2 Inverted microscope

This type of microscope is used to observe the cells in the bottom of the culture vessels such as well-plate and petri dishes. For this purpose, both the condenser and the light source are located in the top of the sample stage. On the other hand, the objectives of the microscope are placed under the stage [208].

3.3.1.9 Contact angle test

Contact angle is a measurement of the wetting properties of surface when the liquid contacts with a solid surface. The angle is formed between three phase boundaries solid, liquid and gas. As simplified in Figure 3.14, the surface is defined as a well-wetting surface (hydrophilic) when the contact angle is lower than 90º while when it is higher than 90º is known is a non-wetting surface (hydrophobic). This measurement is valuable in biological applications such as implant micromachining [209].

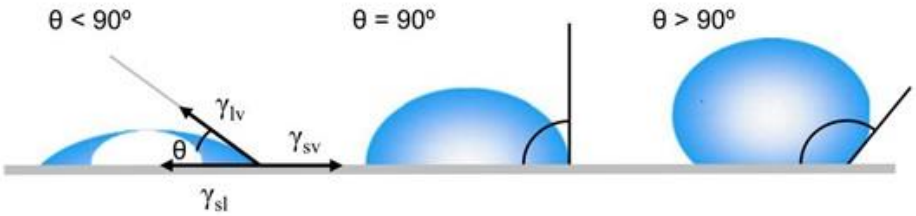

Figure 3.14: Image of different contact angles of liquid drops on the solid surface with different wetting properties *[209]*.

The interfacial tensions of these phases can be determined using Young equation:

$$\gamma_{sv} = \gamma_{sl} + \gamma_{lv} \cos\theta_{\gamma} \qquad (3.6)$$

Where

- Y_{sv}, Y_{sl} and Y_{lv} are interfacial tensions of solid-vapor, solid-liquid and liquid-vapor, respectively.
- θ_Y is Young contact angle [209].

KSV pendant drop CAM 200 optical tensiometer with KSV cam attension theta software was used to measure the contact angle of pellet samples before and after micro-channels using femtosecond pulsed laser, Figure 3.15. The pellet samples were prepared using pressed machine.

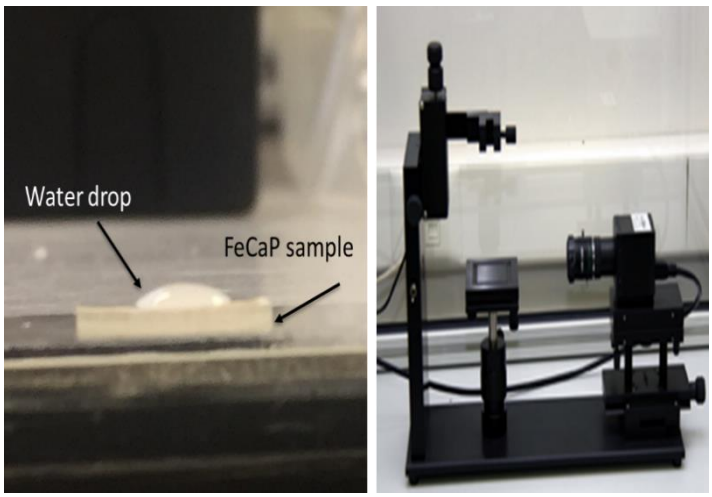

Figure 3.15: a) shows the water drop in the surface of FeCaP sample and b) presents the KSV contact angle instrument.

3.3.2 Thermal characterisation

3.3.2.1 Simultaneous thermal analysis (STA)

STA is an analytical technique that can be used to study the crystallization and decomposition temperatures of material. The STA instrument (PerkinElmer®, STA 8000), combines both differential thermal analysis (DTA) and thermogravimetry (TGA). It can analyse samples across a heating range of 15 to 1500 °C using a small furnace inside the instrument [210].

3.2.2.1.1 Differential thermal analysis (DTA)

DTA is used to determine the phase decompositions temperature of material during heating therefore it measures heat content as a function of temperature. Phases transform during heating by different chemical reactions that involve breaking and forming atoms bonds [211]. Energy is required for breaking bonds while it is released when forming bonds.

To run a DTA analysis, both the sample which is usually put in an aluminium crucible and the reference crucible are transferred into the holder of the DTA furnace, (Figure 3.16). Usually the material for the reference crucible has no thermal reaction until the final temperature of the sample that under examination. Both holders are contacted with thermocouples to measure temperature. When the furnace temperature increases, the reference temperature increases and the thermal reaction of the sample depending on temperature will occur. The endothermal and exothermal reaction takes place according to the temperature of the sample if less or higher than reference temperature. When the temperature of sample is higher than furnace temperature, the exothermal reaction has occurred. After the reaction ends, sample temperature returns to the furnace temperature [212, 213]. For high heating rate the reaction take place quicker and narrow peaks appear whilst broad shallow peaks result from lower heating rate because the testing material will be closer to the equilibrium condition [214].

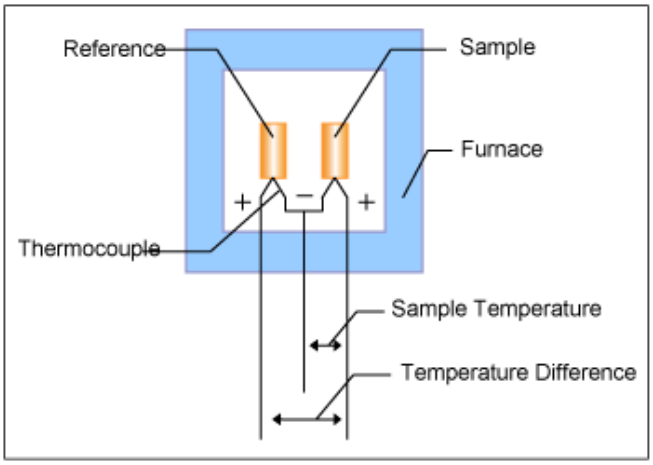

Figure 3.16: Block diagram of differential thermal analysis furnace DTA [215].

3.3.2.1.2 Thermogravimetric analysis (TGA)

TGA was carried out to measure mass losses during the phase transformation as a function of temperature, and also to study the effect of doping Fe^{2+}/Fe^{3+} ions concentrations on the activation energy during CaP (βCPP) synthesis. The holders in STA furnace are linked to a balance which measures both reference mass and the sample mass [213].

In both technique, STA (PerkinElmer®, STA 8000) was used to measure both phase temperature and weight changes for different concentrations of FeCPs samples across temperatures of 30 to 1500 °C and at a heating rate of 20 °C \ min in nitrogen atmosphere. Whereas, for Kinetic analysis different heating rate were applied (10, 20, 15 and 30 °C \ min) with mass of 9 mg. In this experiment alumina powder (Al_2O_3) was used as a reference and in the crucible with the FeCaPs samples to prevent any damage to the crucible.

3.3.3 Mechanical properties and biomaterials characterisation

3.3.3.1 Mechanical properties

Mechanical properties such as hardness (H), Young modulus (E) and densification are important parameters in the tissue engineering scaffolds. Scaffold needs to have suitable mechanical properties. Therefore, densification was calculated by measuring sample's dimensions, also

hardness and Young modulus were measured using nano-indentation technique.

3.3.3.1.1 Nano-indentation technique

Nano-indentation technique can be used to determine mechanical properties of very small part (micron and below) of materials [216]. Since the sample with high doping concentration of Fe^{2+}/Fe^{3+} ion presented here was brittle, nano-indentation with Berkovich diamond indenter with a three-sided pyramid was used, Figure 3.17.

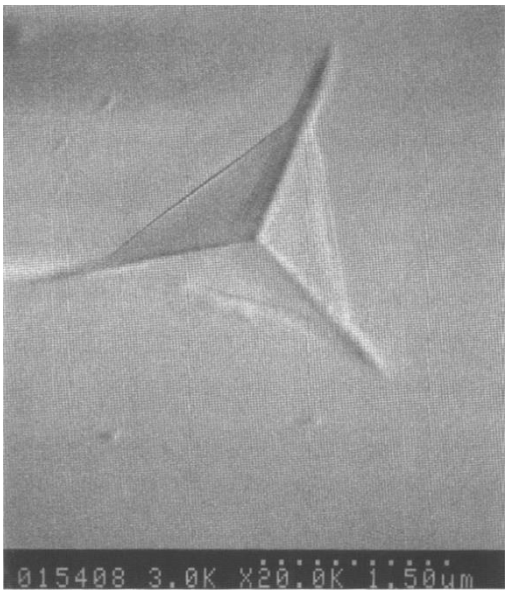

Figure 3.17: Illustration of Berkovich indenter that has a pyramid shape in specimen [217].

Nano-indentation measurement is reported by applying a specific load of indenter to contact with the sample. Once the load is operated, the penetration depth is then measured. From the known angle of the indenter and the depth of indenter on the sample at full load, the area of contact can be measured [216, 218]. Therefore, nano-indentation hardness can be calculated using equation [219]:

$$H = \frac{P}{A} \qquad (3.7),$$

as P is the load mN and A is the projected contact area and it is equal to:

$$A = 24.5h_p^2 \quad (3.8),$$

where: h_p is the projected depth [220]. Young modulus can be measured from the unloading curve by using equation:

$$E = \frac{dP}{dh}\frac{1}{2h_p}\frac{1}{\beta}\sqrt{\frac{\pi}{24.5}} \quad (3.9),$$

where β is constant and equal to 1.034, $\frac{dP}{dh}$ is the slope of unloading curve, Figure 3.18.

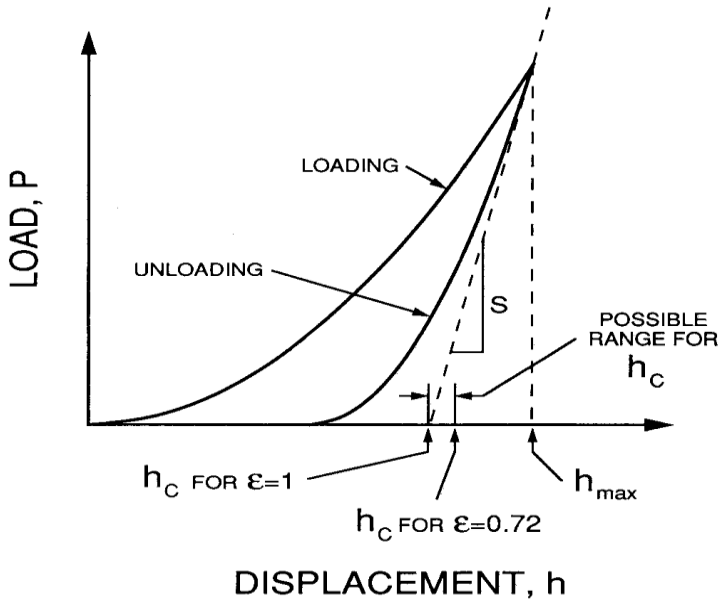

Figure 3.18: Schematic of load (P) versus displacement (h) curve, for loading and unloading curve [217].

In this project, hardness and Young modulus of both sintered and un-sintered layers were measured using a NanoTest machine, equipped with a Berkovich intender and manufactured by Micro Materials Ltd., Wrexham, UK. For each sample, measurement with a load of 100 mN were carried out at 6 different points, for which the average value was taken. Experimental values for hardness (H, GPa) and Young Modulus (GPa) acquired by processing the experimental data with the NanoTest software.

3.3.3.1.2 Density measurement

Density of pellets samples were calculated using dimensional measurement equation [221, 222]:

$$\rho = \frac{m}{V} \qquad (3.10),$$

In equation 3.8

- M is sample mass and was measured using balance (g).
- V volume of sample (cm^3) and since the pellet is in cylinder form the volume equal to:

$$V = \pi r^2 h \qquad (3.11);$$

where r is the radius of pellet and h is the thickness.

To measure the densification of initial and sintered samples relation below were used:

$$Densification = ((\rho_S - \rho_I) \div \rho_S) \times 100 \qquad (3.12);$$

- ρ_S is the density of sintered sample
- ρ_I is density of initial sample

3.3.3.2 Biological experiments

Osteoblasts cell line G292 (departmental frozen stock) were maintained in alpha minimum essential medium (α-MEM) (Gibco, Life Technologies) supplemented with 10% fetal bovine serum (FBS), 2 mM L-glutamine at 37°C in an atmosphere of 5% CO_2 in air. The medium was exchanged twice a week until the cells reached 80 % confluency.

Prior to cell experiments, all sintered FeCaP samples were sterilised by washing them three times with 70% ethanol and 30% distilled water, then dried at 180 ˚C for 3 hrs. Additionally, they were autoclaved on moist heat at 121 ºC for 2hr.

3.3.3.2.1 Biocompatibility evaluation

Biocompatibility of the pellets was determined using two methods contact and extract tests.

3.3.3.2.1.1 Contact cytotoxicity assay

Samples (*n* = 3 per group) were attached to the centre of six-well tissue culture plates using steir-stripe (3M Seince). Dimethyl sulfoxide (DMSO) concentration of 40% and steir-stripe in triplicate were used as positive and negative controls, respectively. G-292 cells were seeded into each well at a density of $5x10^3$ cells/well (2mL volume for each well) then incubated at 37 °C in 5 % (v/v) CO_2 in air for 48 h. Following incubation, the culture medium was carefully aspirated before the wells were washed with phosphate-buffered saline PBS (calcium and magnesium free) and fixed with 10 % (v/v) neutral-buffered formalin (NBF) (Cellpath) for 10 min. The wells were then stained with Giemsa solution (Merck R66 formulation; VWR International, Lutterworth, UK) for five minutes and then repeatedly rinsed with distilled water until clear, after which they were air dried. Changes in cell morphology and confluency were analysed using an Olympus IX 7 inverted microscope under bright field illumination (Cell^B software; Olympus) with all images captured digitally.

3.3.3.2.1.2 Extract cytotoxicity assay

Adenosine triphosphates ATP assay (Perkin Elmer kit), is commonly used to detect the living cells in cell culture, was applied as an extract test [223]. Initially, 15 pellet samples (ratio of $3cm^2$/mL ISO10993-12) were incubated in α-MEM with agitation for 72 hours at 37°C. The extract supernatant was collected, checked for sterility and stored at -20°C until future usage. G292 cell lines, at a density of 5 $x10^4$ cells/200 µL were seeded on 96-well plates and incubated for 24 hours. The culture medium was then aspirated and replaced with 20 µL FBS mixed with 180 µL of test extract or controls to the appropriate wells (in triplicates) and incubated for a further 24 hours. Controls included G292 cells cultured in α-MEM as negative control and 40% dimethyl sulfoxide (DMSO) in α-MEM as positive control. Cell viability (relative cellular adenosine triphosphate (ATP) content) was determined using the ATPLite™ assay (Perkin Elmer Life Sciences) following Perkin Elmer suggested protocol. Eventually, the luminescence was determined using plate reader at a wavelength of 450 nm.

3.3.3.2.2 Cell attachment and proliferation

To restrict cells to the surface of pellets during cell seeding, agarose wells of a diameter 1.3 cm were created by pouring 3% of melted agarose in PBS into each well of 12 well plates containing a stainless-steel rod suspended 2mm above the bottom. After placing the pellets inside the agarose well, 1 mL of media containing 10^4 cells were seeded on the top of each pellet. Cell attachment and proliferation were examined using fluorescence imaging and Picogreen DNA assay, respectively.

3.3.3.2.2.1 Fluorescence imaging

After 2 days in culture, cells on pellets were fixed with 10% NBF for 20 min, washed twice with PBS, permeabilised (0.2% by mass Triton X-100 for 5 min) and rinsed three times with PBS. Samples were stained 1 h in PBS with 20 nmol/L Alexa Fluor 488-phalloidin (Invitrogen) and 4',6-diamidino-2-phenylindole DAPi dye (Sigma-Aldrich) to stain for actin and nuclei, respectively. After staining, cells were washed with PBS, air dried and imaged by confocal fluorescence microscopy (Leica TCS SP8).

3.3.3.2.2.1.1 Confocal fluorescence microscopy

Confocal microscope is a non-destructive tool that give a high resolution of three-dimension shapes. It has been used in industrial applications particularly in biological applications and laboratories to provide a 3D and good focusing of specimen.

The sample response to 3D microscope derive from an in- focus plane while out-focus plane is excluded by pinhole, Figure 3.19. The principle of this microscope is illustrated in Figure 3.20. Generally, the laser light passes through the pinhole. A dichroic mirror reflected this light to the sample and microscope objective will focus the light in a specific spot. The fluorescence from sample fluorophores is transmitted by the same dichroic mirror to the detector since this mirror works by reflecting the shorter wavelength light (488nm) and transmitting longer wavelength light (510nm) [224].

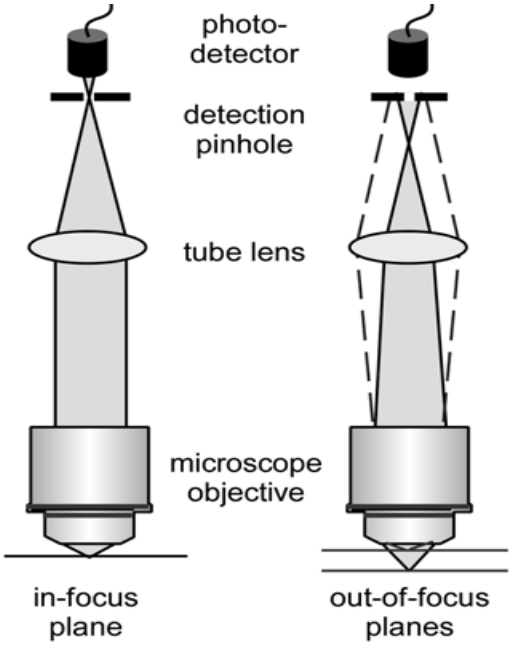

Figure 3.19: Schematic of in-focus plane pass through pinhole to the detector and out- of focus planes is blocked by pinhole in confocal microscope [224].

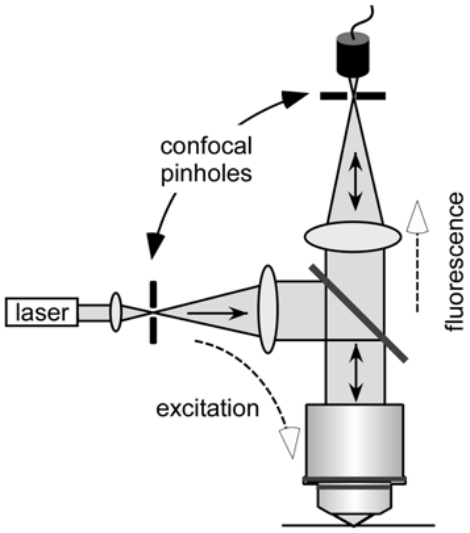

Figure 3.20: The principle of confocal fluorescence microscope, shows the role of dichroic mirror in reflecting and transmitting the different lights [224].

This microscope was used to create a 3D image to get a better image to observe actin and nuclei of cells that were attached on the surface of FeCaP samples before and after micro-channels using ablation by femtosecond pulsed laser.

3.3.3.2.2.2 Picogreen DNA assay

G292 (5X10^4 cells/well) were cultured on pellets and their proliferations was quantified at different times (1 day, 3 days and 7 days) using Picogreen DNA assay (Invitrogen) according to manufacturer's instruction. Briefly, after stipulated time period of incubation, samples were rinsed twice with PBS and subsequently incubated in 300 mL 0.2% Triton in 1x TE buffer (10 mM Tris-HCl, 1 mM EDTA, pH 7.4, (Sigma-Aldrich)) for 15min. The lysates were then centrifuged for 5 min and DNA content was determined in 100 µL of the supernatants using DNA fluorescence (excitation 480 nm, emission 520 nm) measured using Varioskan Flash plate reader (Thermo Scientific). The data were calibrated using a DNA standard curve.

3.3.3.2.3 Statistical analysis

Quantitative data was analysed using one-way analysis of variance ANOVA: single factor using a significance level of 5 % (*p*-value of 0.05). All experiments were performed in triplicates, and the data were analysed using MS Excel Software.

3.3.3.2.4 Biodegradation test

3.3.3.2.4.1 Atomic-absorption spectroscope (AAS)

Atomic absorption spectroscope (AAS) is a simple operation technique in which can be employed to determine concentration of various elements in one sample [225].

The theory of AAS is that electrons of an element are excited to a higher-level energy when the ion absorbs enough energy for excitation to occur. These electrons return to their ground level and will emit a characterise energy is equal to that of absorption energy. As the amount of the element increase in the flame, the emission intensity also increase [226]. Therefore, AAS is based on three important components: light source, flame and detector of the specific wavelength of light. The light source (hollow cathode lamp) consists of the same element that needs to be analysis. Therefore, the light that emit from the source and is absorbed by atoms of element has a specific wavelength. Prior to test, the solution is aspirated to the flame

where heat transfers it to vapour. Thus, the light passes through the evaporation where the absorption occur and the electron is promoted to excited level [226]. When the atoms return to the ground level, they emit a characterise radiation of element which have the same amount of absorption radiation. This amount enter to the detector to be investigated.

AAS (Agilent technology) was used for testing the concentrations of the Ca/Fe ions in FeCaP samples released during degradation test. ISO (10993-14) degradation protocol was utilised. In order to obtain the calibration curve of both Ca and Fe standard a concentration of 3ppm and 15ppm was prepared, respectively. Ca and Fe hollow cathode lamp and an air acetylene flame gas were employed for calculation both Ca and Fe ions, respectively. The concentration result that obtained from AAS software reported as mg/L.

This chapter has described the methods and characterisation techniques used in this investigation. Thus, the analysis and results obtained from these techniques are described in the next chapter.

Chapter 4 Material characterizations and their effect on mechanical properties

Chapter Introduction

The purpose of this chapter is to study the mechanical properties and biological responses of sintered Fe^{2+}/Fe^{3+} doped CaP minerals (β-CPP). In this chapter a conventional powder sintering route is proposed for testing $Fe^{2+/3+}$ doped CaP minerals as potential scaffold for bone tissue regeneration. Since various concentrations of Fe^{2+}/Fe^{3+} ions may have different effect on the mechanical properties, it was necessary to optimize the concentrations of Fe^{2+}/Fe^{3+} ions for the desirable mechanical properties.

Chapter summary

Various doping concentrations of Fe^{2+}/Fe^{3+} ions into CaP minerals were investigated, and the resulting mineral samples in the text are identified as FeCaP minerals, which were synthesized by doping different concentrations of Fe^{2+}/Fe^{3+} ion into brushite using wet chemical precipitation method and characterised. In the synthesized mineral the dominant phase was brushite for minerals up to 20 mol% Fe^{2+}/Fe^{3+} ions, on increasing the concentrations of Fe^{2+}/Fe^{3+} ions to 30 mol%, the resulting mineral structure transformed into an amorphous phase. Thermal sintering at 1000°C transformed brushite into β-CPP; by comparison when the mineral containing high concentrations of Fe (30 mol%) was heat treated at 1000°C, the mineral phase transformed into $FePO_4$ formed. The hardness results for 10 mol% FeCaP was found to be much higher than the undoped β-CPP.

4.1 Material characterizations

4.1.1 The pH measurements and characterisation during mineral synthesis

When synthesizing calcium phosphate minerals, the pH is one of the factors that significantly affects the phase stability and, therefore, the supersaturation condition [227, 228].

With this in mind, changes in pH were monitored during synthesis process after the mixing of phosphate and calcium solutions, as described in chapter 3.1.1. Details of pH variation over time as a function of percentage Fe^{2+}/Fe^{3+} content is presented in Figure. 4.1 [51].

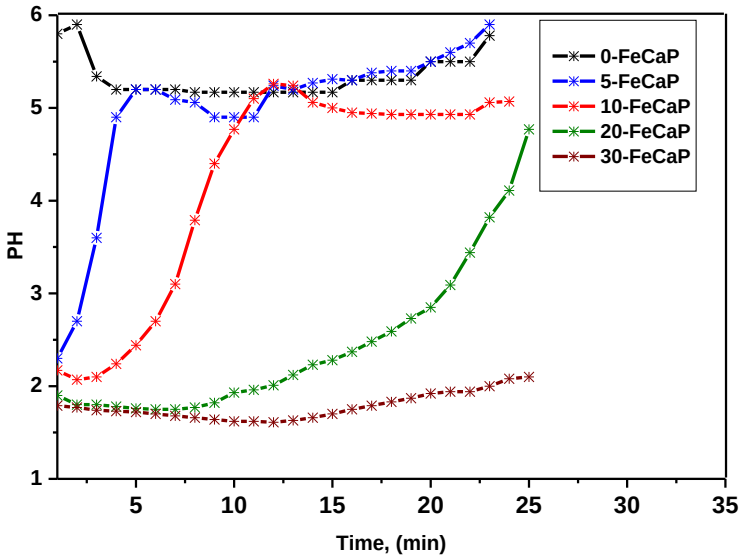

Figure 4.1: The time-dependent pH changes of Fe^{2+}/Fe^{3+} doped CaP solution during the synthesis of calcium phosphate minerals.

It was observed, during the synthesis of undoped calcium phosphate (CaP), that with the addition of the phosphate solution the pH of the resulting mixture, stabilized to around pH = 5.5 (±0.5) and remained relatively stable throughout the whole synthesis process. Based on this and the temperature of synthesis at 37ºC, the resulting phase was brushite structure, which is reported in the literature [229]. From the undoped solution, once the precipitation condition for brushite ($CaHPO_4.2H_2O$) was established, the process of Fe^{2+}/Fe^{3+} ion doped brushite mixtures were planned for

synthesis. The minimum iron-ion doping concentration was 5 mol% and the maximum was 30 mol%.

For a 5 mol% Fe^{2+}/Fe^{3+} ion mixture, the nitrate of iron was doped into the calcium solution resulting in an initial drop in pH to 2.3 before it increased on continuous addition of the PO_4 solution till a pH of 6.0 was reached at the end of the synthesis process. Similar observations were made when the dopant content was increased to 10 mol%. However, the rise in pH occurred over a longer time period (11 min) in comparison with the previous mixture with 5 mol% Fe^{2+}/Fe^{3+} ion concentrations. Also, the final pH at the end of the process was ~ 5.0 as compared to ~ 6.0 for the 5 mol% Fe^{2+}/Fe^{3+} suspension.

When higher than 10 mol% Fe^{2+}/Fe^{3+} ion content was introduced on increasing the Fe^{2+}/Fe^{3+} ion concentration it was observed that the pH drop was faster than the previous two samples. Also there was a time lag of approximately 10 mins during which pH level was strongly acidic, after which the pH of the suspension began to rise gradually. For the 20 mol% FeCaP suspension, the pH levels dropped to around 1.7 during the first few minutes, before it increased to 4.8 after 29 minutes. By comparison, in the 30-FeCaP suspension, the pH levels remained strongly acidic all through and did not rise above 2.3 at the end of the process. The acidic nature of the 20 mol% and 30 mol% Fe^{2+}/Fe^{3+} may be related to the oxidation of Fe^{2+} to Fe^{3+} during the synthesis process, as the synthesis occurred under open atmospheric conditions. As Fe^{2+} converts to Fe^{3+} to it pulls electrons to it. These make the bond between O-H in the water molecule weaker, thereby releasing more H^+ into the solution, according to equations below [230, 231].

$$2Fe^{2+} = 2Fe^{3+} + 2e \quad (4.1)$$

$$OH^- = O^{2-} + H^+ \quad (4.2)$$

$$0.5O_2(atm) + 2e = O^{2-} \quad (4.3)$$

$$HPO_4^{2-} + Fe^{3+} = FePO_4 + H^+ \quad (4.4)$$

4.1.2 X-ray powder diffraction (XRD)

For determining the purity of phases formed, crystallinity, and crystallite size, the X-Ray powder diffraction was used for all FeCaP samples discussed in Figure 4,1. In Figure. 4.2, the powder diffraction patterns are compared for the undoped and Fe^{2+}/Fe^{3+}-doped mineral samples.

In Figure 4.2b, the synthesised samples with different percentage molar of $Fe^{2+}\backslash Fe^{3+}$ ions concentrations are shown. For the undoped material (0-FeCaP) in Figure 4.2a, the main peaks were indexed to the reference pattern of brushite ($CaHPO_4 \cdot 2H_2O$) (JCPDS-00-011-0293) at 2θ = 11.61°, 20.95°, 23.38°, 29.24° and 34.11°. Monetite ($CaHPO_4$) peaks were also identified at 2θ = 26.51° and 30.52° (JCPDS-04-011-3070). Based on the Rietveld refinement, the composition of the 0-FeCaP was calculated to be 73.5% brushite and 26.5% monetite. For the 5-FeCaP and 10-FeCaP materials; only brushite peaks were observed. Also, the peaks appeared to have shifted to a higher 2θ positions (Table 4.1).

For 20-FeCaP, amorphous and crystalline phases where observed. The crystalline phases were a mixture of monetite and brushite with percentage of 37.1% and 62.9%, respectively. On further increasing the dopant concentrations of Fe^{2+}/Fe^{3+} to 30 mol% an amorphous phase was formed. The volume fractions of amorphous and crystalline phases of all the samples are presented in chapter 5.

Changes in the position of the brushite peaks and its lattice parameters were observed via XRD, which may be a result of incorporation of Fe^{2+}/Fe^{3+} into the CaP structure since the ionic radius of Ca^{2+} (0.099 nm) is higher than the ionic radius of Fe^{2+}/Fe^{3+} (0.074\0.068 nm) [231].

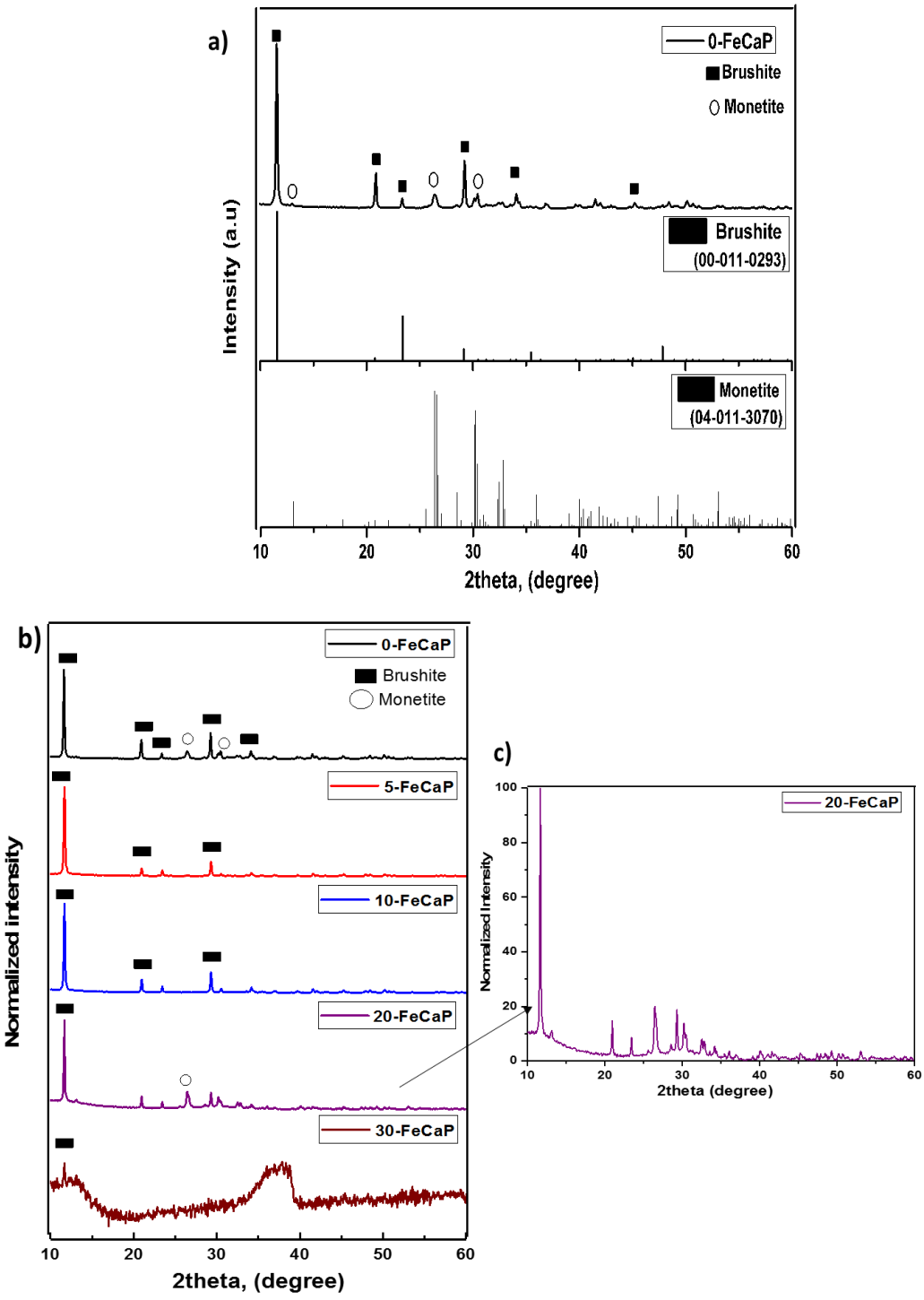

Figure 4.2: a) XRD of undoped CaP in comparison to reference patterns brushite (00-011-0293) and monetite (04-011-3070), b) XRD of synthesised FeCaP minerals with different concentrations of Fe^{2+}\Fe^{3+} ions and c) XRD of 20-FeCaP shows an amorphous phase. All samples was run using X-ray at λ= 1.54Å with a step size of 0.065° and a scan speed of 1° s^{-1}.

It is known that the brushite is considered as metastable materials and its dehydration could start under atmospheric condition which results in transformation to monetite structure [75, 229]. For this reason, the peaks of monetite appeared relatively prominent in the undoped material. Furthermore, Fe^{2+}/Fe^{3+} ion may have stabilized brushite in the 5 and 10 mol% samples since the lattice parameter shifted to higher positions, that could be linked to the stronger complexes between Fe and phosphate than Ca ion and reduce the release of Ca^{2+} in the solution [75, 98, 229, 232]. Whereas for 20 mol%, the appearance of monetite peaks may be because the Fe present became bonded with the phosphate group and formed an second phase (amorphous phase) instead of reducing Ca therefore stabilising the brushite phase as no shifting on the peaks were observed.

$$2Ca^{2+} + 2Fe^{2+} = 2(Ca^{2+}, Fe^{3+}) + 2e \quad (4.5)$$

$$0.5O_2(air) + 2e = O^{2-} \quad (4.6)$$

Table 4.1: Peak positions of CaP at different Fe^{2+}/Fe^{3+} concentrations.

Materials	**Peak positions**			
0-FeCaP	11.61°	20.95°	23.38°	29.24°
5-FeCaP	11.67°	20.95°	23.44°	29.30°
10-FeCaP	11.78°	21.06°	23.56°	29.41°
20-FeCaP	11.67°	20.95°	23.44°	29.30°

Results of X-ray diffraction analysis of the FeCaP minerals with different doping concentrations of Fe^{2+}/Fe^{3+} were sintered at 1000 ^{o}C for 5 hours in air, after which the phase analysis was carried out using the X-ray powder diffraction technique, as before for the synthesized minerals. These results are compared in Figure 4.3.

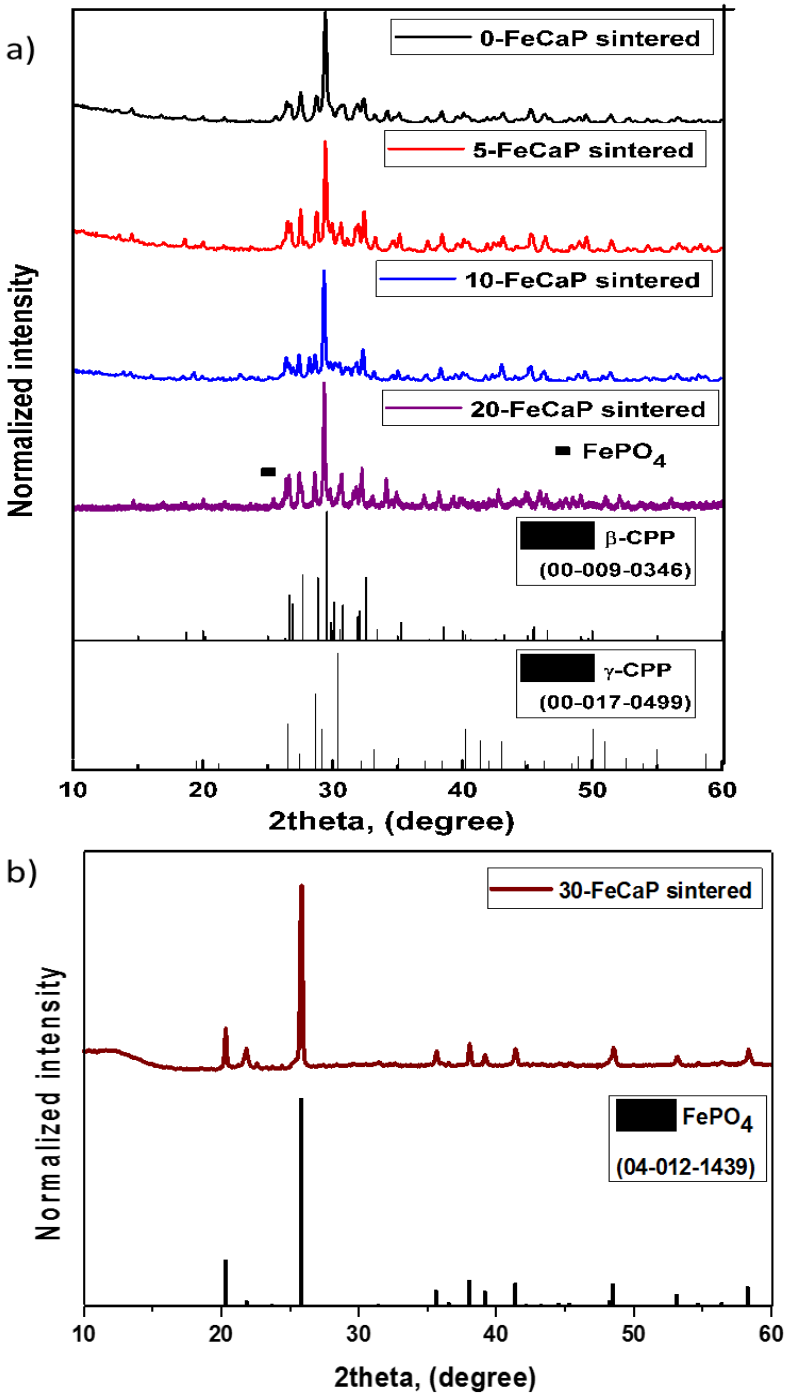

Figure 4.3: XRD of the sintered FeCaP powders at 1000 ˚C for 5 hrs a) 0, 5, 10 and 20-FeCaP powders present β-CPP phase in comparison with β-CPP (Ca_2P2O_7) (00-033-0297) JCPDS file. b) 30-FeCaP transformed into (FePO4) in comparison with JCPDS (04-0012-1439) file.

The X-ray powder diffraction analysis of the sintered materials show that the transformation of brushite to the β-CPP ($Ca_2P_2O_7$) phase had been completed. The diffraction peaks of β-CPP are at Bragg angles, (2θ = 26.99°, 28.97°, 29.66°and 32.62°). Moreover, a weak peak at (2θ = 25.43°) confirmed the presence of FePO4 in the 20-FeCaP sample. Peaks of λ-

CPP (λ-$C_2P_2O_7$) were observed at 2θ = 30.62˚ in 0, 5 and 20-FeCaP (JCPDS 00-017-0499), while for 10-FeCaP full transformation into βCPP happened at temperature of 1000˚C for 5hrs. On the other hand for 30-FeCaP, iron phosphate ($FePO_4$) structure was observed (JCPDS 04-012-1439) (Figure. 4.3b). Increasing the concentration of Fe^{2+}/Fe^{3+} ion up to 30 mol% promotes the biphosphate dissociation reaction : $(HPO_4)^{2-} = H^+ + PO_4^{3-}$ which in the subsequent step combines with Fe^{3+} and forms $FePO_4$. It is for this reason that the pH tends to decrease because of the increasing concentrations of Fe^{3+}-ions [233].

4.1.3 Fourier infrared spectroscopy- attenuated total reflectance (FTIR-ATR)

The initial synthesised and sintered minerals were examined using FTIR (Figure. 4.4 and 4.5). In Figure 4.4, results indicated a brushite structure in the synthesised materials with Fe ion concentration up to 20 mol% (i.e. 0 mol%, 5 mol%, 10 mol% and 20 mol%). Bands at 860 cm^{-1}, 1120 cm^{-1} and 1180 cm^{-1} were linked to the HPO_4^{-2}. Peaks at 520 cm^{-1}, 980 cm^{-1} and 1050 cm^{-1} were assigned to PO_4^{-3}. Finally, the appearance of a peak at 1640 cm^{-1} and 2370 cm^{-1} are attributed to the presence of water molecules. These observations are in agreement with previously reported data for brushite [229, 234-237]. An increase in intensity of the peaks was observed when the concentration of Fe^{2+}/Fe^{3+} increased which might be related to the stabilisation of brushite after doping with Fe ions [231, 238, 239]. Whereas, the intensity of peaks decrease for doping with 20 mol% that could be due to the monetite phase that observed using XRD.

On the other hand, by increasing the concentration of Fe ions (up to 30 mol%), the vibrational peaks were substituted with a single peak, indicating that Fe deformed the brushite structure resulting in an amorphous iron phosphate $FePO_4 \cdot 3H_2O$, as shown in (Figure. 4.4) [240]. The band at 1000 cm^{-1} is related to PO stretching vibration mode while at 1640 cm^{-1} is attributed to stretching variation mode of water molecules. Bands in the range of 500-400 cm^{-1} are attributed to PO stretching vibration mode also

these bands include Fe-O and O-P-O stretching and bending mode, respectively.

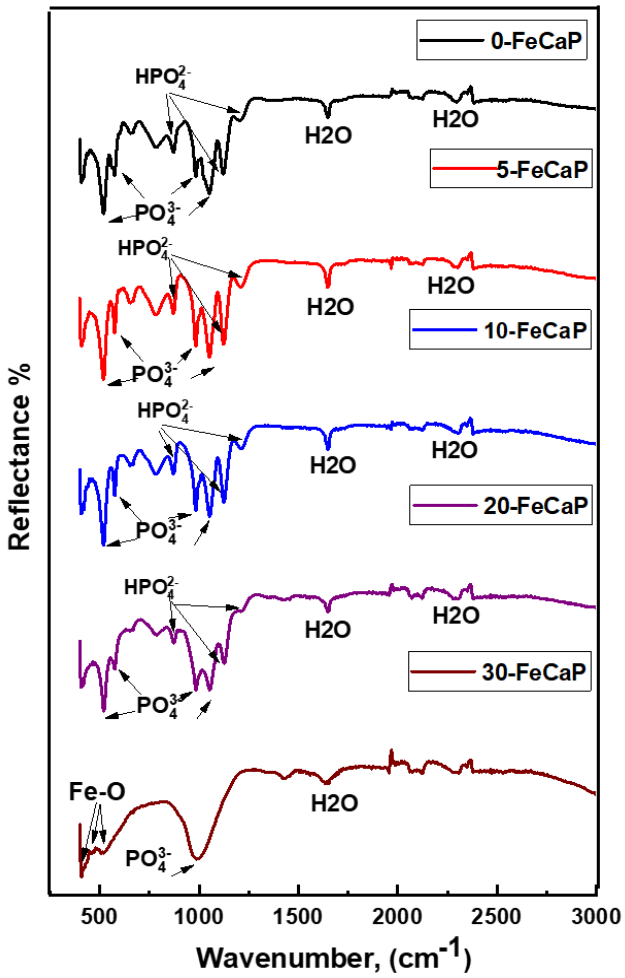

Figure 4.4: FTIR-ATR spectra of the synthesised powders 0, 5, 10, 20 and 30% mol of **Fe^{2+}/Fe^{3+} ions**. For 0, 5, 10 and 20 mol% same structure presented (brushite) whereas for 30-FeCaP $FePO_4.2H_2O$.

Figure. 4.5 shows FTIR spectra of the thermally treated (0, 5, 10, 20 and 30-FeCaP) minerals at 1000 °C for 5 h. The P-O-P stretching mode at 727 cm^{-1} is a known band of β-CPP [237, 241]. Bands at 1211 cm^{-1}, 1153 cm^{-1} and 1076 cm^{-1} are related to PO stretching mode. Peaks between 600 cm^{-1} and 400 cm^{-1} are assigned to PO bending mode. $FePO_4$ crystal structure of 30-FeCaP sintered was confirmed in agreement with literature [240]. The bands of Fe-O stretching vibration modes were observed at 422 cm^{-1},578 cm^{-1} and 624 cm^{-1} [242, 243]. Band at 970 cm^{-1} is corresponding asymmetric stretching mode of PO_4^{3-}.

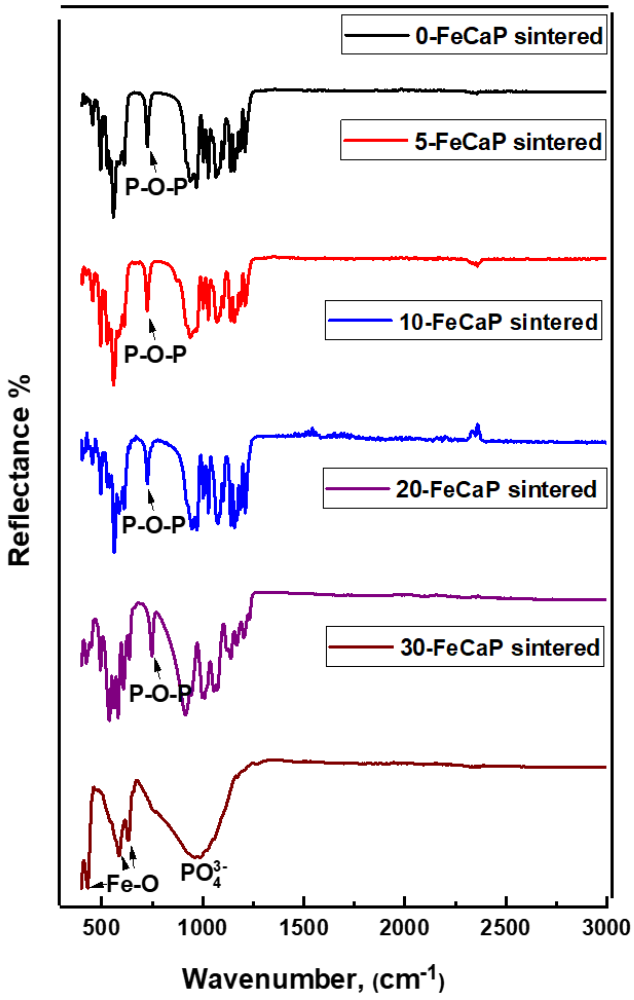

Figure 4.5: FTIR-ATR spectra of the sintered powders 0, 5, 10, 20 and 30% mol of Fe^{2+}/Fe^{3+} ions. For 0, 5, 10 and 20 mol% indicates β-CPP whereas for 30-FeCaP crystalline FePO4.

4.1.4 Raman spectroscopy

Raman spectroscopy was also used to confirm crystallinity of samples. The main Raman peak for the PO_4^{3-} symmetric stretching modes were observed in all FeCaP mineral, as can be seen in Figure. 4.6. For undoped FeCaP this peak was at wavenumber of 988 cm^{-1}. The peak at wavenumber 1147 cm^{-1} was assigned to the antisymmetric stretching mode of HPO_4^{2-} . The bonds at 420 and 385 cm^{-1} were attributed to symmetric bending mode PO_4^{3-} in the brushite phase, Table 4.2. For 5 and 10-FeCaP materials, the relatively small amount of Fe^{2+}/Fe^{3+} ion did not modify the structure of brushite. However, the intensity of 5- and 10-FeCaP increased in comparison to the undoped mineral, which could signify an increase in

crystallinity of the material as was confirmed with XRD (section 4.1.2). Although there was no change in the position of the main peak for 20 mol% Fe^{2+}/Fe^{3+} material, the peak was observed to be relatively broader in comparison to the 5- and 10-FeCaP materials which could be related to decrease of crystallinity and may be attributed to the presence of amorphous iron phosphate.

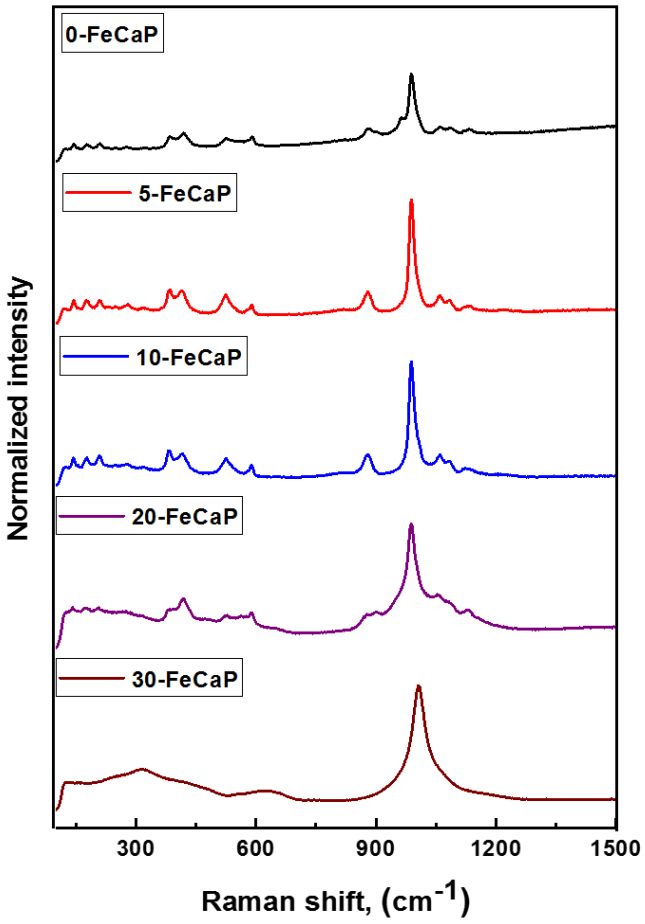

Figure 4.6: Raman spectroscopy of synthesised FeCaP shows different structures. 0, 5, 10 and 20-FeCaP show brushite structure, however, the mean peak of 20 mol% became broad. For 30-FeCaP, amorphous FePO4.2H2O presents.

For 30 mol% the main peak appeared to have shifted to a higher wavenumber at 1009 cm^{-1} than that in the undoped CaP, indicating that the relatively higher Fe^{2+}/Fe^{3+} ion concentration may have led to a change in the structure of CaP. The Raman and FTIR vibrational analysis also confirm the phase transformation reaction. The main peak at 1009 is related to PO_4^{3-} stretching mode whilst peaks at 655 and 456 cm^{-1} correspond to the

PO_4^{3-} asymmetric bending mode and symmetric bending mode respectively [244]. These peaks are corresponding to $FePO_4$ and since they are broad peaks indicating amorphous phase. Table 4.2 below presents peak assignments for synthesised FeCaP samples (brushite and amorphous $FePO_4 \cdot 3H_2O$) in both Raman and FTIR.

Table 4.2: Functional groups of brushite and amorphous $FePO_4.3H_2O$ (cm^{-1}).

Brushite			**$FePO_4 \cdot 3H_2O$**		
	Raman	IR		Raman	IR
PO(H) stretching modes	877	874	PO_4 stretching mode	1009	987
HPO_4^{2-} antisymmetric stretching modes	1137		Fe-O	626	582-
PO_4^{3-} symmetric stretching modes	991 - 1091- 1053	1124- 1053-981	O-P-O bending mode	313	432
PO_4^{3-} symmetric bending modes	423-385	668-572- 521	H-O-H		1600
O–H stretching of water		2297			
H-O-H		1650			

Raman spectroscopy after sintering the FeCaP samples at 1000 ˚C for 5 h is also shown in Figure. 4.7. For sintered 0, 5-FeCaP, peaks at 1200 cm^{-1}, 1170 cm^{-1} and 1140 cm^{-1} are assigned to asymmetric PO stretching mode.

The mean peak at 1050 cm^{-1} and the peak at 1000 cm^{-1} of 0 and 5-FeCaP are corresponding to symmetric PO stretching mode. Whereas, the peak at 737 of both samples are related to symmetric P-O-P group. Thus, these peaks were corresponding to β-CPP [245, 246].

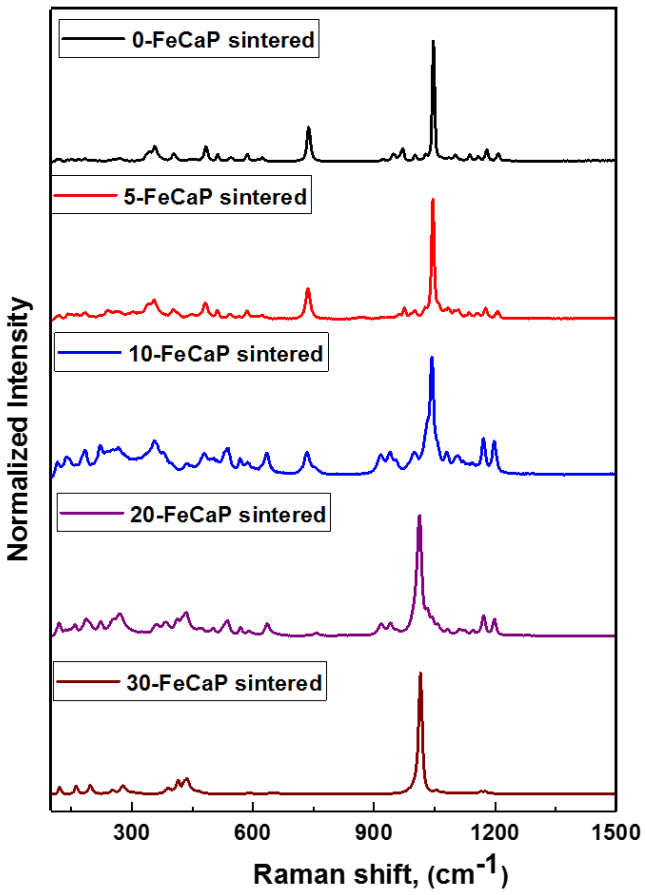

Figure 4.7: Raman spectroscopy of sintered FeCaP shows β-CPP for 0, 5, 10 and 20-FeCaP and crystalline $FePO_4$ for 30-FeCaP.

For 10-FeCaP, same peaks presented as in 0-FeCaP and 5-FeCaP sample, however, new peak was observed at 919 cm^{-1} that is attributed to asymmetric P-O-P band of β-CPP [247]. . For 20 mol% the main peak was observed to have shifted from 1047 cm^{-1} to lower wavenumber (1015 cm^{-1}). This might be linked to peak shifting of β-CPP and $FePO_4$ formation [248]. Peaks between 280 cm^{-1} and 123 cm^{-1} are related to Fe-O or/and P-O bending mode. On the other hand, sintered 30-FeCaP presented PO_4 stretching mode at 1013 cm^{-1}. Peaks at 440 cm^{-1}, 418 cm^{-1}, 385 cm^{-1}, 280 cm^{-1}, 205, 170, 156 and 123 cm^{-1} are assigned to different bending and stretching mode of Fe-O and P-O [248]. Theses peaks are related to

crystalline $FePO_4$. Table 4.3 shows the functional groups for crystalline FePO4 and β-CPP.

Table 4.3: Peak assignments for β-CPP and $FePO_4$ (cm^{-1})

β-CPP			**$FePO_4$**		
	Raman	**IR**		**Raman**	**IR**
PO asymmetric stretching modes	1212 -1170 -1140-1099	1211-1153-1140-1076	PO_4 stretching mode	1013	987
PO symmetric stretching modes	1050 -1000		Fe-O	440-385-201-125	582
P-O-P symmetric stretching modes	737	727	O-P-O bending mode	385-201-165-125	432
P-O-P asymmetric stretching modes	919	973			
PO asymmetric bending modes	688 -622 -586 -543	555			
PO symmetric bending modes	511 -482-380 -270	495-491			

4.1.5 Simultaneous thermal analysis (STA)

Differential thermal analysis (DTA) and thermogravimetry (TGA) analysis was carried out for all FeCaP minerals in order to study the decomposition

of these samples within the temperature range of 30 ℃ -1450 ℃. The constant heating rate was set at 20℃/minute. During the heating, the weight and enthalpy changes were also recorded simultaneously, as shown in Figures 4.8 and 4.9.

4.1.5.1 Differential thermal analysis DTA

For the undoped material, there were five stages of decomposition: the first endothermic peak at ~202 °C due to transformation of brushite into monetite accompanied by the loss of two water molecules (eq. 4.7). A second endothermic thermal event at approximately 471 °C is the decomposition of monetite to γ-CPP and the resulting loss in mass decreases due to the loss of ½ H_2O between 300 and 400 °C (eq. 4.8). The exothermic peak at 890°C is linked to the transformation of γ-CPP into β-CPP while the adjoining endothermic peak of α-CPP appeared at 1280°C. Due to the unstable nature of α-CPP phase, it converted back to β-CPP during cooling [4, 249]. The melting point of undoped material was 1328 °C.

$$2\mathrm{CaHP}O_4 \cdot 2H_2\mathrm{O}\ (\mathrm{brushite}) \Rightarrow 4H_2\mathrm{O} + 2\mathrm{CaHP}O_4\ (\mathrm{monetite}) \quad (4.7)$$

$$2CaHPO_4\ (monetite) \Rightarrow H_2O + Ca_2P_2O_7\ (\lambda - CPP) \quad (4.8)$$

In the materials doped with 5, 10 and 20 mol% Fe^{2+}/Fe^{3+} ion, similar decomposition patterns were observed, as shown Figure 4.8. However, it was observed that increasing the concentration of Fe^{2+}/Fe^{3+} ions shifted the onset of phase transformations to lower temperatures, as can be seen in table 4.4, which is consistent with reported data in literature [4, 238, 249]. The decrease in the temperature of thermal events in the doped materials may be attributed to the incorporation of Fe^{2+}/Fe^{3+} into CaP lattice, which has a smaller ionic radius than Ca^{2+} that leads to an increase in the lattice strain, hence decreasing decomposition temperatures [4, 129]. Also, the exothermic peak of β-CPP became clearer and sharper in the doped minerals in comparison to the undoped. However, monetite temperature for 5 and 10-FeCaP increased in comparison to undoped and 20-FeCaP. This is attributed to that in case of undoped and 20-FeCaP monetite were

observed in the initial structure. Therefore, lower temperature is needed to fully transformation of monetite.

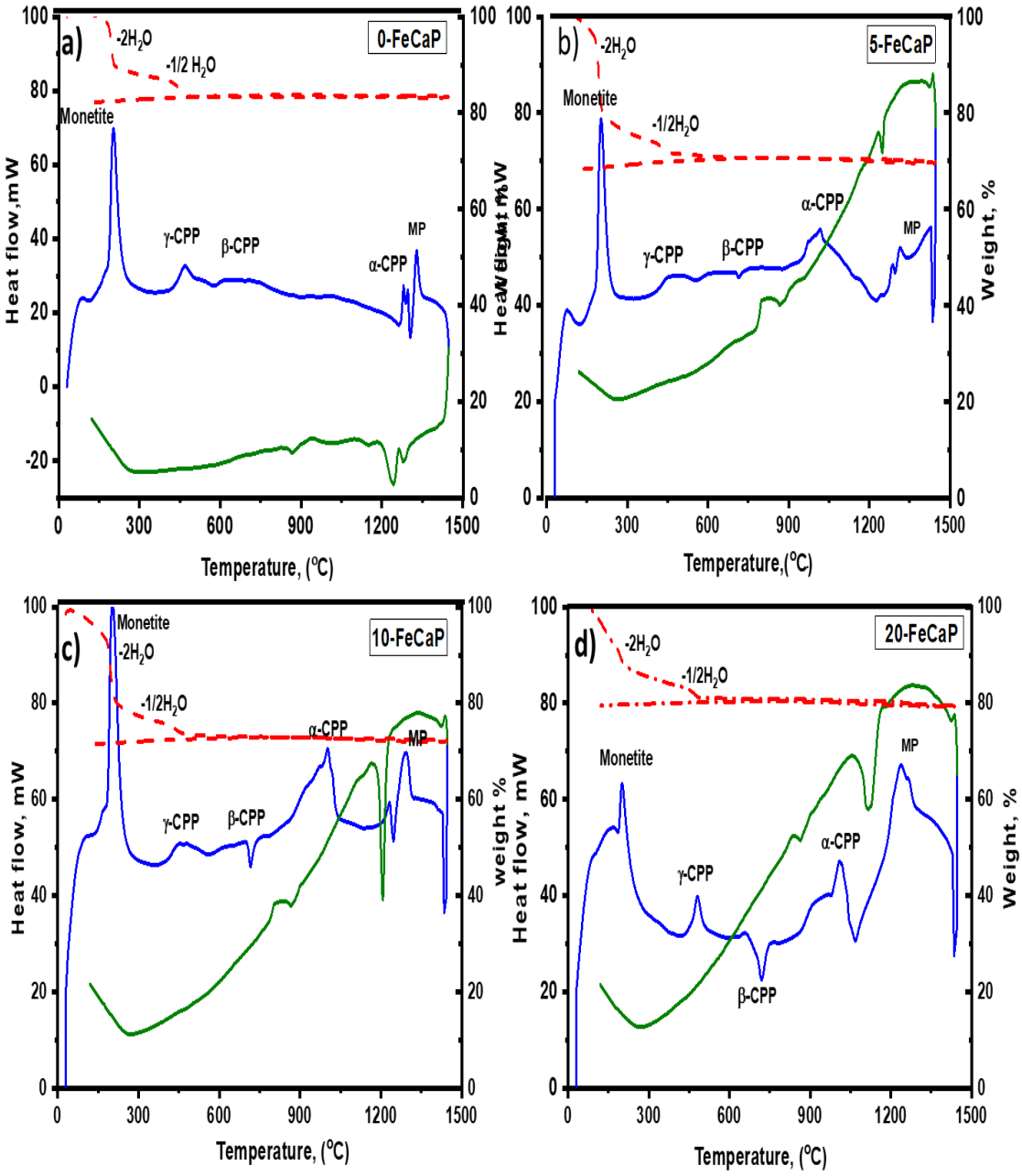

Figure 4.8: DTA (solid blue (during heating) and green lines (during cooling) and TGA (dash red line) of 0. 5. 10 and 20-FeCaP showing the decomposition temperature of brushite at temperature between 30-1450ºC and heating rate of 20 ºC /m.

Table 4.4: Decomposition temperature of FeCaP minerals.

Samples	Monetite	γ-CPP	β-CPP	α-CPP	Melting Point
0-FeCaP	201 ºC	471 ºC	890 ºC	1280 ºC	1329 ºC
5-FeCaP	203 ºC	470 ºC	717 ºC	1015 ºC	1315 ºC
10-FeCaP	203 ºC	468 ºC	715ºC	1004ºC	1290ºC
20-FeCaP	200 ºC	479 ºC	720 ºC	1010 ºC	1240 ºC

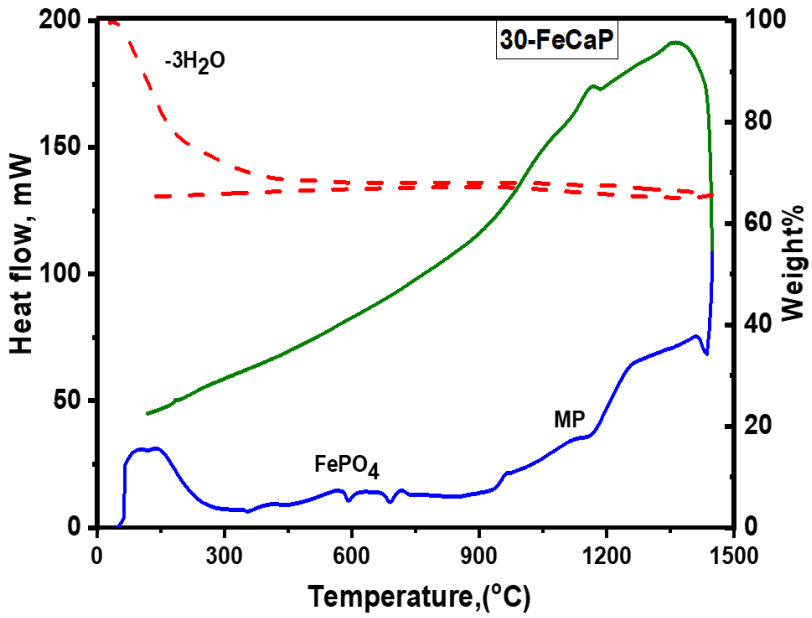

Figure 4.9: DTA and TGA of 30-FeCaP for temperature between 30-1450˚C and heating rate of 20 ˚C/m.

Since the phase formed in the 30 mol% sample was amorphous, it is expected to have different decomposition stages, (Figure. 4.9). peak at 160˚C was water molecules were lost from the amorphous $FePO_4$; however

total transformation to crystalline was at 594 ˚C which is in agreement with literature [240, 250]. The transformation from trigonal to orthorhombic form of $FePO_4$ happen at 689˚C [251, 252]. However, the trigonal phase seems to be thermodynamically stable since orthorhombic phase does not revert during cooling. The resulting melting point due to Fe^{2+}/Fe^{3+} ions doping was found to be around 1143 ˚C.

4.1.5.2 Thermogravimetry TGA

The TGA was investigated for characterising the weight change during thermal process, as shown in Table 4.5. The value of mass reduction for 0-FeCaP in the decomposition from brushite into monetite was 13%, while the remaining mass loss 4% is corresponding to the loss of the proton bound to PO_4 when monetite transformed to γ-CPP at 470°C. For 5-and 10-FeCaP, the water loss in the conversion of brushite to monetite was 21% which agrees with the theoretical amount of water loss of brushite that is 21%. The transformation of monetite into γ-CPP was accompanied with 6% weight of water loss.

In 20-FeCaP the total mass loss was 20%, 13% was corresponding to water loss during decomposition of brushite to monetite and the rest 7% as mentioned decomposition of monetite to γ-CPP. The initial peak of water loss in all samples is related to both transformation of monetite and the water surface [72, 81]. 0-and 20-FeCaP was lower than 5 and 10-FeCaP, this might be due to the mixture of brushite and monetite presented in 0 and 20-FeCaP. Since the transformation of brushite to monetite result in loss of 2 of H_2O, therefore half of the transformation is needed for full decomposition.

For 30-FeCaP, the overall mass reduction was around 30%. The mass reduction of 20% at 160 ºC was related to the elimination of water (eq. 4.9). The loss of 10% in mass at 590 ºC was also corresponding to water and transformation of amorphous to crystalline structure. Therefore, total mass loss was 29% that is near to the theoretical amount of mass loss in FePO4.3H2O which is 26%.

$$FePO_4 \cdot 3H_2O \rightarrow FePO_4 \cdot H_2O + 2H_2O \quad (4.9)$$

$$FePO_4 \cdot H_2O \rightarrow FePO_4 + H_2O \quad (4.10)$$

Table 4.5: Mass reduction in FeCaP samples using TGA.

Materials	Mass reduction
Undoped	17%
5% Fe doped	28%
10% Fe doped	27%
20% Fe doped	20%
30% Fe doped	29%

4.1.7 Scanning electron microscopy (SEM)

The morphology and the chemical composition of the synthesised and sintered materials has been examined under the SEM and EDX-SEM was employed to observe the effect of Fe^{2+}\Fe^{3+} concentrations on the substructure of both samples.

Figure. 4.10 shows the SEM images obtained at different magnification for the synthesised 0, 5 and 10-FeCaP samples. A plate-like structure was noticed for 0, 5 and 10-FeCaP minerals which is a known structure of brushite. The dimensions of brushite were in the range of 5 – 20 μm in width and in the range of 20 – 40 μm in the length, which is similar to the dimensions reported in a previous study [253]. However, a small size of plate-like structure with number of agglomerates appeared in the 20 mol% sample, Figure 4.11a. At higher magnification, Figure. 4.12 shows a spherical particle of 20 mol% that might be attributed to amorphous

$FePO_4.3H_2O$. Whereas, no spherical particles of amorphous iron phosphate were observed for 5-FeCaP and 10-FeCaP, as shown in Figure 4.13.

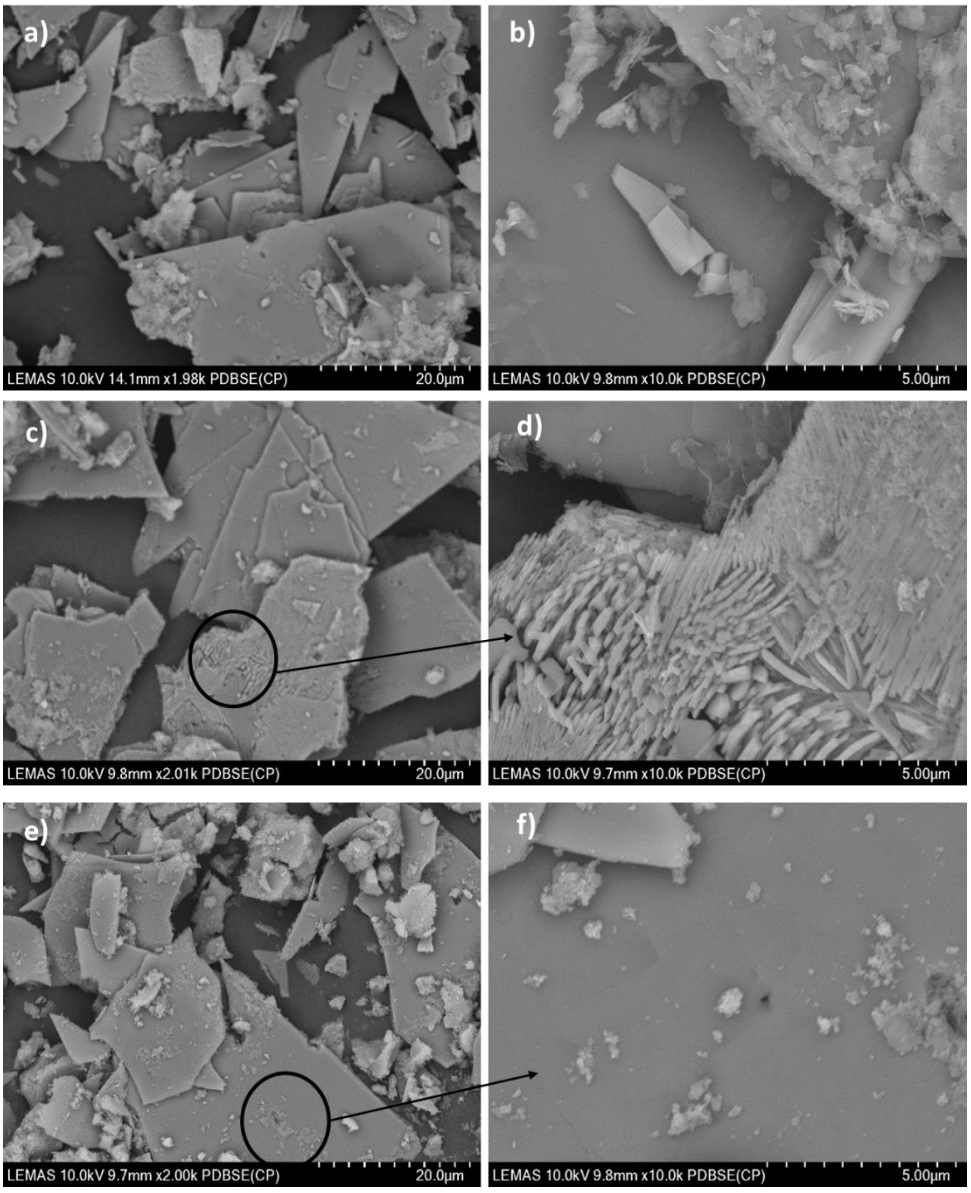

Figure 4.10: SEM images of 0-FeCaP (a and b), 5-FeCaP (c and d) and 10-FeCaP (e and f) minerals powders at different magnifications.

For 30-FeCaP an amorphous phase was present (Figure. 4.11c). A significant number of agglomerates were observed in 30-FeCaP, which may be attributed to the pH and zeta potential as the pH was around 2.0, the charge may change and the crystal agglomerate [254].

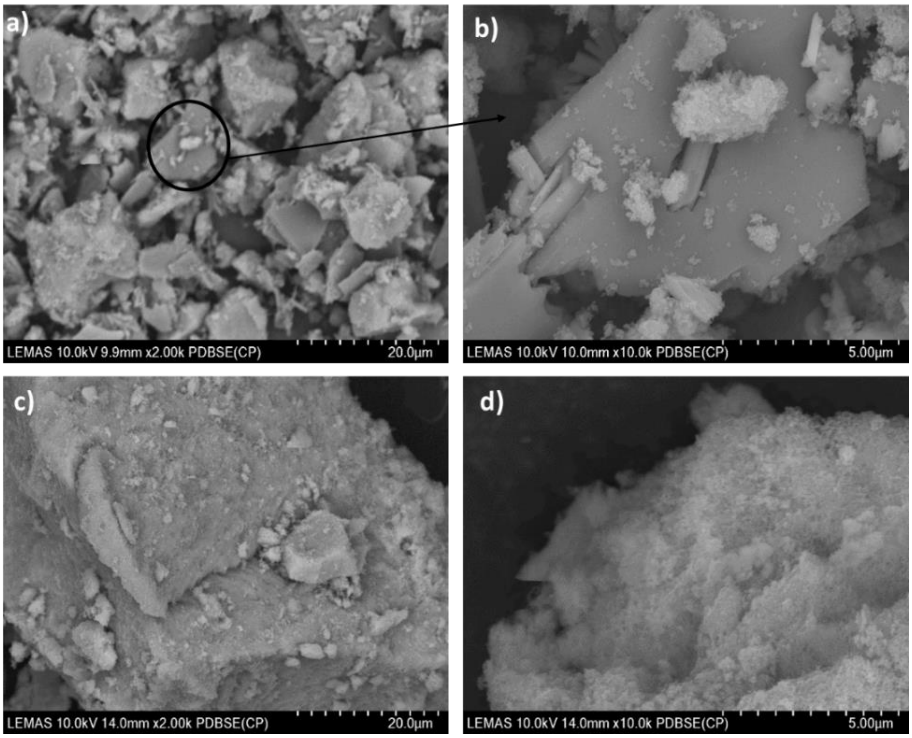

Figure 4.11: SEM images a), b), 20 and c), d) 30-FeCaP minerals powders at different magnifications.

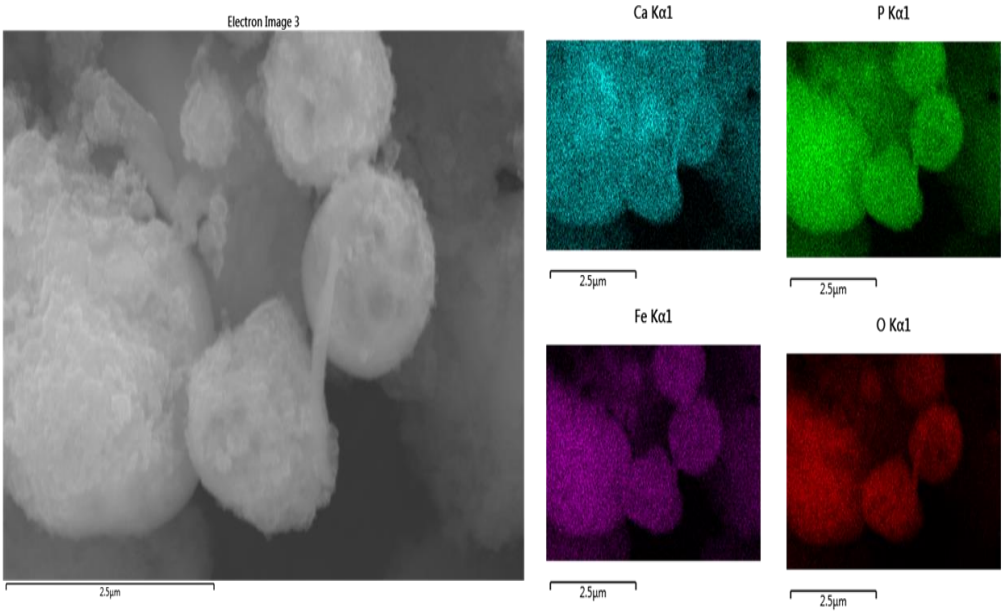

Figure 4.12: EDX-XRD of 20-FeCaP mineral indicates iron phosphate and illustrated the material compositions.

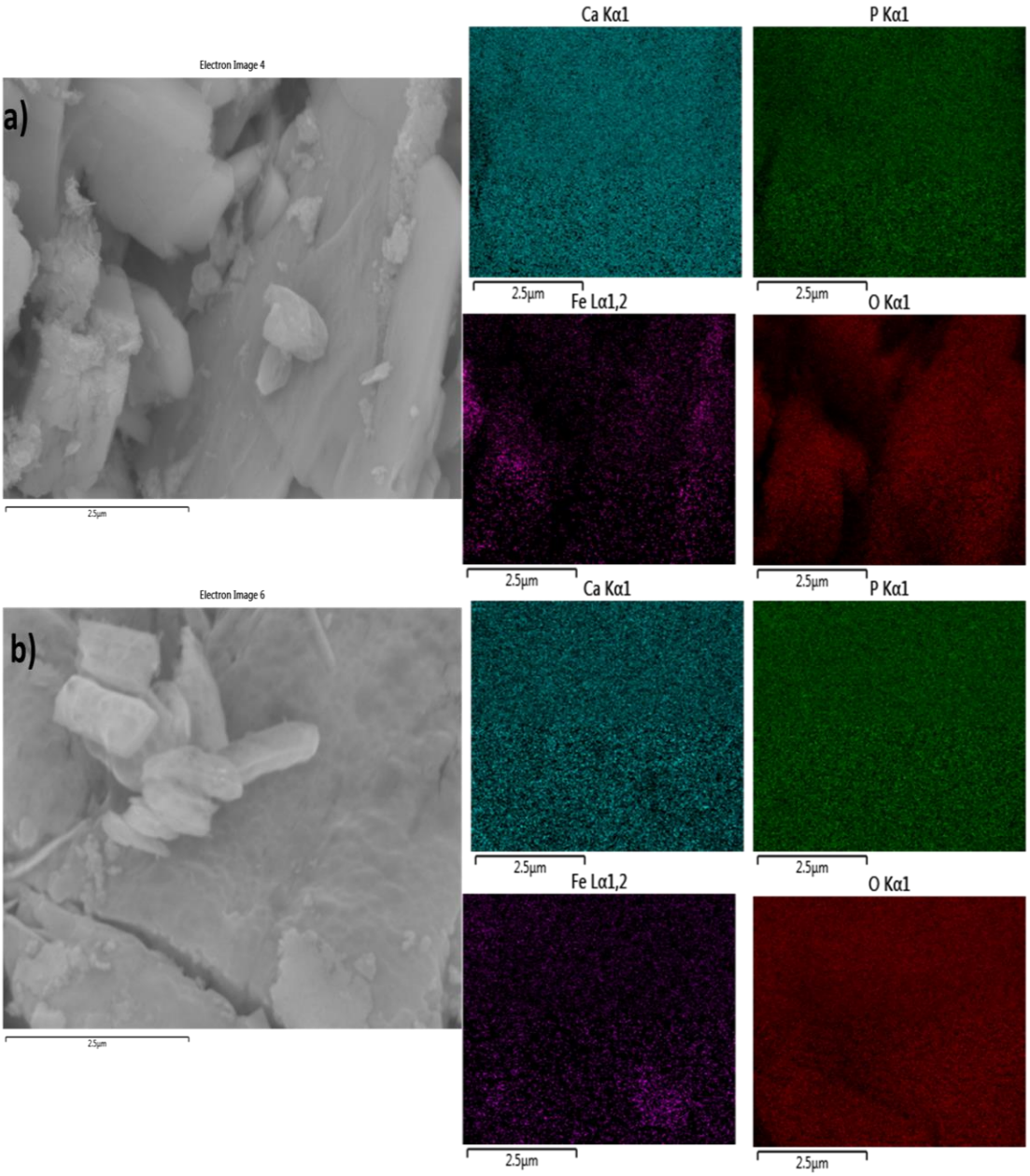

Figure 4.13: EDX-XRD of 20-FeCaP mineral indicates iron phosphate and illustrated the material compositions

The morphology of sintered FeCaP materials, as shown in Figure. 4.14, was also analysed. The 0-FeCaP composition retains plate-like geometry but the extended porosity is presented at the surface of the crystals (Figure 4.14a). According to mechanism of sintering in solid phase, herein the mechanism are either surface diffusion or lattice diffusion from the surface. Therefore, coarsening occurs lead to decrease driving force of sintering that causes number of porosity.

For the Fe^{2+}/Fe^{3+} doped materials reoredering of the crystal structure and remineralisation can be observed which illustrate high dense materials, as shown in Figure 4.14c,d,e,f and Figure 4.15. Dopant materials can affect on sintering process they may increase or decrease the densification as explained in literature. It can be form as second phase or increase the vacancy since the dopant has smaller ionic radius. Fe ion was found as a second phase in 20-FeCaP also melting was observed that may fill the pores and increased densifications.

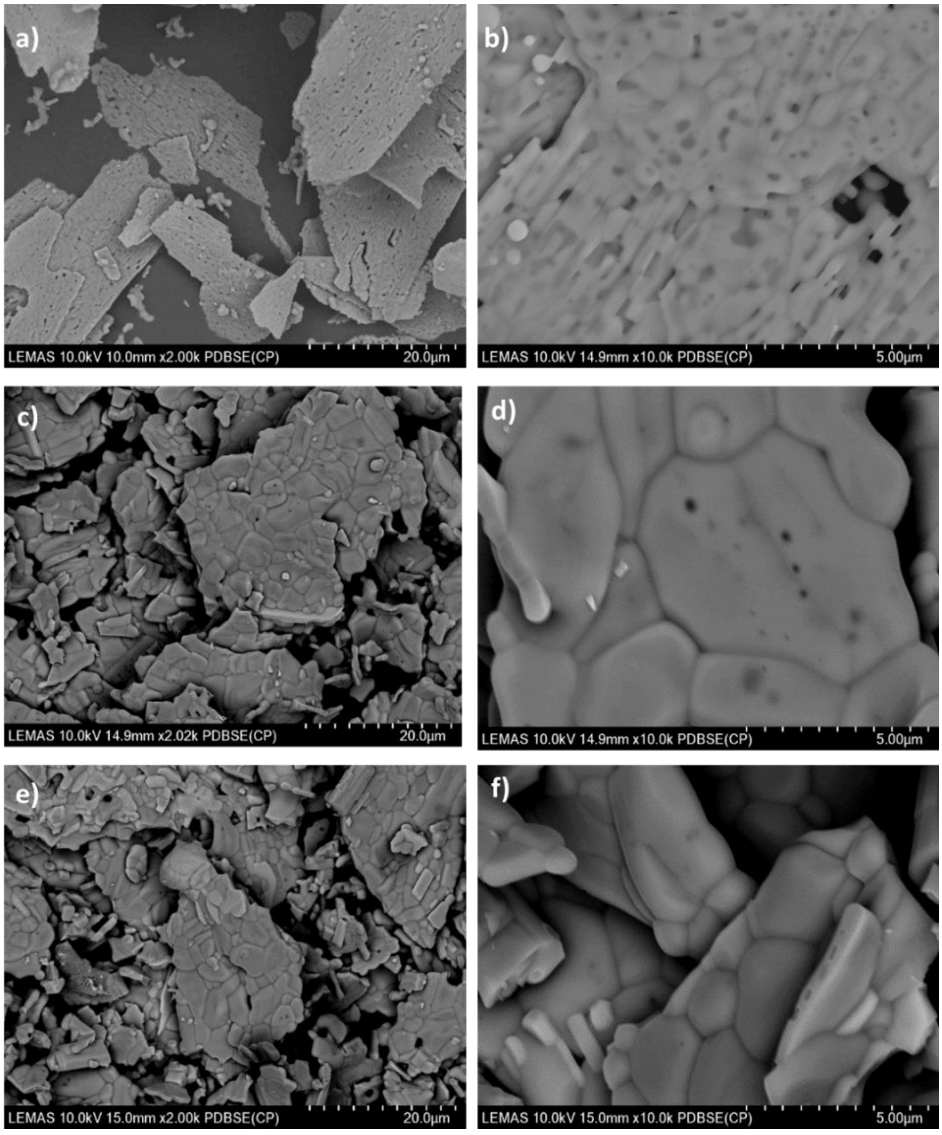

Figure 4.14: SEM images of a), b) 0-FeCaP and c), d) 5-FeCaP and e), f) 10-FeCaP minerals sintered at 1000 ˚C for 5 h.

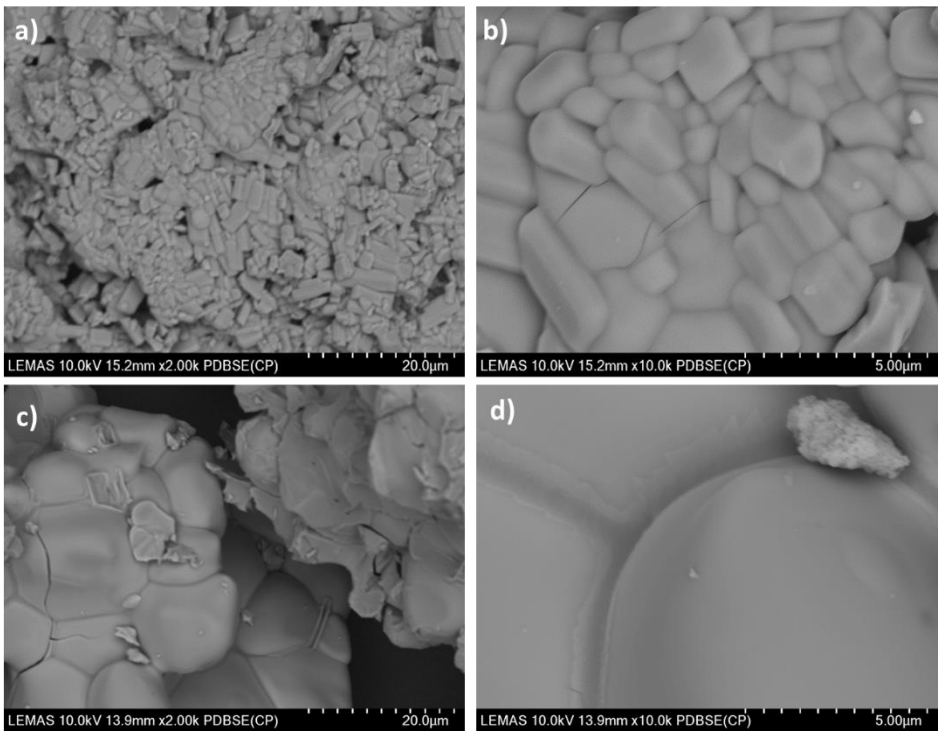

Figure 4.15: SEM images of a), b) 20-FeCaP and c), d) 30-FeCaP minerals sintered at 1000 ˚C for 5 h.

4.1.8 Transmission electron microscopy (TEM)

The 20 mol% sample was further examined under using TEM with TEM-SAED used to probe the amorphous phase present in the sample. Electron micrographs of both the as prepared material and the post-synthesis products were examined under the microscope Figure 4.16.

Results from TEM-SAED indicated that the initial (unsintered) sample contained an amorphous phase as shown in (Figure 4.16a, b), while the sintered sample was found to contain a crystalline phase (Figure 4.16c, d). The d-spacing, of the crystalline material was measured and confirmed to be β-CPP, as indexed by JCPDS 00-009-0346 (Table 4.5).

Table 4.6: TEM calculation presenting d-spacing of 20-FeCaP.

Intensity %	d-spacing Å	(h k l)	d-spacing Reference Å
100%	3.04	(0 0 8)	3.02 (00-009-0346)
20%	1.99	(2 1 9)	1.99 (00-009-0346)

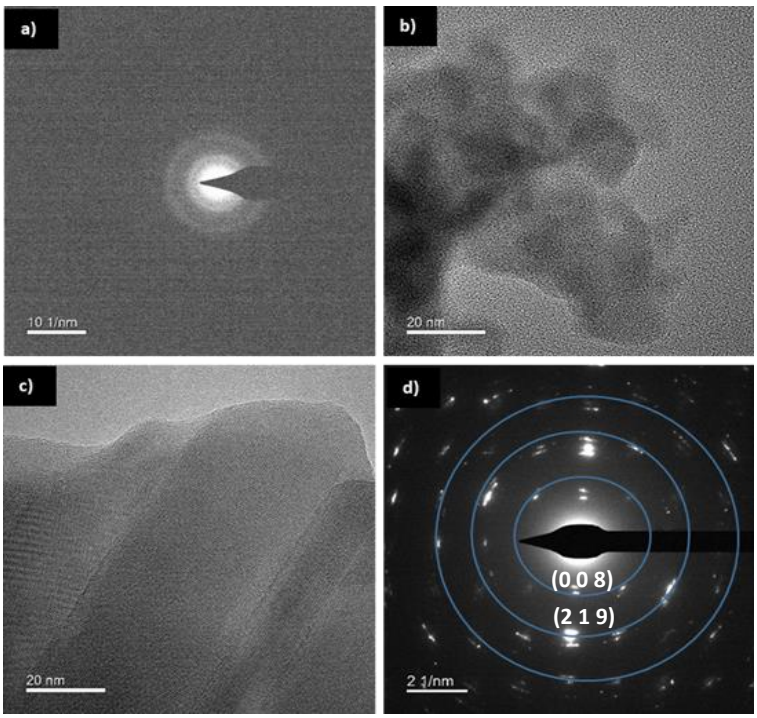

Figure 4.16: a) SAED a) and b) TEM image of amorphous phase for unsintered 20 mol% sample. While c) and d) same sample after sintering procedure.

4.2 Mechanical properties

The effect of Fe^{2+}\Fe^{3+} ions on the mechanical properties of the FeCaP biomaterials was examined by measuring the densification, hardness and Young modulus of the FeCaP materials as a function mol% Fe content.

4.2.1 Densification tests

Figure 4.17 shows results of densification tests that was measured using eq. 3.12. It was observed that upon heating brushite, the density of sintered dopant materials increased with increasing Fe^{2+}/Fe^{3+} ion (5.4%, 22.5%, 30.2% and 33.2% for 5, 10, 20 and 30-FeCaP, respectively) since the volume of the samples was dramatically decreased. No reduction of volume was observed for undoped mineral after sintering; the loss of water molecules results 22% reduction of initial weight (0.2g), since brushite loses 2 molecules of water during heating. Also, as the porosity increased after sintering according to SEM, this caused reduction in densification for undoped materials. As has been shown in SEM analysis of undoped

mineral Figure 4.14, a number of pores appeared represented as defects. Pores was found to reduce the mechanical properties of the materials [255]. Nevertheless, the pores reduced for 5-FeCaP after sintering wile it eliminated by increasing the concentration of Fe^{2+}/Fe^{3+} ions as seen in SEM Figure 4.14 and 4.14 for 10, 20 and 30-FeCaP.

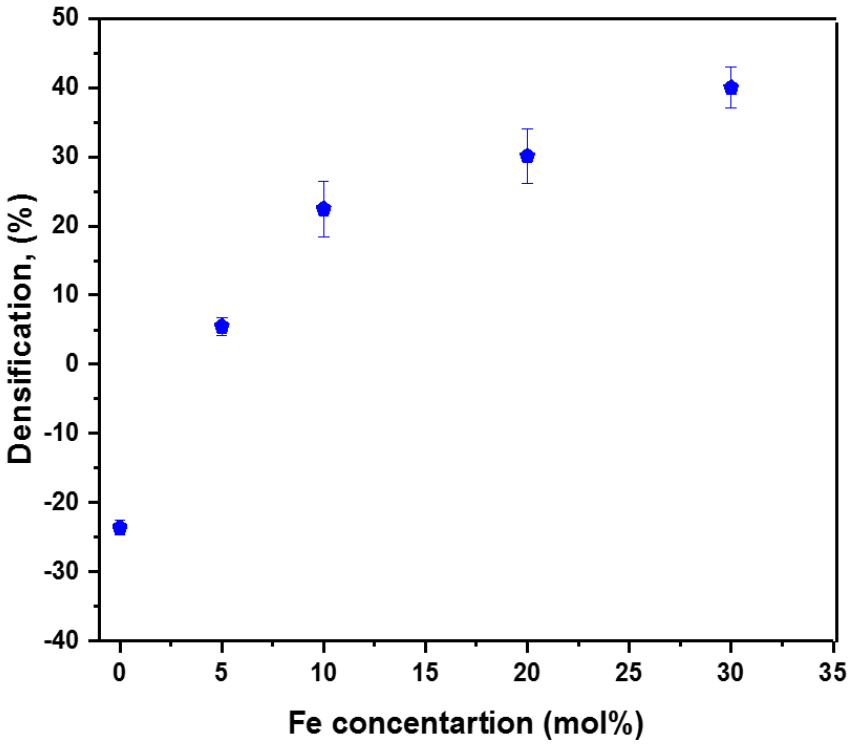

Figure 4.17: Densification of (both synthesised and sintered) FeCaP materials. Error bars present standard deviation.

4.2.2 Hardness and Young modulus

Using nano-indentation technique as seen in Figure 4.18, both hardness and Young modulus were measured (Table 4.6). Also, the loading and unloading curves for all samples during the nano-indentation experiment to measure both hardness and Young modulus are presented in Figure 4.19, 4.20 and 4.21.

From Figure 4.19, 4.20 and 4.21, it is shown that the penetration depth decreased when the materials sintered at temperature of 1000℃ for 5 h.

The pop-in events that appears in some loading line usually related to the discontinuity during depth measurement [256]. Different mechanisms can cause this event such as phase transformation during loading, densification and the formation of the cracks [257]. Therefore, the pop-in event that appears in Figure 4.21 of 30-FeCaP could be related to the formation of the cracks since the sample was so brittle.

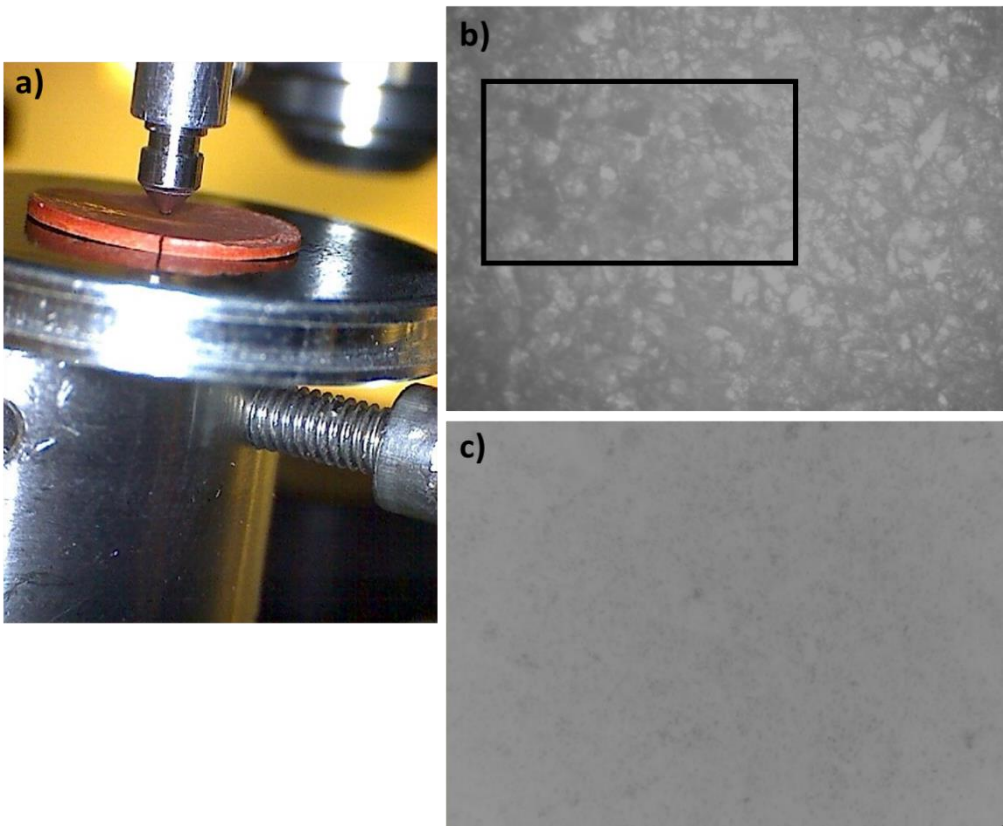

Figure 4.18: Nano-indentation a) experimental setup shows the loading using Berkovich indenter and the FeCaP sample, b) and c) sample before and after nano-indention experiment, the black squared shows the six pyramid shape of the indenter.

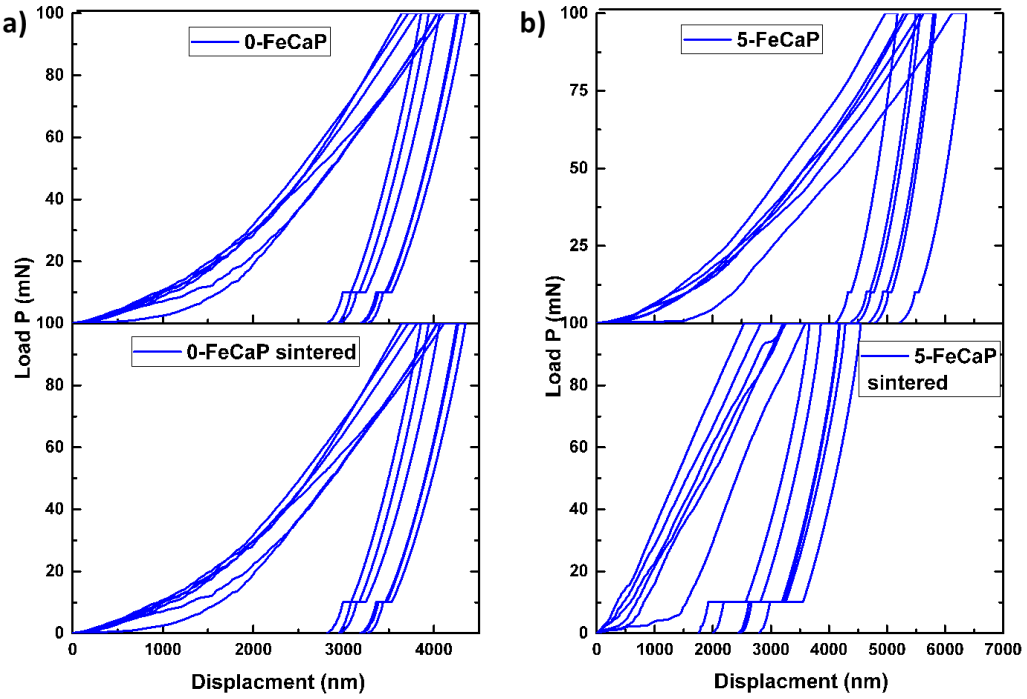

Figure 4.19: Loading and un-loading curves of a) 0-FeCaP, b) 5-FeCaP before and after sintering at load of 100 mN.

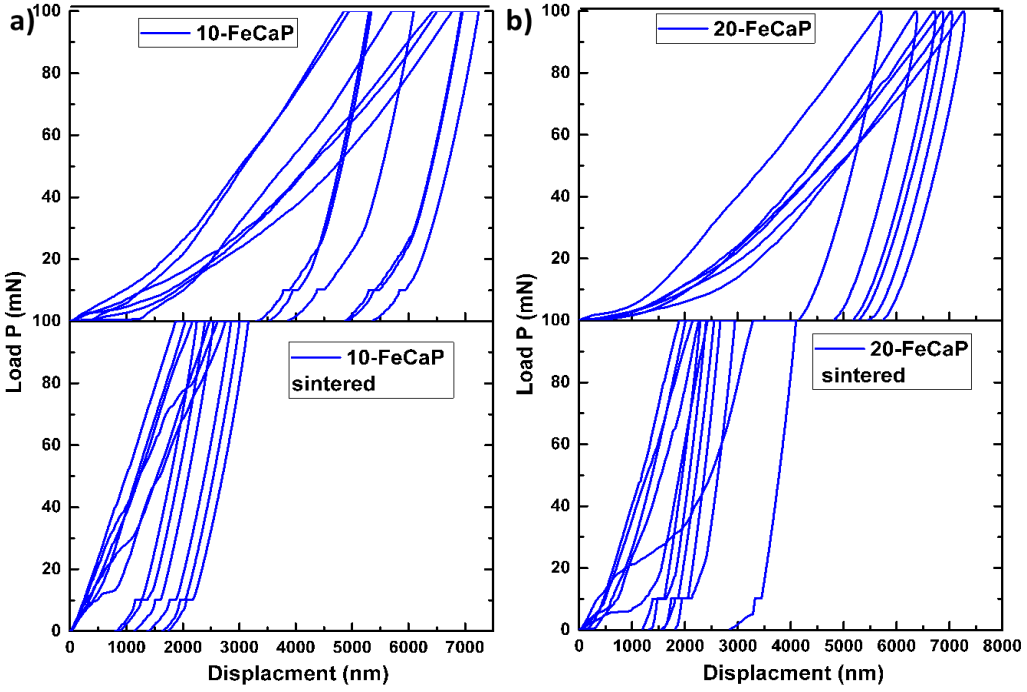

Figure 4.20: Loading and un-loading curves of a) 10-FeCaP, b) 20-FeCaP before and after sintering at load of 100 mN.

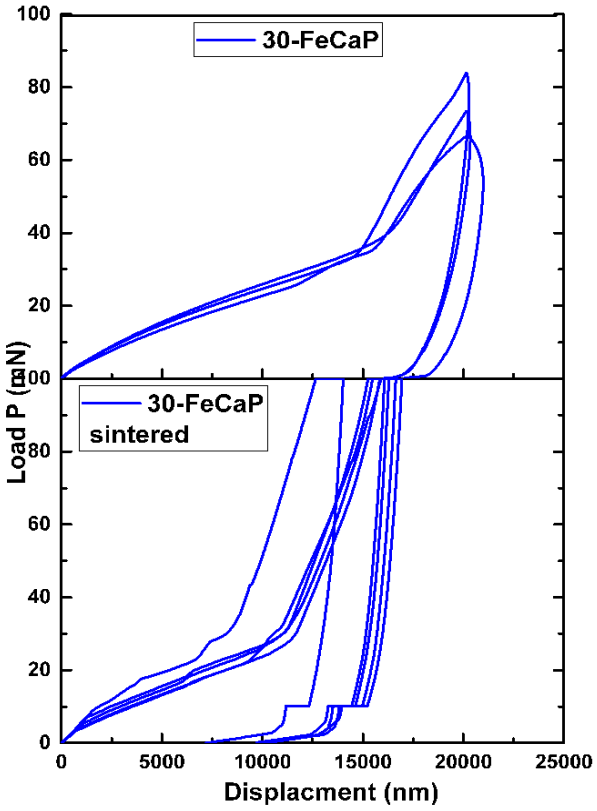

Figure 4.21: Loading and un-loading curves of 30-FeCaP before and after sintering at load of 100 mN.

In Figure 4.22, no changes were observed for both pre/post sintering 0-FeCaP. Doping with Fe ion decreased the hardness and Young modulus before sintering process for all doping concentrations. Since hardness is related to the microstructure of material as mentioned in literature, dopant can increase or decrease hardness by providing barrier to dislocation motion or increase dislocation by producing defects, respectively. The decreasing of these properties may be due to the substitution of $Fe^{2+/}Fe^{3+}$ ion with Ca^{2+} ion that could lead to distortions, as the ionic radius of $Fe^{2+/}Fe^{3+}$ ion is smaller than of Ca^{2+} therefore, may increase the dislocations [258]. Whereas, for undoped no defects were presented that could explain the same result showed for initial and sintered sample.

Table 4.7: Mechanical properties of the initial and sintered FeCaP minerals.

Materials	Hardness (GPa)		Young modulus (GPa)	
	Initial	Sintered	Initial	Sintered
0-FeCaP	0.34±0.03	0.34±0.05	7.84±0.4	7.7±0.5
5-FeCaP	0.2±0.02	0.4±0.07	5.86±0.4	6.4±0.4
10-FeCaP	0.15±0.04	1.1±0.4	3.6±0.6	10.5±1.0
20-FeCaP	0.1±0.02	0.9±0.3	3.1±0.3	13.3±2.6
30-FeCaP	0.01±0.002	0.02±0.003	0.3±0.2	1.2±0.07

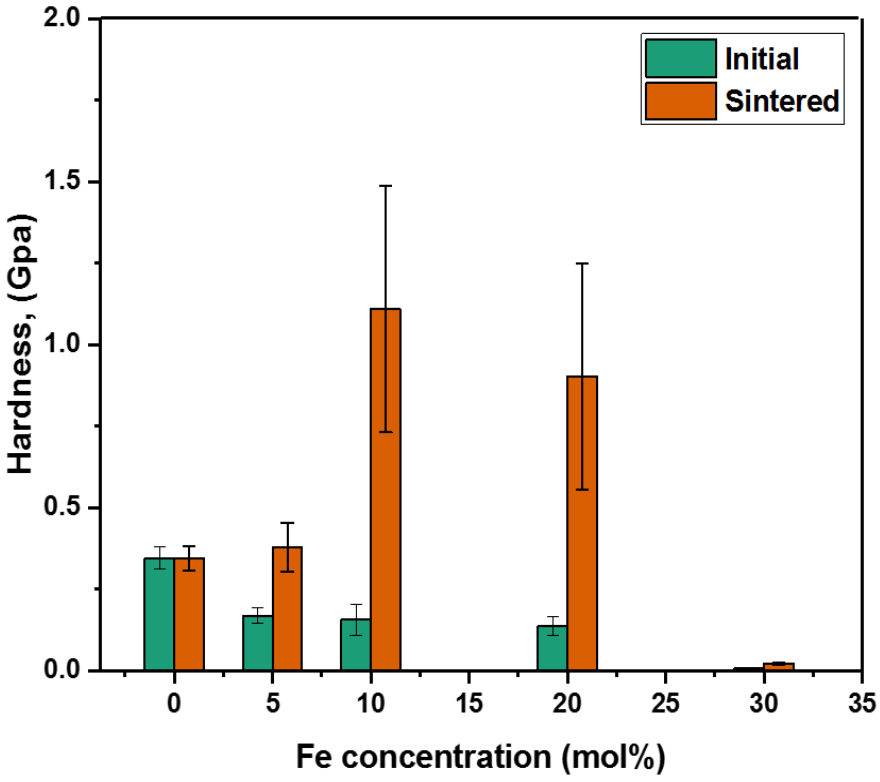

Figure 4.22: Nano-hardness of FeCaP samples at load of 100 mN. Error bars present standard deviation.

However, for sintering materials up 10 mol% Fe content, both hardness and Young modulus where higher in the sintered FeCaP when compared to the initial materials. It was found that Fe ion increases the grain growth that increases the densifications which increases the hardness [259]. On the other hand, for 20- and 30-FeCaP lower values of hardness were obtained. It is thought that this could be related to $FePO_4$ presented in both phases and might need more sintering time process.

According to Figure 4.14 and 4.15, the grain size of sintered sample decreases when the concentration of Fe^{2+}/Fe^{3+} ion increases. This result may explain the increase of Young modulus of concentration up to 20 mol% [260].

The chapter that follows moves on to consider the effect of thermal sintering on phase transformation of FeCaP samples.

Chapter 5 Phase transformation of Fe^{2+}/Fe^{3+} ion doped calcium phosphate minerals after thermal sintering.

Chapter Introduction:

For mechanical strength, the mineral require sintering of synthesised FeCaP materials, which may be carried out by either conventional sintering for a given shape, or using a laser. For medicine application, the most practical laser appears to be a femtosecond pulsed laser. In this chapter , the influence of Fe^{2+}/Fe^{3+} leading to the formation of an amorphous phase at 30 mol% Fe^{2+}/Fe^{3+} concentration has been investigated using the XRD and zeta potential technique. Also, in this chapter, the composition dependence of phase transformation in FeCaP mineral has been explained.

Chapter summary

In this chapter, the formation of an amorphous 30-FeCaP phase in samples sintered at different temperatures was discussed. Results obtained from zeta potential measurements of a suspension of these materials was also presented and discussed. Measurements of activation energy for both 5 and 10-FeCaP showed an inverse relationship between activation when the concentration of Fe increases. The crystalline volume fraction of 0-FeCaP was 70.47%, while it increased for 5 and 10-FeCaP minerals to 78.44% and 83.4%, respectively indicated the stabilization of brushite after doping with Fe^{2+}/Fe^{3+} ion. On analysing the contribution of energies in the stabilization of amorphous phase at 30 mol% Fe^{2+}/Fe^{3+} in brushite, it was found via zeta potential technique that the surface energy of the composition at 30 mol% increased and was maximum. In independent annealing and thermal analysis experiments, it was observed the calcium phosphate mineral at 30 mol% Fe^{2+}/Fe^{3+} also demonstrated delayed tendency for crystallisation than other compositions investigated herein.

Non-ambient X-ray diffraction analysis of both 0 and 10-FeCaP showed that that the presence of Fe ions accelerated the sintering procedure and decreased transition duration for conversion to β-CPP in comparison to the undoped mineral.

5.1 Amorphous phase

5.1.1 X-ray powder diffraction (XRD)

Results from X-ray diffraction investigations into the effect of Fe^{2+}/Fe^{3+} ion concentration on brushite structure were discussed in chapter 4.

It was observed, that when the Fe^{2+}/Fe^{3+} ion concentrations increased from 0 mol% to 20 mol%, the proportion of monetite and amorphous phases become more dominant than that at 0 mol% Fe^{2+}/Fe^{3+} ion concentration. When the concentration of Fe^{2+}/Fe^{3+} ion reached to 20 mol% and 30 mol%, the resulting phase composition had more amorphous fraction than the crystalline monetite and brushite. The evolution of phase composition is summarised in Figure 5.1.

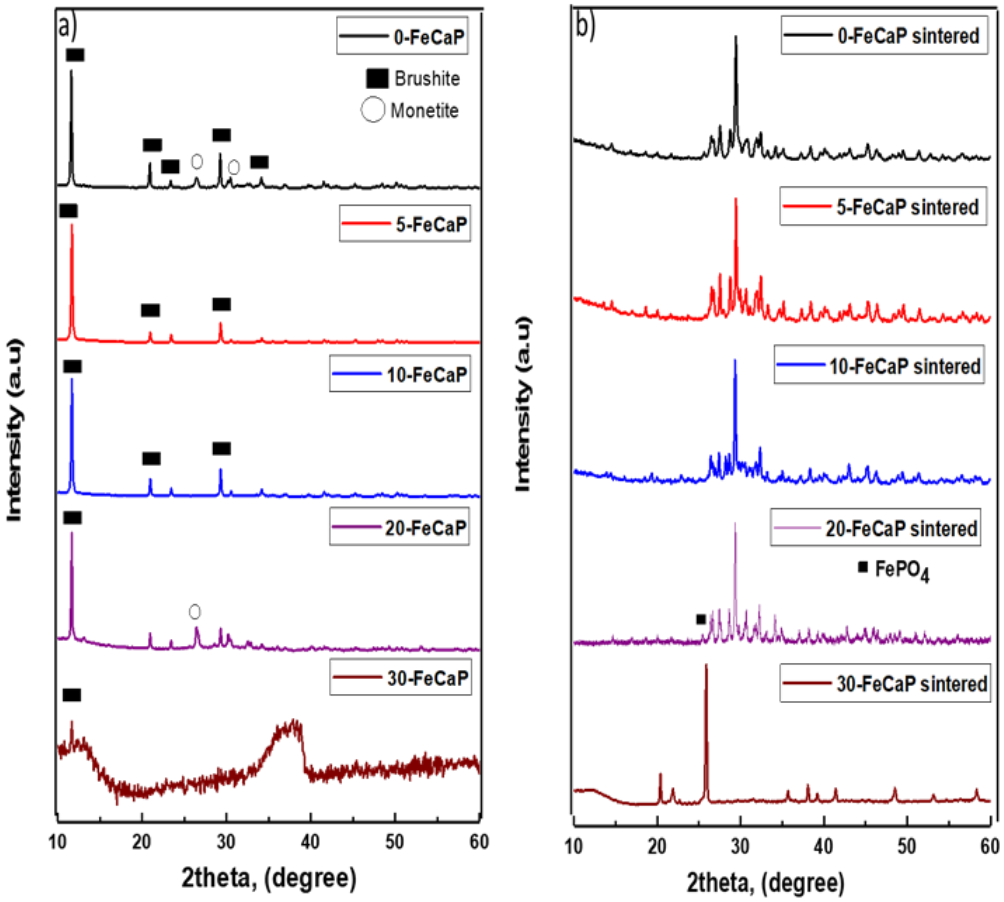

Figure 5.1: XRD of the a) initial FeCaP samples showing the presence of brushite structure up to 20 mol% Fe concentration in the unsintered material, and how doping with 30 mol% Fe generates an amorphous phase and b) sintered (0, 5, 10 and 20) FeCaP samples showing phase transformation to β-CPP. For 30 FeCaP sample the amorphous iron phosphate transformed to crystalline $FePO_4$.

Further examination of this amorphous phase using the FTIR technique revealed that its composition to be amorphous iron phosphate ($FePO_4 \cdot 3H_2O$), as discussed in chapter 4. The presence of a secondary phase (i.e. amorphous $FePO_4 \cdot 3H_2O$) in addition to brushite in the 20-FeCaP sample could be indicative of the absence of interaction between the Fe ion and the initial brushite phase that occurred. This observation is in agreement with previous studies as reported by [98, 261, 262]. Some of the know factors that could influence CaP precipitation include: ratio of Ca/P, temperature, time, pH and the addition of dopant materials [227]. Prior to Zeta potential measurements, all the FeCaP samples were mixed with distilled water to create suspensions. In this section, the role of Fe^{2+}/Fe^{3+} in the formation of an amorphous phase will be investigated.

To study the phase transformation of 30-FeCaP sample, it was sintered at different temperature and compared with TGA/DTA curves, Figure 5.2 and 5.3.

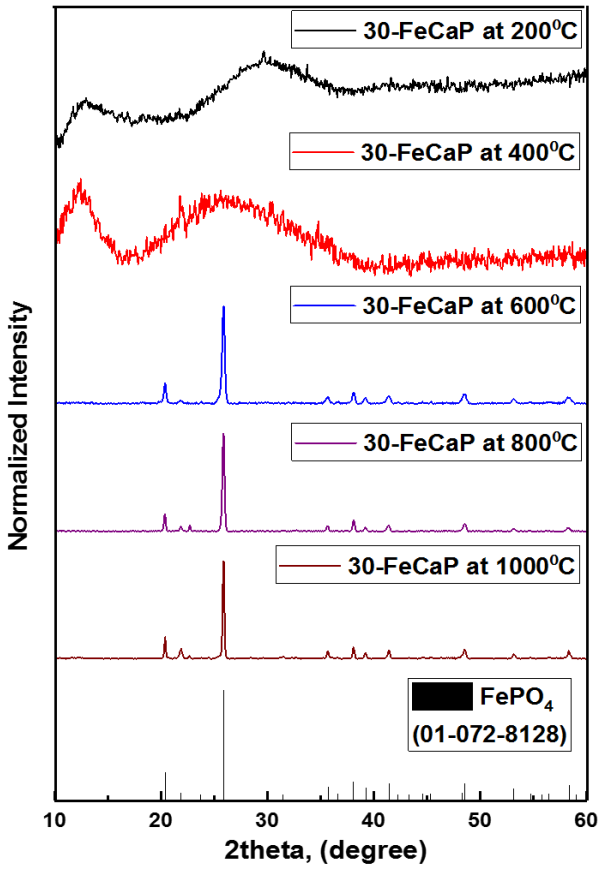

Figure 5.2: a) X-ray diffraction of 30-FeCaP sintered at different temperature.

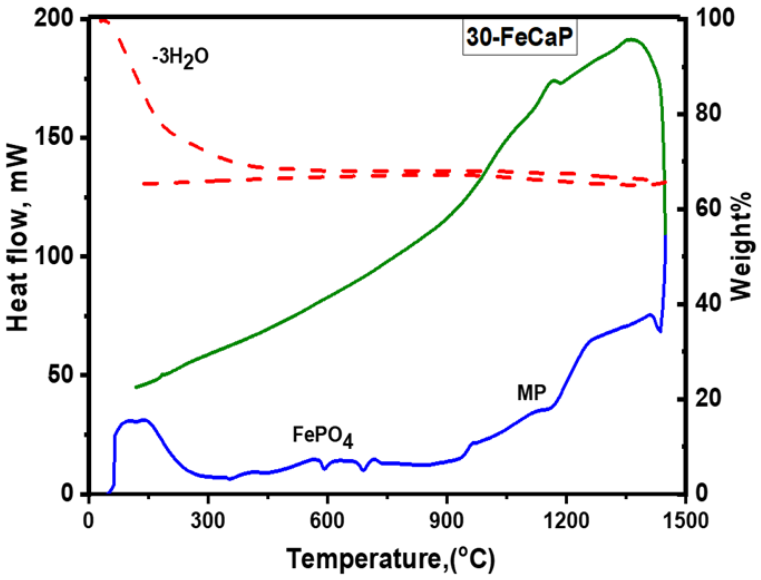

Figure 5.3: DTA/TGA of 30-FeCaP between 30-1450°C at heating rate of 20°C/m.

In Figure 5.2 sintering the sample until temperature of 400 ℃ showed an amorphous, whilst in Figure 5.3 the endothermic peak of DTA at 160 ℃ related to the dehydration [263, 264]. However, sintering at 600 ℃ showed a crystalline $FePO_4$ that agreed with the exothermic peak at 590 ℃ of a DTA [265]. Diffraction peaks at a temperature of 800 ℃ offered same structure, nevertheless a new peak at approximately 2θ = 24º was observed. By looking at DTA curve and since no weight loss was noticeable after 400 ℃, the exothermic peak at 700 ℃ could be correspond to the α-β transition $FePO_4$ as mentioned in chapter 4 [251, 252, 266].

5.1.2 Zeta Potential (ZP)

Zeta potential measures the value of the charge around a solid surface in colloidal dispersions and it is an important parameter that describe the stability of a suspension [267]. The higher magnitude of Z-potential indicate relative high degree of stability of the suspension [267]. For high value of Z-potential of sample (either positive or negative), a repulsion force between the particles must be presented. However, for low value the force will disappear then the particles will attract each other and agglomerate [267, 268].

From classical thermodynamics, it is known that for given composition, a crystalline phase is thermodynamically more stable than an amorphous phase. During synthesis of calcium phosphate minerals, when an amorphous phase forms it is likely to be metastable with respect to the corresponding equilibrium crystalline state. As it can be seen in table 5.1, the values of zeta potential decreases as Fe doping increases. This results indicate that due to high doping concentration with Fe ions could be influencing the surface charge of the material. This may also explain the observation of agglomerations on the SEM and the decrease in the pH values as mentioned earlier in chapter 4, Figure 4.11 and 4.1, respectively.

Table 5.1: Zeta potential of FeCaP suspensions.

Sample	Zeta Potential (mV)	SD
0-FeCaP	-13.23	0.76
5-FeCaP	-9.98	0.48
10-FeCaP	-11.36	0.49
20-FeCaP	-8.24	0.56
30-FeCaP	-1.79	0.39

The relationship between Z-potential, ion concentration, setting time and temperature, leading to the formation of amorphous phase at higher iron concentration could be explained by classical nucleation theory, Figure 5.4. It is assumed that increases in the concentration of Fe ions might lead to an increase the surface energy of the solution. Consequently, as the surface energy increase, the critical radius becomes larger, therefore the nucleation time increases. As a result, to reduce surface energy more setting time is needed for the phase to equilibrate or increase temperature so that it becomes thermodynamically more stable [269-272]. In Tampieri et al. [273], have found that Mg^{2+} doped HAp reduced the crystalline structure and at

high concentration of Mg^{2+} hindered the formation of crystallinity. It has been mentioned that the change in Ca/P ratio will change the structure, therefore increasing the concentration of Mg^{2+} reduces the ratio of Ca/P and the crystal size and increase the defects as the Mg substituted the Ca^{2+} site [273, 274]. Consequently, the ratio of crystal growth and nucleation increase which denotes more setting time could be needed [275].

According to El.dek et al. [276], who synthesized Fe doped brushite of different concentrations, at high concentration of Fe the brushite transformed into crystalline iron phosphate. In their method, the stirring process of brushite with Fe took 6 hours that could be a good reaction time for the iron phosphate to form. The agglomeration of the particles that was observed in 30-FeCaP sample could have occurred to reduce the surface energy [277]. The agglomeration can be determined as the sum of repulsive force and van der walls force according to the classical Derjaguin Landau Verwey Overbeek (DLVO) theory. Therefore, increase in zeta potential will increase the repulsive force and thus stop agglomerations [254].

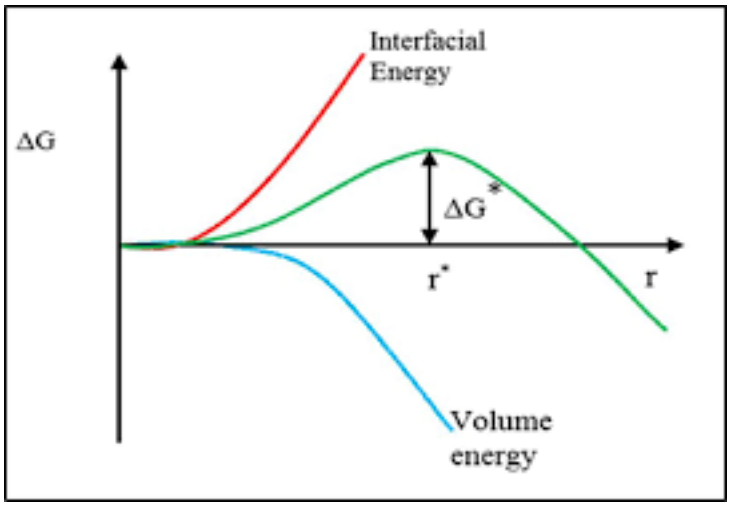

Figure 5.4: Illustration of classical nucleation theory, where r* is the critical radius [278].

5.1.3 Non-ambient X-ray diffraction analysais

Since the presence of Fe ions in CaP minerals shifted decomposition temperature to lower temperature as shown by DTA. In Figure.5.5 and

Figure 5.6 X-ray diffraction peaks at different temperature for 10 and 20-FeCaP in comparison to undoped mineral is displayed.

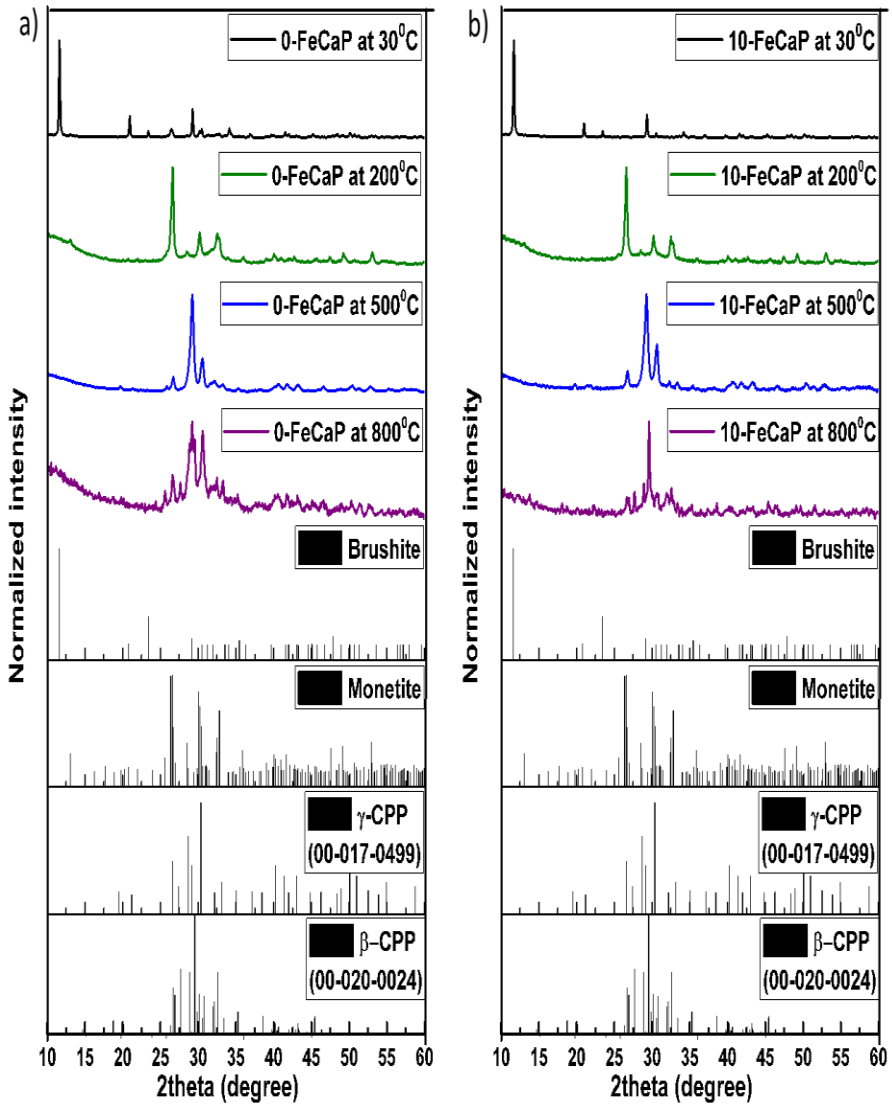

Figure 5.5: X-ray diffraction peaks of 10-FeCaP at different temperature in comparison with 0-FeCaP in order to study the effect of Fe^{2+}/Fe^{3+} ions in the transformation temperature.

For 0-FeCaP and 20-FeCaP the initial sample at 30 ˚C is brushite with a lower intensity peak at 26.3˚ of monetite, whereas for 10-FeCaP the initial sample contained only brushite as the presence of Fe ion stabilized the structure of brushite [277]. By sintering both samples of 0 and 20-FeCaP at 300 ˚C and since the decomposition temperature of brushite to monetite around 180 ˚C, monetite structure appeared. Same structure was observed for 10-FeCaP sintered at 200 ˚C. At a temperature between 500 ˚C and 600

°C transformation into the new phase which is γ-CPP was observed in all the samples analysed [279]. Sintering of 10-FeCaP at 800 °C instigated a full transformation to β-CPP. On the other hand, for the 0-FeCaP sample this transformation did not occur at the same temperature which agrees with evidence from literature [280]. By comparing 0-FeCaP with 20-FeCaP at 700 °C, a second crystalline phase of $FePO_4$ for 20 mol% was observed. In this regard, doping with 10 mol% of Fe accelerated the transformation process of β-CPP as Fe was incorporated into the structure.

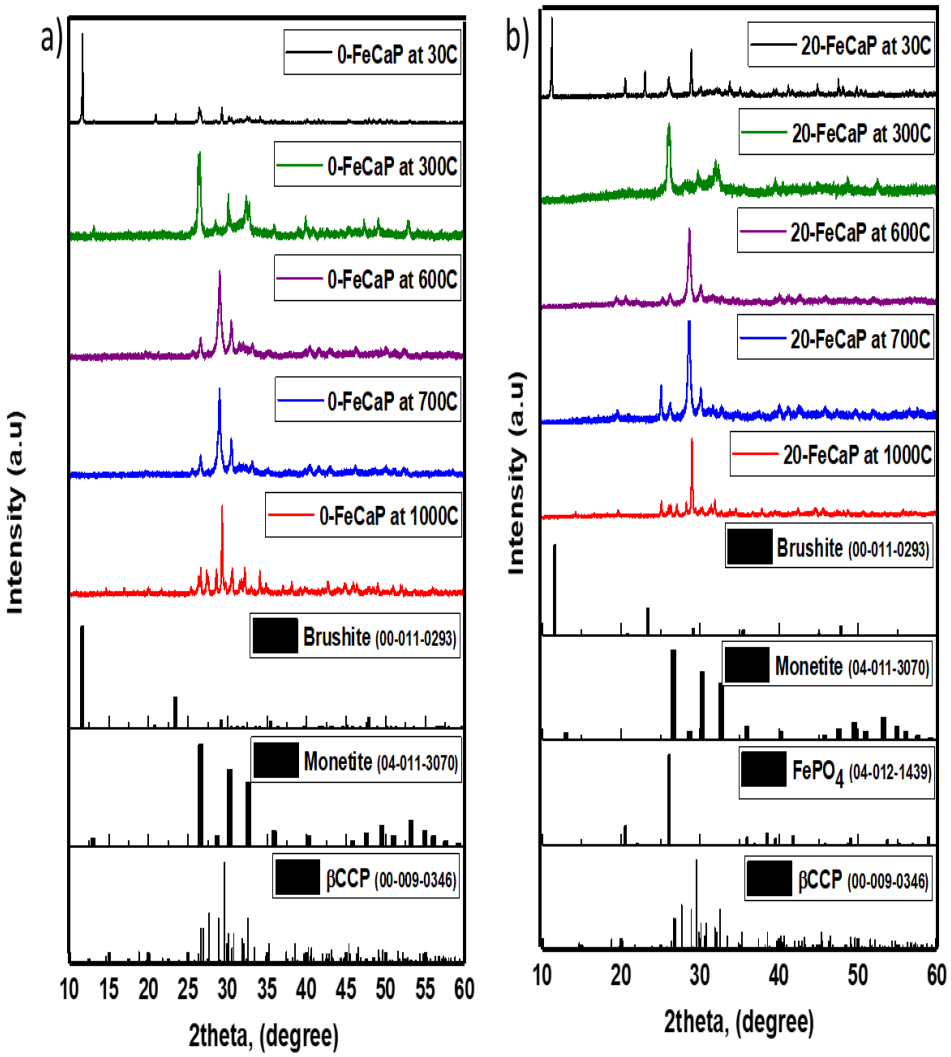

Figure 5.6: X-ray diffraction patterns of 0- and 20-FeCaP mineral samples at different temperature (30, 300, 600, 700, 1000 °C).

5.2 Analysis of the kinetics of phase transformation and overall activation energy (E_a)

Activation energy (E_a) for both 5 and 10-FeCaP samples were measured to investigate the influence of Fe^{2+}/Fe^{3+} ion on the reaction time of β-CPP which is the phase of research interest. To achieve this process, DTA and TG curves were run for both samples at different heating rates (10, 15, 20 and 25 ˚C/m) between temperature 650-800 ˚C with a mass of 9.4 mg, Figure. 5.7. At higher heating rate the peak shifts to higher temperature with higher intensity. Since it is non-isothermal conditions, Kissinger equation was used, (eq. 5.1) [281-285].

$$\ln\frac{\beta}{T_p^2} = -\frac{E_a}{RT_p} + Const \qquad (5.1)$$

Where:

- T_p is the peak temperature,
- β is the heating rate (K/min),
- E_a is activation energy (KJ/mol) and
- R is gas constant which is equal to 8.314 J/Kmol.

Kinetic constant can be measured using Arrhenius equation,

$$K_t = K_0 \exp(-\frac{E_a}{RT}) \qquad (5.2)$$

K_t and K_0 is the kinetic constant and pre exponential factor, respectively.

From Figure 5.7b and d the activation energy and Kinetic constant can be calculated from the slope and interceptor, respectively, of the curve between $\ln(\beta/Tp^2)$ verses (1000/Tp). In order to convert E_a from Joules to Kilojoules, 1000 was divided by Tp as shown in Figure 5.7b and d, as the slope will equal to $\ln(\beta/Tp^2)Tp/1000$. It was found that the E_a of the transformation of γ-CPP into β-CPP was 587.21 KJ/mol and 375.54 KJ/mol and K_t was 0.044 (1/min) and 0.078 (1/min) for 5 and 10-FeCaP, respectively.

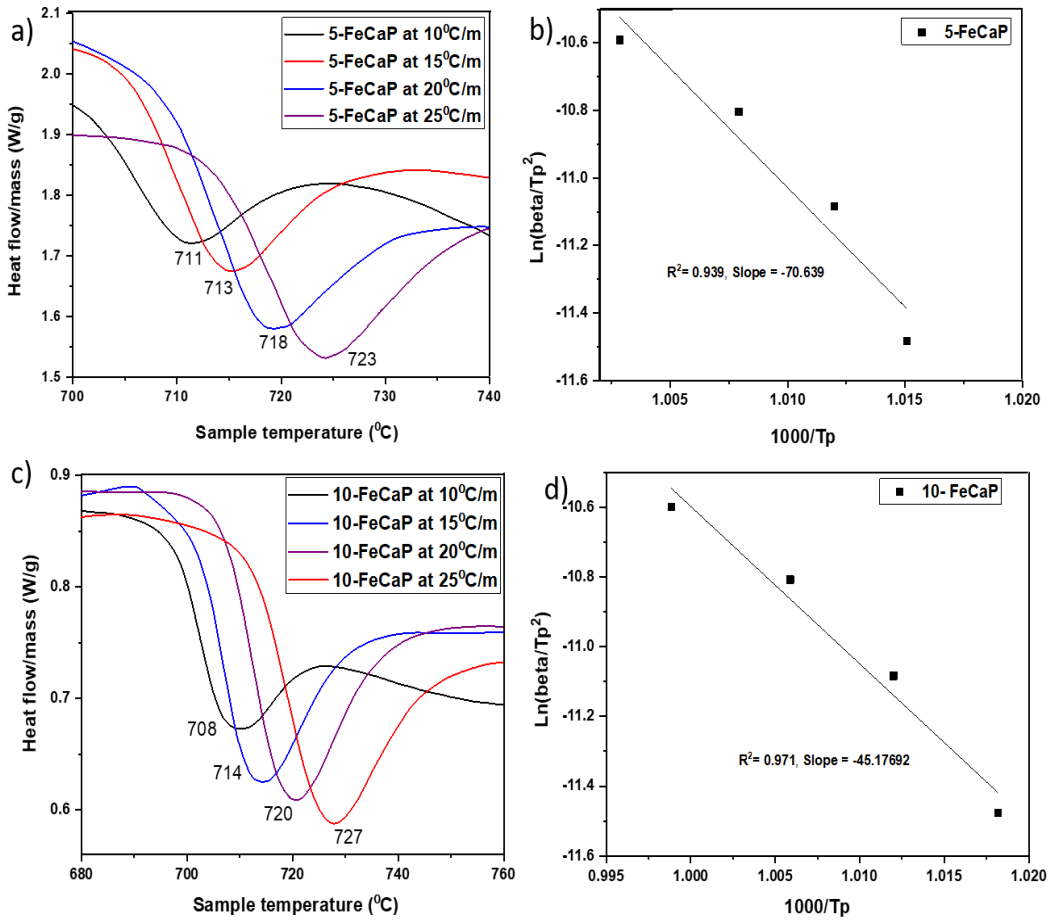

Figure 5.7: 10-FeCaP sample presents a) heat flow divided by mass loss as a function of sample temperature at different heating rates, b) Plot of ln(beta/Tp^2) as a function of 1000/Tp to measure the activation energy using Kissinger method.

This result indicates that the crystallization into β-CPP for 10 mol% Fe doped sample was faster in comparison to the 5 mol% Fe doped sample. This validates the premise that the incorporation of Fe^{2+}/Fe^{3+} ion into CaP minerals accelerated the reaction process of β-CPP.

5.3 The influence of Fe^{2+}/Fe^{3+} ion on brushite crystal structure

Brushite is a monoclinic crystal system with unit cell parameters of a=5.837 Å, b= 15.192 Å and c= 6.265 Å, and α = γ = 90.00˚ and β= 116.47˚ while β-CPP is a tetragonal structure with space group $P4_1$ (Figure. 5.8) [77]. In order to study the incorporation of Fe^{2+}/Fe^{3+} ions in brushite, d-spacing and unit cell parameters were measured.

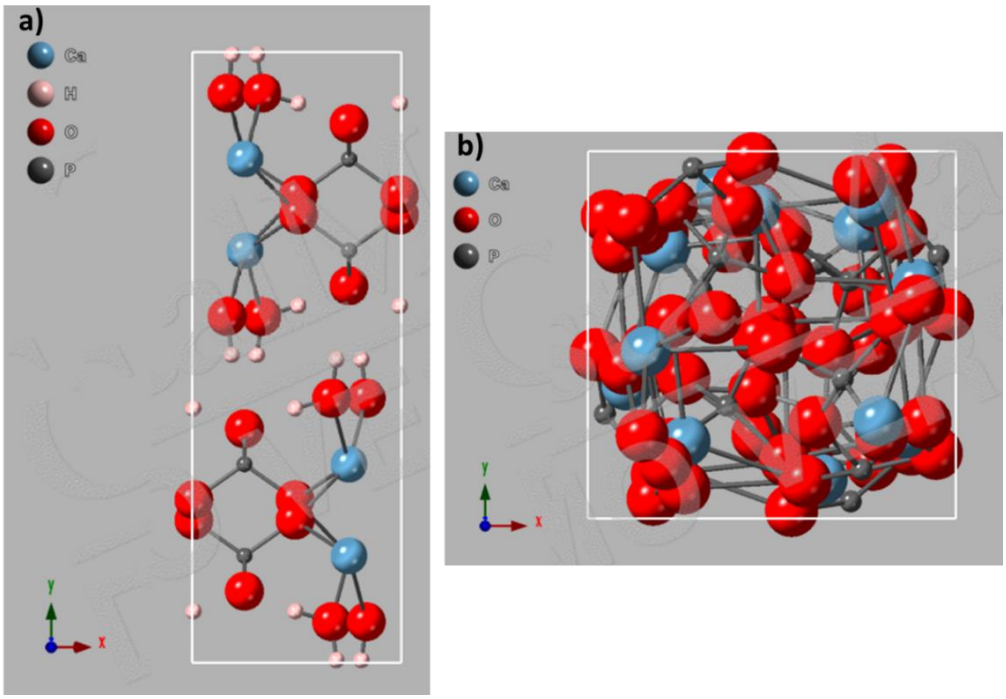

Figure 5.8: Crystal structure of brushite and β-CPP using crystalmaker ® software.

According to Bragg's law, d-spacing for synthesised samples of 0, 5, 10 and 20 mol% Fe^{2+}/Fe^{3+} ions (in brushite form) was measured using the following formula [286],

$$d = \frac{\lambda}{2\sin\theta} \qquad (5.3)$$

Where λ is the wavelength (=1.54 Å) and θ is the angle of the diffraction peaks. From equation (5.3), unit cell parameters of monoclinic system can be measured [286],

$$\frac{1}{d^2} = \frac{1}{sin^2\,\beta}\left(\frac{h^2}{a^2} + \frac{k^2\,sin^2\,\beta}{b^2} + \frac{l^2}{C^2} + \frac{2hl\cos\beta}{ac}\right) \qquad (5.4)$$

Whereas, cell volume of monoclinic system is:

$$V = a.b.c.\sin\beta \qquad (5.5)$$

Table 5.2: Unit cell parameters a,b, c and cell volume of synthesised FeCaP.

Materials	a Å	b Å	c Å	V Å
0-FeCaP	5.71	15.23	6.09	475.10
5-FeCaP	5.70	15.15	6.08	471.01
10-FeCaP	5.68	15.04	6.06	463.59
20-FeCaP	5.70	15.15	6.09	471.89

The lattice parameters and cell volume for 5 and 10-FeCaP decrease when the Fe concentration increases, table 5.2. These results could elucidate the integration of the ions into the brushite structure replacing Ca^{2+} due to the smaller ionic radius of Fe^{2+}/Fe^{3+} ion as explained earlier. Whereas, for 20-FeCaP the decrease in cell volume was similar to 5-FeCaP. This could be explained by that some of Fe^{2+}/Fe^{3+} ion substituted Ca^{2+} ion while the other Fe ions bonded with PO_4 group to form $FePO_4 \cdot 3H_2O$.

Crystallite size of FeCaP sample in brushite were measured using Debye-Scherrer relation [287],

$$\beta = \frac{0.9\lambda}{D\ cos\theta} \quad (5.6),$$

where:

- β is the full width at half maximum (FWHM)
- D is the crystal size

The relation between crystal size of sample and doping concentration of Fe^{2+}/Fe^{3+} illustrates in Figure 5.9. It is confirm that increase concentrations of dopant decrease the crystal size of 5-FeCaP and 10-FeCaP. However, doping with 20 mol% of Fe^{2+}/Fe^{3+} a small reduction in the crystal size was observed. The decrease in crystal size explain the shrinkage on the crystals which confirm the incorporation of Fe ion in the crystal. Whereas, for 20-

FeCaP this related to that Fe^{2+}/Fe^{3+} ions bond with phosphate groups to form iron phosphate phase.

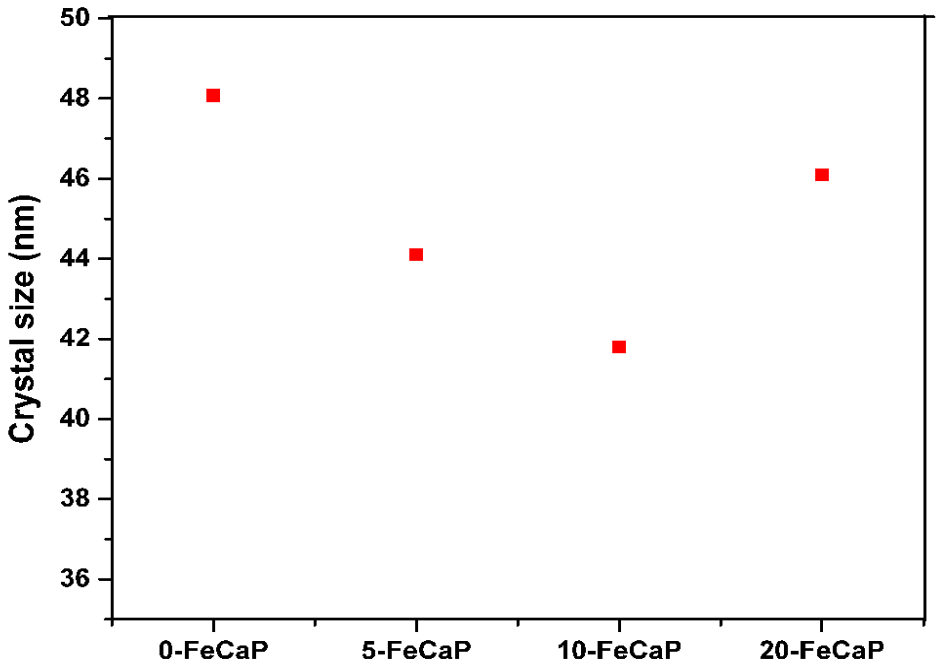

Figure 5.9: The decrease of crystal size of FeCaP samples after doping with different concentration of Fe^{2+}/Fe^{3+} ions.

The synthesised undoped minerals presented a mixture of monetite and brushite beside an amorphous phase could be presented that might be attributed to amorphous calcium phosphate phase ACP, therefore volume fraction of crystalline and amorphous phases was calculated from XRD data for 0, 5, 10 and 20-FeCaP. First the background of diffraction peak for each material was determined by subtracting any amorphous peak, then the area under peaks was measured. After that, the whole area with an amorphous phase was also collected. Using eq. 5.7, volume fraction of both amorphous and crystalline can be assumed [288];

$$V_f = \frac{A_{crystalline}}{A_{crystalline} + A_{amorphous}} \quad (5.7)$$

For 0-FeCaP, volume fraction of crystalline phase was 70.47%, whilst doped with Fe ion increase the value of crystalline to be 78.44% and 83.4% for 5 and 10-FeCaP, respectively. However, doping with 20 mol% the value

percentage became 61.40% and this due to the formation of amorphous $FePO_4.3H_2O$.

The decrease in the crystallinity of 0-FeCaP could be attributed to the amorphous phases that form when brushite converse into monetite as was found in the previous study since some of monetite peaks presented in brushite structure [72]. In their study, two amorphous phases was found in study that are ($Ca_2PO_4 \cdot 0.75H_2O$ and $Ca_2PO_4 \cdot H_2O$) [72]. The formation of amorphous phase occur when the brushite loses water, therefore the Ca will bond with O from phosphate group. However, when doped with Fe^{2+}/Fe^{3+} ion up to 10 mol%, the Fe ion stabilise brushite structure which could explain the increase in the crystallinity of 5 and 10-FeCaP.

In the chapter that follows, I present the effect of ablation using femtosecond pulsed laser on FeCaP samples to study micro-channels in these sample. Therefore, how these channels could have a positive effect on biological performance.

Chapter 6 Femtosecond pulsed laser micromachining for Bone Tissue Engineering

Chapter introduction

Over the last decade, femtosecond laser pulsed micromachining has become an important tool for a wide range of scientific and industrial processes particularly in bone regeneration. The advantages of using femtosecond pulsed laser in micromachining are the ablation of very small and precise structure in the target materials [142, 154]. One of the advantages of using micromachining in bone scaffolds is that it has been found to have a strong positive impact on cells adhesion and proliferation [289]. In this chapter, the mechanism of creating micro-channels (ablation) using femtosecond pulsed laser is discussed. First an ablation threshold was established by characterising the ablation threshold fluence. UV-vis, XRD, FTIR, bright field optical microscope and SEM were employed for sample characterisation for pre and post laser irradiation samples. The effect of different concentrations of Fe^{2+}/Fe^{3+} ion doped CaP on the depth of these channels was also investigated.

Chapter summary

Ablation threshold fluence was measured using the D^2 method for Fe^{2+}/Fe^{3+} -doped CaP. It was recorded that the doping with Fe^{2+}/Fe^{3+} increased the fluence required for ablation threshold, consequently high energy intensity is required for engineering micro-channels. However, when the concentrations of Fe^{2+}/Fe^{3+} above 20 mol% led to partial melting and cracks on the surface due to large optical absorptivity of Fe^{2+}/Fe^{3+} doped minerals, which increased the energy stored and lead to thermal shock induced cracking, resulting from rapid heat dissipation, instead of ablation.

6.1 Ablation threshold of Fe doped CaP minerals

In laser machining, the ablation threshold is defined as the minimum energy required to remove materials from the surface of an irradiated. For ablation to occur, the material must absorb laser radiation, either in the linear or nonlinear regime. In the absence of absorption, the laser either travels through the medium and/or gets reflected from the surface [142]. For the scaffold micromachining experiments discussed in this chapter, a femtosecond pulsed laser LIBRA-S-1K was used with laser parameters: 800 nm wavelength, 100 Hz to 1 kHz repetition rate, 80-100 fs pulse duration, 4.9 mm working distance, 20x objective lens and speed of 1.6 mm/s for 0.1 mm distance.

In order to achieve the desired micro-channels in the samples surface, the ablation threshold was calculated. The ablation threshold fluence was measured for all FeCaP minerals using the D^2 method [290-292].

$$D^2 = 2\omega_\circ^2 ln E_p \qquad (6.1)$$

$$F_{th} = \frac{2E_p}{\pi\omega_\circ^2} \qquad (6.2)$$

$$\omega_\circ^2 = \frac{D^2}{lnE_p\ 2} \qquad (6.3)$$

Where: D^2 is the diameter squared of the craters,
F_{th} ablation thershold fluence,
E_p pulse energy and
ω_0 minimum beam radius

In order to calculate the ablation threshold from the D^2 graph as a function of lnE_p, ω_0 was calculated first from the slope using equation (6.3).
The average power, P, was calculated using, [162] :

$$P = E_{pulse} \times Repetion\ rate \qquad (6.4)$$

A rang pulse energies were selected (220, 200,180,160,140,120,100, 80, 60 and 40μJ). Experiments were carried out at a fixed energy with

composition of FeCaP minerals, in the first instance. The diameter of the resulting irradiation spot or craters on the sample surface were measured using bright field optical microscope, as shown in Figure.6.1.

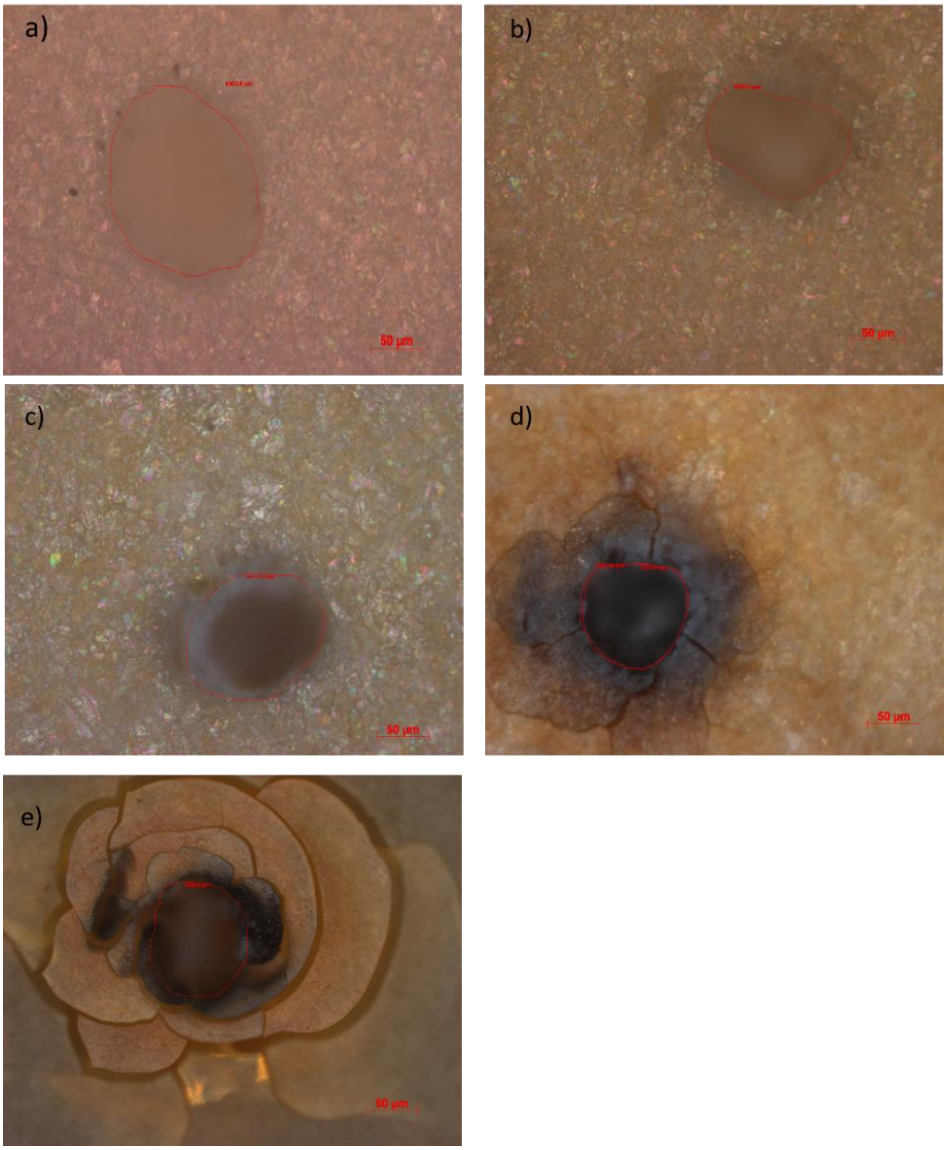

Figure 6.1: Images from bright field optical microscope showing the diameter squared size of the spot at pulse energy of 200µJ of the FeCaP materials a) 0 mol%, b) 5 mol% c) 10 mol%, d) 20 mol% and e) 30 mol%.

In Figures 6.1a) to c), there are apparent cracks, except discoloration arising as a consequence of laser irradiation. However, the irradiation induced cracks and damage can be seen in the irradiated areas for composition with 20 mol% (d) and 30 mol% (e). These cracks have arisen as a result of thermal stress during the cooling cycle after irradiation [293].

Figure. 6.2 shows the plote of D^2 as a function of lnE_{pulse} for determining the values ω_0 and F_{th}.

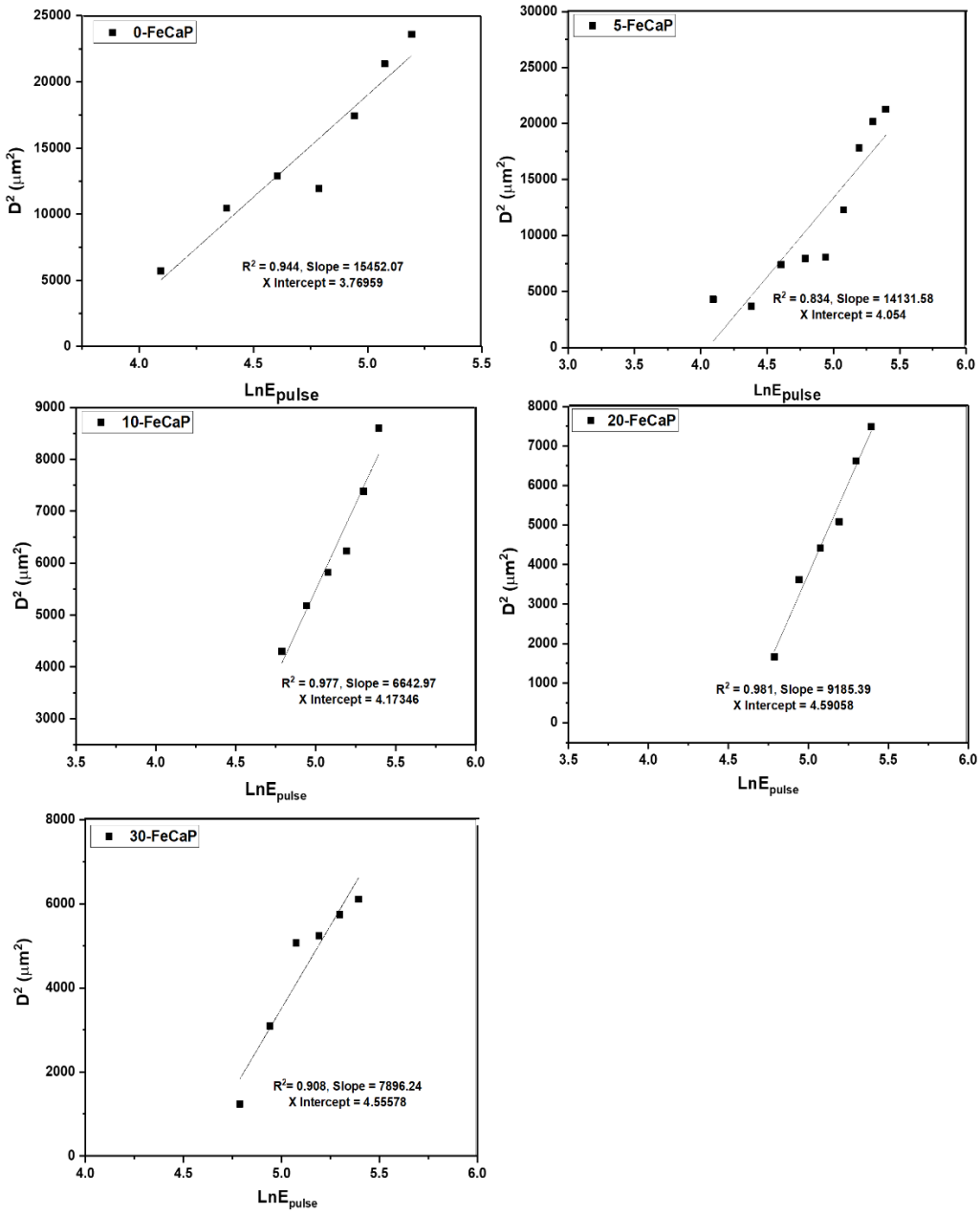

Figure 6.2: The plot of squared diameter size of the craters as a function of logarithmic pulse at different pulse energies of 0 mol%, 5 mol%, 10 mol%, 20 mol% and 30 mol% to determine the F_{th}.

From the graphs in Figure 6.2, the derived values F_{th} of the FeCaP minerals were found to increase with the concentrations of Fe^{+2}/Fe^{3+} in the minerals. The derived values were found to be 0.2 J/cm^2, 0.5 J/cm^2, 1.2 J/cm^2, 1.4

J/cm^2 and 1.8 J/cm^2 for 0, 5, 10, 20 and 30-FeCaP minerals, respectively, which are plotted against composition in Figure 6.3. This graph does not appear to linear, which suggests that the standard linear absorption model is not applicable here. Alternatively, it might be possible to propose that there two linear regimes which change across the 10 mol% Fe^{+2}/Fe^{3+} ion concentrations.

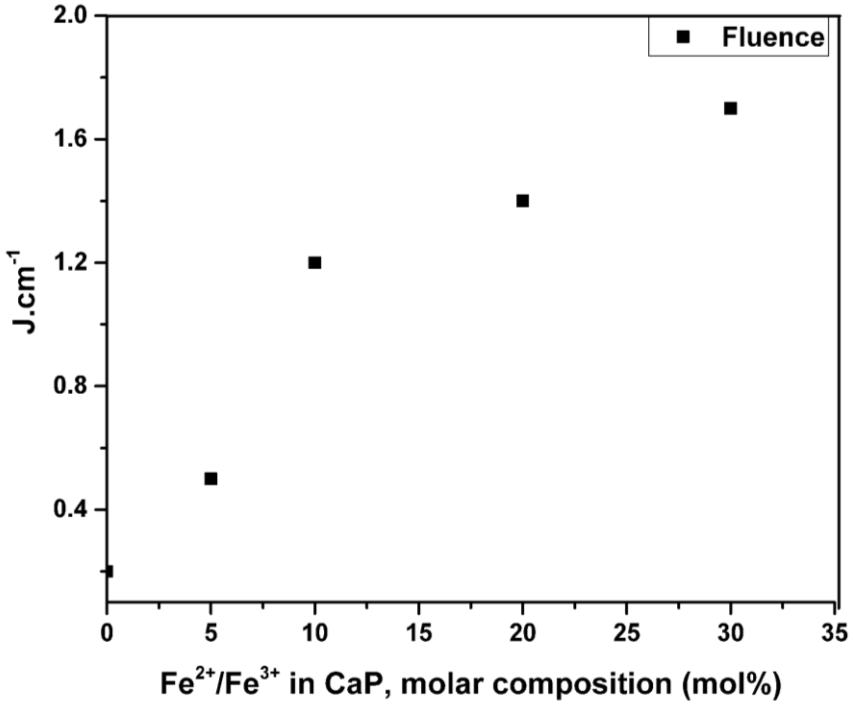

Figure 6.3: Composition dependence of the threshold energy in FeCaP minerals at 200 μJ incident energy.

From the data presented in Figure 6.2 gathered using fixed laser parameters for all FeCaP samples. It was necessary to investigate the effect of Fe^{2+}/Fe^{3+} ion doping on the optical absorption properties of the samples, which was investigated using the ultraviolet-visible spectrophotometric technique.

6.2 Ultraviolet visible spectroscopy UV-vis

For comparing the relative absorption of laser radiation, the UV-visible spectroscopy on samples was adopted to characterize surface reflectivity of pressed pellects of FeCaP minerlas. Since the laser wavelength for the ablation process was 800 nm, the reflectivity of the

FeCaP minerals was measured at this wavelength. As can be seen in (Figure. 6.4), reflectivity was found to decrease with increasing Fe^{2+}/Fe^{3+} ion concentration. This indicated higher absorption properties of Fe^{2+}/Fe^{3+} ion doped minerals relative to the undoped materials. This implies that a significant amount of laser energy will be absorbed for the Fe^{2+}/Fe^{3+} ion doped materials. Based on the findings of UV-Vis investigations, the influence of Fe^{2+}/Fe^{3+} ion on the ablation threshold fluence of the minerals was reviewed in the light UV-visible spectroscopy data. The reflectivity data observed at 800 nm was found to be consistent with an earlier observation on the reflectivity analysis of iron-doped apatite and brushite minerals for dental enamel restoration [4].

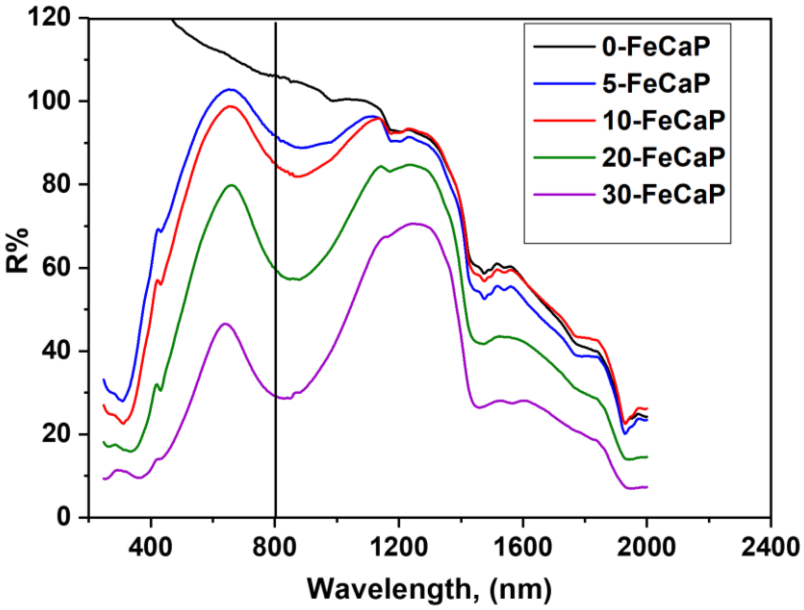

Figure 6.4: UV-visible measuring the reflectivity of FeCaP, that shows decrease when Fe concentration increases, particularly at 800nm.

Based on the observations that the laser irradiation depth at 100 to -200 µJ fluence only affected the up to 100 µm depth of the iron doped mineral surfaces, for phase transformation studies in the irradiated layer of materials, the surface of the mineral samples (around 100 µm penetration depth) was analysed using the grazing incidence angle X-ray diffraction (GIXRD). The analysis was performed for each irradiated mineral sample.

6.3 Characterization of FeCaP samples before and after laser irradiation

According to F_{th} result, two pulses energies (100, 200 μJ) with average powers of 0.1 and 0.2 W, respectively were used to attain the desired micro-channels on the surface of samples suitable for biomaterials application in order to test the cells growth into these channels. XRD, FTIR, bright field optical microscope and SEM sample characterisation was performed for pre and post laser irradiation FeCaP minerals samples obtained using both energies.

6.3.1 Grazing angle incidence X-ray diffraction (GIXRD)

6.3.1.1 0-FeCaP

Figure 6.5 contains results of X-ray diffraction analysis of 0-FeCaP sample after it had been laser irradiated. From previous phase analysis data, presented in chapter 4, it has been established that the undoped sample (i.e. 0-FeCaP) comprised of a mixture of bruhsite and monetite with volume fraction of 73.5% for brushite and 26.5% for monetite, GIXRD analysis of the irradiated area showed that the sample largely unchanged after irradiation with the 100 μJ laser energy, however, there is unambiguous evidence for the presence of monetite with ratio of 29.3%.

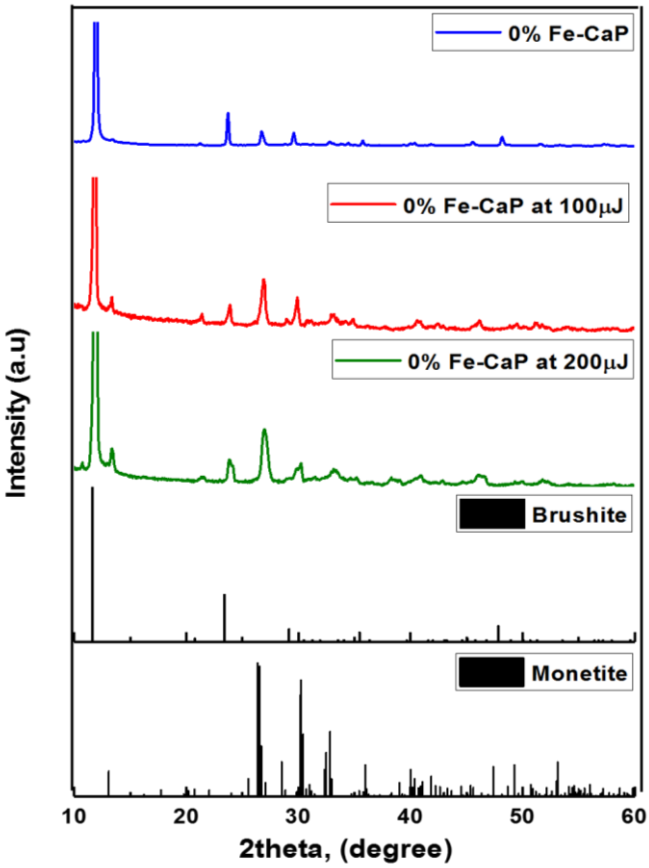

Figure 6.5: GIXRD of the 0-FeCaP shows the structure after laser irradiation at 100 μJ and 200 μJ in comparison with JCPDS files.

As observed in the case of 100 μJ irradiation process, the mineral irradiation at 200 μJ also yielded both monetite and brushite, however under this condition the phase fraction of monetite in the irradiated volume increased (30%). This is evident from the comparison of the GIXRD patterns in Figure 6.5. In this figure, the relative intensity of monetite diffraction peaks is much stronger than that observed in the irradiate samples at 100 μJ. Since the brushite to monetite phase transformation occurs below 200 ℃, it is likely that the laser irradiation in the 100 to 200 μJ transforms brushite partially into monetite in Fe^{2+}/Fe^{3+} ions free mineral samples.

6.3.1.2 5-FeCaP and 10-FeCaP

From chapter 4, XRD confirmed that by adding 5 mol% Fe^{2+}/Fe^{3+} ions, the dopant material stabilised the brushite structure and no monetite phase was observed. For Irradiation with a 100 μJ laser led to brushite phase being

transformed into a mixture structure of brushite and monetite with ratio of 67.8% and 32.2%, respectively, as shown in Figure 6.6. When 5-FeCaP was subjected to 200 μJ laser irradiation, the intensity of monetite peaks in the 5-FeCaP sample was observed to have increased relative to the pristine sample and the ratio of monetite to brushite is 70.5% and 29.5%, respectively. This result denotes that the irradiation of 200 μJ for 5 mol% Fe^{2+}/Fe^{3+} ion transforms brushite partially to monetite with ratio of monetite higher than that present in 0-FeCaP.

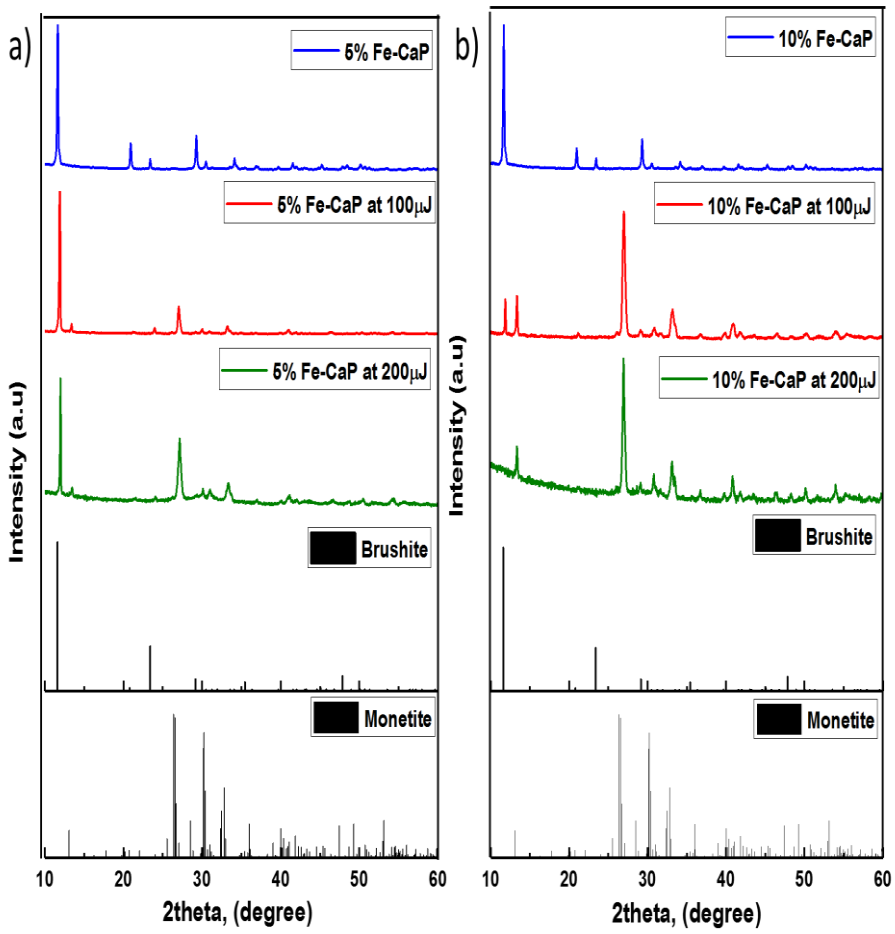

Figure 6.6: GIXRD of the a) 5 and b) 10-FeCaP after laser irradiation at 100 μJ and 200 μJ in comparison with JCPDS files.

For the samples containing 10 mol% Fe^{2+}/Fe^{3+} ion, the initial sample shows only brushite structure, Figure 6.6. Laser irradiation with 100 μJ transformed the brushite to a mixture of brushite with ratio of 20% and monetite with ratio of 80%, The monetite peaks in the 10-FeCaP sample having a higher

relative intensity than in 5-FeCaP at the same laser intensity (100 μJ). Increase laser intensity to 200 μJ for the 10-FeCaP sample, a full transformation from brushite to monetite was observed. This implies that irradiation the 10 mol% Fe^{2+}/Fe^{3+} ion doped sample with 200 μJ causes the temperature to rise to 200 ℃ (brushite to monetite transformation temperature).

6.3.1.3 20-FeCaP and 30-FeCaP

Figure 6.7 shows X-ray diffraction peak of 20 and 30-FeCaP samples after being irradiated.

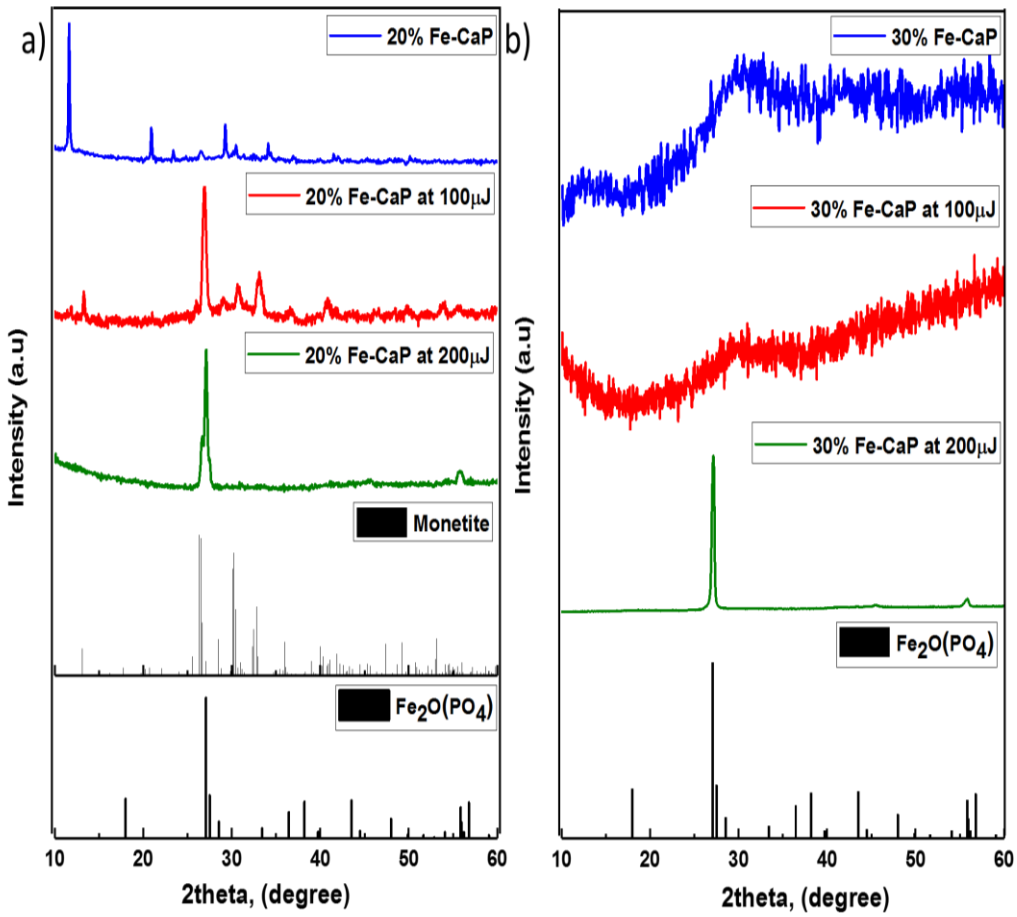

Figure 6.7: GIXRD of the a) 20 and b) 30-FeCaP after laser irradiation at 100 μJ and 200 μJ in comparison with JCPDS files.

When the 20 mol% Fe^{2+}/Fe^{3+} ion doped CaP sample was exposed to a lower energy intensity (100 μJ) irradiation, it was observed that the initial monetite and brushite mixture transformed into a monetite phase. It was also observed that the X-ray pattern obtained for this samples has some

broad peaks which could be attributed to the emergence of an amorphous $FePO_4.3H_2O$ phase that was observed in the initial structure. Since the transformation of brushite into monetite at temperature of 200℃ and the transformation of amorphous iron phosphate into crystalline structure at 590℃, it believes that after irradiation with 100 µJ the temperature was above 200℃.

On the other hand, when the 30 mol% Fe^{2+}/Fe^{3+} ion doped CaP sample was exposed to 100 µJ laser energy irradiation, no significant compositional changes were observed. Significant changes in phase was observed on application so the high energy intensity (200 µJ), both the 20-FeCaP and 30-FeCaP were found to have converted into iron oxide phosphate ($Fe_2O(PO_4)$). According to Beurmann [294], $Fe_2O(PO_4)$ can be prepared first by the evaporation of a solution consisting of iron nitrate $Fe(NO_3)_3$ and ammonium phosphate $(NH_4)_2HPO_4$ at 400℃ after that the reduction of H2-H2O gas was applied in an ambient pressure and a temperature of 450℃. A similar solution was used in our experiment to synthesise Fe doped materials. It is most likely, that the $FePO_4.3H_2O$ became converted to $Fe_2O(PO_4)$) during the laser irradiation process. Beside the $Fe(NO_3)_3$, that presented in 20 mol% after laser intensity of 200 µJ, peak at 26.53º is related to monetite phase. However, only $Fe(NO_3)_3$ was observed in 30 mol% Fe^{2+}/Fe^{3+} ion as a small amount of calcium (1.5 %) was noticed in the initial phase according to the SEM result.

In order to confirm the structures of the samples that were obtained using GIXRD, FTIR-ATR was aslo used.

6.3.2 Fourier Transform Infrared - Attenuated Total Reflectance (FTIR-ATR)

FTIR-ATR was conducted on the materials to examine the surface structure of materials, being investigated after laser irradiation. Presented in Figure 6.8 are details of FTIR-ATR spectra obtained from the samples subjected to irradiation at 2 different laser energies.

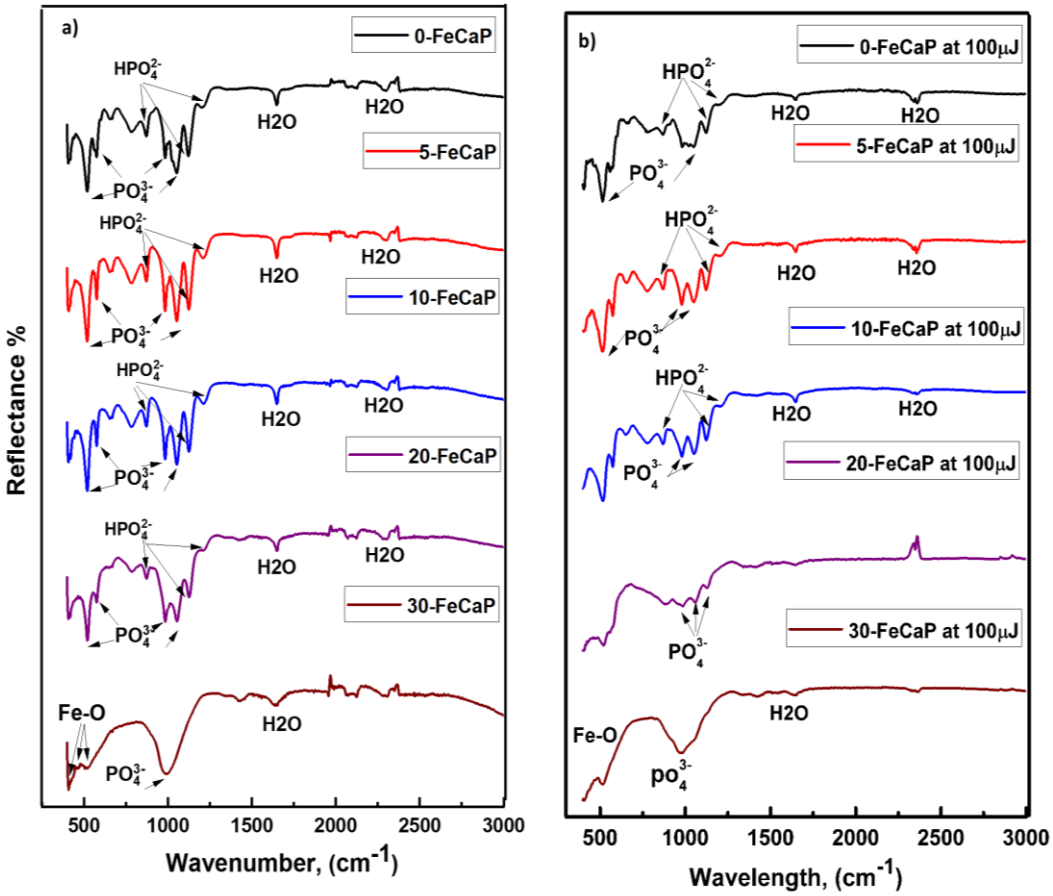

Figure 6.8: FTIR of a) synthesised and b) laser irradiation at 100 µJ and of 0, 5, 10, 20 and 30-FeCaP minerals.

After laser irradiation (100 µJ), the FTIR spectra of samples containing 0 mol%, 5 mol% and 10 mol% of Fe^{2+}/Fe^{3+} ions doped into CaP showed bands at around 2353 cm^{-1} and around 1650 cm^{-1} which were assigned to H-O-H free water of brushite. A P-O-H bending was observed at peak of around 1201 cm^{-1} and 760 cm^{-1} of brushite structure while peaks at 1120 cm^{-1}, 1040 cm^{-1} and 972 cm^{-1} indicate a P-O stretching mode of monetite. Further bands at ~890 cm^{-1} was observed and is related to P-O(H) stretching present in brushite and monetite structures. O-P-O(H) bending mode at 570 cm^{-1} and 530 cm^{-1} that appear in both structure was presented. This was in agreement for monetite and brushite structure as reported in literature [238].

FTIR spectra of the 20 mol%, which is a mixture of monetite and brushite after laser irradiation at 100 µJ showed monetite related events. Peaks at ~2351 cm^{-1} related to (P)O-H stretching mode in monetite. However, the

band at ~1650 cm^{-1} present in brushite and is linked to free water. Additionally, 1120 cm^{-1}, 1047 cm^{-1} and 977 cm^{-1} are related to P-O stretching mode of monetite structure. Bands present at 891 cm^{-1} was assigned to P-O(H) stretching mode in monetite structure [295].

Amorphous Iron phosphate ($FePO_4 \cdot 3H_2O$) presented in both structure of 30-FeCaP before and after laser irradiation (100 µJ). Band at wavenumber 1610 cm^{-1} was assigned to water molecules. The band for $FePO_4$ were located between 400 cm^{-1} and 1200 cm^{-1} [296, 297]. However, the intensity of these peak decreased in 30 mol% after laser irradiation [296, 297]. Table 6.1, shows the functional groups for the phases presented in FeCaP samples after laser irradiation with 100 µJ and 200 µJ.

Likewise in Figure 6.9, for 0 mol%, 5 mol% and 10 mol% at high laser radiation (200 µJ) presented monetite.

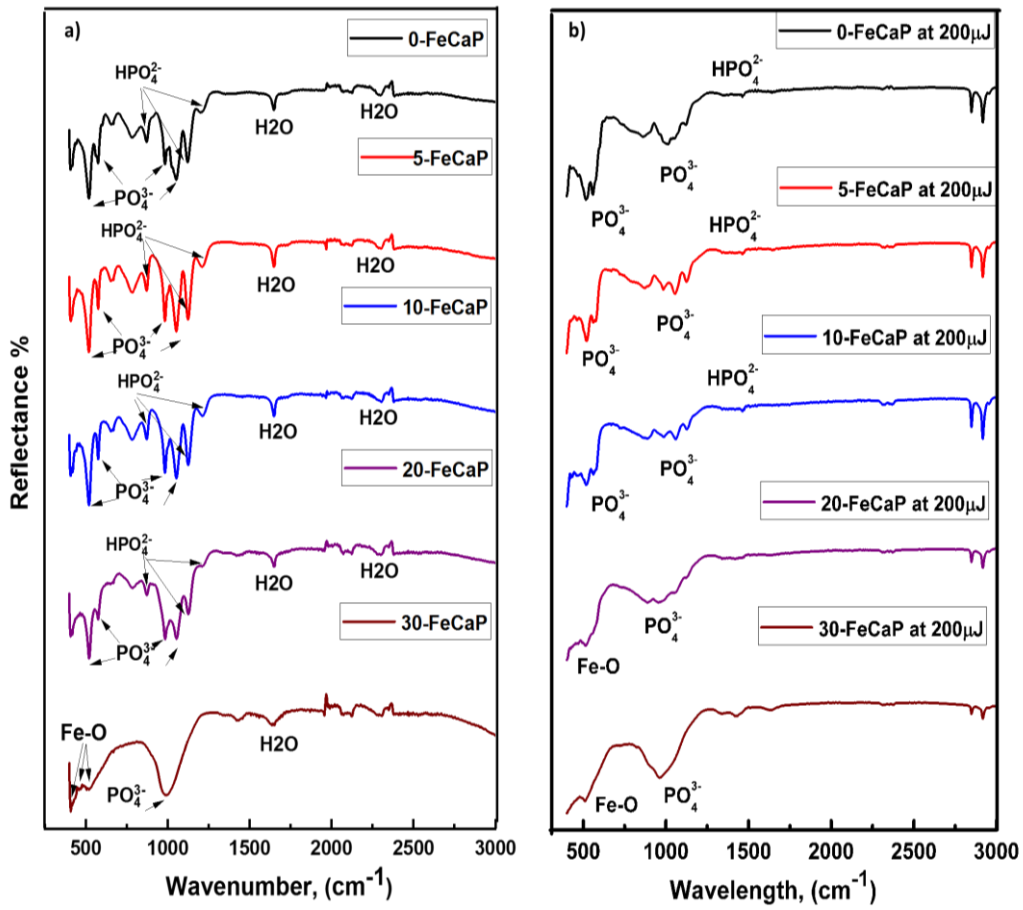

Figure 6.9: FTIR of a) synthesised and b) laser irradiation at 200 µJ of 0, 5, 10, 20 and 30-FeCaP minerals.

For 20 mol%, the peaks between 980 cm^{-1} and 1200 cm^{-1} of monetite and brushite structure present disappears, only few peaks observed (990 cm^{-1} and 1040 cm^{-1}) with small intensity that assigned to PO stretching mode. In addition, the same peak appears at 1000 cm^{-1} could be also related to PO stretching mode for $Fe_2O(PO_4)$ structure. On the other hand, laser intensity at 200 µJ for 30 mol% shifted the main peak at 1013 cm^{-1} that is linked to PO stretching mode of $FePO_4$ to smaller wavenumber 990 cm^{-1} which might be referred to $Fe_2O(PO_4)$. Thus, the results of all phases obtained from FTIR spectroscopy were in agreement with observations from GIXRD.

Table 6.1: Functional groups of brushite, monetite and iron phosphate (cm^{-1}).

	Wavenumber (cm^{-1})				
Functional groups	Brushite	Monetite	Functional groups	$FePO_4.3H_2O$	$FePO_4$
(P)O-H stretching modes	2930	2351	PO_4 stretching mode	987	987
PO stretching modes	1124-1053-981	1170-1120-1047and 977	Fe-O	582-	582
P-O-H bending modes	1200-750	1300	O-P-O bending mode	432	432
P-O(H) stretching	870	891	H-O-H	1600	
H-O-H bending of free water	2300-1650	1600			

6.3.3 Bright field optical microscopy

Images obtained from the optical microscope (Figure. 6.10) display the micro-channels on the surface of the FeCaP materials after laser ablation using energy pulse of 100 μJ and 200 μJ.

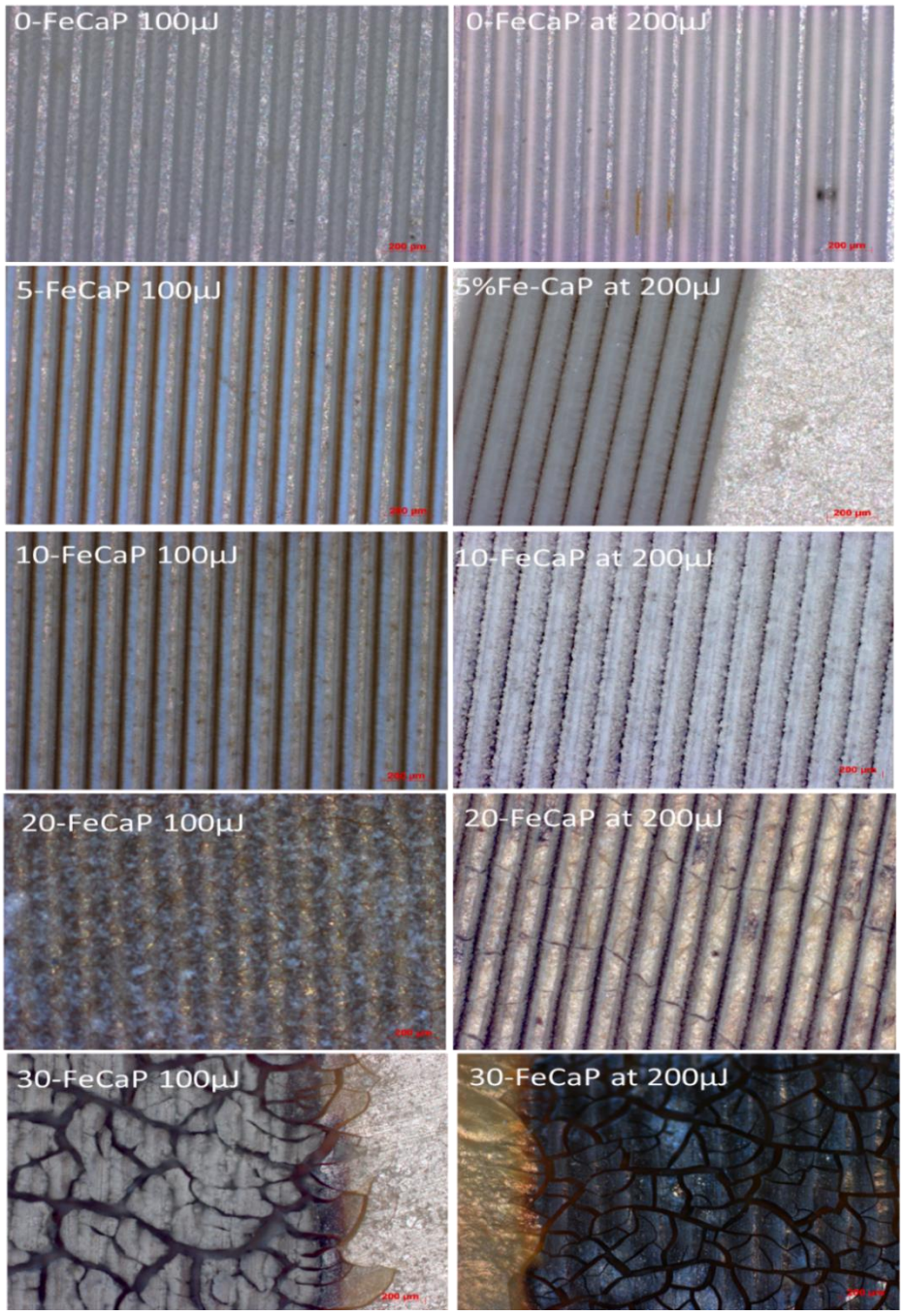

Figure 6.10: Bright field optical microscope of micro-channels at 100-200 μJ for 0%, 5%, 10%, 20% and 30% pelleted FeCaP samples.

The width of the micro-channels created by the 100 μJ laser on the 0-FeCaP was 63.3 μm. It was observed, that as the concentration of Fe^{+2}/Fe^{3+} ion increased in the sample, the width of the micro-channels reduced i.e. they became narrower for the first three samples (56.9 μm for 5-Fe-CaP and 54 μm for 10-FeCaP, respectively). However, no laser ablation micro-channels where observed in the 20-FeCaP and 30-FeCaP samples; instead extensive cracks were seen in the samples.

As mentioned, the ablation threshold of Fe^{2+}/Fe^{3+} doped materials increased when the concentration of Fe^{2+}/Fe^{3+} ion increased. Thus, when using a laser energy of 200 μJ, the following micro-channel widths were measured: 85.7 μm, 76.6 μm, 75.7 μm and 61.8 μm for 0, 5, 10 and 20-FeCaP samples, respectively. However, cracks also were also observed in the 20-FeCaP sample while the 30-FeCaP sample had a similar appearance to that obtained with 100 μJ laser. This due to the heat dissipation that decreases the production of plasma heat delivers to area around irradiation subsequently thermal transformations exist [298, 299].

6.3.4 Scanning electron microscopy (SEM)

SEM images of the samples after laser irradiation (100, 200 μJ) as presented in Figure. 6.11, 6.12, 6.13 and 6.14 showed micro-channels of 0-FeCaP, 5-FeCaP, 10-FeCaP, 20-FeCaP and 30-FeCaP samples.

For sample with concentration up to 10 mol% Fe^{2+}/Fe^{3+} ions, micro-channels prepared using 200 μJ laser irradiation were deeper than at the ones created by the 100 μJ, as shown in Figure 6.11 and Figure 6.12. The plate-like structure of brushite was observed in the area around laser irradiation of 0, 5 and 10-FeCaP which indicates that the irradiation only affect the target area. Results obtained from SEM microscopy corroborated the observations on the optical microscope in terms of reduction in microchannel width.

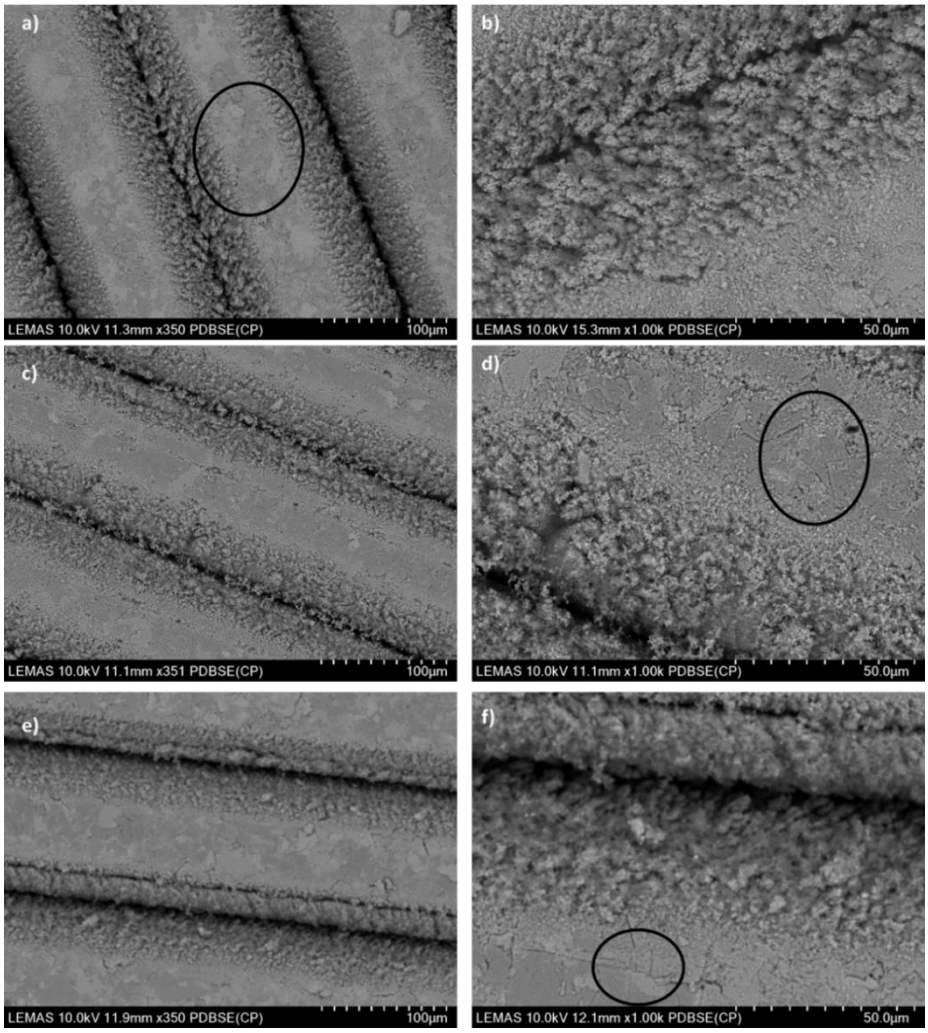

Figure 6.11: SEM images of a), b) 0-FeCaP, c),d) 5-FeCaP and e), f) 10-FeCaP after irradiation of laser (100 µJ) at different magnifications where the black circle shows the plate-shape structure of brushite.

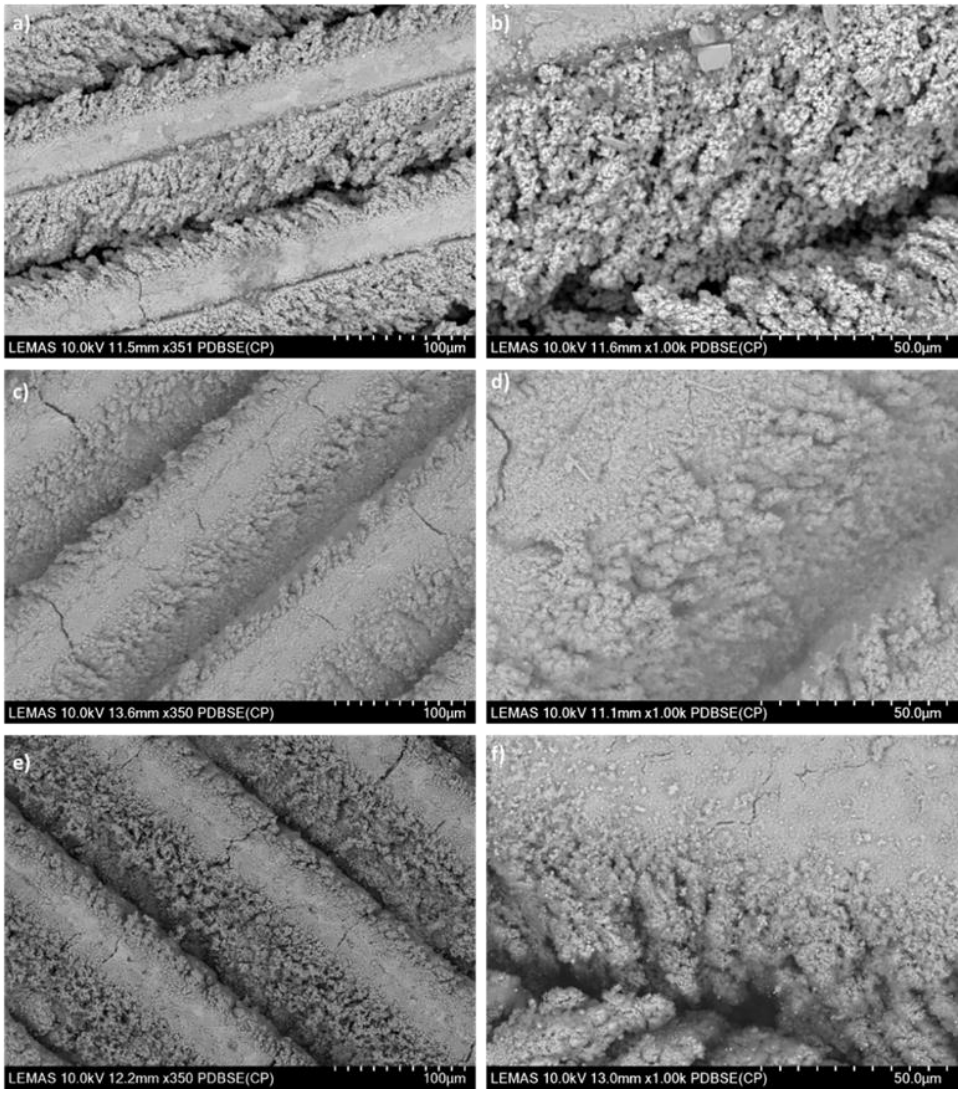

Figure 6.12: SEM images of a), b) 0-FeCaP, c),d) 5-FeCaP and e), f) 10-FeCaP after exposing to high intensity of laser (200 μJ) at different magnifications.

As Fe content increased (20 mol% and 30 mol%), cracks were being observed, as shown in Figure 6.13 and Figure 6.14. The cracks observed at higher Fe content could be because at high doping concentrations of Fe^{2+}/Fe^{3+} ions, the mineral absorbed more laser energy. Rapid high temperature have resulted in thermal stress due to significant temperature difference between area exposed to laser and surrounding areas which led to the formation of cracks appear in the 20-FeCaP and 30-FeCaP samples. Melting was also observed in both samples as a result of heat dissipation process that shows in Figure 6.13 and 6.14. Therefore, to produce micro-

channels a higher laser energy than energy of ion binding in the sample is in demand to produce the plasma thereby eject ions from the material [300].

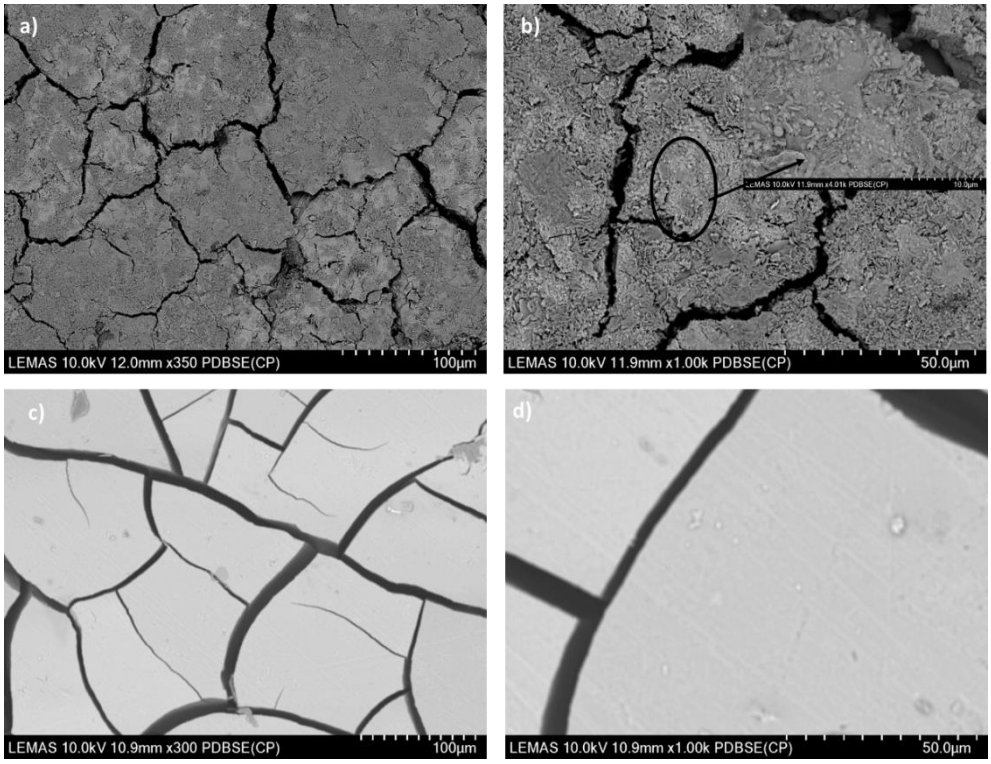

Figure 6.13: SEM images of a), b) 20-FeCaP and c), d) 30-FeCaP after irradiation of laser (100 µJ) at different magnifications and the black circle shows the melting area.

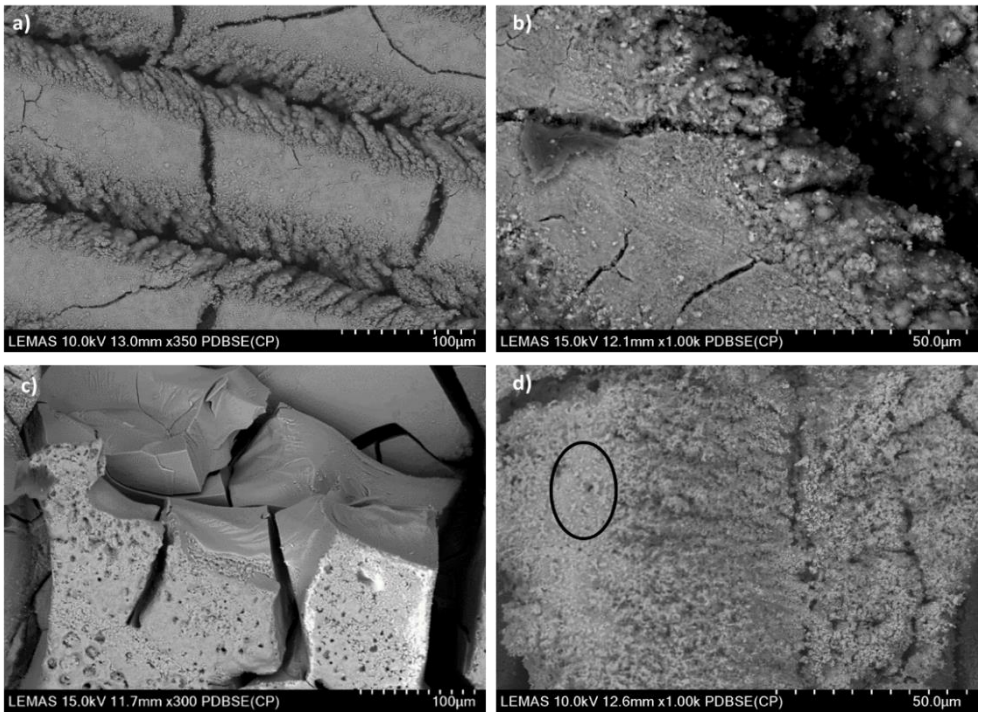

Figure 6.14: SEM images of a), b) 20-FeCaP and c), d) 20-FeCaP after exposing to high intensity of laser (200 µJ) at different magnifications.

From Figure 6.14, by increasing the laser intensity to 200 μJ for 20 mol%, the micro-channels were formed whereas, only melting and cracks were observed for 30 mol% sample after irradiation of 200 μJ. This results emphasize the result that obtained of UV-vis which indicated the high optical absorption of samples doped with Fe^{2+}/Fe^{3+} ions than un-doped. The chemical compositions of the samples after irradiation with 100 μJ and 200 μJ for the irradiated and non-irradiated areas were investigated.

6.3.4.1 Chemical compositions of samples using energy depressive X-ray EDX

The chemical compositions were also observed to vary with pulse energies. Figure 4.15 shows the chemical compositions presented in the 0-FeCaP after laser irradiations of 100 μJ and 200 μJ in comparison with non-irradiation 0-FeCaP.

For the non-irradiated 0-FeCaP as was confirmed with XRD both brushite and monetite are observed. The elemental composition using EDX presented agreed with theoretical of chemical compositions of monetite, Table 6.2. Also, for 0-FaCaP after irradiation with 100 μJ, same result was observed. Increasing the intensity to 200 μJ, the chemical compositions were related to both monetite and bruhite structure. This result implies that for undoped sample, using intensity of 200 μJ only rise temperature to few degrees.

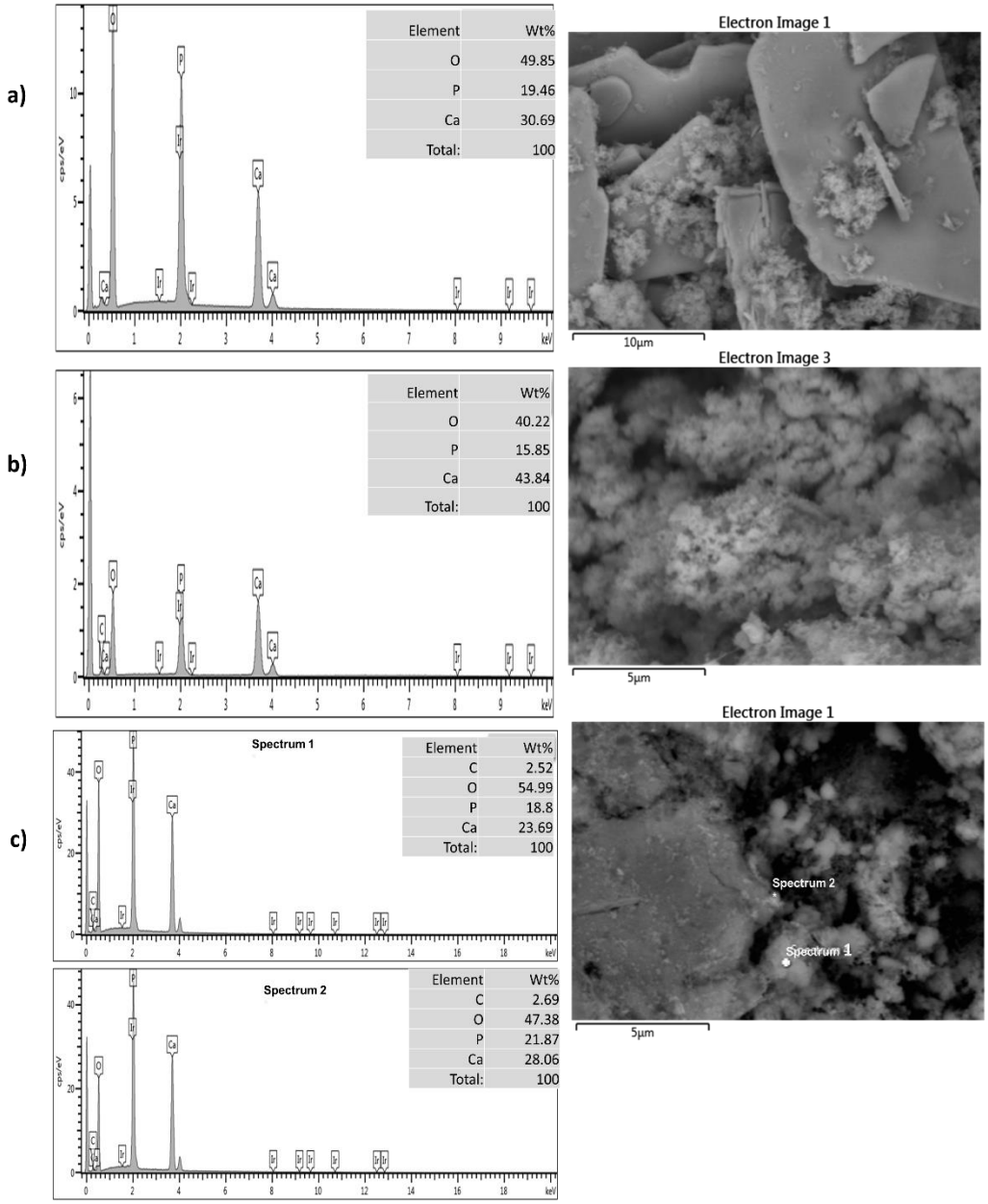

Figure 6.15: EDX of a) non-irradiated 0-FeCaP, b) 0-FeCaP after laser irradiation of 100 µJ and c) 0-FeCaP after laser intensity of 200 µJ.

For 5-FeCaP, the non-irradiated area was brushite as proved from the chemical composition spectrum and was compared with the theoretical of chemical compositions of brushite, Figure 6.16. After laser irradiation with 100 µJ and 200 µJ, elemental compositions after both intensity were in agreement with that present in monetite. This result reveal the presence of monetite beside the brushite structre as was investigated using GIXRD.

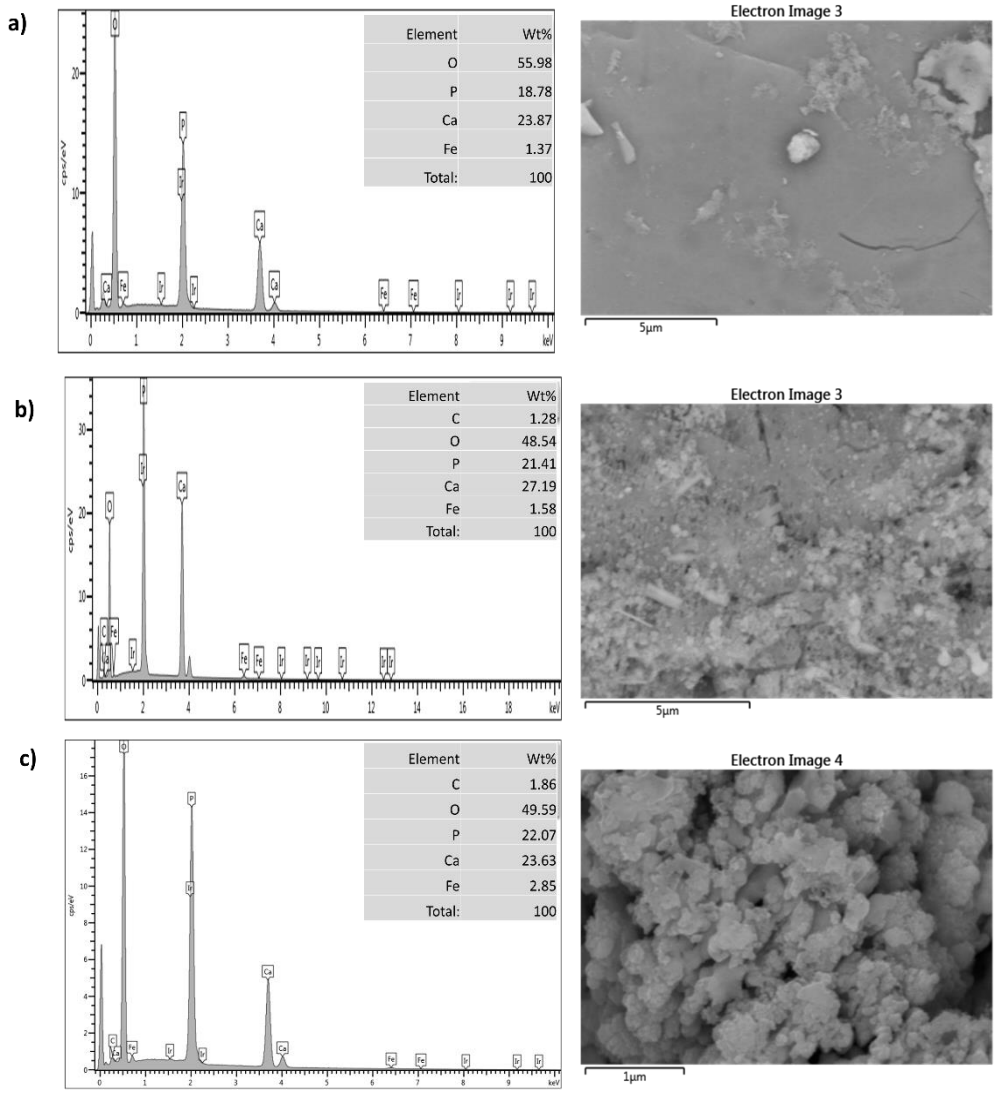

Figure 6.16: EDX of a) non-irradiated 5-FeCaP shows chemical compositions of brushite, while b) 5-FeCaP after laser irradiation of 100 µJ and c) 5-FeCaP after laser intensity of 200 µJ show chemical compositions of monetite.

Looking at elemental composition of the 10-FeCaP sample, exhibited same result that was observed in 5-FeCaP. By comparing the initial sample with sample after exposure to 100 µJ and 200 µJ laser ablation; O_2 content decreased in 10-FeCaP samples and was around 47 wt% which could suggest a partial or total transformation into monetite. The result of 5-FeCaP and 10-FeCaP support the result of GIXRD and UV-vis that show the transformation of brushite into monetite as doped with Fe^{2+}/Fe^{3+} ions increase the optical absorption of the sample.

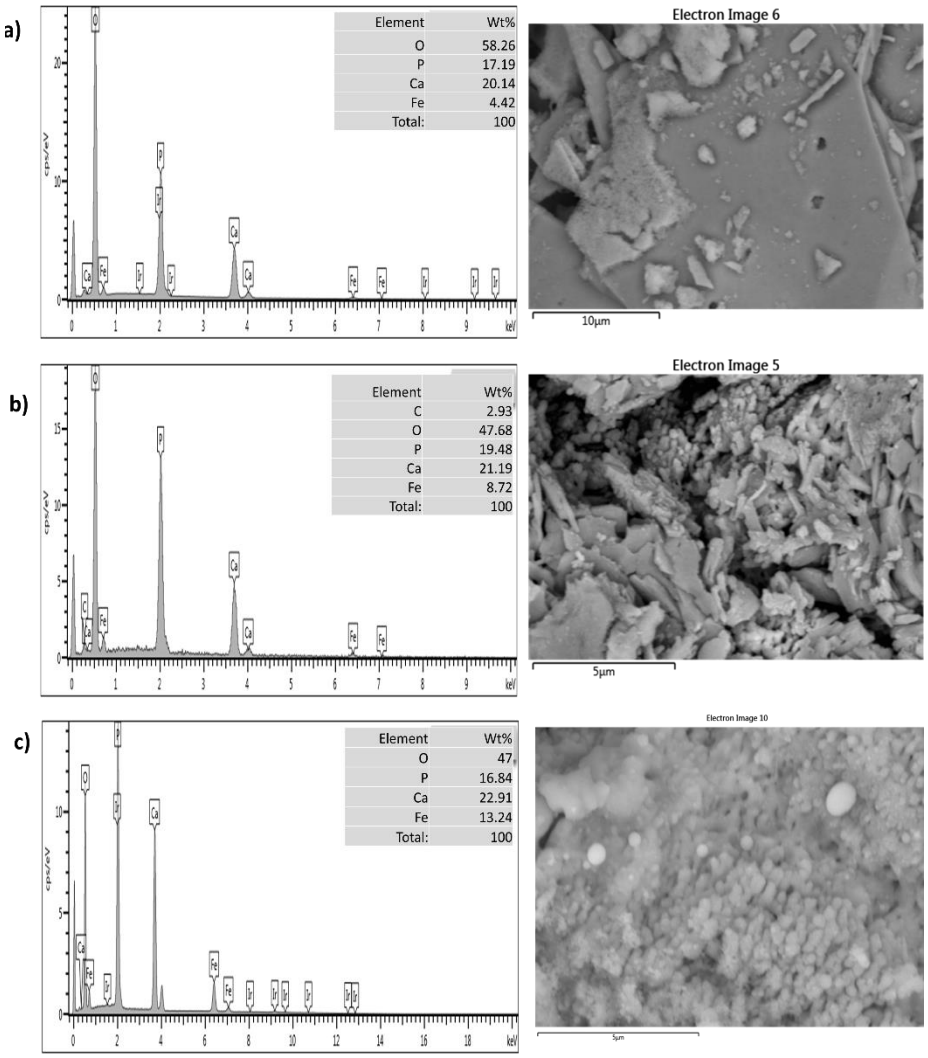

Figure 6.17: EDX of a) non-irradiated 10-FeCaP shows chemical compositions of brushite, while b) 10-FeCaP after laser irradiation of 100 µJ and c) 10-FeCaP after laser intensity of 200 µJ show chemical compositions of monetite.

For 20-FeCaP at 100 µJ, O_2 decreased From 58 wt% to 45.7 wt% that agreed with one present in monetite, as shown in Figure 6.18. Meanwhile, laser at 200 µJ offered the same percentage of chemical composition that might be related to ($Fe_2O(PO_4)$), table 6.2. The presence of Ca ion in 20-FeCaP after laser intensity of 200 µJ could be demonstrated the existence of moentite as the peak was observed by GIXRD.

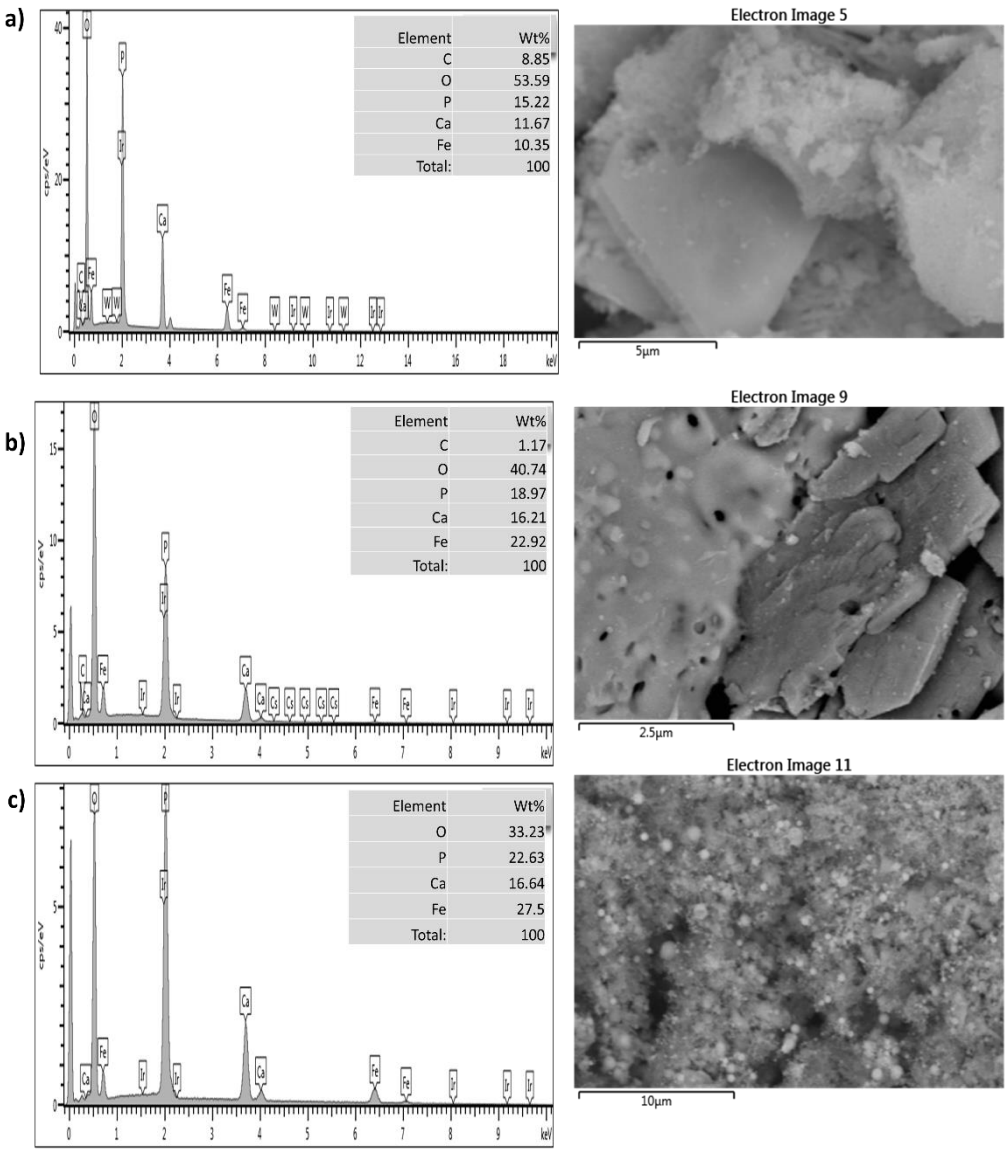

Figure 6.18: EDX of a) non-irradiated 20-FeCaP shows chemical compositions of brushite, while b) 20-FeCaP after laser irradiation of 100 µJ shows monetite compositions and c) 20-FeCaP after laser intensity of 200 µJ show chemical compositions of $Fe_2O(PO_4)$.

From Figure 6.19, Percentage of elements shows in 30-FeCaP agreed with amorphous $FePO_4.3H_2O$ for the initial sample and since the water molecular decrease after the laser irradiated the percentage of O_2 decreased after irradiation of 100 µJ [301]. After laser intensity of 200 µJ, the chemical compositions was similar to that observed in 20-FeCaP at the same laser intensity ($(Fe_2O(PO_4))$). However, the percentage of Ca ion was only 1.4 wt% which explains the absent of any calcium phase in the structure.

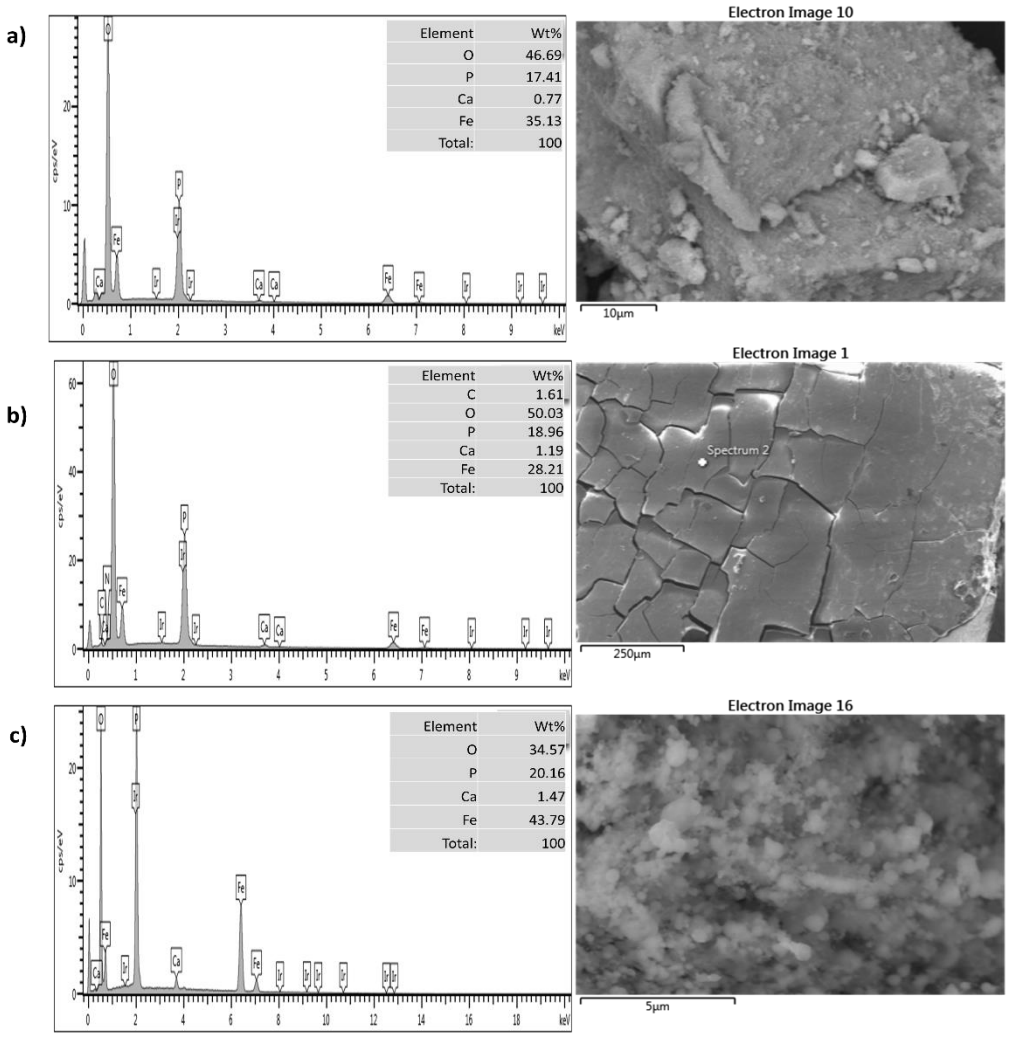

Figure 6.19: EDX of a) non-irradiated 30-FeCaP, while b) 30-FeCaP after laser irradiation of 100 µJ and c) 30-FeCaP after laser intensity of 200 µJ.

Table 6.2: Theoretical of chemical compositions of brushite, monetite, $FePO_4.2H_2O$ and $Fe_2O(PO_4)$ [4].

Compositions	Brushite (wt%)	Monetite (wt%)	$FePO_4.2H_2O$ (wt%)	$Fe_2O(PO_4)$ (wt%)
O	57.5	47.4	51.39	36.0
P	23.9	29.6	16.5	13.9
Ca	18.6	23.0	-	-
Fe	-	-	29.7	50.0

6.3.4.2 Cross section of micro-channels

The cross sections were made from the samples to measure the depth of the micro-channels for each of the FeCaP sample after irradiation with 200 µJ in order to investigate the effect of Fe^{2+}/Fe^{3+} ions concentration in these channels, Figure 6.20. In Figure 6.20, was found that the depth decreases when the concentrations of Fe^{2+}/Fe^{3+} increases 178 µm, 136 µm, 100 µm and 27 µm for 0 mol%, 5 mol%, 10 mol% and 20 mol%, respectively. This result confirms that the ablation threshold of FeCaP increases.

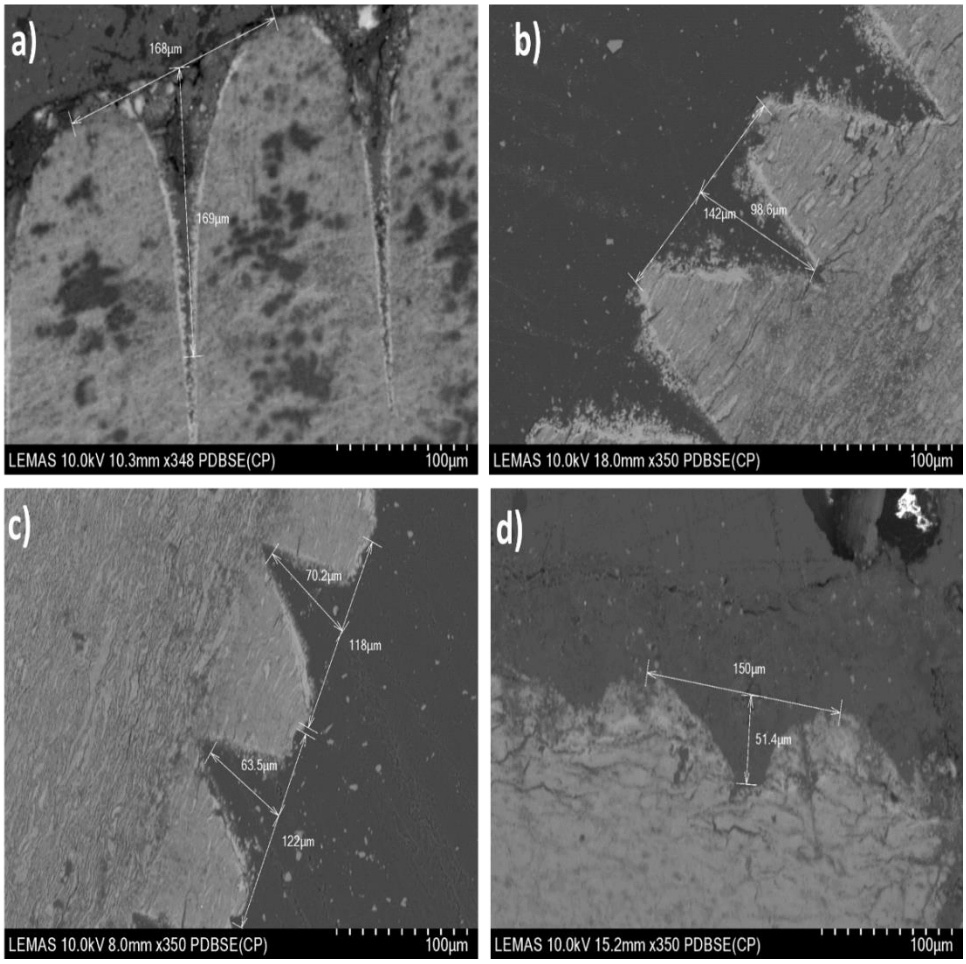

Figure 6.20: SEM cross section of FeCaP (brushite) after laser irradiation at 200 µJ where a), b), C) and d) are 0, 5, 10 and 20-FeCaP.

EDX of samples is shown in Figure 6.21 and Figure 6.22. Fe-rich area of 5 mol%, 10 mol% and 20 mol% was noticed around the irradiation area after ilaser intensity of 100 µJ. Melting also was observed in 20-FeCaP, as shown in Figure 6.21c.

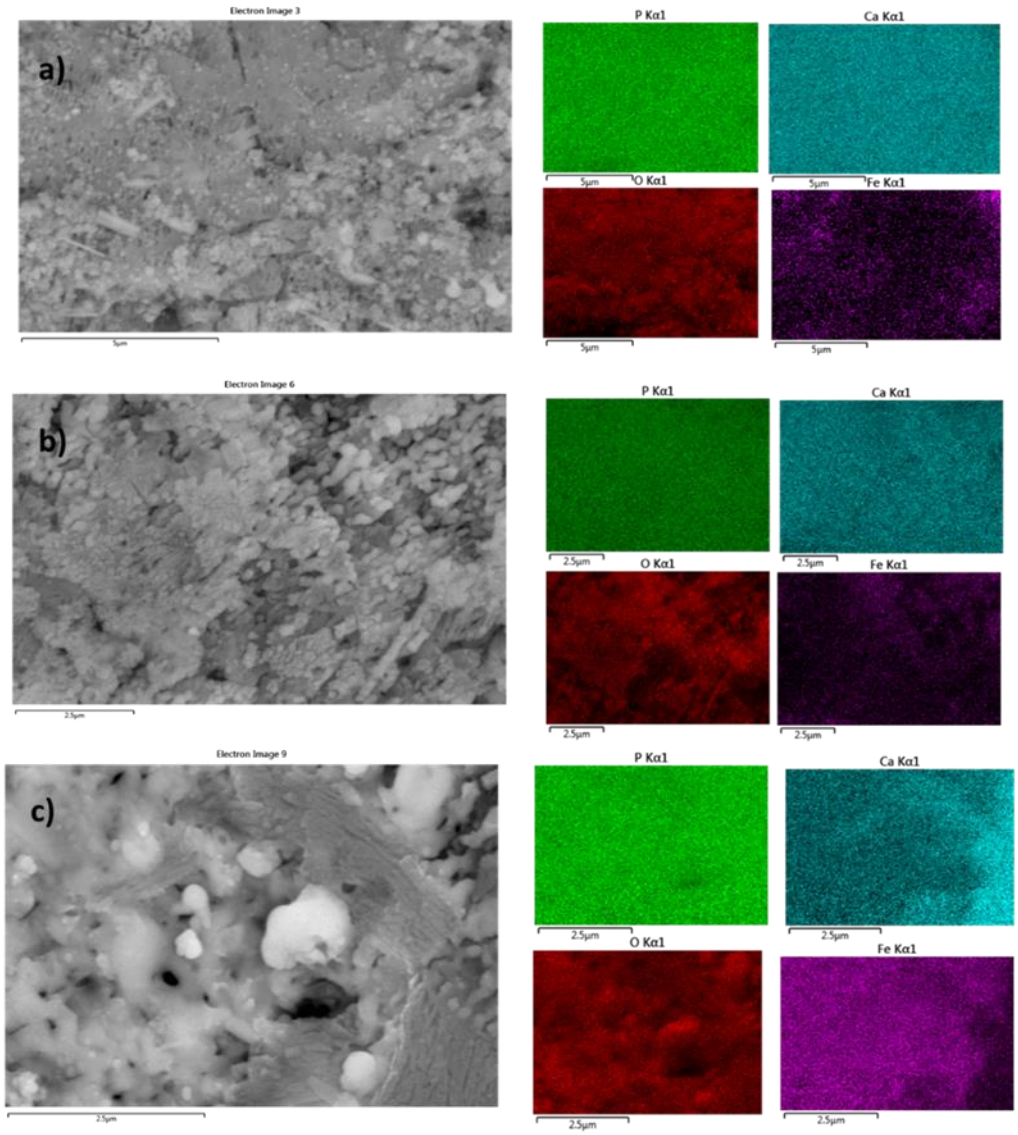

Figure 6.21: SEM-EDX show chemical composition of a) 5 mol%, b) 10 mol% and c) 20 mol% after irradiation of 100 µJ.

After laser irradiation of 200 µJ, small area of melting was noticed for 10-FeCaP. The melting was increased by increasing the concentration of Fe ion. Therefore, for 30-FeCaP all the area that exposure to laser presented melting instead of creating micro-channels, Figure 6.22.

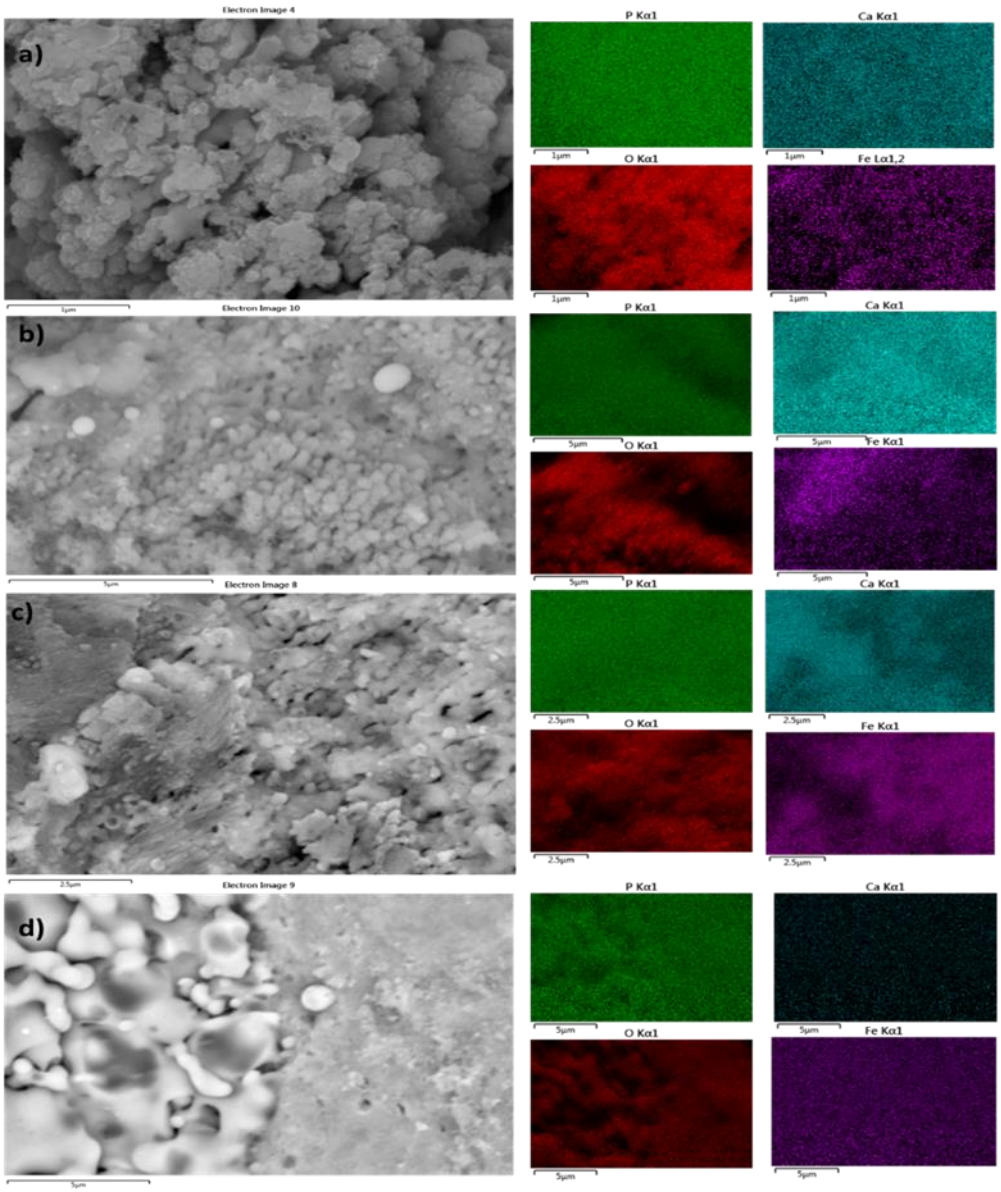

Figure 6.22: SEM-EDX of a) 5, b) 10, c) 20 and d) 30-FeCaP after laser irradiation of 200 µJ offer the chemical compositions of these materials and indication of some melting areas particularly at 20 and 30-FeCaP.

6.3.4.3 The effect of energy density or power density of femtosecond pulsed laser on FeCaP minerals

Laser intensity 150 µJ was employed to form micro-channels formation on the surface of 0, 5 and 10 mol% FeCaP samples and compared with 200 µJ, as shown in (Figure. 6.23). Cross section of these channels and their lengths were measured on the SEM. The purpose of this was to explore the role that Fe^{2+}/Fe^{3+} ions could play in the ablation and the length of micro-channels that formed. For intensity of 150 µJ, the micro-channel length was 103 µm, 92 µm and 86.4 µm of 0, 5 and 10 mol%, respectively. Higher laser

intensity (200 µJ) led to an increase in mico-channels length to 175 µm, 142 µm and 100 µm for 0, 5 and 10 mol%, FeCaP respectively. Therefore, ablation using laser intensity of 200 µJ was used to examine the role of cell adhesion in these channels since the length and shape of micro-channels using 200 µJ are better than laser intensity of 150 µJ.

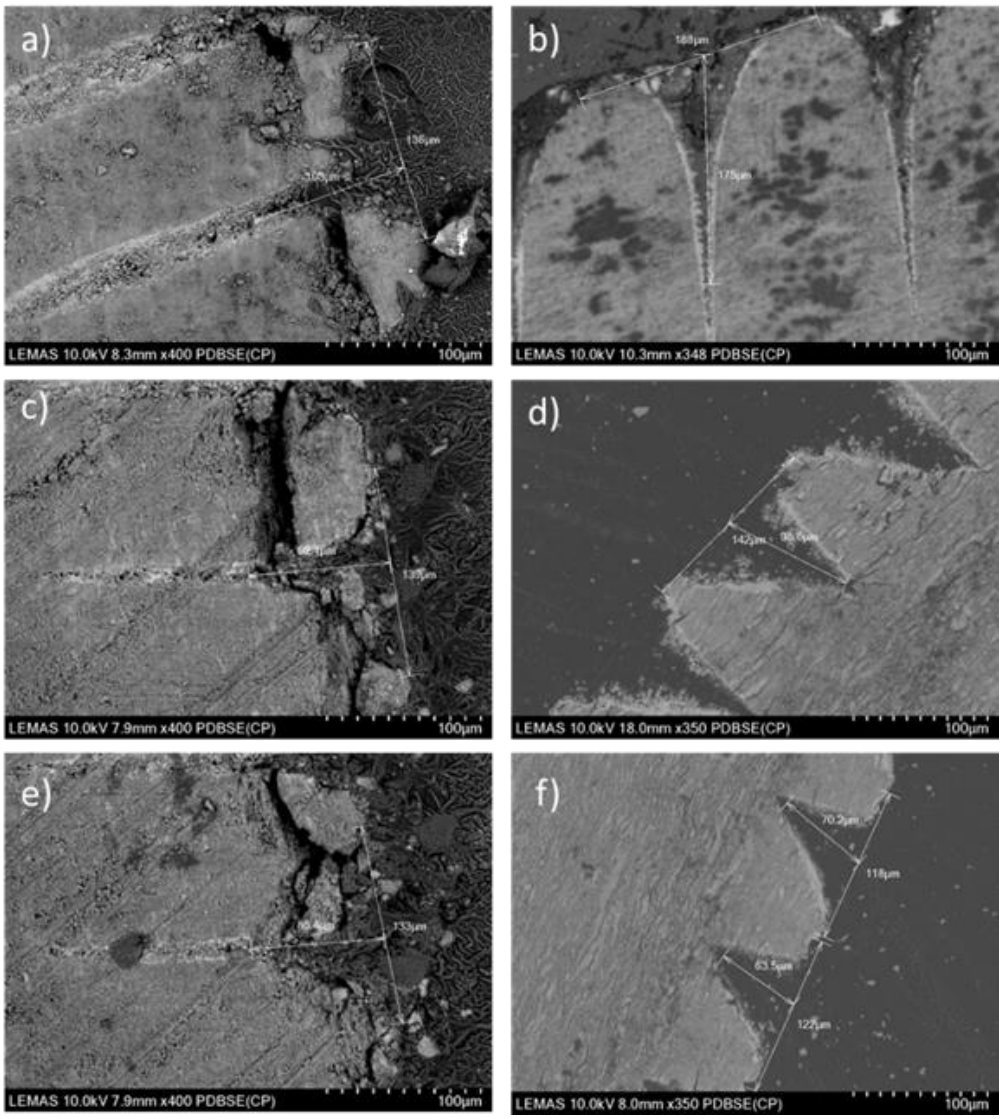

Figure 6.23: SEM image showing cross section of the micro-channels on the surface of FeCaP minerals, a) and b) 0-FeCaP at 150µJ and 200µJ, respectively. c) and d) 5-FeCaP at 150µJ and 200µJ, respectively and e) and f)10-FeCaP at 150µJ and 200µJ, respectively.

It has been demonstrated the mechanism of the ablation threshold, therefore, since the Fe^{2+}/Fe^{3+} materials will transfer more heat to the lattice structure melting will occur. As stated by Beer-Lambert law, (eq. 6.5) the

ejection of material above the threshold fluence increase with increasing the energy, thus high laser intensity is required for the ablation to proceed [142, 302].

$$I(z) = I_0 e^{-\alpha z} \qquad (6.6)$$

Where

- α is absorption coefficient of material.
- Z is the depth.
- I is the intensity which is for constant α, decays exponentially with z.
- I_0 is surface intensity.

Optical absorption coefficient were measured for FeCaP samples by calculation the thickness of pellet samples and Beer-Lambert law. The thickness were 1.1 cm, 0.93 cm, 0.9 cm, 0.88 cm, 0.76 cm for 0, 5, 10, 20 and 30-FeCaP respectively, while the reflectivity from UV-Vis spectroscopy were 0.99, 0.89, 0.83, 0.5, 0.28 for 0, 5, 10, 20 and 30-FeCaP, respectively. From Figure 6.24, optical absorption coefficient increased as the Fe ion concentration increased.

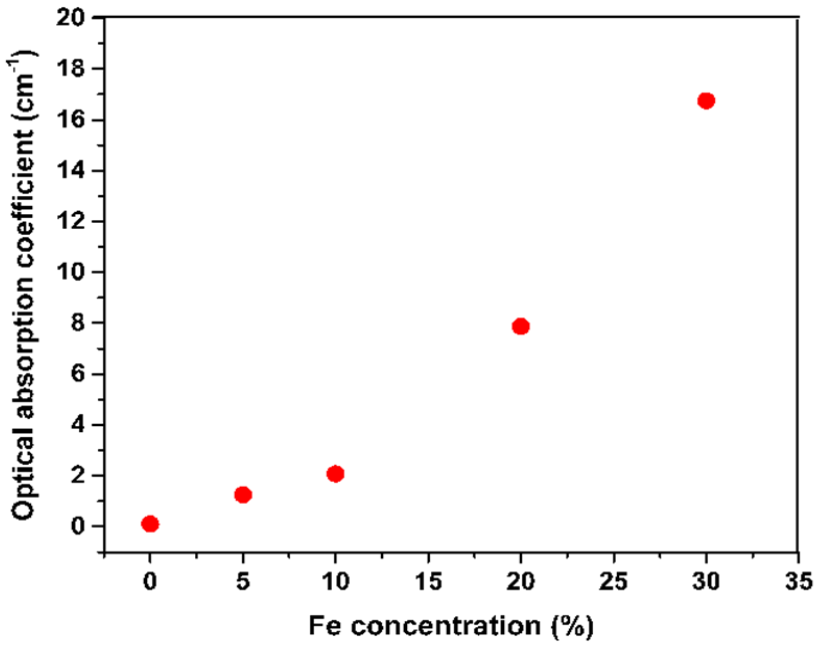

Figure 6.24: Optical absorption coefficient as a function of Fe^{2+}/Fe^{3+} ion concentrations.

When laser energy is absorbed by the target materials this might lead to ablation or/and melting and thermal diffusion depends on the optical and thermal properties of the materials. Thermal diffusion after ablation could also lead to structure changes on the irradiation area. It could be that high concentrations of Fe^{2+}/Fe^{3+} ions led to increased conversion of laser energy to heat and thus causing a melting of the surface instead of ablation as observed in the 20 and 30-FeCaP samples [142, 303, 304]. However, for 10-FeCaP the melting area was smaller for doped with 10 mol% at 200 µJ.

In this chapter, it has been determined the ablation threshold of FeCaP samples in order to create micro-channels in the samples surface. The chapter that follows moves on to consider the effect of different concentration of Fe^{2+}/Fe^{3+} ion on cytotoxicity of samples and cell proliferation. The effect of microchannel on the top of sample surface is also considered.

Chapter 7 The effect of sintered FeCaP materials on biological performance before and after mico-channels

Chapter introduction

Various concentrations of Fe^{2+}/Fe^{3+} were tested in order to investigate the effect of concentration on cell viability and growth. In addition, micro-channels using femtosecond pulsed laser was also created in the top of samples surface to study their effect on cell adhesion.

Chapter summary

The sintered iron-doped minerals were found to be non-toxic and promoted greater degree of cell growth than that observed for undoped minerals. Micro-channels using ablation technique was found to induce the cell attachment on the sample surface. Contact angle of the samples after micro-channels was measured to understand the effect of ablation in the surface properties.

7.1 Evaluation of biocompatibility and cell growth

In vitro evaluation of cytotoxicity effects of sintered FeCaP minerals on osteoblast cell line G292 was conducted in both Contact and extract assay.

7.1.1 Contact and extract assay

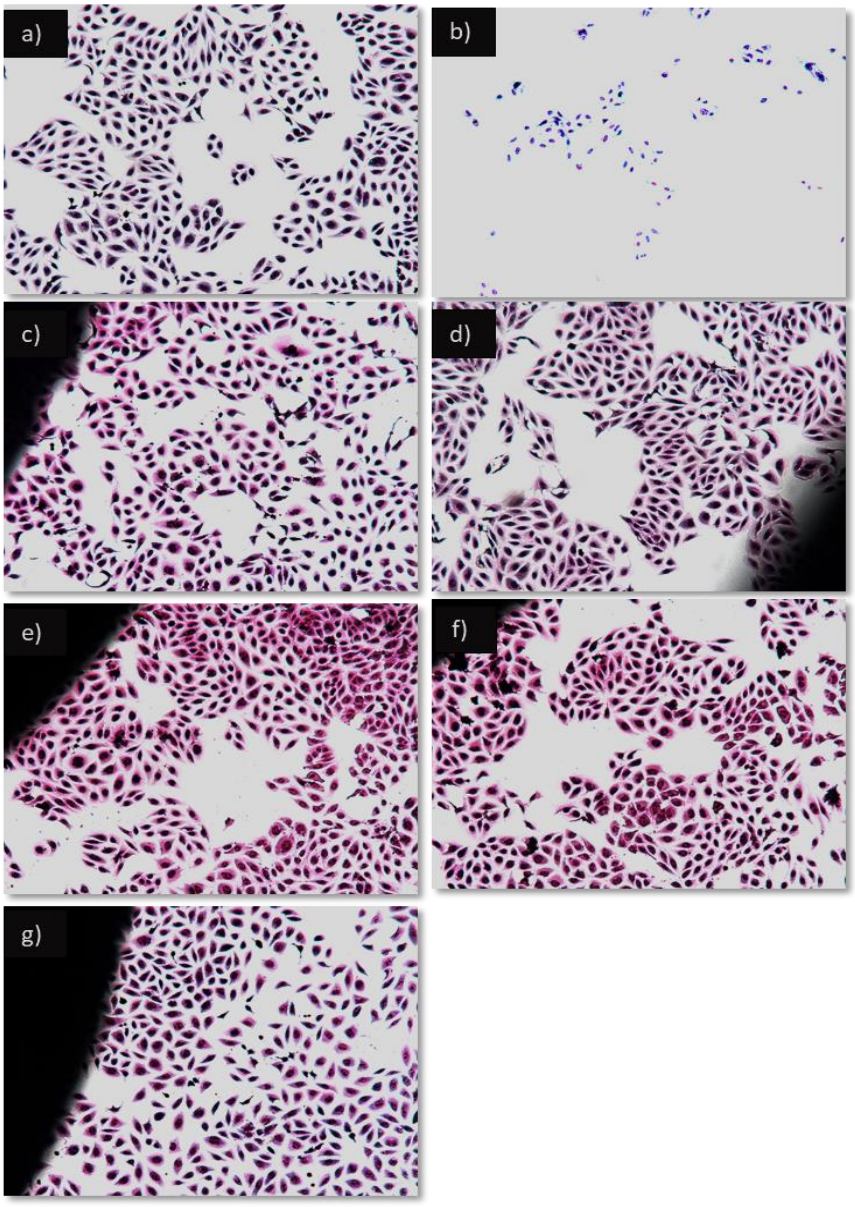

Figure 7.1: Cytotoxicity assay of sintered FeCaP minerals, contact test: a) negative and b) positive controls (40% DMSO) was seeded with osteoblast cell line in comparison with c) 0-FeCaP, d) 5-FeCaP, e) 10-FeCaP, f) 20-FeCaP and g)30-FeCaP pellets.

In contact assay, microscopic analysis of cell culture of sintered Fe^{2+}/Fe^{3+} doped and undoped CaP mineral samples showed similar results to that of the negative control; no signs of cytotoxicity, G292 culture presented no

zones of morphological change nor cell lysis were noted and cell growth up in contact with the sintered samples of 0-FeCaP, 5-FeCaP, 10-FeCaP, 20-FeCaP and 30-FeCaP (Figure. 7.1a, c, d, e, f and g). Cells were growing around all the FeCaP samples indicated no release of toxic materials from the samples. While 40% dimethyl sulfoxide (DMSO) (positive control) resulted in cell lysis as shown in Figure. 7.1b.

In the extract cytotoxicity assay**,** there was no significant reduction in the cellular ATP levels of the G292 cells following incubation with soluble extracts of sintered FeCaP samples (compared with that of the DMEM (negative control) (*P> 0.05*). Doped with Fe^{2+}/Fe^{3+} ion increased the cell viability with about 12% than undoped sample. While the positive controls, 40% DMSO caused an almost total loss of ATP and it was significantly difference in comparison to negative control ($P < 0.05$), as shown in Figure. 7.2.

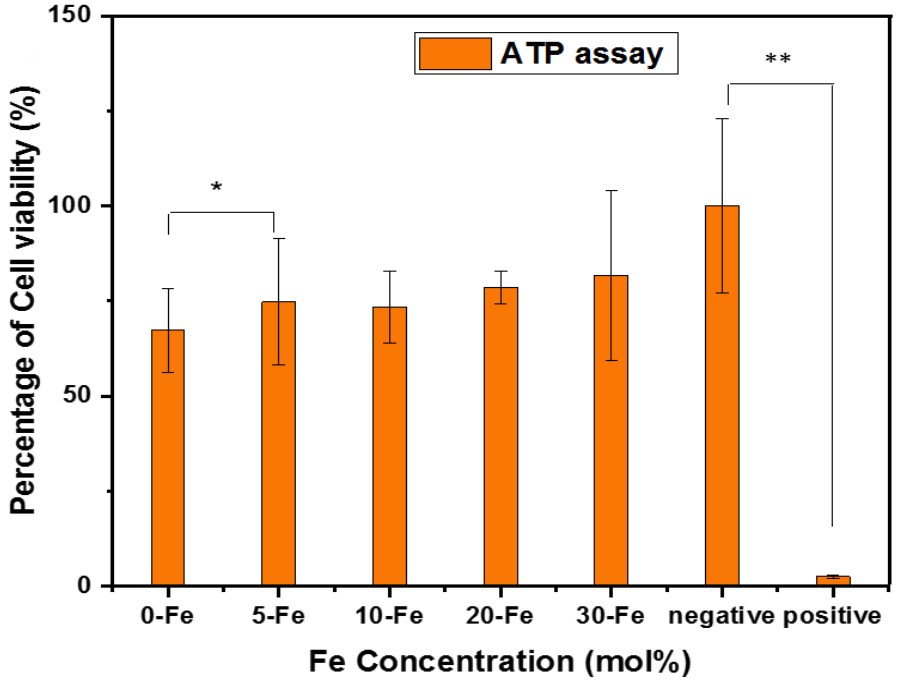

Figure 7.2: Effect of sintered FeCaP on cell viability: 0- FeCaP, 5-FeCaP, 10- FeCaP, 20-FeCaP and 30- FeCaP. Negative and positive controls represent cell treated with media and 40% DMSO, respectively. Error bars represent standard deviation, ** illustrates significant difference between negative control and other materials while * illustrates significant difference between FeCaP samples, (P<0.05).

7.1.2 Cell attachment and proliferation

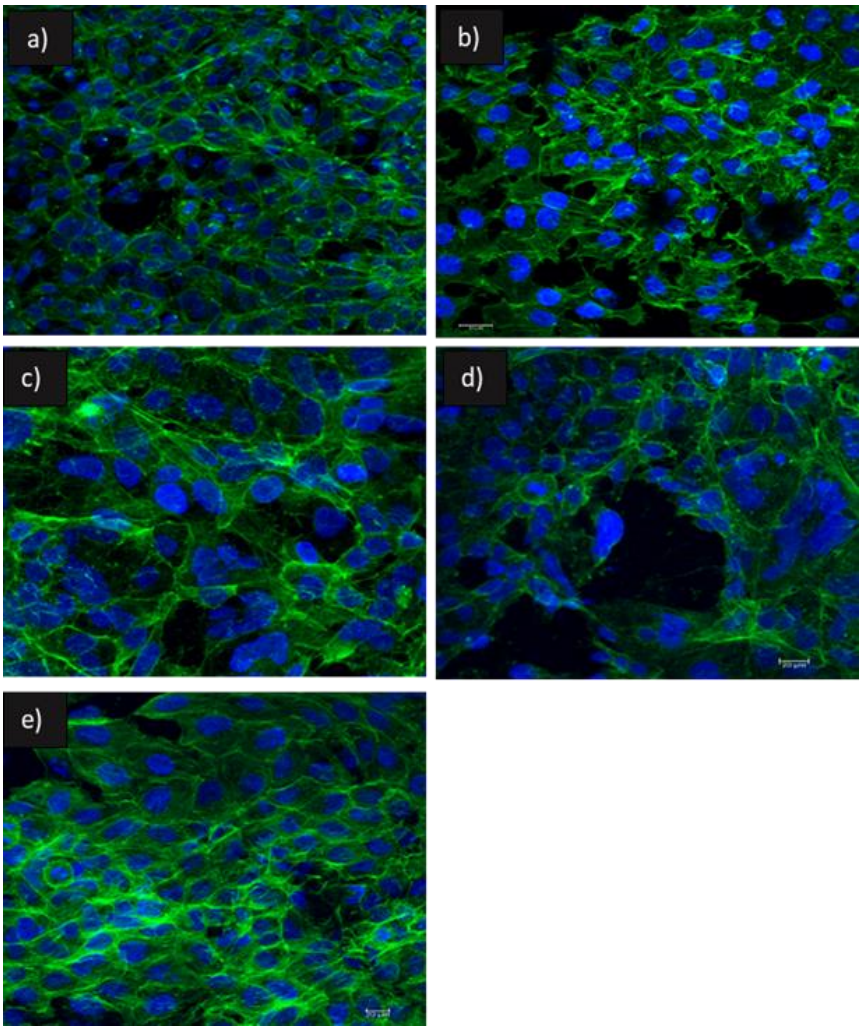

Figure 7.3: FeCaP, d) 20-FeCaP and e) 30-FeCaP sintered pellets after seeding osteoblast cells for 48 hrs. The green color represent actin and blue color represent nucleus. Scale bars: 50 µm.

Quantitative and qualitative approaches for cell growth on the top of sintered FeCaP were examined. Since the cell adhesion is the first stage for cell to proliferate, the qualitative test using confocal microscopy was employed, and images are shown in Figure. 7.3. Results show the cells growth after incubation for 48 hrs, the cells were attached and proliferated on the top of all the pellets samples.

The effect of sintered FeCaP materials on biological performance before and after micro-channels

To discover the ideal concentration of Fe^{2+}/Fe^{3+} ion for the cell proliferation, quantitative method is important to apply for measuring the number of cells in each sintered FeCaP samples, Figure 7.4.

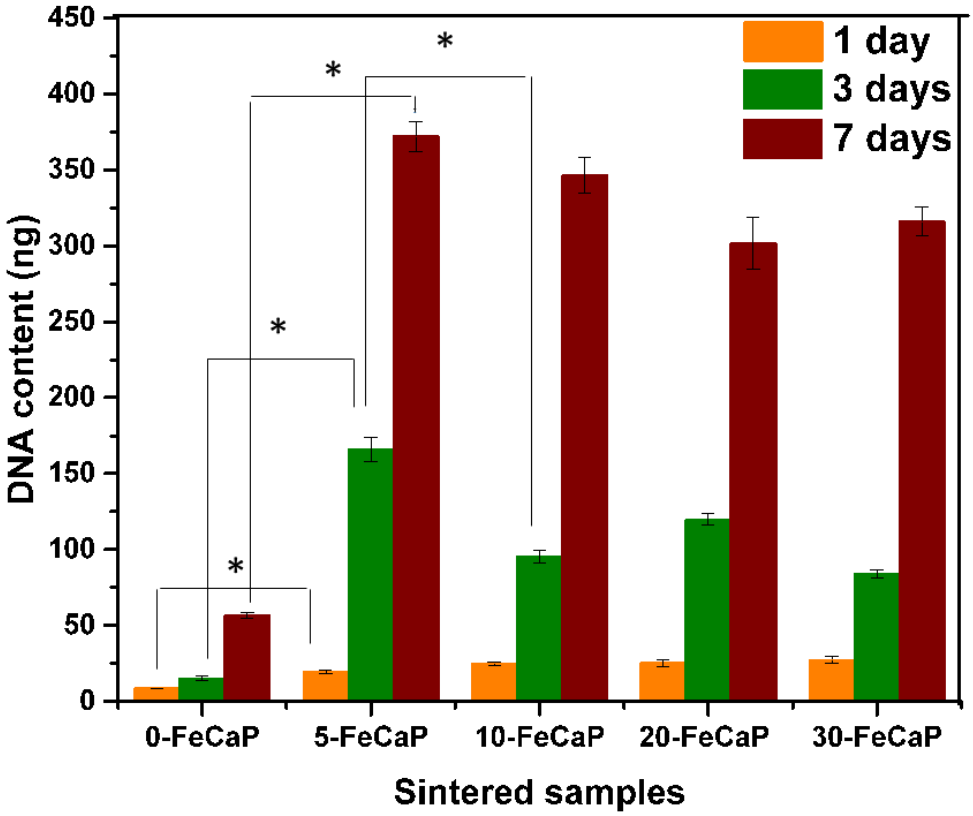

Figure 7.4: Effect of sintered FeCaP on cell proliferation. Cell proliferation was monitored at 1, 3 and 7 days. Error bars represent standard deviation. * illustrates a significant difference ($P<0.05$).

Consequently, picogreen protocol was analysed for different intervals (1, 3 and 7 days), as seen in Figure. 7.4. DNA content of cells attached to each sample after incubation for 1 day showed significantly higher number of cells on all minerals that were doped with Fe^{2+}/Fe^{3+} compared to undoped mineral ($P < 0.05$). Cell proliferation assay showed a significant increase of cell number from day 1 to day 3 then to day 7 in all tested samples including doped minerals and undoped one. Furthermore, at each time point, the number of cells was significantly higher in all doped mineral compared to undoped mineral ($P < 0.05$).

According to Xia et al. [305], Fe ions might increase the occurrence of protein that is responsible for cell adhesion thus more cells adheres to FeCaP in comparison with undoped sample which is the important stage for

cell growth. Moreover, the microstructure and surface morphology have an impact on cell behaviour, it was found that Fe_2O_3/CaP scaffolds with small and spherical shape structure attract cells more than samples with large and spindle shape [25]. A large plate-like structure appears for sintered undoped CaP, however, doping with Fe^{2+}/Fe^{3+} ions decreases the structure size after sintering procedure. Furthermore, Fe^{2+}/Fe^{3+} ion has an essential role in transferring oxygen in the human blood and therefore releases of this ion from the materials may be internalised on the cells and thereby affect cells behaviour [306]. It was also found that fibronectin adsorption which is important for cell adhesion and proliferation increase at the presence of Fe ion [98, 307, 308].

7.1.3 Confocal microscopy

In Figure. 7.5, the osteoblast cells line (G-292) was seeded in the top of sintered FeCaP samples. It was noticed that cells adhered in the micro-channels for 0 mol%, 5 mol% and 10 mol%. However, due to the cracks in 20 mol% cells were spread in the whole samples surface. The micro-channels on the samples surface act to organise the cells, this process is called a contact guidance [142, 173]. In the contact guidance the cells arrange along the channels shape which in our samples was in straight line. Although, the alignment of cells has advantages on supporting cells growth and adhesion [142, 173]. The understanding of the impact of micro-channels in cell adhesion and proliferation is still unclear.

Chen et al.[174], reported that the reason of cell adhesion therefore cells growth in the micro-channels pattern could be linked to the high concentrations of extracellular matrix proteins interact with the focal adhesions in these channels. It has been found that focal adhesion were spread over the smooth sample surface in heterogeneous way whereas on laser treatment samples focal adhesion assembled in the micro-channels [175, 176].

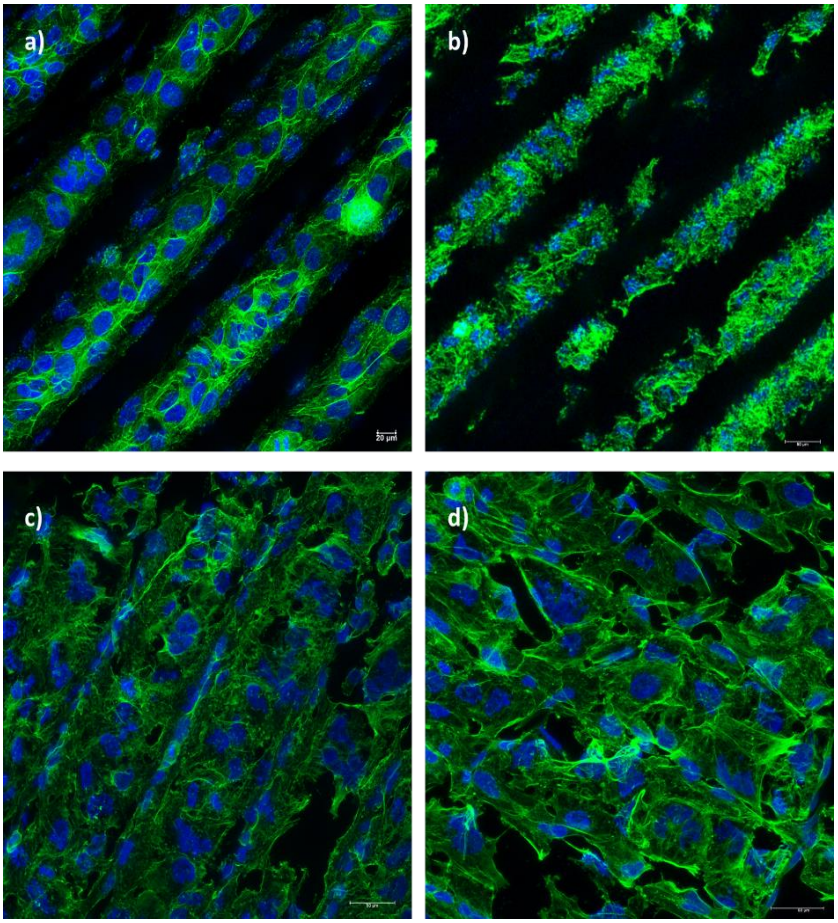

Figure 7.5: Confocal microscope showing the adhesion of osteoblasts cells line into the micro-channels of sintered FeCaP samples a) 0 mol%, b) 5 mol%, c) 10 mol% and d) 20 mol%.

Previous studies have reported that cell adhesion and surface hydrophilicity are interrelated [309, 310]. Herein, we have explored the effect of the presence of micro-channels on the contact angle of the sample surface by measuring the water contact angle for (0 mol%, 5 mol% and 10 mol%) sintered FeCaP pelleted samples with and without micro-channels.

7.3 Contact angle

Sample surface can be said to be hydrophilic when the contact angle is ≤90˚, also hydrophilicity increases when the contact angle decreases. Figure 7.6 are images taken during KSV contact angle measurement. It can be seen for samples before laser micromachining, the contact angle decreases for materials doped with Fe^{2+}/Fe^{3+} ions. Furthermore, contact angle reduced dramatically for the minerals with micro-channels. From

Figure 7.6 it can be noticed that the water spreads linear along the micro-channels which indicating the effect of capillary force.

The significant decrease of contact angle on micro-channels surface points out to the strong capillary force in the microchannel surfaces created by femtosecond laser [169].

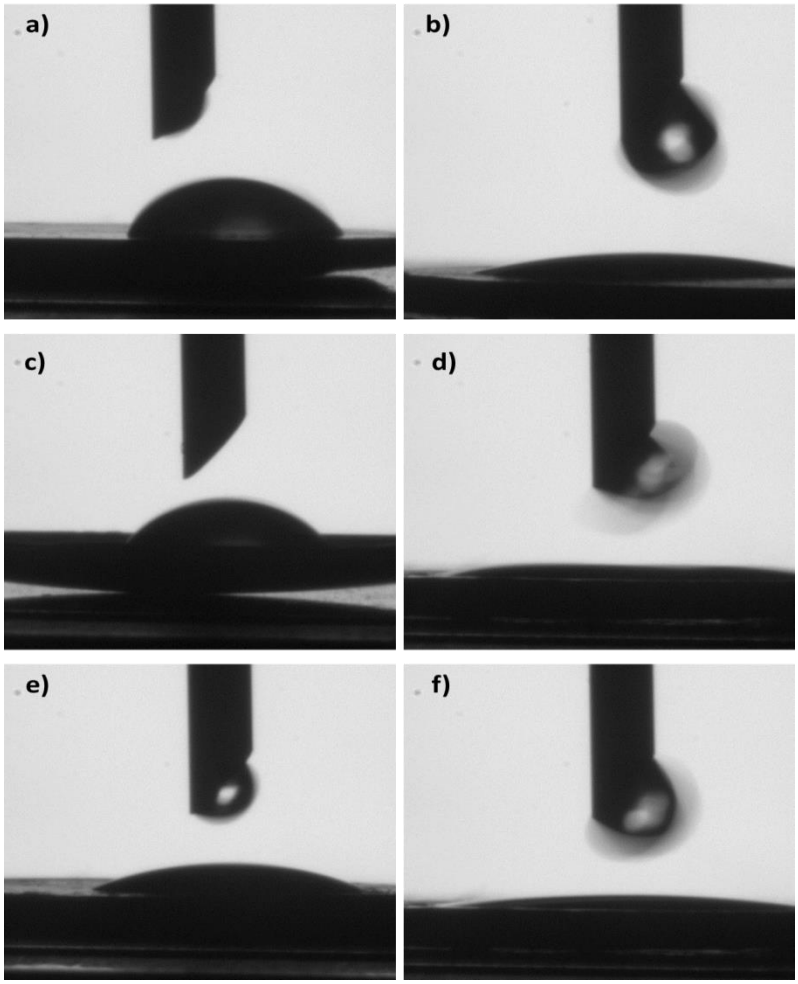

Figure 7.6: KSV contact angle presenting the shape of water drop on the top of sintered FeCaP samples to measure the contact angle of a) and b) 0 mol% before and after micro-channels, respectively. While, c) and d) 5 mol% before and after micro-channels, respectively. For e) and f) 10 mol% samples before and after micro-channels, respectively.

Besides the change on the surface roughness, there are other factors could modify surface wettability properties such as chemistry and microstructure of sample surface and this was observed for materials doped with Fe^{2+}/Fe^{3+} ions [142]. Material structure and chemistry as well charge can play a significant role in cell behaviour and response [311]. Therefore, micro-

channels in the top of FeCaP minerals could increase cell proliferation and thus increase formation of new bone in the scaffolds and it may facilitate oxygen transferring between cells in the scaffolds as well. Table 7.1 provides details of contact angle of sintered FeCaP samples before and after laser irradiation.

Table 7.1: contact angle of sintered FeCaP samples before and after laser irradiation (micro-channels).

Materials	Contact angle	
	Left angle	**Right angle**
0% Fe-βCPP without micro-channels	64.88º	59.63º
0% Fe-βCPP micro-channels	9.41º	9.80º
5% Fe-βCPP without micro-channels	26.41º	33.18º
5% Fe-βCPP micro-channels	9.46º	9.54º
10% Fe-βCPP without micro-channels	30.98º	26.54º
10 % Fe-βCPP micro-channels	9.68º	9.59º

7.4 Degradation test

To study the ions release (Ca and Fe) from the sintered FeCaP, atomic absorption spectrometry AAS, was carried out. Table 7.2 presents the Ca and Fe ions release in the solution after 1, 3 and 7 days to study their effect on the cells behaviour since the proliferation was tested for 1, 3 and 7 days.

The degradation of sintered FeCaP samples were measured for 7 days and 15 days.

Table 7.2: The concentration of Ca and Fe ions release during 1, 3 and 7 days.

Ions		0-FeCaP	5-FeCaP	10-FeCaP	20-FeCaP
Ca	1 day	9.1±1.2	1.4±0.07	0.8±0.07	0.4±0.07
	3 days	9.4±0.7	1.4±0.2	0.9±0.001	0.5±0.14
	7 days	12.4±0.9	1.9±0.14	1.1±0.01	0.5±0.07
Fe	1 day	-	-	-	-
	3 days	-	0.02±0.01	0.01±0.02	0.11±0.02
	7 days	-	0.02±0.02	0.02±0.01	0.11±0.04

Concentration of Ca^{2+} released during the degradation for all FeCaP sample increased in 1, 3 and 7 days particularly for undoped materials. However, no releasing of Fe ion for 5 mol%, 10 mol% and 20 mol% samples was observed for the first day. Whereas, in the 3 and 7 days concentration of Fe^{2+}/Fe^{3+} ions released increased as the concentration of Fe increased.

As no release of Fe ion was observed in the day 1 of the degradation, the increase of cell proliferation in the sintered CaP doped with Fe^{2+}/Fe^{3+} ion could be related to the increase of cell adhesion as was confirmed with contact angle experiment. However, after 3 days the Fe ion started to

release and since the cell viability test was done after 3 days it implies the effect of Fe ion in increase of cell viability and proliferation after 3 days.

Mass reduction of sintered (0 mol%, 5 mol%, 10 mol% and 20 mol%) FeCaP samples during degradation process for 7 and 14 days were investigated, as shown in Figure 7.7. It was found that doping with 5 mol% Fe^{2+}/Fe^{3+} ions increases the degradation rate, however, increase the concentration decreases the degradation rate. Degradation of 5 and 10-FeCaP are slightly higher than degradation of 0-FeCaP. While for 20-FeCaP, the degradation rate decreases in comparison with 0-FeCaP.

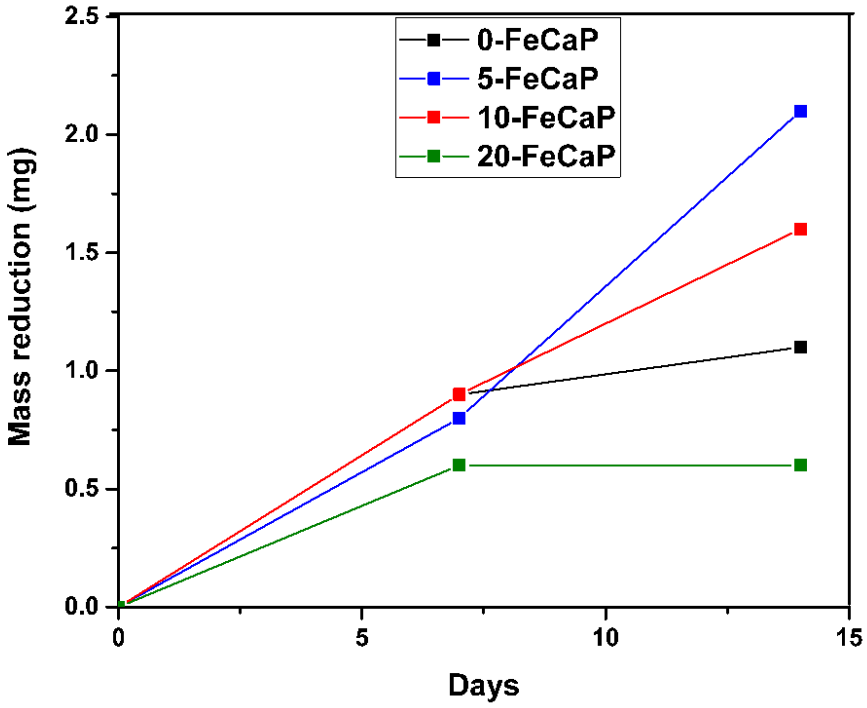

Figure 7.7: Mass reduction of FeCaP samples during degradation for 7 and 14 days.

In general, the degradation ratio was very low in all sintered FeCaP as the initial mass was 200 mg. This result may be related to that the degradation process *in vitro* differ than *in vivo* as enzyme can trigger degradation [121, 268]. Therefore, since 5 and 10-FeCaP did not reduce the degradation ratio of samples, it is suggested that *in vivo* application the degradation in the presence of enzyme could be faster than *in vitro*.

A summary of the main findings, together with future work are provided in the next chapter.

Chapter 8 Conclusions and future work

This chapter summarises the important findings of this project. As well, the future work was discussed.

8.1 Conclusions

- The results of investigations into Fe^{2+}/Fe^{3+} doping of CaP showed that up to 20 mol% Fe concentration the dominant phase was brushite structure. Monetite peaks were observed for both 0 and 20 mol% Fe^{2+}/Fe^{3+} ion, indicating that Fe ion stabilise brushite structure until 10 mol% and after which it became a second phase. On increasing the concentration of Fe ion, an amorphous iron phosphate observed as a secondary phase in 20 mol% whereas at 30 mol% the amorphous phase was a dominant phase.

- Thermal sintering of Fe doped CaP at 1000C for 5 hrs transformed brushite phase into β-CCP for samples containing 0, 5, 10 and 20 mol % Fe. On the other hand, 30 mol% amorphous $FePO_4.3H_2O$ became crystalline $FePO_4$.

- Results obtained from zeta potential measurements of a suspension of these materials was also presented and discussed. Measurements of activation energy for both 5 and 10 mol % FeCaP showed an inverse relationship between activation when the concentration of Fe increases. The crystalline volume fraction of 0 mol %FeCaP was 70.47%, while it increased for 5 and 10 mol % FeCaP minerals to 83.4% and 78.44%, respectively this indicated the stabilization of brushite after doping with Fe^{2+}/Fe^{3+} ion. In accordance with the classical nucleation theory, it was found that an increase in Fe ion content led to an increase in the surface energy of the samples. Therefore, longer sintering times or higher sintering temperatures would be needed to obtain a crystalline structure. It was found that ionic Fe ion played an important role in the sintering process. After comparing FeCaP samples with different molar % Fe content, it was found that the 10 % mol Fe-CaP (10-FeCaP) had improved mechanical and biological properties as mentioned in chapter 4. Non-ambient X-ray diffraction analysis of both 0 and 10-FeCaP showed that that the presence of Fe ions accelerated the sintering

procedure and decreased transition duration for conversion to βCPP in comparison to the undoped mineral.

- Densification of samples doped with Fe ion increased as concentrations increased whereas for undoped materials it decreased.

- Hardness and Young modulus increased when Fe concentration increased up to 10 mol%, however, for 20 and 30 mol% it decreased.

- The mechanism of creating microchannels (ablation) using femtosecond laser is discussed. First an ablation threshold was established by measuring the ablation threshold fluence. UV-vis, XRD, FTIR, bright field optical microscope and SEM were employed for sample characterisation for pre and post laser irradiation samples. Results showed that ablation threshold of Fe doped CaP increased as the concentration increased.

- Ablation using 100 µJ showed Gaussian profile micro-channels for undoped materials whereas for 5 mol% and 10 mol% it showed a shallow micro-channels. No induction of channels for 20 and 30 mol% were observed rather cracks and melting appeared. Channel depth for 0, 5 and 10 mol% increased at laser intensity of 200 µJ. for 20 mol% the channels observed, however, partial melting appeared. Whereas for 30 mol% the same as 100 µJ observed. Micro-channels on the surface of sintered FeCaP by ablation mechanism using femtosecond laser showed an increase in cells adhesion in the micro-channels. However, the cell spread into 20 mol% samples since cracks existed. In both doped with Fe ion and creation of micro-channels increased hydrophilic property of FeCaP samples.

- Optical absorption properties improved by doping with Fe ion especially at 800 nm and 1045 nm that is the wavelength of femtosecond pulsed laser for ablation and sintering mechanisms, respectively.

- Cytotoxicity assay of sintered FeCaP indicated non-toxic materials. Cell proliferation increased when the doping concentration of Fe ion increased particularly for 5 mol% and 10 mol%.
- Degradation ratio of sintered samples with concentration Fe^{2+}/Fe^{3+} ions up to 10 mol% were higher than sintered un-doped sample.

- Concentration of Fe ion at 10 mol% of β-CPP seems promising candidate for both mechanical and biological properties together with femtosecond pulsed laser for micromachining.

8.2 Future work

In this thesis, thermal annealing was employed for simulating and comparing the sintering condition, when using a femtosecond pulsed laser, operating at a wavelength of 1045 nm, repetition rate1GHz and pulse duration of 130-190 fs to form high dense β-CPP samples.

Although, several generic properties of Fe^{2+}/Fe^{3+}-doped calcium phosphate were characterised in details, there is still need for future work. During the project, there was only limited time to investigate a large number of pulsed laser sintered minerals for detailed phase transformation characterisation. In this respect, the relationship between the energies of pulsed laser used for phase transformation requires further studies together with the sintering properties. In this aspect, the study plan may also include the effect of iron oxide doping in CaP mineral under different irradiation conditions.

In a biomaterials characterisation for regenerative tissue engineering, the cell proliferation, attachment and differentiation form a comprehensive body of work. The detailed work requires time and it is laborious. For this reason, a systematic study on optimally laser sintered materials for cell attachment, proliferation, differentiation and stem cell expression may be required for future studies.

In terms of materials characterisation, there was limited time for characterising the changes in the oxidations states of Fe^{2+}/Fe^{3+}-ions in CaP

during cell studies, which underpin oxygen transport. For laser-assisted materials fabrication, an electrochemical based oxidation reaction analysis may be useful for osteogenesis. In this regard, more materials characterisation after electrochemical oxidation may employed using X-ray diffraction, X-ray photoelectron spectroscopy (XPS), and mechanical properties, which may provide supplemental information, for tissue scaffold engineering.

One of the main challenges to developing bone tissue materials is the lack of vascularisation that leads to cell death. Fe ion is known for its potential role in oxygen regulation in human body and from the relatively successful cell proliferation results that was obtained in the samples. It is recommended that further vascularisation assays test be conducted, for example endothelial cells assay to examine the effect of Fe ion on the proliferation of endothelial cells as these cells are from the inner surface of blood vessels thus can form vascularisation networks.

From results of this research work, it appears that doping calcium phosphate with 10 mol % Fe and sintering to obtain 10 mol% Fe β-CPP seems a promising candidate with respects to bone tissue materials as both mechanical (hardness and Young modulus) and biological performance (cell proliferation) showed comparatively good results. It is, therefore, recommended that this composition be tried in bone scaffolds. Also, it can be applied as a coating material for titanium substrate as titanium has poor osteointegration property.

Appendices

Appendix.1 Characterisation of micro-channels cross section

Chemical compositions of cross section of FeCaP samples after laser irradiation of 200 µJ for creation micro-channels were examined using SEM-EDX, Figure 0.1-0.3, (see chapter 6).

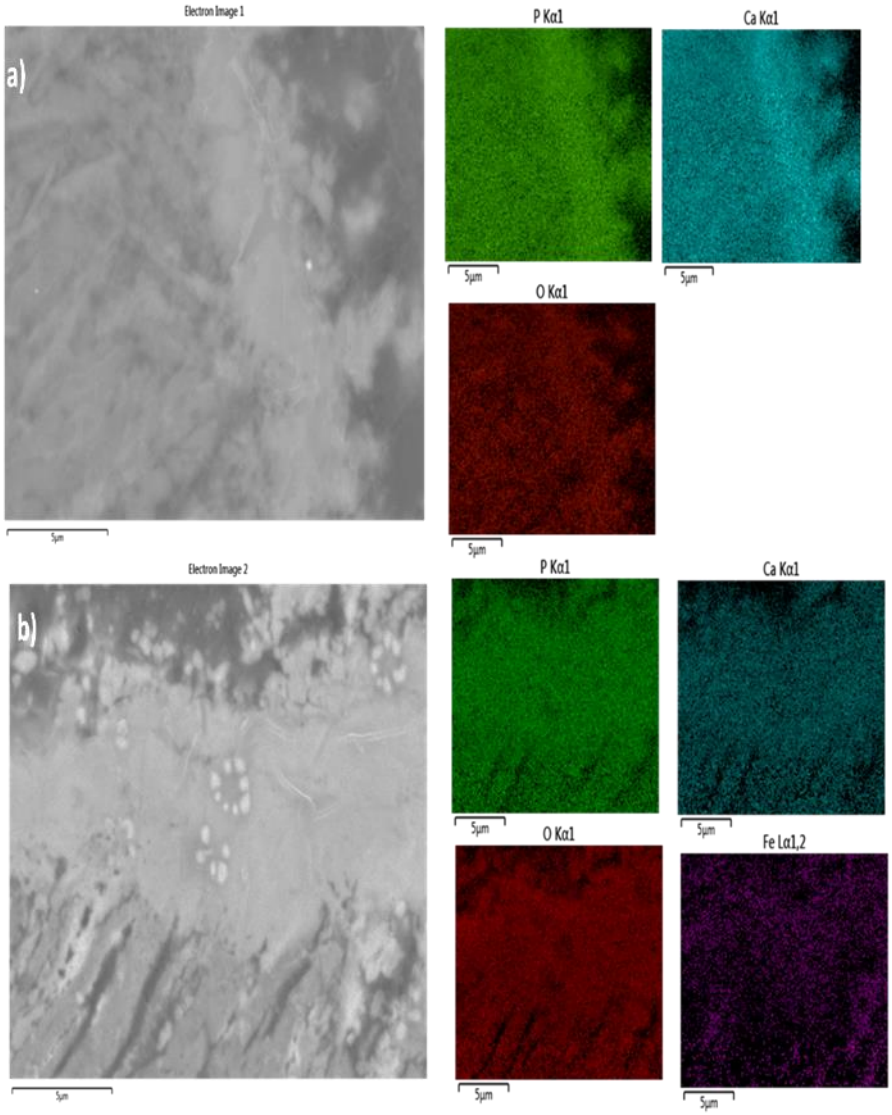

Figure 0.1: Chemical compositions mapping using EDX of a) 0-FeCaP and b) 5-FeCaP (brushite form) cross section after laser irradiation at 200 µJ.

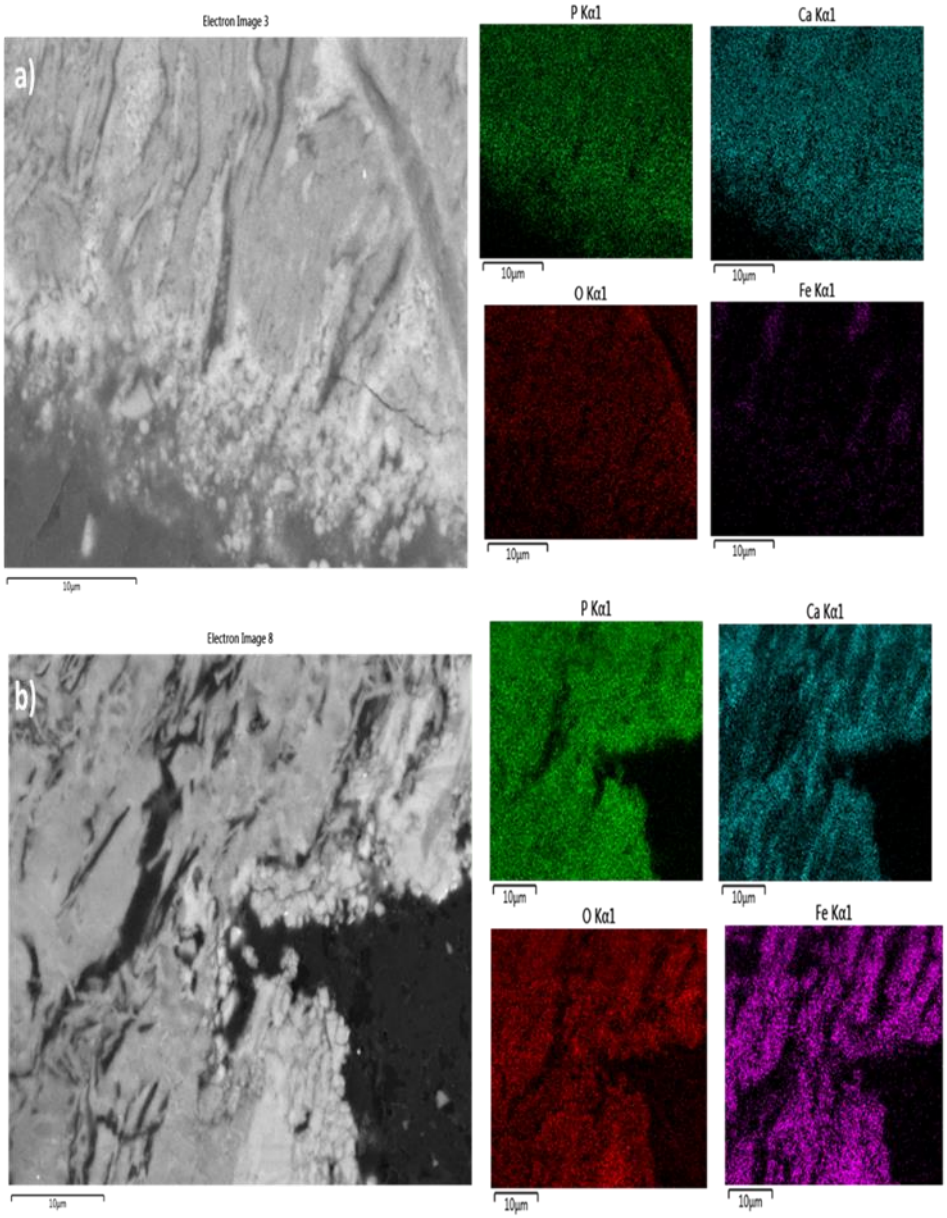

Figure 0.2: Chemical compositions mapping using EDX of a) 10-FeCaP and b) 20-FeCaP (brushite form) cross section after laser irradiation at 200 µJ.

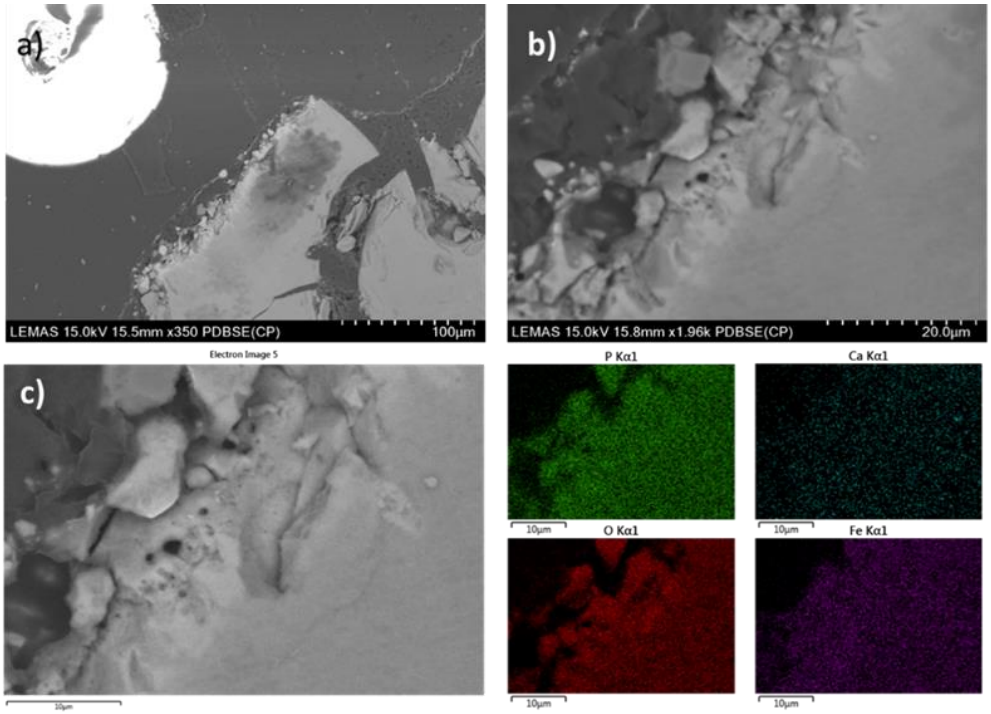

Figure 0.3: SEM cross section of FeCaP after laser irradiation of 200 µJ at different magnifications a),b) and c) chemical composition mapping using EDX of 30 mol%.

Appendix.2 Experimental protocols

Cell adhesion protocol for confocal microscope

- After seeding the sample with the specific cell density, it was incubated for 48 days.

- Samples were wash with PBS and incubated with 1 mL of 10% formalin for 20 min at room temperature.

- Formalin was removed and samples were incubated with PBS until the day of the staining.

0.2.1.1 Alexa fluor 488 dye.

- First, Alexa fluor was diluted in PBS with concentration of 1:20 ml.
- 300 ml of the dilution was added to the samples and incubated at room temperature for 2 hrs in the dark.
- After removing the dilution solution, samples were washed with PBS 3 times.

0.2.1.2 DAPi (4', 6-diamidino-2-phenylindole) dye

- Dilute DAPi in pure water to have 0.1 µg/ml of DAPi.

- 1 ml of the dilution were added to the samples and were incubated for 15 min.
- The samples were washed 3 times with PBS and were incubated with PBS until the day of testing.

Proliferation experiment using PicoGreen dsDNA assay

This protocol was used for the quantitative of cell proliferation:

- After seeding the sample with $5x10^5$ cell density, they were incubated for 1 day, 3 days and 7 days.
- Picogreen dsDNA kit was used after washing the samples with PBS.
- First, 1x TE buffer was prepared by dilution 1ml of 20x TE buffer in 19 ml of nuclease free water.
- Then dsDNA standard (100µg/ml) was prepared by dilution 20 µl in 980 µl TE buffer to prepare concentration of 1000 ng/ml, 500 ng/ml, 100ng/ml, 10 ng/ml and the blank (TE buffer only), table 0.1.
- 10 µl concentrated of PicoGreen was diluted in 1990 µl TE buffer to prepare PicoGreen solution.
- Then 1µl of DNA samples were added to 99 µl of TE in well plate.
- For DNA quantitation, 100 µl of PicoGreen solution was added to sample well plate in triplicate and incubated at room temperature for 5 min in the dark.
- They were tested by placing them in plate reader at excitation wavelength 480 nm and emission of 520 nm.

Table 0.1: The concentration of DNA to prepare DNA standard.

TE µl	DNA (2µg/ml) µl	Final DNA concentration (ng/ml)
0	100	1000
50	50	500
90	10	100
99	1	10
100	0	blank

References

1. Ali, M.S., *The Holy Qur'an: Arabic Text and English Translation*. 2004: Islam International.
2. Laurencin, C.T. and L.S. Nair, *Nanotechnology and regenerative engineering: the scaffold*. 2014: CRC Press.
3. Crichton, R., *Iron metabolism: from molecular mechanisms to clinical consequences*. 2016: John Wiley & Sons.
4. Anastasiou, A., et al., *Sintering of calcium phosphates with a femtosecond pulsed laser for hard tissue engineering.* Materials & Design, 2016. **101**: p. 346-354.
5. Ram, R.R., *HIERARCHY OF BONE STRUCTURE REPORT.* 2006.
6. Dimitriou, R., et al., *Bone regeneration: current concepts and future directions.* 2011. **9**(1): p. 66.
7. Bates, P., A. Yeo, and M. Ramachandran, *Bone injury, healing and grafting*, in *Basic orthopaedic sciences*. 2018, CRC Press. p. 205-222.
8. Giannoudis, P.V., H. Dinopoulos, and E. Tsiridis, *Bone substitutes: an update.* Injury, 2005. **36**(3): p. S20-S27.
9. Marsh, D., *Concepts of fracture union, delayed union, and nonunion.* Clinical Orthopaedics and Related Research®, 1998. **355**: p. S22-S30.
10. Andrzejowski, P., P.V.J.J.o.O. Giannoudis, and Traumatology, *The 'diamond concept'for long bone non-union management.* 2019. **20**(1): p. 21.
11. Chiarello, E., et al., *Autograft, allograft and bone substitutes in reconstructive orthopedic surgery.* Aging clinical and experimental research, 2013. **25**(1): p. 101-103.
12. Zimmermann, G. and A. Moghaddam, *Allograft bone matrix versus synthetic bone graft substitutes.* Injury, 2011. **42**: p. S16-S21.
13. Ikada, Y.J.J.o.t.R.S.I., *Challenges in tissue engineering.* 2006. **3**(10): p. 589-601.
14. Gupta, C., *Role of iron (Fe) in body.* IOSR Journal of Applied Chemistry (IOSR-JAC), 2014. **7**(11): p. 38-46.
15. Anastasiou, A., et al., *β-pyrophosphate: A potential biomaterial for dental applications.* Materials Science and Engineering: C, 2017. **75**: p. 885-894.
16. Nandi, S., et al., *Orthopaedic applications of bone graft & graft substitutes: a review.* 2010. **132**(1): p. 15-30.
17. Bauer, T.W., G.F.J.C.O. Muschler, and R. Research®, *Bone graft materials: an overview of the basic science.* 2000. **371**: p. 10-27.
18. Florencio-Silva, R., et al., *Biology of bone tissue: structure, function, and factors that influence bone cells.* BioMed research international, 2015. **2015**.
19. Kanis, J.A., et al., *The diagnosis of osteoporosis.* Journal of bone and mineral research, 1994. **9**(8): p. 1137-1141.
20. Cummings, S.R., et al., *Appendicular bone density and age predict hip fracture in women.* Jama, 1990. **263**(5): p. 665-668.
21. Lauritzen, J.B., et al., *Changing incidence and residual lifetime risk of common osteoporosis-related fractures.* Osteoporosis international, 1993. **3**(3): p. 127-132.
22. Foundation, I.O. *Osteoporosis & Musculoskeletal Disorders - Osteoporosis - What is Osteoporosis? -Epidemiology*. [cited 2019; Available from: https://www.iofbonehealth.org/epidemiology.
23. Finkemeier, C.G., *Bone-grafting and bone-graft substitutes.* JBJS, 2002. **84**(3): p. 454-464.
24. Fillingham, Y. and J. Jacobs, *Bone grafts and their substitutes.* The bone & joint journal, 2016. **98**(1_Supple_A): p. 6-9.

25. Khan, S.N., et al., *The biology of bone grafting.* JAAOS-Journal of the American Academy of Orthopaedic Surgeons, 2005. **13**(1): p. 77-86.
26. Giannoudis, P.V., H. Dinopoulos, and E.J.I. Tsiridis, *Bone substitutes: an update.* 2005. **36**(3): p. S20-S27.
27. Damien, C.J. and J.R. Parsons, *Bone graft and bone graft substitutes: a review of current technology and applications.* Journal of Applied Biomaterials, 1991. **2**(3): p. 187-208.
28. Keating, J. and M. McQueen, *Substitutes for autologous bone graft in orthopaedic trauma.* The Journal of bone and joint surgery. British volume, 2001. **83**(1): p. 3-8.
29. Nazirkar, G., et al., *Effortless effort in bone regeneration: a review.* 2014. **6**(3): p. 120.
30. García-Gareta, E., M.J. Coathup, and G.W.J.B. Blunn, *Osteoinduction of bone grafting materials for bone repair and regeneration.* 2015. **81**: p. 112-121.
31. Sarkar, S.K. and B.T.J.T.K.j.o.i.m. Lee, *Hard tissue regeneration using bone substitutes: an update on innovations in materials.* 2015. **30**(3): p. 279.
32. Basha, R.Y., S.K. TS, and M. Doble, *Design of biocomposite materials for bone tissue regeneration.* Materials Science and Engineering: C, 2015. **57**: p. 452-463.
33. Alvarez, K. and H. Nakajima, *Metallic scaffolds for bone regeneration.* Materials, 2009. **2**(3): p. 790-832.
34. Alvarez, K. and H.J.M. Nakajima, *Metallic scaffolds for bone regeneration.* 2009. **2**(3): p. 790-832.
35. Zdeblick, T.A. and F.M.J.S. Phillips, *Interbody cage devices.* 2003. **28**(15S): p. S2-S7.
36. Prasad, K., et al., *Metallic biomaterials: Current challenges and opportunities.* 2017. **10**(8): p. 884.
37. Tuan, R.S., A.F. Chen, and B.A. Klatt, *Cartilage regeneration.* The Journal of the American Academy of Orthopaedic Surgeons, 2013. **21**(5): p. 303.
38. Gentile, P., et al., *An overview of poly (lactic-co-glycolic) acid (PLGA)-based biomaterials for bone tissue engineering.* International journal of molecular sciences, 2014. **15**(3): p. 3640-3659.
39. Avgoustakis, K., *Polylactic-co-glycolic acid (PLGA).* Encyclopedia of biomaterials and biomedical engineering. Taylor & Francis, 2005: p. 1-11.
40. Pan, Z. and J. Ding, *Poly (lactide-co-glycolide) porous scaffolds for tissue engineering and regenerative medicine.* Interface focus, 2012. **2**(3): p. 366-377.
41. Rezwan, K., et al., *Biodegradable and bioactive porous polymer/inorganic composite scaffolds for bone tissue engineering.* 2006. **27**(18): p. 3413-3431.
42. Layer, T.M.J.J.C.D., *Development of a fluoridated, daily-use toothpaste containing NovaMin technology for the treatment of dentin hypersensitivity.* 2011. **22**(3): p. 59-61.
43. Vallittu, P.K.J.J.o.M.S., *Bioactive glass-containing cranial implants: an overview.* 2017. **52**(15): p. 8772-8784.
44. Norström, A., et al., *Treatment of E-glass fibres with acid, base and silanes.* 2001. **194**(1-3): p. 143-157.
45. Xynos, I., et al., *Bioglass® 45S5 stimulates osteoblast turnover and enhances bone formation in vitro: implications and applications for bone tissue engineering.* Calcified tissue international, 2000. **67**(4): p. 321-329.
46. Fu, Q., et al., *Bioactive glass scaffolds for bone tissue engineering: state of the art and future perspectives.* 2011. **31**(7): p. 1245-1256.
47. Bonfield, W., M. Wang, and K.J.A.M. Tanner, *Interfaces in analogue biomaterials.* 1998. **46**(7): p. 2509-2518.

48. Swetha, M., et al., *Biocomposites containing natural polymers and hydroxyapatite for bone tissue engineering.* International journal of biological macromolecules, 2010. **47**(1): p. 1-4.
49. Huang, J., et al., *Development of nano-sized hydroxyapatite reinforced composites for tissue engineering scaffolds.* 2007. **18**(11): p. 2151-2157.
50. Niu, C.-C., et al., *Trapezoidal titanium cage in anterior cervical interbody fusion: a clinical experience.* 2005. **28**(4): p. 212-221.
51. Bohner, M.J.I., *Calcium orthophosphates in medicine: from ceramics to calcium phosphate cements.* 2000. **31**: p. D37-D47.
52. Roberts, T.T. and A.J. Rosenbaum, *Bone grafts, bone substitutes and orthobiologics: the bridge between basic science and clinical advancements in fracture healing.* Organogenesis, 2012. **8**(4): p. 114-124.
53. Engstrand, J., C. Persson, and H.J.J.o.t.m.b.o.b.m. Engqvist, *The effect of composition on mechanical properties of brushite cements.* 2014. **29**: p. 81-90.
54. Kay, M.I., R. Young, and A. Posner, *Crystal structure of hydroxyapatite.* 1964.
55. Young, R., *Implications of atomic substitutions and other structural details in apatites.* Journal of dental research, 1974. **53**(2): p. 193-203.
56. Ma, M.-G., Y.-J. Zhu, and J. Chang, *Monetite formed in mixed solvents of water and ethylene glycol and its transformation to hydroxyapatite.* The Journal of Physical Chemistry B, 2006. **110**(29): p. 14226-14230.
57. Sakae, T. and H. Nakada, *Historical review of biological apatite crystallography.* Journal of Hard Tissue Biology, 2015. **24**(2): p. 111-122.
58. Dorozhkin, S., *History of Calcium Phosphates in Regenerative Medicine*, in *Advances in Calcium Phosphate Biomaterials*. 2014, Springer. p. 435-483.
59. Dorozhkin, S.V., *Self-setting calcium orthophosphate formulations: cements, concretes, pastes and putties.* International Journal of Materials and Chemistry, 2011. **1**(1): p. 1-48.
60. Mathew, M., S.J.J.o.r.o.t.N.I.o.S. Takagi, and Technology, *Structures of biological minerals in dental research.* 2001. **106**(6): p. 1035.
61. Ajaxon, I., et al., *Mechanical properties of brushite calcium phosphate cements.* 2017. **3**: p. 285-300.
62. Prakasam, M., et al., *Fabrication, properties and applications of dense hydroxyapatite: a review.* 2015. **6**(4): p. 1099-1140.
63. Kamitakahara, M., et al., *Synthesis of octacalcium phosphate intercalated with dicarboxylate ions from calcium carbonate and phosphoric acid.* 2008. **116**(1351): p. 481-485.
64. Mirhadi, B., et al., *Synthesis of nano-sized β-tricalcium phosphate via wet precipitation.* 2011. **5**(4): p. 193-198.
65. Charrière, E., et al., *Mechanical characterization of brushite and hydroxyapatite cements.* Biomaterials, 2001. **22**(21): p. 2937-2945.
66. Boroujeni, N.M., *Monetite cement composites for orthopedic and dental applications*. 2012, University of Toledo.
67. Calafiori, A.R., et al., *Low temperature method for the production of calcium phosphate fillers.* Biomedical engineering online, 2004. **3**(1): p. 8.
68. Wang, C., X. Zhou, and M. Wang, *Influence of sintering temperatures on hardness and Young's modulus of tricalcium phosphate bioceramic by nanoindentation technique.* Materials Characterization, 2004. **52**(4-5): p. 301-307.
69. Kumar, A.R. and S.J.M.R.B. Kalainathan, *Microhardness studies on calcium hydrogen phosphate (brushite) crystals.* 2010. **45**(11): p. 1664-1667.

70. Tas, A.C.J.J.o.t.A.C.S., *Transformation of Brushite (CaHPO4· 2H2O) to Whitlockite (Ca9Mg (HPO4)(PO4) 6) or other CaPs in physiologically relevant solutions.* 2016. **99**(4): p. 1200-1206.
71. Jones, D. and J.J.J.o.t.C.S. Smith, *268. The structure of brushite, CaHPO 4, 2H 2 O.* 1962: p. 1414-1420.
72. Dosen, A. and R.F. Giese, *Thermal decomposition of brushite, CaHPO4· 2H2O to monetite CaHPO4 and the formation of an amorphous phase.* American Mineralogist, 2011. **96**(2-3): p. 368-373.
73. Toshima, T., et al., *Morphology control of brushite prepared by aqueous solution synthesis.* 2014. **2**(1): p. 52-56.
74. Engstrand, J., C. Persson, and H. Engqvist, *The effect of composition on mechanical properties of brushite cements.* Journal of the mechanical behavior of biomedical materials, 2014. **29**: p. 81-90.
75. Laskus, A. and J. Kolmas, *Ionic substitutions in non-apatitic calcium phosphates.* International journal of molecular sciences, 2017. **18**(12): p. 2542.
76. Casciani, F. and R.J.J.o.S.S.C. Condrate Sr, *The Raman spectrum of monetite, CaHPO4.* 1980. **34**(3): p. 385-388.
77. Webb, N.J.A.C., *The crystal structure of β-Ca2P2O.* 1966. **21**(6): p. 942-948.
78. Boudin, S., et al., *Redetermination of the β-Ca2P2O7 structure.* 1993. **49**(12): p. 2062-2064.
79. Lee, J.H., et al., *The first clinical trial of beta-calcium pyrophosphate as a novel bone graft extender in instrumented posterolateral lumbar fusion.* 2011. **3**(3): p. 238-244.
80. Lee, J.H., et al. *Porous beta-calcium pyrophosphate as a bone graft substitute in a canine bone defect model*. in *Key Engineering Materials*. 2003. Trans Tech Publ.
81. Dosen, A. and R.F.J.A.M. Giese, *Thermal decomposition of brushite, CaHPO4· 2H2O to monetite CaHPO4 and the formation of an amorphous phase.* 2011. **96**(2-3): p. 368-373.
82. Ferna, E., et al., *Calcium phosphate bone cements for clinical applications. Part I: solution chemistry.* 1999. **10**(3): p. 169-176.
83. CHOW, L.C., *Next generation calcium phosphate-based biomaterials.* Dental materials journal, 2009. **28**(1): p. 1-10.
84. Uchida, A., et al., *The use of calcium hydroxyapatite ceramic in bone tumour surgery.* 1990. **72**(2): p. 298-302.
85. Matsumine, A., et al., *Calcium hydroxyapatite ceramic implants in bone tumour surgery: a long-term follow-up study.* 2004. **86**(5): p. 719-725.
86. Wang, B., et al., *A histomorphometric study on osteoconduction and osseointegration of titanium alloy with and without plasma-sprayed hydroxyapatite coating using back-scattered electron images.* 1993. **4**(4): p. 394-403.
87. Bose, S., et al., *Understanding of dopant-induced osteogenesis and angiogenesis in calcium phosphate ceramics.* Trends in biotechnology, 2013. **31**(10): p. 594-605.
88. Ma, J., S. Tan, and S. Zhang, *Biomimetic Ion-Substituted Calcium Phosphates*, in *Developments and Applications of Calcium Phosphate Bone Cements*. 2018, Springer. p. 333-353.
89. Yang, L., et al., *The effects of inorganic additives to calcium phosphate on in vitro behavior of osteoblasts and osteoclasts.* Biomaterials, 2010. **31**(11): p. 2976-2989.

90. Pina1a, S., et al., *Biological responses of brushite-forming Zn-and ZnSr-substituted β-tricalcium phosphate bone cements.* European Cells and Materials, 2010. **20**: p. 162-177.
91. Kundu, B., et al., *Development of new localized drug delivery system based on ceftriaxone-sulbactam composite drug impregnated porous hydroxyapatite: a systematic approach for in vitro and in vivo animal trial.* 2010. **27**(8): p. 1659-1676.
92. Canalis, E., et al., *The divalent strontium salt S12911 enhances bone cell replication and bone formation in vitro.* 1996. **18**(6): p. 517-523.
93. Takahashi, N., et al., *S 12911‐2 inhibits osteoclastic bone resorption in vitro.* 2003. **18**(6): p. 1082-1087.
94. Panzavolta, S., et al., *Setting properties and in vitro bioactivity of strontium‐enriched gelatin‐calcium phosphate bone cements.* 2008. **84**(4): p. 965-972.
95. Amini, A.R., C.T. Laurencin, and S.P.J.C.R.i.B.E. Nukavarapu, *Bone tissue engineering: recent advances and challenges.* 2012. **40**(5).
96. Tamimi, F., Z. Sheikh, and J.J.A.b. Barralet, *Dicalcium phosphate cements: Brushite and monetite.* 2012. **8**(2): p. 474-487.
97. Pittman, R.N. *Regulation of tissue oxygenation*. in *Colloquium Series on Integrated Systems Physiology: From Molecule to Function*. 2011. Morgan & Claypool Life Sciences.
98. Vahabzadeh, S. and S.J.A.o.b.e. Bose, *Effects of iron on physical and mechanical properties, and osteoblast cell interaction in β-tricalcium phosphate.* 2017. **45**(3): p. 819-828.
99. Katsumata, S.-i., et al., *Dietary iron deficiency decreases serum osteocalcin concentration and bone mineral density in rats.* 2006. **70**(10): p. 2547-2550.
100. Medeiros, D.M., et al., *Bone morphology, strength and density are compromised in iron-deficient rats and exacerbated by calcium restriction.* 2002. **132**(10): p. 3135-3141.
101. Li, Y., C.T. Nam, and C.P. Ooi. *Iron (III) and manganese (II) substituted hydroxyapatite nanoparticles: characterization and cytotoxicity analysis*. in *Journal of Physics: Conference Series*. 2009. IOP Publishing.
102. Manchón, A., et al., *A new iron calcium phosphate material to improve the osteoconductive properties of a biodegradable ceramic: a study in rabbit calvaria.* Biomedical Materials, 2015. **10**(5): p. 055012.
103. Panseri, S., et al., *Intrinsically superparamagnetic Fe-hydroxyapatite nanoparticles positively influence osteoblast-like cell behaviour.* Journal of nanobiotechnology, 2012. **10**(1): p. 32.
104. Iafisco, M., et al., *Magnetic bioactive and biodegradable hollow Fe-doped hydroxyapatite coated poly (l-lactic) acid micro-nanospheres.* Chemistry of Materials, 2013. **25**(13): p. 2610-2617.
105. Li, Y., et al., *Synthesis and cytocompatibility of manganese (II) and iron (III) substituted hydroxyapatite nanoparticles.* Journal of Materials Science, 2012. **47**(2): p. 754-763.
106. Ereiba, K.M.T., et al., *In vitro study of iron doped hydroxyapatite.* 2013. **269**(1683): p. 1-28.
107. Ishak, S.A., et al. *Angiogenesis in tissue engineering: from concept to the vascularization of scaffold construct*. in *IOP Conference Series: Materials Science and Engineering*. 2014. IOP Publishing.
108. Bose, S., M. Roy, and A. Bandyopadhyay, *Recent advances in bone tissue engineering scaffolds.* Trends in biotechnology, 2012. **30**(10): p. 546-554.

109. Zhang, J., et al., *Good hydration and cell-biological performances of superparamagnetic calcium phosphate cement with concentration-dependent osteogenesis and angiogenesis induced by ferric iron.* Journal of Materials Chemistry B, 2015. **3**(45): p. 8782-8795.
110. Landel, R.F. and L.E. Nielsen, *Mechanical properties of polymers and composites*. 1993: CRC press.
111. Pelleg, J., *Mechanical properties of materials*. Vol. 190. 2012: Springer Science & Business Media.
112. Liu, X., F. Yuan, and Y. Wei, *Grain size effect on the hardness of nanocrystal measured by the nanosize indenter.* Applied Surface Science, 2013. **279**: p. 159-166.
113. Sebastiani, M., et al., *Measurement of fracture toughness by nanoindentation methods: Recent advances and future challenges.* Current Opinion in Solid State and Materials Science, 2015. **19**(6): p. 324-333.
114. Michael, F.M., et al., *Effect of nanofillers on the physico-mechanical properties of load bearing bone implants.* 2016. **67**: p. 792-806.
115. Turner, C.H., et al., *The elastic properties of trabecular and cortical bone tissues are similar: results from two microscopic measurement techniques.* Journal of biomechanics, 1999. **32**(4): p. 437-441.
116. Rho, J.-Y., T.Y. Tsui, and G.M. Pharr, *Elastic properties of human cortical and trabecular lamellar bone measured by nanoindentation.* Biomaterials, 1997. **18**(20): p. 1325-1330.
117. Yan, J., et al., *Fracture toughness of manatee rib and bovine femur using a chevron-notched beam test.* Journal of biomechanics, 2006. **39**(6): p. 1066-1074.
118. Khanal, S.P., et al., *Improvement of the fracture toughness of hydroxyapatite (HAp) by incorporation of carboxyl functionalized single walled carbon nanotubes (CfSWCNTs) and nylon.* Materials Science and Engineering: C, 2016. **60**: p. 204-210.
119. Shuai, C., et al., *Correlation between properties and microstructure of laser sintered porous β-tricalcium phosphate bone scaffolds.* Science and technology of advanced materials, 2013. **14**(5): p. 055002.
120. Moussa, H., et al., *High strength brushite bioceramics obtained by selective regulation of crystal growth with chiral biomolecules.* 2020.
121. Grover, L.M., et al., *The effect of amorphous pyrophosphate on calcium phosphate cement resorption and bone generation.* 2013. **34**(28): p. 6631-6637.
122. Naga, S.M., et al., *Biological Performance of Calcium Pyrophosphate ‐coated Porous Alumina Scaffolds.* 2014. **11**(1): p. 1-11.
123. Lin, F.-H., et al., *Mechanical properties and histological evaluation of sintered β-Ca2P2O7 with Na4P2O7· 10H2O addition.* 1995. **16**(10): p. 793-802.
124. Zhang, X., *Preparation and characterization of calcium phosphate ceramics and composites as bone substitutes*. 2007, UC San Diego.
125. Ganachari, S., et al., *Rapid synthesis, characterization, and studies of hydroxyapatite nanoparticles.* 2016. **1**.
126. Zhou, H. and J.J.A.b. Lee, *Nanoscale hydroxyapatite particles for bone tissue engineering.* 2011. **7**(7): p. 2769-2781.
127. Vallet-Regi, M. and J.M.J.P.i.s.s.c. González-Calbet, *Calcium phosphates as substitution of bone tissues.* 2004. **32**(1-2): p. 1-31.
128. Liu, Y., et al., *Additive manufacturing techniques and their biomedical applications.* 2017. **5**(4): p. 286-298.
129. Kang, S.-J.L., *Sintering: densification, grain growth and microstructure*. 2004: Elsevier.

130. De Jonghe, L.C. and M.N. Rahaman, *4.1 sintering of ceramics.* Handbook of advanced ceramics: materials, applications, processing and properties, 2003. **2**: p. 187.
131. OLAJIDE, O.I., *Akanu Ibiam Federal Polytechnic, Unwana.*
132. Fang, Z.Z., H. Wang, and V. Kumar, *Coarsening, densification, and grain growth during sintering of nano-sized powders—a perspective.* International Journal of Refractory Metals and Hard Materials, 2017. **62**: p. 110-117.
133. Kang, S.-J.L.J.S.d., grain growth and e.A.E.B.-H. microstructure, UK, *Initial stage sintering.* 2005: p. 39.
134. Povarnitsyn, M.E., et al., *Material decomposition mechanisms in femtosecond laser interactions with metals.* Physical Review B, 2007. **75**(23): p. 235414.
135. Kingery, W., et al., *Introduction to ceramics, 1976.* p. 135-144.
136. Hung, I., et al., *The properties of sintered calcium phosphate with [Ca]/[P]= 1.50.* 2012. **13**(10): p. 13569-13586.
137. Sugioka, K., Y.J.L.S. Cheng, and Applications, *Ultrafast lasers—reliable tools for advanced materials processing.* 2014. **3**(4): p. e149.
138. Vorobyev, A.Y. and C. Guo, *Direct femtosecond laser surface nano/microstructuring and its applications.* Laser & Photonics Reviews, 2013. **7**(3): p. 385-407.
139. Peltola, S.M., et al., *A review of rapid prototyping techniques for tissue engineering purposes.* 2008. **40**(4): p. 268-280.
140. Savalani, M., L. Hao, and R.A.J.P.o.t.I.o.M.E. Harris, Part B: Journal of Engineering Manufacture, *Evaluation of CO2 and Nd: YAG lasers for the selective laser sintering of HAPEX®.* 2006. **220**(2): p. 171-182.
141. Parker, S.J.I.J.L.D., *Laser: Tissue interaction and its application in clinical dentistry.* 2011. **1**: p. 1-8.
142. Brown, M.S. and C.B. Arnold, *Fundamentals of laser-material interaction and application to multiscale surface modification*, in *Laser precision microfabrication*. 2010, Springer. p. 91-120.
143. Niemz, M.H., *Laser-tissue interactions*. 2007: Springer.
144. Girard, B., et al., *Effects of femtosecond laser irradiation on osseous tissues.* 2007. **39**(3): p. 273-285.
145. Jha, A., et al., *Microstructural characterization of laser sintered synthetic calcium phosphate-natural dentine interface for the restoration of enamel surface.* AIMS Materials Science, 2014. **1**(3): p. 148-158.
146. Le Harzic, R., et al., *Comparison of heat-affected zones due to nanosecond and femtosecond laser pulses using transmission electronic microscopy.* Applied Physics Letters, 2002. **80**(21): p. 3886-3888.
147. Kautek, W. and J. Krüger. *Femtosecond pulse laser ablation of metallic, semiconducting, ceramic, and biological materials*. in *Laser materials processing: industrial and microelectronics applications*. 1994. International Society for Optics and Photonics.
148. Paital, S.R. and N.B. Dahotre, *Calcium phosphate coatings for bio-implant applications: Materials, performance factors, and methodologies.* Materials Science and Engineering: R: Reports, 2009. **66**(1-3): p. 1-70.
149. Symietz, C., et al., *Femtosecond laser induced fixation of calcium alkali phosphate ceramics on titanium alloy bone implant material.* 2010. **6**(8): p. 3318-3324.
150. Paital, S.R. and N.B. Dahotre, *Laser surface treatment for porous and textured Ca–P bio-ceramic coating on Ti–6Al–4V.* Biomedical Materials, 2007. **2**(4): p. 274.

151. Kurella, A. and N.B. Dahotre, *Laser induced hierarchical calcium phosphate structures.* Acta biomaterialia, 2006. **2**(6): p. 677-683.
152. Paital, S.R., et al., *Fabrication and evaluation of a pulse laser-induced Ca–P coating on a Ti alloy for bioapplication.* Biomedical Materials, 2008. **4**(1): p. 015009.
153. Liu, X., D. Du, and G.J.I.j.o.q.e. Mourou, *Laser ablation and micromachining with ultrashort laser pulses.* 1997. **33**(10): p. 1706-1716.
154. Krüger, J. and W.J.L.P.-L.-. Kautek, *The femtosecond pulse laser: a new tool for micromachining.* 1999. **9**: p. 30-40.
155. Miller, P.R., et al., *Laser micromachining for biomedical applications.* 2009. **61**(9): p. 35-40.
156. Gamaly, E.G., et al., *Ablation of solids by femtosecond lasers: Ablation mechanism and ablation thresholds for metals and dielectrics.* Physics of plasmas, 2002. **9**(3): p. 949-957.
157. Shirk, M. and P. Molian, *. A REVIEW OF ULTRASHORT PULSED LASER ABLATION OF MATERIALS.* UIVQ, 1998: p. 14.
158. Lucas, L. and J.J.I.L.S.f.m. Zhang, *Femtosecond laser micromachining: a back-to-basics primer.* 2012. **7**.
159. Bonse, J., et al. *Femtosecond laser micromachining of technical materials*. in *High-Power Laser Ablation III*. 2000. International Society for Optics and Photonics.
160. Forrester, P., et al. *Effects of heat transfer and energy absorption in the ablation of biological tissues by pulsetrain-burst (> 100 MHz) ultrafast laser processing*. in *Photonics North 2006*. 2006. International Society for Optics and Photonics.
161. Aguilar, C.A., et al., *Direct micro-patterning of biodegradable polymers using ultraviolet and femtosecond lasers.* 2005. **26**(36): p. 7642-7649.
162. Prevosti, S., *Ablation of Si with femtosecond laser*. 2016.
163. Kautek, W., *Physical Chemistry of Ultrafast Laser Interactions with Solids*, in *Laser Ablation and its Applications*. 2007, Springer. p. 215-229.
164. Zhang, D. and L. Guan, *Laser ablation.* 2014.
165. Kautek, W., et al., *Physico-chemical aspects of femtosecond-pulse-laser-induced surface nanostructures.* Applied Physics A, 2005. **81**(1): p. 65-70.
166. Phipps, C., *Laser ablation and its applications*. Vol. 129. 2007: Springer.
167. Eaton, S., G. Cerullo, and R. Osellame, *Thermal writing of photonic devices in glass and polymers by femtosecond lasers*, in *Laser Growth and Processing of Photonic Devices*. 2012, Elsevier. p. 333-373.
168. Jiang, L. and H.-L. Tsai, *Energy transport and material removal in wide bandgap materials by a femtosecond laser pulse.* International Journal of Heat and Mass Transfer, 2005. **48**(3-4): p. 487-499.
169. Vorobyev, A.Y., C.J.L. Guo, and P. Reviews, *Direct femtosecond laser surface nano/microstructuring and its applications.* 2013. **7**(3): p. 385-407.
170. Brunette, D.M., et al., *Titanium in medicine: material science, surface science, engineering, biological responses and medical applications*. 2012: Springer Science & Business Media.
171. Webster, T.J., R.W. Siegel, and R. Bizios, *Nanoceramic surface roughness enhances osteoblast and osteoclast functions for improved orthopaedic/dental implant efficacy.* Scripta Materialia, 2001. **44**(8-9): p. 1639-1642.
172. Ulerich, J.P., et al. *Modifications of Ti-6Al-4V surfaces by direct-write laser machining of linear grooves*. in *Photon Processing in Microelectronics and Photonics VI*. 2007. International Society for Optics and Photonics.

173. Flemming, R., et al., *Effects of synthetic micro-and nano-structured surfaces on cell behavior.* 1999. **20**(6): p. 573-588.
174. Chen, J., et al., *Cell/surface interactions and adhesion on Ti‐6Al‐4V: Effects of surface texture.* Journal of Biomedical Materials Research Part B: Applied Biomaterials: An Official Journal of The Society for Biomaterials, The Japanese Society for Biomaterials, and The Australian Society for Biomaterials and the Korean Society for Biomaterials, 2007. **82**(2): p. 360-373.
175. Chen, J., et al., *An investigation of the initial attachment and orientation of osteoblast-like cells on laser grooved Ti-6Al-4V surfaces.* 2009. **29**(4): p. 1442-1452.
176. Bailly, M. and J. Condeelis, *Cell motility: insights from the backstage*. 2002, Nature Publishing Group.
177. Betke, A. and G.J.I. Kickelbick, *Bottom-up, wet chemical technique for the continuous synthesis of inorganic nanoparticles.* 2014. **2**(1): p. 1-15.
178. Rico, A., M. Garrido, and J.J.B.D.L.S.E.D.C.Y.V. Rodríguez, *The problem of determining Young's modulus and hardness of high stiff ceramics by nanoindentation.* 2008. **47**(2): p. 110-116.
179. Rahimian Koloor, S.S., et al., *Effects of Sample and Indenter Configurations of Nanoindentation Experiment on the Mechanical Behavior and Properties of Ductile Materials.* 2018. **8**(6): p. 421.
180. prize, T.N. *The Nobel prize in physics 2018*. 2018 [cited 2019; Available from: https://www.nobelprize.org/prizes/physics/2018/press-release/.
181. Krüger, J. and W. Kautek, *Ultrashort pulse laser interaction with dielectrics and polymers*, in *polymers and light*. 2004, Springer. p. 247-290.
182. Raja, P.a.B., A. *X-ray Crystallography*. 2019 01/09/2019]; Available from: https://chem.libretexts.org/Bookshelves/Analytical_Chemistry/Book%3A_Physical_Methods_in_Chemistry_and_Nano_Science_(Barron)/07%3A_Molecular_and_Solid_State_Structure/7.3%3A_X-ray_Crystallography.
183. Cullity, B.D. and S.R. Stock, *Elements of X-ray Diffraction*. Vol. 3. 2001: Prentice hall New Jersey.
184. Speakman, S.A., *Basics of X-ray powder diffraction.* Massachusetts-USA, 2011a. Disponível em:< http://prism. mit. edu/xray/Basics% 20of% 20X-Ray% 20Powder% 20Diffraction. pdf, 2011.
185. Stanjek, H. and W. Häusler, *Basics of X-ray Diffraction.* Hyperfine interactions, 2004. **154**(1-4): p. 107-119.
186. Larkin, P., *Infrared and Raman spectroscopy: principles and spectral interpretation*. 2017: Elsevier.
187. El-Azazy, M., *Introductory Chapter: Infrared Spectroscopy-A Synopsis of the Fundamentals and Applications*, in *Infrared Spectroscopy-Principles, Advances, and Applications*. 2018, IntechOpen.
188. Berzina-Cimdina, L. and N. Borodajenko, *Research of calcium phosphates using Fourier transform infrared spectroscopy*. 2012: INTECH Open Access Publisher.
189. Smith, B.C., *Fundamentals of Fourier transform infrared spectroscopy*. 2011: CRC press.
190. Shai, Y.J.B.e.B.A.-B., *ATR-FTIR studies in pore forming and membrane induced fusion peptides.* 2013. **1828**(10): p. 2306-2313.
191. Akhtar, K., et al., *Scanning Electron Microscopy: Principle and Applications in Nanomaterials Characterization*, in *Handbook of Materials Characterization*. 2018, Springer. p. 113-145.
192. Wikipedia. 2019 10/9/2019]; Available from: https://en.wikipedia.org/wiki/Scanning_electron_microscope.

193. Jeol. *SEM scanning electron micrsocopy A to Z*. Available from: https://www.jeol.co.jp/en/applications/pdf/sm/sem_atoz_all.pdf.
194. Lohumi, S., et al., *Raman imaging from microscopy to macroscopy: Quality and safety control of biological materials.* 2017. **93**: p. 183-198.
195. Bumbrah, G.S. and R.M. Sharma, *Raman spectroscopy–Basic principle, instrumentation and selected applications for the characterization of drugs of abuse.* Egyptian Journal of Forensic Sciences, 2016. **6**(3): p. 209-215.
196. Way2Science. *Raman spectroscopy*. 2016; Available from: http://way2science.com/raman-spectroscopy-2/.
197. Spectronic, T.J.T.S., *Basic UV-Vis theory, concepts and applications.* 2012: p. 1-28.
198. Shimadzu. *ABC's of the Diffuse Reflection Method*. 2019; Available from: https://www.shimadzu.com/an/ftir/support/ftirtalk/talk1/intro.html.
199. Torrent, J. and V.J.M.o.s.a.P. Barrón, *Diffuse reflectance spectroscopy.* 2008. **5**: p. 367-387.
200. Bain, G.J.T.F.S., Madison, Wisconsin, *Integrating sphere diffuse reflectance technology for use with UV-visible spectrophotometry.* 2007.
201. Shimadzu. *Diffuse Reflectance measurement*. 2019; Available from: https://www.shimadzu.com/an/molecular_spectro/uv/accessory/solidsample/solid.html.
202. Williams, D.B. and C.B. Carter, *The transmission electron microscope*, in *Transmission electron microscopy*. 1996, Springer. p. 3-17.
203. research, M.t.f.a. *Transmission electron microscopy*. Available from: http://www.ammrf.org.au/myscope/pdfs/tem.pdf.
204. CcBER. *The transmission electron microsscope*. Available from: https://www.ccber.ucsb.edu/collections-botanical-collections-plant-anatomy/transmission-electron-microscope.
205. Joseph, E. and G. Singhvi, *Multifunctional nanocrystals for cancer therapy: a potential nanocarrier*, in *Nanomaterials for Drug Delivery and Therapy*. 2019, Elsevier. p. 91-116.
206. Pepper, I.L., et al., *Environmental microbiology*. 2011: Academic Press.
207. Di Gianfrancesco, A., *Technologies for chemical analyses, microstructural and inspection investigations*, in *Materials for Ultra-Supercritical and Advanced Ultra-Supercritical Power Plants*. 2017, Elsevier. p. 197-245.
208. Olympus. *Basics of inverted microscope*. Available from: https://www.olympusamerica.com/files/seg_bio/basics_of_inv-microscope.pdf.
209. Yuan, Y. and T.R. Lee, *Contact angle and wetting properties*, in *Surface science techniques*. 2013, Springer. p. 3-34.
210. Earnest, B.C.K.P.M.C., *Use of the STA 8000 Simultaneous Thermal Analyzer for Melt Analysis of Alloys.* 2012.
211. Council, N.R., *Beyond the molecular frontier: challenges for chemistry and chemical engineering*. 2003: National Academies Press.
212. Grim, R.E., *Method and application of differential thermal analysis.* Annals of the New York Academy of Sciences, 1951. **53**(5): p. 1031-1053.
213. Coats, A. and J. Redfern, *Thermogravimetric analysis. A review.* Analyst, 1963. **88**(1053): p. 906-924.
214. Edwards, D., *Phase Diagram Determination of Ceramic Systems*, in *Methods for Phase Diagram Determination*. 2007, Elsevier. p. 341-360.
215. GLOBAL, H.H.-T. *Principle of differential thermal analysis (DTA)*. Available from: https://www.hitachi-

hightech.com/global/products/science/tech/ana/thermal/descriptions/dta.html
.
216. Wang, C., X. Zhou, and M.J.M.C. Wang, *Influence of sintering temperatures on hardness and Young's modulus of tricalcium phosphate bioceramic by nanoindentation technique.* 2004. **52**(4-5): p. 301-307.
217. Oliver, W.C. and G.M. Pharr, *An improved technique for determining hardness and elastic modulus using load and displacement sensing indentation experiments.* Journal of materials research, 1992. **7**(6): p. 1564-1583.
218. Zamiri, A. and S.J.J.o.t.m.b.o.b.m. De, *Mechanical properties of hydroxyapatite single crystals from nanoindentation data.* 2011. **4**(2): p. 146-152.
219. Dejun, M., et al., *Determination of Young's modulus by nanoindentation.* 2004. **47**(4): p. 398-408.
220. Chicot, D., et al., *A contact area function for Berkovich nanoindentation: Application to hardness determination of a TiHfCN thin film.* Thin Solid Films, 2014. **558**: p. 259-266.
221. Chanda, A., et al., *Microwave sintering of calcium phosphate ceramics.* 2009. **29**(4): p. 1144-1149.
222. Engstrand Unosson, J., C. Persson, and H. Engqvist, *An evaluation of methods to determine the porosity of calcium phosphate cements.* Journal of Biomedical Materials Research Part B: Applied Biomaterials, 2015. **103**(1): p. 62-71.
223. Mempin, R., et al., *Release of extracellular ATP by bacteria during growth.* BMC microbiology, 2013. **13**(1): p. 301.
224. Muller, M., *Introduction to confocal fluorescence microscopy*. Vol. 69. 2006: SPIE press.
225. Welz, B. and M. Sperling, *Atomic absorption spectrometry*. 2008: John Wiley & Sons.
226. Levinson, R., *More modern chemical techniques*. 2001: Royal Society of Chemistry.
227. Mekmene, O., et al., *Effects of pH and Ca/P molar ratio on the quantity and crystalline structure of calcium phosphates obtained from aqueous solutions.* 2009. **89**(3-4): p. 301-316.
228. Madsen, H.E.L. and F.J.J.o.C.G. Christensson, *Precipitation of calcium phosphate at 40 C from neutral solution.* 1991. **114**(4): p. 613-618.
229. Lee, D. and P.N. Kumta, *Chemical synthesis and stabilization of magnesium substituted brushite.* Materials Science and Engineering: C, 2010. **30**(7): p. 934-943.
230. Wiberg, N., *Holleman-Wiberg's inorganic chemistry.* Academic Press, New York, 2001.
231. Anee, T., et al., *Influence of iron and temperature on the crystallization of calcium phosphates at the physiological pH.* Materials Letters, 2004. **58**(3): p. 478-482.
232. Kannan, S., et al., *Synthesis and structural characterization of strontium-and magnesium-co-substituted β-tricalcium phosphate.* 2010. **6**(2): p. 571-576.
233. Hsieh, C.-T., et al., *Synthesis of iron phosphate powders by chemical precipitation route for high-power lithium iron phosphate cathodes.* Electrochimica Acta, 2012. **83**: p. 202-208.
234. Singh, S., et al., *Synthesis of brushite nanoparticles at different temperatures.* Chemical Papers, 2010. **64**(4): p. 491-498.
235. Mandel, S. and A.C. Tas, *Brushite (CaHPO 4· 2H 2 O) to octacalcium phosphate (Ca 8 (HPO 4) 2 (PO 4) 4· 5H 2 O) transformation in DMEM solutions at 36.5° C.* Materials Science and Engineering: C, 2010. **30**(2): p. 245-254.

236. Corrêa, T. and J. Holanda, *Calcium pyrophosphate powder derived from avian eggshell waste.* Cerâmica, 2016. **62**(363): p. 278-280.
237. Vasant, S.R. and M. Joshi, *Synthesis and characterization of nanoparticles of calcium pyrophosphate.* Modern Physics Letters B, 2011. **25**(01): p. 53-62.
238. Sivakumar, G., et al., *Crystallization and characterization of calcium phosphates: brushite and monetite.* 1998. **33**(2): p. 197-205.
239. Morrissey, R., L. Rodriguez-Lorenzo, and K.J.J.o.M.S.M.i.M. Gross, *Influence of ferrous iron incorporation on the structure of hydroxyapatite.* 2005. **16**(5): p. 387-392.
240. Al-Hasni, B.M., G. Mountjoy, and E. Barney, *A complete study of amorphous iron phosphate structure.* Journal of Non-Crystalline Solids, 2013. **380**: p. 141-152.
241. Mulongo-Masamba, R., et al., *Synthesis and thermal dehydroxylation kinetic of anhydrous calcium phosphate monetite CaHPO 4.* Journal of Thermal Analysis and Calorimetry, 2016. **124**(1): p. 171-180.
242. Boonchom, B. and S.J.P.B.C.M. Puttawong, *Thermodynamics and kinetics of the dehydration reaction of FePO4· 2H2O.* 2010. **405**(9): p. 2350-2355.
243. Okada, S., et al., *Cathode properties of amorphous and crystalline FePO4.* 2005. **146**(1-2): p. 570-574.
244. Li, C.-L., B. Zhang, and Z.-W. Fu, *Physical and electrochemical characterization of thin films of iron phosphate and nitrided iron phosphate for all-solid-state batteries.* Journal of The Electrochemical Society, 2006. **153**(9): p. E160-E165.
245. Cornilsen, B.C., *Solid state vibrational spectra of calcium pyrophosphate dihydrate.* Journal of molecular structure, 1984. **117**(1-2): p. 1-9.
246. De Waal, D. and C. Hutter, *Vibrational spectra of a solid solution of cadmium and calcium pyrophosphate.* Materials research bulletin, 1994. **29**(11): p. 1129-1135.
247. Cornilsen, B., R.J.J.o.I. Condrate Sr, and N. Chemistry, *The vibratonal spectra of β-Ca2P2O7 and γ-Ca2P2O7.* 1979. **41**(4): p. 602-605.
248. Zhang, L. and R.K. Brow, *A Raman study of iron–phosphate crystalline compounds and glasses.* Journal of the American Ceramic Society, 2011. **94**(9): p. 3123-3130.
249. Gozalian, A., et al., *Synthesis and thermal behavior of Mg-doped calcium phosphate nanopowders via the sol gel method.* 2011. **18**(6): p. 1614-1622.
250. Boonchom, B. and S. Puttawong, *Thermodynamics and kinetics of the dehydration reaction of FePO4· 2H2O.* Physica B: Condensed Matter, 2010. **405**(9): p. 2350-2355.
251. Yang, S., et al., *Reactivity, stability and electrochemical behavior of lithium iron phosphates.* Electrochemistry Communications, 2002. **4**(3): p. 239-244.
252. Boonchom, B., C.J.I. Danvirutai, and E.C. Research, *Thermal Decomposition Kinetics of FePO4 ⊙ 3H2O Precursor To Synthetize Spherical Nanoparticles FePO4.* 2007. **46**(26): p. 9071-9076.
253. Toshima, T., et al., *Morphology control of brushite prepared by aqueous solution synthesis.* Journal of Asian Ceramic Societies, 2014. **2**(1): p. 52-56.
254. Suttiponparnit, K., et al., *Role of surface area, primary particle size, and crystal phase on titanium dioxide nanoparticle dispersion properties.* 2011. **6**(1): p. 27.
255. Crespo Petit, F., *Effect of porosity on the mechanical properties of zirconia based ceramics obtained via 3D printing.* 2016.
256. Dey, A. and A.K. Mukhopadhyay, *Nanoindentation of brittle solids*. 2014: CRC Press.
257. Pathak, S., et al., *Understanding pop-ins in spherical nanoindentation.* Applied Physics Letters, 2014. **105**(16): p. 161913.

258. Zhang, T., et al., *Sintering, microstructure and grain growth of Fe-doped Ce0. 9Gd0. 1O2− δ ceramics derived from oxalate coprecipitation.* 2005. **274**(3-4): p. 603-611.
259. Nogueira, R., et al., *Structural and mechanical study of the sintering effect in hydroxyapatite doped with iron oxide.* 2008. **403**(19-20): p. 3826-3829.
260. Chaim, R. and M.J.J.o.m.s. Hefetz, *Effect of grain size on elastic modulus and hardness of nanocrystalline ZrO 2-3 wt% Y 2 O 3 ceramic.* 2004. **39**(9): p. 3057-3061.
261. Nogueira, R., et al., *Structural and mechanical study of the sintering effect in hydroxyapatite doped with iron oxide.* Physica B: Condensed Matter, 2008. **403**(19-20): p. 3826-3829.
262. Silva, C., et al., *Magnetic properties study on Fe-doped calcium phosphate.* Physica Scripta, 2009. **80**(5): p. 055706.
263. Liu, Y., et al., *The transformation from amorphous iron phosphate to sodium iron phosphate in sodium-ion batteries.* 2015. **17**(34): p. 22144-22151.
264. Zhu, Y.-m., et al., *Research status in preparation of FePO 4: a review.* 2014. **20**(11): p. 1501-1510.
265. Wang, W., et al., *A sodium ion intercalation material: a comparative study of amorphous and crystalline FePO 4.* 2015. **17**(6): p. 4551-4557.
266. Hong, Y.-S., et al., *Amorphous FePO 4 as 3 V cathode material for lithium secondary batteries.* 2002. **12**(6): p. 1870-1874.
267. Zeta-Meter, I.J.T.N., *Zeta-Potential: A Complete Course in 5 Minutes.* 1997: p. 1-8.
268. Chen, L.-j., et al., *Effect of Tb/Mg doping on composition and physical properties of hydroxyapatite nanoparticles for gene vector application.* 2018. **28**(1): p. 125-136.
269. Xiao, Y., et al., *Preparation and performance of the cathode precursor ferric phosphate for Li-ion battery facilitated by impinging stream.* Int. J. Electrochem. Sci, 2013. **8**: p. 938-948.
270. Wang, Y., et al., *Ultra-low cost and highly stable hydrated FePO4 anodes for aqueous sodium-ion battery.* Journal of Power Sources, 2018. **374**: p. 211-216.
271. Zhang, L., *Phase equilibria in iron phosphate system.* 2010.
272. Madsen, H.E.L.J.J.o.C.G., *Influence of foreign metal ions on crystal growth and morphology of brushite (CaHPO4, 2H2O) and its transformation to octacalcium phosphate and apatite.* 2008. **310**(10): p. 2602-2612.
273. Tampieri, A., et al. *Magnesium doped hydroxyapatite: synthesis and characterization*. in *Key Engineering Materials*. 2004. Trans Tech Publ.
274. Bigi, A., et al., *Rietveld structure refinements of calcium hydroxylapatite containing magnesium.* Acta Crystallographica Section B: Structural Science, 1996. **52**(1): p. 87-92.
275. Boanini, E., M. Gazzano, and A. Bigi, *Ionic substitutions in calcium phosphates synthesized at low temperature.* Acta biomaterialia, 2010. **6**(6): p. 1882-1894.
276. El-dek, S., et al., *Microstructural features of flower like Fe brushite.* 2017. **27**(4): p. 520-526.
277. Nabiyouni, M., *Doctor of Philosophy Degree in Engineering*. 2014, The University of Toledo.
278. Karthika, S., et al., *A review of classical and nonclassical nucleation theories.* 2016. **16**(11): p. 6663-6681.
279. Zyman, Z.Z., A.V. Goncharenko, and D.V. Rokhmistrov, *Phase evolution during heat treatment of amorphous calcium phosphate derived from fast nitrate synthesis.* Processing and Application of Ceramics, 2017. **11**(2): p. 147-153.

280. Zyman, Z.Z., et al., *Phase evolution during heat treatment of amorphous calcium phosphate derived from fast nitrate synthesis.* 2017. **11**(2): p. 147-153.
281. Liu, X., S. Shen, and A.J.J.o.m.r. Jha, *Investigation on the kinetics of devitrification of GeS 2-based glasses.* 2005. **20**(4): p. 856-863.
282. Avrami, M.J.T.J.o.c.p., *Granulation, phase change, and microstructure kinetics of phase change. III.* 1941. **9**(2): p. 177-184.
283. Frasnelli, M., *Calcium Phosphate Powders for Biomedical Applications: Synthesis, Thermal Behavior and Non-Conventional Sintering*. 2018, University of Trento.
284. Bretcanu, O., et al., *Sintering and crystallisation of 45S5 Bioglass® powder.* Journal of the European Ceramic Society, 2009. **29**(16): p. 3299-3306.
285. Jordan, W. and A.J.J.o.t.a. Jha, *A review of the role of DSC analysis in the design of fluorozirconate glasses for fibre optic applications.* 1994. **42**(4): p. 759-770.
286. Blake, A.J., et al., *Crystal structure analysis: principles and practice*. Vol. 13. 2009: Oxford University Press.
287. Gamal, G., et al., *Effect of iron additives on the microstructure of hydroxyapatite.* 2013. **3**(6): p. 532-539.
288. Yang, H., et al., *Evaluation of the volume fraction of nanocrystals devitrified in Al-based amorphous alloys.* 2009. **355**(4-5): p. 235-238.
289. Cei, S., et al., *Effect of laser micromachining of titanium on viability and responsiveness of osteoblast-like cells.* 2011. **20**(4): p. 285-291.
290. Bonse, J., et al., *Ultrashort-pulse laser ablation of indium phosphide in air.* 2001. **72**(1): p. 89-94.
291. Liu, J.J.O.l., *Simple technique for measurements of pulsed Gaussian-beam spot sizes.* 1982. **7**(5): p. 196-198.
292. Nathala, C.S., et al., *Ultrashort laser pulse ablation of copper, silicon and gelatin: effect of the pulse duration on the ablation thresholds and the incubation coefficients.* 2016. **122**(2): p. 107.
293. Gonzales, P., et al. *Femtosecond ablation scaling for different materials*. in *International Congress on Applications of Lasers & Electro-Optics*. 2003. LIA.
294. Schmid-Beurmann, P.J.J.o.S.S.C., *Synthesis and phase characterization of a solid solution series between β-Fe2 (PO4) O and Fe4 (PO4) 3 (OH) 3.* 2000. **153**(2): p. 237-247.
295. Tortet, L., et al., *Study of protonic mobility in CaHPO4· 2H2O (brushite) and CaHPO4 (monetite) by infrared spectroscopy and neutron scattering.* Journal of solid state chemistry, 1997. **132**(1): p. 6-16.
296. Bouamer, H.O., et al., *Growth and characterization of electrodeposited orthorhombic FePO4. 2H2O material.* 2018.
297. Burba, C.M. and R. Frech, *Vibrational spectroscopic investigation of structurally-related LiFePO4, NaFePO4, and FePO4 compounds.* Spectrochimica Acta Part A: Molecular and Biomolecular Spectroscopy, 2006. **65**(1): p. 44-50.
298. Kautek, W., et al. *Ultrashort pulse lasers: new aspects of materials interaction*. in *High-Power Laser Ablation V*. 2004. International Society for Optics and Photonics.
299. Zhang, Y., D. Tzou, and J.J.a.p.a. Chen, *Micro-and nanoscale heat transfer in femtosecond laser processing of metals.* 2015.
300. Gamaly, E.G., et al., *Ablation of solids by femtosecond lasers: Ablation mechanism and ablation thresholds for metals and dielectrics.* 2002. **9**(3): p. 949-957.
301. Thomas, M. and K. George, *Characterisation and magnetic properties of nanocrystalline FePO 4.* 2010.

302. Ji, P. and Y.J.A.P.A. Zhang, *Melting and thermal ablation of a silver film induced by femtosecond laser heating: a multiscale modeling approach.* 2017. **123**(10): p. 671.
303. Chichkov, B.N., et al., *Femtosecond, picosecond and nanosecond laser ablation of solids.* 1996. **63**(2): p. 109-115.
304. Domański, R., M. Jaworski, and M.J.J.o.P.T. Rebow, *Laser Radiation Interaction with Solids.* 1995. **79**.
305. Xia, Y., et al., *Injectable calcium phosphate scaffold with iron oxide nanoparticles to enhance osteogenesis via dental pulp stem cells.* Artificial cells, nanomedicine, and biotechnology, 2018: p. 1-11.
306. Wang, Q., et al., *Response of MAPK pathway to iron oxide nanoparticles in vitro treatment promotes osteogenic differentiation of hBMSCs.* Biomaterials, 2016. **86**: p. 11-20.
307. Tran, N., D. Hall, and T.J. Webster, *Mechanisms of enhanced osteoblast gene expression in the presence of hydroxyapatite coated iron oxide magnetic nanoparticles.* Nanotechnology, 2012. **23**(45): p. 455104.
308. Tran, N. and T.J. Webster, *Increased osteoblast functions in the presence of hydroxyapatite-coated iron oxide nanoparticles.* Acta biomaterialia, 2011. **7**(3): p. 1298-1306.
309. Feng, B., et al., *Characterization of surface oxide films on titanium and adhesion of osteoblast.* 2003. **24**(25): p. 4663-4670.
310. Curtis, A., et al., *Adhesion of cells to polystyrene surfaces.* 1983. **97**(5): p. 1500-1506.
311. Kim, S.-Y., et al., *Effect of topographical control by a micro-molding process on the activity of human Mesenchymal Stem Cells on alumina ceramics.* 2015. **19**(1): p. 23.